COMPACT TEST PLATFORM FOR IN-SITU INDENTATION AND SCRATCHING INSIDE A SCANNING ELECTRON MICROSCOPE (SEM)

THÈSE N^{O} 3593 (2006)

PRÉSENTÉE LE 18 AOÛT 2006

À LA FACULTÉ DES SCIENCES ET TECHNIQUES DE L'INGÉNIEUR

Laboratoire de systèmes robotiques 2

SECTION MICROTECHNIQUE

ÉCOLE POLYTECHNIQUE FÉDÉRALE DE LAUSANNE

POUR L'OBTENTION DU GRADE DE DOCTEUR ÈS SCIENCES

PAR

Rodolfo RABE

Master en sciences mécaniques, Université Fédérale de Santa Catarina, Brésil
de nationalité brésilienne

acceptée sur proposition du jury:

Prof. P. Renaud, président du jury
Dr J. M. Breguet, Dr J. Michler, directeurs de thèse
Prof. M. Troyon, rapporteur
Dr B. Bellaton, rapporteur
Dr Y. Leterrier, rapporteur

ÉCOLE POLYTECHNIQUE
FÉDÉRALE DE LAUSANNE

Lausanne, EPFL
2006

Abstract

In-situ materials tests have the advantage to link visual and sensor based information during a dynamic experiment.

In this thesis, a compact indenter-scratch test device has been built at EPFL-LSRO and installed inside a Scanning Electron Microscope (SEM) at EMPA-Thun. This indenter has been designed having high resolution and long-range stick-slip piezoelectric actuators to position and test the samples.
The combination of the SEM high magnification / high depth of focus images and the high resolution positioning system has permitted to identify and test very particular regions of interest. The output of the test is an associated video/image sequence with the Load – Penetration depth (P x h) graph.

The stick-slip actuator is a special type of inertial drive. Its working principle uses a stick phase (static friction) to drive and a quick redraw movement to create the slip phase (using dynamic friction). The movement is thus a sequence of 300-400nm steps. The drawback is an inherent backlash (from 30-100nm) and a microvibration after each slip phase. A rather low driving force (≈ N range) is another known limitation of stick-slip actuators.

The first contribution of this thesis has been to evaluate the impact of using stick-slip actuators to realize indentation and scratching. For this, different materials have been tested with Cube Corner and Berkovich tips in two driving modes – continuous and stick-slip mode. The comparison has been realized visually (videos, pictures) and through the P x h graph. Scratch test has also been performed in these two driving modes, but has been limited to visual comparison only.

Results during indentation have not shown perceptible differences in the P x h graphs nor in the image obtained in both modes. The P x h curve overlap has been mainly congruent in both driving modes. This has been assessed in Fused Silica, GaAs and Zn-BMG. However, a scratch in AlCu, Zr-BMG and in GaAs has revealed the presence of a visual pattern, which has been related to the actuator's slip phase. The results are discussed in the text.

The second contribution is the optimization of stick-slip actuators. The goal was to obtain a given driving force with a minimum amount of jump-back. Various solutions have been proposed and then validated through simulations and experiments. A reduction of the jump-back size by factor of four has been achieved. This is considered to be the demonstration of the promising potentialities of the proposed methods.

The work also includes a design guide for a SEM environment as well as an overview of several tests that have been made using the in-situ indenter. Examples apart from nanoindentation are surface patterning capability and micropillars compressions tests.

The thesis has successfully demonstrated that stick-slip actuators can be an option to build compact and SEM compatible devices for material characterization, and especially for a SEM-indenter.

Keywords: SEM in-situ material tests, piezoelectric actuators, precision engineering

Kurzfassung

In-situ Materialtests haben den Vorteil, dass sie während eines dynamischen Experiments visuelle und sensorische Informationen verbinden können.

In dieser Doktorabeit wurde eine kompakte Eindruckversuch-Ritzversuch-Vorrichtung an der EPFL-LSRO entwickelt und in ein Raster-Elektronenmikroskop (REM) der EMPA Thun eingebaut. Dieser Indenter wurde mit einem piezoelektrischen Stick-slip-Antrieb mit hoher Auflösung und grossem Verfahrweg entworfen, um Proben zu positionieren und prüfen zu können.

REM-Bilder mit hoher Vergrösserung und grosser Tiefenschärfe kombiniert mit einem hochauflösenden Positionierungssystem liessen genauere Untersuchungen von speziell interessierenden Materialregionen zu. Der Output des Tests ist eine gekoppelte Video-Bildsequenz mit einem dazugehörenden Graph, der die Beziehung Ladung-Eindringungstiefe beschreibt (P x h).

Der Stick-slip-Antrieb ist ein spezieller Trägheitsantrieb. Sein Funktionsprinzip beinhaltet eine Haftphase (statische Reibung), als Antrieb und ein schnelles Rückzugsmoment, um die Gleitphase zu erzeugen (mit dynamischer Reibung). Die Bewegung besteht deshalb aus einer Abfolge von 300-400nm grossen Schritten. Die Beeinträchtigungen sind ein dem System anhaftender Rückschlag (von 30-100nm) und eine Mikrovibration nach jeder Haft-Gleitphase. Eine eher niedriege Antriebskraft (≈ N) ist eine weitere bekannte Einschränkung des Stick-slip Antriebs.

Das erste Ziel dieser Arbeit war, den Einfluss zu bewerten, welcher der Stick-slip-Antrieb auf den Eindruckversuch und den Ritzversuch hat. Dazu wurden verschiedene Materialien mit Cube-Corner-Eindringkörper und Berkovich-Spitzen getestet. Es wurden dabei zwei unterschiedliche Antriebsmodi verwendet: Ein kontinuierlicher Modus und ein haft-gleit Modus. Der Vergleich der Einschnitte wurde sowohl visuell (Video und Bilder) als auch anhand der P x h – Graphen durchgeführt. Der Ritztest wurde ebenfalls in diesen beiden Modi durchgeführt, aber liess nur einen visuellen Vergleich zu.

Die Ergebnisse der Eindruckversuche haben weder wahrnehmbare Unterschiede in den P x h –Graphen ergeben, noch gab es in den beiden Modi Bildunterschiede. Die Überlappung der P x h –Graphen war grösstenteils deckungsgleich in beiden Antriebsmodi. Das wurde anhand Quarzglas, GaAs und Zn-BMG gezeigt. Aber das Einritzen in AlCu, Zr-BMG und GaAs hat sichtbare Muster hervorgebracht, welche der Gleitphase des Antriebs zugeschrieben werden. Die Ergebnisse werden im Text diskutiert.

Das zweite Ziel war, den Haft-Gleit-Antrieb zu optimieren. Es wurde der Frage nachgegangen, Wie mit einem Minimum an Rückstoss eine gegebene Antriebskraft erreicht werden kann. Hypothesen sind auf gestellt und mit Simulationen und

Experimenten geprüft worden. Es wurde eine Reduktion der Rückstossamplitude um den Faktor vier erreicht. Dies wird als Bestättigung des vielversprechenden Potentials der vorgeschlagenen Methoden angesehen.

Die Arbeit beeinhaltet ebenfalls Konstruktionsrichtlinen für Aufbauten in einem REM sowie einen Überblick über verschiedene Experimente, die mit dem in-situ Indenter durchgeführt wurden. Neben Nanoindentation sind dies beispielsweise Oberflächenstrukturierungen oder Mikrosäulen Kompressionstests.

Diese Doktorarbeit hat erfolgreich gezeigt, dass Stick-slip - Antriebe eine Möglichkeit bieten, um kompakte und SEM kompatible Vorrichtungen zur Materialuntersuchung zu bauen.

Stichwörter: REM in-situ Materialtests, Piezoelektrische Aktoren, Feinwerktechnick

Acknowledgements

And everything has initiated, almost by chance, during a visit to a starting nanomechanics group at EMPA-Thun.
Life can provide us with a lot of chances (and challenges), but good luck is just a starting point. Thus, what at the end will make us to reach the goals are our strength values and certainly, all the cooperation and support from those people that once we had the chance to know.

It makes therefore sense to start the acknowledgments with my many thanks to Dr. Jean-Marc Breguet and Dr. Johann Michler for accepting the task of supervising me in quite different domains: Precision robotics and material characterization. I wish that this fruitful association will continue to attract more people into this nice mix of subjects.
I would also like to extend my acknowledgments to Dr. Lukas Rohr (EMPA-Thun) and Prof. Reymond Clavel (EPFL-LSRO) for supporting me as a part of their respective research groups.

Many thanks go to the jury members, Prof. Michel Troyon (Université de Reims Champagne Ardenne), Dr. Bertrand Bellaton (CSM-Instruments) and Dr. Yves Leterrier (EPFL- LTC) for having accepted to evaluate my work as well as to Prof. Philippe Renaud for having headed the PhD defense.

EMPA and EPFL have given to me a nice working place, and the chance to meet many people in different fields of expertise.
In the Nanomechanic group at EMPA-Thun, many thanks go to Patrick Schwaller and Benedikt Moser (specially for the unofficial supervision and everything concerning indentation), Stephan Fahlbusch (for all the discussions concerning nanomanipulation and integration inside the SEM), Kilian Wasmer and Cédric Pouvreau (for many of the nice recent works using the SEM indenter) and to Sven Stauss (for the feedbacks at the earlier stages of in-situ indentation inside a SEM). Thanks also to Gerhard Bürki for all the help with the SEM – and to many other actual and former colleagues from this and other EMPA groups.

At EPFL-LSRO high precision robotics group, many thanks go to: Arvid Bergander, Walter Driesen and Sébastien Mazerolle (for all the discussion and answers concerning microrobotics, piezos and mechanical design), Tierry Varidel and Robert Dunsch (for the help with electronics, tips about control and, why not, subjects outside engineering) and for the new colleagues Fabian Kaegi and Thomas Cimprich. Thanks also to all LSRO members and for the students that I had the chance to have in semester or diploma projects. There is no better way to learn than by coaching.

Special thanks to the administrative support given by Heidi Banz (LSRO) and Katrin Gurtner (EMPA-Thun). To the *mécaniciens* from EPFL – IPR's Atelier, who were

able to perfectly give form to my (sometime crazy) mechanical designs. Thanks for all the technical staff at EMPA and EPFL for the hardware-software support.
An unquestionable *herzliches Dankeschön* to Stephanie (for her love and an almost endless Swiss patience) as well as to the Schmidlin-Schwyzer family. A special *obrigado* to my family and all the phone-news during these last five years. Finally, a warm thanks to my good old (and new) friends at both sides of the Atlantic. There is nothing better than a good conversation to calm some *unruhige Gefühle* / *inquietudes* when life and heart are being shared between two continents.

List of Symbols

F_{vc}	Force generated in a voice coil actuator
F_a	Generated force (parallel) in an electrostatic actuator
F_x	Generated force (normal) in an electrostatic actuator
F_b	Blocking force of a piezoactuator
A	Projected area of an indentation tip
$\theta°$	Tip semi angle
$\alpha(°)$	Effective cone angle
β	Tip Geometry correction factor
P	Indentation force
h	Penetration depth
P x h	Indentation graph
h_r , h_p	Size of the residual imprint
h_e , h_a	Size of the imprint elastic deformation
h_t	Total penetration depth
S	Unloading stiffness
h_{raw}	Uncorrected penetration depth
h_c	Corrected penetration depth
C_f	Instrument frame compliance
E	Material Young's modulus
H	Material hardness
E^*, E'	Combined material Young's modulus
ν	Material Poisson' coefficient
σ_y	Material yielding stress
σ_u	Material stress at 29% strain
ϕ, ψ	Curve loading fitting parameters
B, m	Curve unloading fitting parameters
P_t	Maximum indentation force
h_t	Maximum indentation depth
P_l, P_u	Force during loading, unloading
h_l, h_u	Indentation depth during loading, unloading
θ	Ration between σ_y and σ_u
K_{spl}	Sample stiffness
K_{inst}	Combined instrument frame stiffness
m	Combined weight mass-holder
C_{inst}	Instrument combined damping
c_f	Stick-slip actuator foot damping
k_f	Stick-slip actuator foot stiffness
F_N	Actuator preload normal force
m_f	Mass of the stick-slip foot
x_f	Movement amplitude of the stick-slip foot
g	Gravity
$\dot{x}$	Relative velocity between foot and carrier

σ_0	Foot-carrier tangential contact stiffness
σ_1	Foot-carrier damping coefficient
σ_2	Foot-carrier viscous friction coefficient
$g(\dot{x})$	Stribeck effect
α_c	Tilted angle (stick-slip foot, carrier)
v_s	Foot-carrier viscous friction coefficient
F_{col}	Coulomb (dynamic) friction force
F_{sta}	Static friction force
μ_{col}	Coulomb (dynamic) friction coefficient
μ_{sta}	Static friction coefficient
δ_y	Parasitic vertical movement of a parallelogram table
σ	Stress
$\varepsilon, \dot{\varepsilon}$	Strain, strain rate
$\dot{P}$	Loading rate
K_c	Fracture toughness
B	Magnet - flux density
$\emptyset$	Magnet – flux
B_r	Magnet - remanent flux density
H_c	Magnet - coercivity of the material
BH_{max}	Magnet - maximum energy product

Table of contents

Chapter 1

Dynamic Experiments in the SEM and Work Overview

1.1 Materials testing

Materials testing is a specific field that is constantly being pushed to contribute more to the development of materials for micro parts/components. In order to gain a fundamental understanding of the material properties at micro scales, like failures or its non-conformities, there is an increasing demand to have the possibility to observe the material's microscopic behavior during testing or during some typical operations as cutting, cleaving, stretching, bending, etc.
In this case the possibility to observe in locus what is happening provides additional support for the standard sensor based measurements and consequently a more accurate result interpretation [1].

One of the basic tests is to determine the material's fundamental mechanical properties like Elastic modulus (***E***), hardness (***H***), Poisson ratio (***ν***), toughness, etc. that are properties of a material that involves a relation between stress and strain or elastic/inelastic reactions of a material to an external force.
Thus, different devices can be used to determine these properties.

- Tensile tests can be used to determine Young's modulus, stress/strain curves; hardness and other important information like yield strength, ultimate strength, etc.
- Torsion and bending devices can also be used to determine these properties and are common in studies of delamination, fracture toughness and so on.
- Hardness test mainly is used to, as the name indicates, to determine the resistance of the material against a penetration of another material. It can also be used to correlate hardness and strength or even fracture toughness in ceramics, since the device provides directly the facilities to visualize and measure the crack length.
- Acoustic emission test are used to determine the Young's modulus.
- Instrumented Indentation combines in one device the capabilities to determine the properties mentioned above [1].

For each sample to be studied there is a procedure (and a device) that can cover most of the parameters to be measured. For example, tensile testing allows calculating a number of materials properties in a straightforward way.
However, the measurement itself imposes restrictions. Bending and tensile tests need a sample in a standard shape. These are additional steps to realize a measurement and limit the possibility to analyze straightforwardly a material on its original shape.

Moreover, these tests are considered as a destructive test and are used for microscopic samples that can be produced and handled easily.

A hardness test can be used in in-situ (directly over a part) and in small portions of the material. The requirement is an imprint able to be measured with accuracy. Thus, the imprint can have few micrometers in size, if an optical microscope with high magnification is used. This can define the method as a non-destructive test.
Among several methods to test and characterize mechanical properties, Instrumented Indentation Testing (IIT) is one of the most versatile methods, as almost any mechanical property determined through uniaxial tension or compression can also be measured or estimated by IIT. [2-4]
Originally, IIT is an extension of the hardness test. It has been developed as a new method to calculate the mechanical properties without the need to measure the imprint size. The method has gained its bases with continuous recording of the indentation test as originally developed in the former Soviet Union [5]. This has been possible once the attention has also been turned to the fact that recording load and displacement during the indentation could provide a "fingerprint graph" of the material, where hardness and Young's modulus could be determined [1].
The IIT method correlates indirectly the contact area (imprint), using the depth of penetration of the tip into the surface. No more direct imprint measurement is required, speeding up the test. In addition, it becomes possible to realize tests where the required indentation depth generates shallow imprints, difficult to be measured with an optical microscope.
Finally, mechanical properties of thin films, coating deposited over a bulk substrate or a surface treatment that changes the original material surfaces properties on submicron depth, can be better characterized. New and specific measurements could be developed. Some typical examples are polymers (viscoelasticity) or thin films (adhesion and friction coefficient through scratch – a modification of IIT).

Investigations on IIT have started in the late 1970's and since then many articles have been written about interpretation of indentation data, application domains (detection of cracking, phase transformation) and possible extension techniques to very small volumes of materials. The latter is today more known as nanoindentation techniques.
As the load requirements are now in the sub-micro Newton range, the scale of deformation in a nanoindentation test became comparable to the size of the material defects like dislocations and grain sizes [6]. Hence, assumptions and equations used to determine the residual impression (called contact area in nanoindentation) from the measured indentation depth are not longer reliable. Lack of proper procedure[2] is not the unique source of errors for determining the mechanical properties. At this scale, small amounts of material shaping up around the tip (sink-in or pile-up) modify the size of the contact area to be determined [5, 6] but they have not been considered on the calculus except if corrected once its existence is later observed or previously documented for the material in test.

As imprints in nanoindentation are far from the resolution of an optical microscope, additional ways have been developed to measure the imprint size. In particular

[1] A description of the load-displacement curves as well as its main parameters will be introduced in Chapter 2.
[2] Tip calibration, surface preparation, drift compensation, initial penetration depth, etc.

Atomic force microscopy, scanning tunneling microscopy and scanning electron microscopy has been used to measure the imprint size.
Although most factors affecting nanoindentation data have been studied and well characterized (as instrumented indentation is a standard test today), there are still demands to visualize the imprint during the test (in-situ indentation).

1.2 In-situ observation of material testing

As previously mentioned, there are several devices that can be used for material characterization and the interest to see the material behavior during the test. This is even more interesting (and difficult) when the focus is on its microscopic behavior.
Bending and tensile/compressing stages to be installed inside the SEM are available since several years as products [7]. Moreover, they have been used in transmission electron microscopes (TEM) since earlier 1960s, although, at that time, only for visualization purposes (no mechanical measurements) [8]. Push-Out stages have been developed to study fibers bond strength with composite materials [9]. Indentation stages to be used inside the TEM have been employed to visualize material nucleation, dislocations propagation during nanoindentation [10] and an in-situ TEM device is also commercialized [11]. Micro hardness tests have been built in a SEM for better imprint measurement and fracture toughness calculation at very low loads [12, 13]. Scratch tests have also been performed inside the SEM [14] to model the interaction of an abrasive particles with the material.
The conceptions of these devices are similar, as a continuous mechanical deformation of the material is required to enable dynamic observation of dislocation, movements, formation and propagation of micro cracks or sliding of grain boundaries. In addition, these processes can be better explained from direct observation.
An instrumented indentation test in the SEM (SEM indentation) is one of these devices adapted to realize dynamic tests with image feedback (in-situ indentation – as shown in Figure 1.1), with the additional advantage to correlate images with the information output by the Force x Displacement graph (indentation graph).

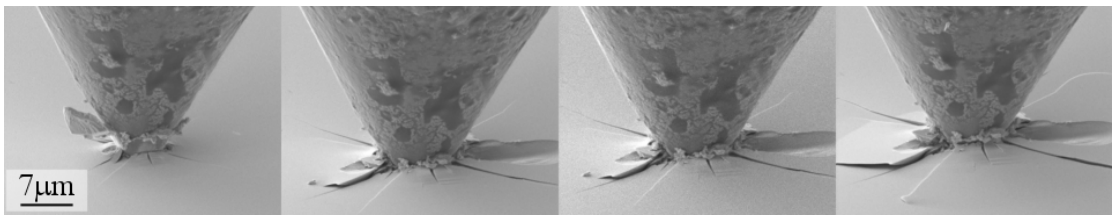

Figure 1.1: A picture sequence of in-situ indentation[3] in GaAs with a 60° conical tip. SEM observation provides quick change in magnification and sharper images with higher depth of focus when compared with optical microscopes at same magnification.

1.3 SEM indentation

Publications related to in-situ indentation have shown more interest in the microstructure behavior of the material rather than in topographical analysis. This explains the reason for more developments for TEMs than for SEMs.
In addition, observing the material's behavior around the tip during Nanoindentation can mean to observe events that are very close to the image resolution provided by the SEM, being very time demanding to be obtained. Typical in-situ applications in nanoindentation cannot be defined as dynamic observation, since the imprint analysis

[3] Source, Cédric Pouvreau, EMPA-Thun

(mainly by AFM) is actually a post indentation analysis. Nevertheless, it has been proven very useful to analyze piling-ups, sinking-ins and measuring crack length. Today an AFM facility is available as an option in different commercial nanoindenters.

Performing in-situ nanoindentation in the SEM can be difficult but in terms of design constraints, it should have fewer restrictions than for TEMs. Thus, this cannot justify the reason of so few experiments involving in-situ nanoindentations and even indentations at a higher scale (up to microindentation).
Events shown in a indentation graph like pop-in (a discontinuous load displacement event during indentation), pop-out (during unload), crack formation during loading-unloading and everything else that can be observed around the indentation tip can be correlated to images, helping to understand material behavior at several ranges of indentation forces.
A SEM indenter has been developed during the Robosem project [15] for helping material researches to better study the material behavior during indentation [16, 17]. The indenter has then be adapted to perform other typical tests like scratch or milling in exploratory experiments [18, 19].

1.4 Motivation and contributions

The research/development stage of a new products or devices involving micro scale demands adequate tools, for example commercial Nanoindenters. Unfortunately, for a specific need, not always a specific tool is directly available. Thus, it may demand a lot of adaptations and creativity. This requires time and slows down the research itself. Based on several technologies available today for macropositioning, load and measurement systems, the final goal of this work is to propose a compact platform for material characterization to work inside a SEM.

This work results in a test platform oriented for material characterization inside the SEM. Piezoactuators (inertial/impact drives) and flexure mechanisms can be combined in order to study solutions for an indenter/scratch device.
The originality will be to study the viability to use stick-slip actuators (Figure 1.2) as a tip driving principle to realize material characterization. These compact and long-range actuators have nanometric resolution; can be easily integrated in the instrument, what could significantly reduce the size of an SEM indenter. In addition, stick-slip actuators are easy to control, providing a fast and easy setup of the indenter.

However, they are not free of drawbacks. As shown in Figure 1.2, at the same time they generate micro vibrations and jump-back movements.

Low driving force is another of its known limitations. This could restrict their applications for indentation or scratching. This study will first identify the impact of these effects on material characterization, identifying the limits of this technology for this application. Secondly, solutions will be proposed to bypass those limits identified during the first part of the study.

This thesis will thus contribute in two fields: Providing a better knowledge of stick-slip actuators and a better knowledge of material characteristics at the nanometer scale by allowing new investigations and tests inside the SEM. It is also expected that this indenter/scratch device will be used in the future for other applications such as the

creation of micro patterns or micro milling, using a diamond tool in virtually any kind of material. This opens further possibilities for new research on areas such as manufacturing of optics, microelectronics, etc.

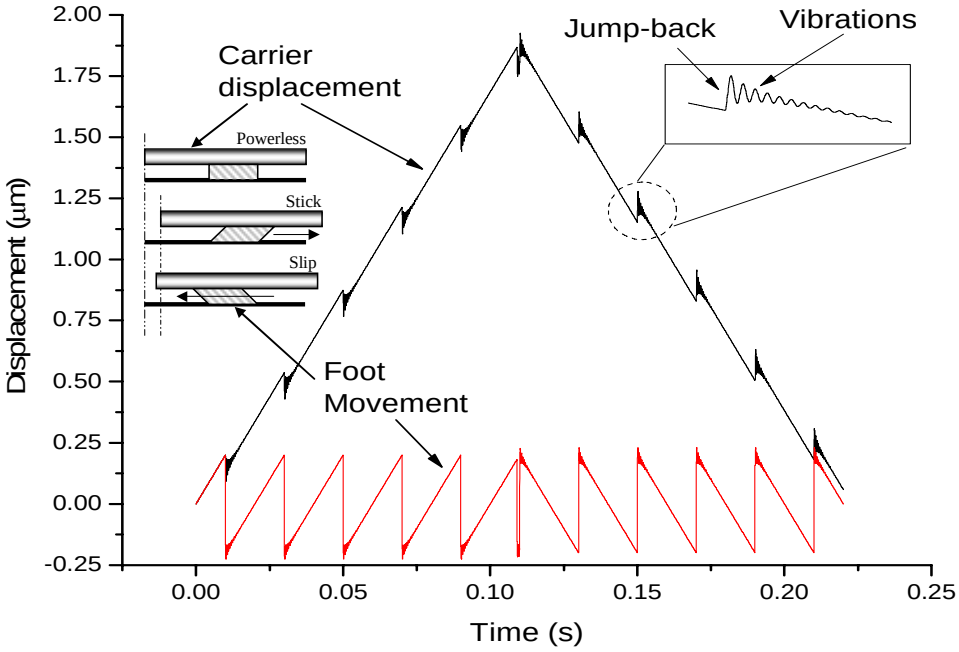

Figure 1.2: Simulation of a two-direction displacement of a carrier driven by a stick-slip actuator. Changing the driving direction is given by the way as the foot is driven. Detail shows typical vibrations present after each slip phase.

1.5 Thesis structure

Chapter 2 will introduce the main topics related to a compact platform for in-situ material tests inside a SEM. This includes an overview of a Scanning Electron Microscope (SEM), actuators usually utilized in micro-nano positioning systems, indentation tips and finally the characteristics and outputs of a material test through instrumented indentation (the Force x Displacement - P x h - indentation graph).

Chapter 3 will be focused on computational modeling of what could be an indentation or scratch being realized by a special kind of actuator also known as stick-slip actuators. The result will be used to evaluate some specific designs of very compact indenters as well as to point out any restriction in using this kind of this driving principle in micro/nanoindentations as well as for scratching.

Complementing simulation, Chapter 4 will present experiments comparing the results on indentation and scratch in two modes: a continuous indentation movement (as available in commercial nanoindenters) and through stick-slip. Experiments will be carried out by in-situ tests (using a IIT designed for working inside a SEM) and using a simple stick-slip indenter built to work outside the SEM. Comparisons between both driving modes are also realized comparing the load-displacement behavior.

Chapter 5 will be a design guide based on what has been observed in Chapter 3 and 4. The outputs are new proposals involving stick-slip actuators in material testing or any application involving manipulation inside a SEM. A more practical contribution is a compact material test platform to be installed inside a SEM.

Finally, Chapter 6 will present applications where the compact material test platform (simply called SEM indenter) has been utilized in material research. As new ideas and applications appeared during research, new functionalities had to be included in the original instrument design. This has opened new fields where a compact IIT device could be applied, as it will be shown in this chapter.

Chapter 2

Basics of In-situ Indentation / Scratching

2.1 Introduction

In this chapter, the main components of an in-situ indentation/scratching test will be presented. This will include the main components of a scanning electron microscope, type of actuators normally used in commercially available nanoindenters, types of indentation tips and finally the P x h graph, that correlates force and indentation depth obtained from an IIT (or depth sensing) device.
These introductions will be necessary to better explain the role of the mentioned components during the design of a material test platform to work inside the SEM, as:

- The actuator used for sample positioning and/or indentation must be compatible with the SEM environment.
- Tip geometry can make in-situ indentation difficult, as the setup must be tilted to avoid the obstruction of the viewpoint by the tip.
- In the way as reaction forces faced by the test platform (and consequently by the actuators) could be described and characterized during indentation.

2.2 Scanning electron microscope

Since the environment to provide direct visualization of the test is a SEM, a quick introduction is presented, already focusing on the relevant points related to in-situ indentation. The goal is to show how a device placed inside the SEM can interact with the microscope itself, even disturbing the image.

2.2.1 From light to electrons

The advantage of electrons for direct dynamic observation begins when the event to be observed is below the resolution of an optical microscope (less than 1μm) and/or when high depth of focus is required.
The resolutions of the new SEMs (between 5nm for thermionic guns up to less than 1 nm for cold field emission sources) may still be inferior than easily achieved in a TEM. However, compared to TEM, the SEM sample preparation is easier. Since the electron beam does not need to go through the sample, as in a TEM, the surface (or even just below it) of bulk materials can be directly observed in a SEM [20].
SEMs are on the market since 1965 (Cambridge Instrument Company) and since then a standard tool in research or technology field. Since its introduction, several devices have been added to extend SEM capabilities, such as for chemical, electrical, crystallographic observations and so on [21]. However, topographic observation is still the main use of SEMs. For the specific field of in-situ indentation its main utilization is for dynamic topographic observations at a sufficiently high magnification, so that individual events can be observed in details [8].

2.2.2 Image formation:

A SEM image is formed when electrons from an electron source (electron gun - Figure 2.1) hit the sample in a raster mode (point by point, forming a 2D matrix). At the same time the electrons generated by the interaction between the incident electron and the sample create a range of electrons or electromagnetic radiations that are picked-up by a specific set of detectors. The signal is then amplified and processed.
Each of these points will output an energy that is related to the sample topography and composition. Therefore, each point of the matrix corresponds to a 2D coordinate on the sample and the signal intensity (often a calibrated grayscale value) can be considered as its 'height'. Finally, each fully defined point is calibrated to correspond to a pixel in the image, as for example a screen. Magnification is a ratio of the size of the displayed image to the size of the area being viewed.

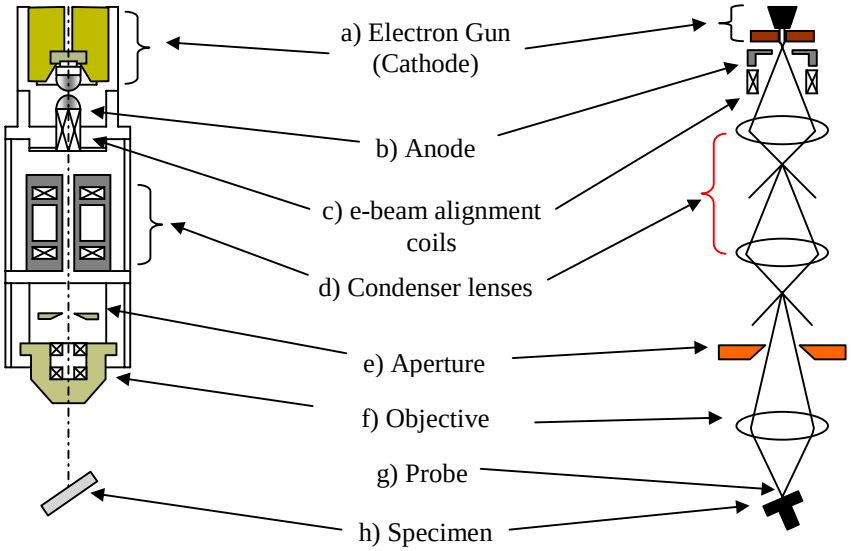

Figure 2.1: Overview of a SEM column (left) and beam formation (right) (from a Zeiss DSM 962)

Figure 2.1 shows an overview of a typical SEM column. A Thermionic, Schottky or Field Emission cathode creates electrons that are accelerated through a voltage differential (0.1-50keV) between the cathode and the anode (*a*, *b*). Similar to an optical microscope, the electron gun is in charge to "illuminate the surface"[4]. Each type of the cathodes referenced above will provide a maximum brightness (amount of current), proportional to the voltage applied to the gun (anode-cathode). Schottky or Field Emission guns can provide higher brightness compared to Thermionic guns. [20]
Then, the beam must be condensed (through electromagnetic or electrostatic lenses, (*c*, *d*) until the objective lens (*f*) produces a small electron probe at the sample (*h*). The probe size is what gives the microscope its theoretical resolution. Unfortunately, each of the steps to concentrate the beam includes some aberrations from the lenses. A small probe size is thus limited by the amount of optical aberrations generated.
The objective aperture (*e*) can be used to select only the electrons that are really in focus (mainly the ones at the center of the beam). This minimizes the chromatic and spherical aberration, improving the depth of focus. As the SEM manufacturers

[4] The light source is generated by electron gun but analyzing a SEM picture the interpretation is that the observer viewpoint is placed collinear the electron beam source while the light is coming from where the electron detector is placed.

improve the lenses' design, new solutions are put on the market to avoid or correct these aberrations. This includes placing the sample between the lenses, making a combination of scanning and transmission electron microscope or even accelerating the beam to reduce (chromatic) aberration.
Field-Emission guns produce already a small beam (small virtual source) that minimizes the number of steps to tight it. This helps to explain why the smallest electron probes (higher resolution) are achieved with this kind of source[5].

2.2.3 Detectors

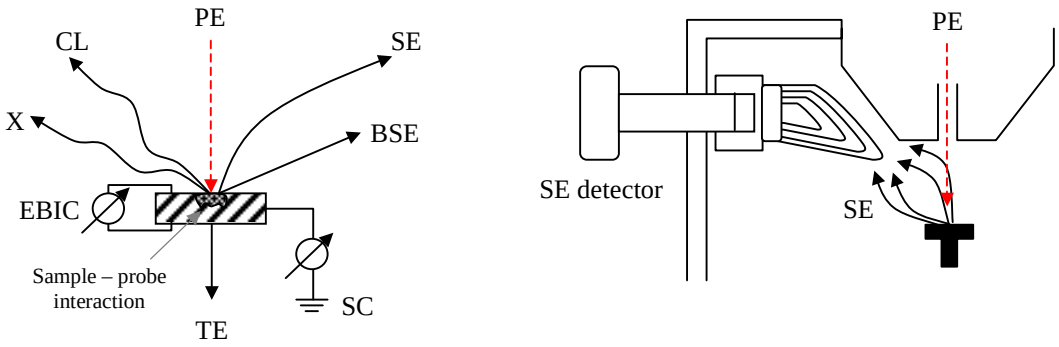

Figure 2.2: Electron beam – sample interaction and detectors

Figure 2.2 shows the electron beam-sample interaction, and why different detectors are needed. The primary source of electrons (PE) generates a group of different signals on the sample that are detected by a set of specific detectors like Secondary Electrons (SE), backscattered electrons (BSE), X-Ray, Electron Beam Induced Current (EBIC), etc.
For topographic observations, SE is the main detector. BSE is also useful because it can spot different materials in a sample, shown as contrast related to each material's atomic number (from dark for low atomic to bright for higher ones). In addition, some techniques used to introduce topographical contrast and 3D reconstruction can be easier realized through segmented BSE detectors, since they can provide different viewpoints.
The advantage here is to use one of the available sensors to choose a specific point in order to realize the indentation and observe the material behavior through SE detectors.
The detector can easily collect secondary electrons, attracting them when a positive electrical field is applied on it. Secondary Electrons, as opposed to other electro-sample interactions, have low exit energy (few electron volts). This means that they can be easily disturbed through the presence of gas molecules (poor vacuum) and electrical or magnetic perturbation inside or outside the SEM chamber.

2.2.4 Image quality

The magnification in a SEM can easily be switched to several thousand times and still keep a very good depth of focus[6]. As the demand for high magnification increases, the number of problems related to image sharpness increases. Several of the parameters

[5] Fields emission microscopes are the best options when resolution is an issue. On the other hand its cost of a standard device (without additional detectors) are still superior to a Tungsten microscope.
[6] Approximately hundred times more than the light microscope at a given magnification

used to tune the image acquisition are coupled, thus, it is likely to expect that optimizing one parameter will disturb another one. Some examples:
A large work distance[7] (WD) provides a comfortable space to accommodate the test instrument (the SEM indenter). However, large WD also means that the path covered by the beam is longer. The beam is thus more exposed to mechanical (vibrations) or electrical perturbations. Increasing the acceleration voltage stabilizes the beam and produces a smaller electron probe. This improves the resolution in samples with high atomic numbers, but has the opposite effect for samples with low atomic numbers. High magnification and resolution is reached with small electron probes. Selecting small apertures (only a part of the beam with a small angle will be used) reduces the electron probe diameter, produces higher depth of focus and limits the number of electrons over the sample (less damage). However, now the sample is 'poorly illuminated', worsen thus the signal to noise ratio. This demands an additional treatment (and considerably more time) to form the image.
High amounts of electrons produced could also physically damage the sample and will increase the concentration of the electrons on it. The later can create edge and charging effects, especially in non-electrically conductive materials. Charged areas (the electron is repelled from the sample) decrease the topographical contrast, and surface details. To bypass this constraint, a standard solution is to cover the sample with conductive material. The use of low vacuum or special gas in the chamber can minimize the charging effect but deteriorates SE contrast, as explained before.
The diamond tip used for indentation is not conductive and has a sharp edge. This contributes to making it strongly charged, which makes it impossible to analyze the details around the tip during indentation. A typical solution is the deposition of a thin layer of conductive material over the diamond. However, this coating will wear out after a few indentations (as can be seen in Figure 2.3). A variable pressure chamber (conductive gas) or playing with the acceleration voltage are more difficult ways to find a compromise between charging/sample resolution. The first requires a special SEM (low pressure or environmental SEM) and the second some experience, since each sample will behave in a particular way.

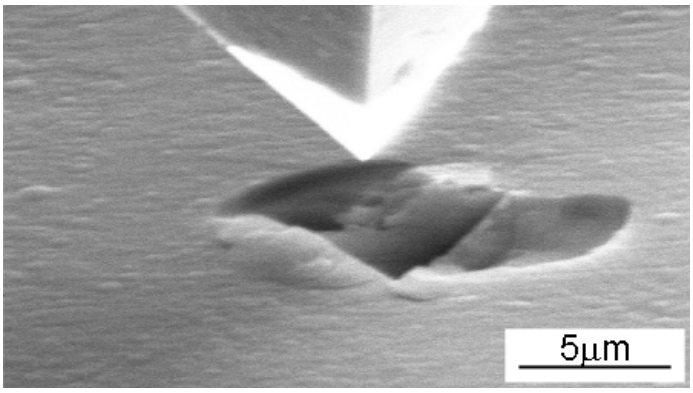

Figure 2.3: Diamond tip has lost conductive layer after indentation, becoming charged.

The material used to build up the test instrument has also an influence on the SEM operation. Plastic components, glues and some assembly or manufacture procedures (vented screw holes) can continually degas (outgassing), which creates a poor vacuum [22]. This increases the time necessary to reach the minimum (operational) vacuum in

[7] The distance between the sample and the objective lens

high vacuum systems (like in Thermionic microscopes) or makes it impossible to reach ultra high vacuum.
For a sharper image the electron probe must be completely circular. Contamination problems on the diaphragm change the probe to an elliptical shape. This can be partially compensated (astigmatism correction), but not when the perturbation is strong, as when as coming from the instrument placed inside the SEM or from the sample. Permanent magnetic fields (depending to the field intensity) blurry the image but in low magnification still permit sharp but completely distorted images as the image will follow the magnetic field[8]. Non-magnetic materials or the ones that do not keep any residual magnetic field and are thus preferable.
Electromagnetic perturbation, as produced by an electric actuator inside the SEM, can easily interact with the SE detector or with the electron beam. The image gets completely perturbed; making it impossible to focus or take pictures (Figure 2.4*a*, *b*). Hence, all electric actuators, contacts or connections must be shielded or kept far from the sample. This adds construction problems and increases the size of the device.
When stiffness is an issue and size/weight a constraint, an alternative engineering material can be used, for example ceramics. Non-electrically conductive materials can start to charge quicker if the electron beam is close. A charging near the observation region does not reduce imaging quality through contrast reduction (bright area). It makes the image to drift, creating blurry pictures.
To get full visual access around the tip during the indentation, it is necessary to tilt the tip-sample intersections related to the beam[9]. Tilting the sample increases the contrast, but causes an optical illusion, as the depth is still in focus. Any distance measurement in depth direction must consider the tilted angle for correction. A correct tilting of the sample toward the detector improves the image (fundamental for BSE detectors). The tip geometry and the indenter size constrain the usable tilting angles. Sometimes the best angle range to observe the indentation is not the same as for the detector (for example, Figure 2.4*c*). Moving the indenter inside the SEM is always a risk to touch any part of the SEM electronic, like for example, sensors.

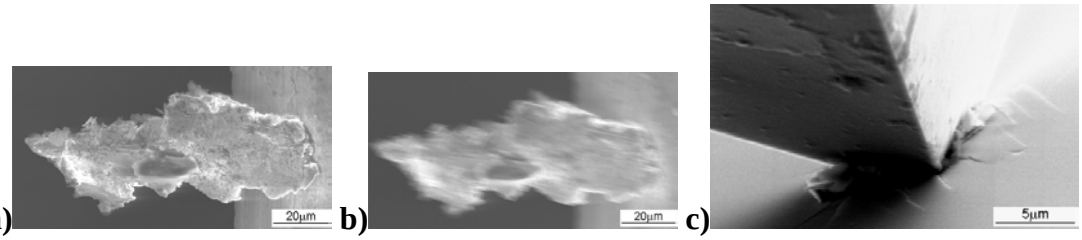

Figure 2.4: Some samples visualization problems: a) no electrical field near the sample, b) a electrical field near the sample, c) non uniform illumination - tip incorrectly orientated to SE detector.

A high-end microscope can be a solution for some of these problems related to image quality. However, its technology and manufacture demands high investments making it high priced equipments.
A Cold Field Emission microscope can provide high quality pictures quite easily when compared to a Thermionic type (tungsten gun). This is the same for live images at same magnification. Thus, a strong advantage of Field Emission over Thermionic type is to have a better signal to noise ratio images at same magnifications. Dynamic observations are thus better and can be realized at higher frame rate.

[8] See for example Figure 5.39 (Chapter 5).
[9] The main indentation tips and its geometries will be later on presented in Paragraph 2.4.

Apart of the price, another restrictions of these high performance SEMs are its design to make the best observation in small samples[10]. They are much less tolerant to perturbations, as caused through the presence of a dynamic test device. A design for this kind of microscope surely will have more constraints.

For practical purposes, the design and space constraint (to get good images as quick as possible and to fit inside), considered from here on, are based on the SEM available for the tests: a tungsten gun microscope from Zeiss (DSM 962). The main observation will be carried out with SE detectors.

2.3 Actuators

The objective of this section is to provide an overview of the common actuators used in nanoindentation [6] and after that, to present other "SEM compatible" possibilities.

2.3.1 **Voice coil –** or moving coil

Is one of the most common actuators used into commercial nanoindenters (MTS system, Micro Material ltd, CSM instruments, Elionix Inc.). Figure 2.5a shows some typical shapes and sizes (for linear and angular movements)
They are inherent force actuators. The input generates force that must be converted in displacement (example, using a linear spring). So minimum amount of current applied over the coil will result in an immediate movement. Its movement is very linear in function of the current and the range is limited by the size of the moving coil [23]. The force generated (F_{vc}) is proportional to the current applied (i), the flux density across the gap of the permanent magnet utilized (B_{mag}), the length of the moving coil (l) and the number of turns used to build the coil (N).

$$F_{vc} = B_{mag} \cdot l \cdot i \cdot N \qquad \textbf{Eq. 2.1}$$

a)

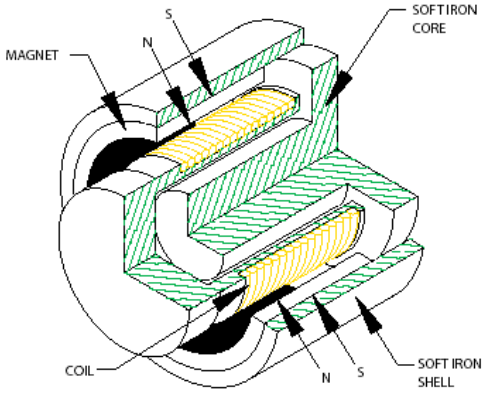

b)

Figure 2.5: a) Example of commercial voice coils actuators (BEI Kimco Magnetics), b) Voice coil scheme [24]

Since the moving coil is free and the force must be converted in displacement, guiding springs are arranged to provide linear displacement (not sown in Figure 2.5b). This

[10] Often the maximum sample size for the best nominal resolution version is from few cm^3 (ex. Hitachi), passing by large but flat samples (JEOL, FEI) up to big samples (Zeiss), although this changes at each new release.

arrangement can explore at a maximum the good resolution of this kind of actuators, as the guiding springs are frictionless and the applied force is controlled through *i*.
Its applicability for in-situ indentation can be prejudiced due to difficulties in heat dissipation (worst in vacuum conditions), the volume necessary for a given driven force (the volume occupied by the actuator increases a lot more than the gain in driving force) and finally the shield of the strong permanent magnets used for its construction, increasing its size.
A compact voice coil has thus a low range indentation force (as driving force and actuator size are connected) and the need of additional space for the electromagnetic shield. Nevertheless, voice coils also have the load measurement "integrated"[11] in the actuator, reducing thus the space occupied by the SEM indenter.

2.3.2 Electrostatic actuators

Similar to voice coils, these are also non-contact force actuators. Two electrodes separated by an insulating barrier are attracted against each other as an electric potential difference is applied [25].
For rectangular, parallel and overlapped electrodes (Figure 2.6), the generated forces parallel (F_a) and normal (F_x) to the electrode are:

$$F_a = \frac{\varepsilon b V^2}{2x}$$
$$F_x = \frac{\varepsilon a b V^2}{2x^2}$$

Eq. 2.2

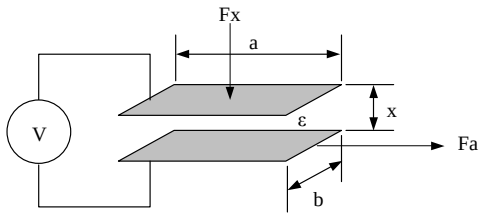

Figure 2.6: Scheme of a capacitive actuator

Where ε is the permittivity of the gap, *a* is the length of the overlapped electrodes, *b* the electrode width (both), *x* the perpendicular separation and *V* the input voltage. The driving force is small (a few mN generated by a small voltage in several squared millimeter plates) but these plates can be easier combined in parallel, in a very compact way, to increase the force (for example, some MEMS comb drivers). The solution adopted by Hysitron [26] on the low load option for TriboIndenter is reported to have a maximum range of 10μm with a sub nanometer resolution. The maximum indentation force (also calculated directly through the actuator) is 30mN.
An electrostatic actuator working inside the SEM must also be shielded, since the electrical field generated on the electrode plates will perturb the electron beam. This can be a solution as actuator for in-situ indentation, but in most designs, a piezoactuator would be a more suitable option for its range and the available force.

2.3.3 Piezoactuator

A piezoelectric actuator changes its shape when an electric field is applied across it. These ceramics are quite anisotropic materials, which means that different piezoelectric or mechanical properties are related to the material's internal crystallographic orientation. Relation between an input displacement or force output is

[11] The load is calculated reading the current on the actuator (*F* is proportional to *I*) as it changes because of an external force, like produced during the material indentation. The actuator has an internal stiffness (the guiding spring with known stiffness). Subtracting the spring force, the indentation force is obtained.

related to the material's piezoelectric property, size/shape of the actuator and direction of the electrical excitation. As a result, it is necessary to describe the desired property following a standard system of notation (Figure 2.7a) that is related to the polarization axis (vector).

Parameter ***l***, ***w*** and ***t*** are the physical piezoactuator dimensions. Numbers 1 to 3 denote translation in X to Z and numbers 4 to 6 represent rotation around the same axis (producing shear). The ***ij*** coefficients are a common way to describe a specific piezoactuator characteristic. The subscript ***i*** is the direction of the input (an electrical field, a deformation, etc.) and ***j*** is the material response (strain, electrical field, force, etc.). Preceding this coefficient is the piezo property, like charge, dielectric constant, Young's modulus and so on. For piezo actuators, an important value is the piezoelectric strain constant ***d*** (m/V) that represents the amount of strain as function of an input electrical field. Typical coefficient designations for axial, transversal and shear actuators are respectively d_{33}, d_{31}, d_{15} (m/V). Although d_{ij} is defined as constants, its value can change with temperature or material aging.

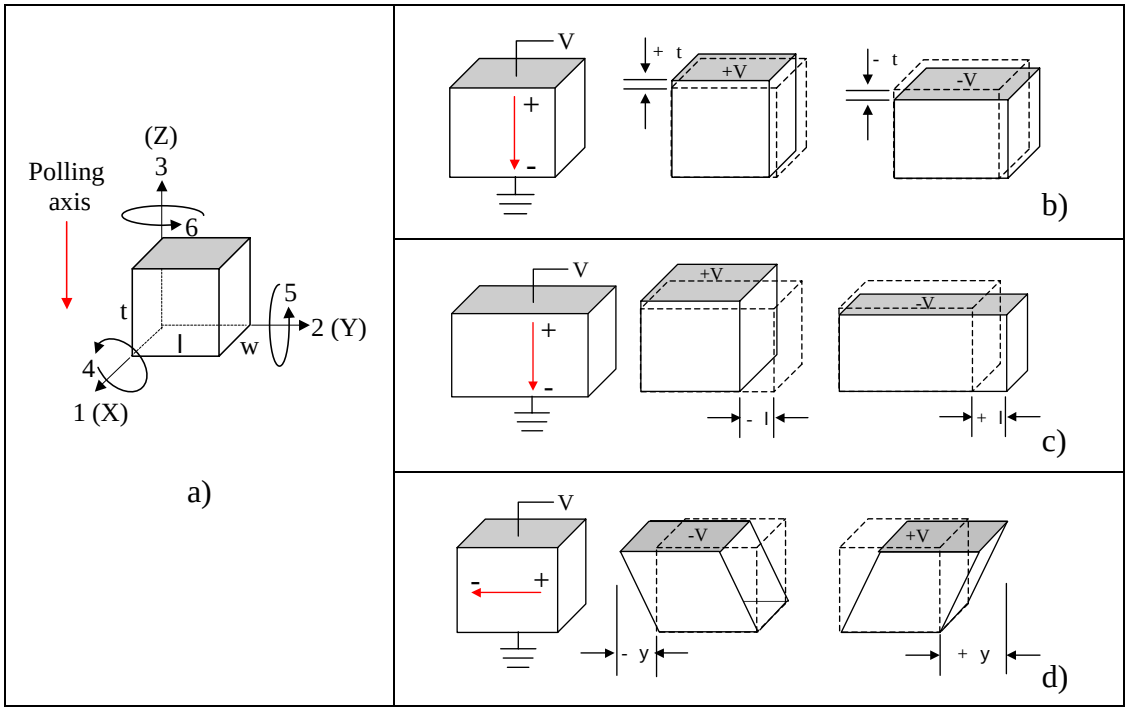

Figure 2.7: Piezo basics: a) System of notation, b) axial, c) transversal, d) shear mode

Practical considerations: Quite often a scheme of the piezo actuator presented in a brochure will try to represent it in a practical operation (which part is fixed, which can move) or with the polarized axis matching the direction ***Z***. The electrode could also be represented in different positions. Although the coordinate system can be standard, the position of the electrode will change according to how a given property is read. In this case, a picture will always be necessary. Fortunately, most piezo catalogs provide the same scheme. For this reason the representation d_{33}, d_{31} and d_{15} are today analogous to indicate respectively axial, transversal and shear piezoactuators.
As already mentioned, the output displacement depends on the actuator's shape. An actuator with a cubic shape has $d_{31} = d_{32}$, denoting same strain responses. Piezos can easily be shaped in their green form and after sintering; it is no problem to cut it with

a diamonded wire or disk. Table 2-1 (based on [27]) shows some of the important relations for piezoactuators.

Table 2-1: Piezo actuators mechanical response.

	Axial	Transversal	Shear
Displacement	$\Delta = d_{33}V$	$\Delta = d_{31}V\frac{l}{t}$	$\Delta = d_{15}V$
Blocking force	$F_b = \frac{d_{33}V}{s_{33}}\frac{lw}{t}$	$F_b = \frac{d_{31}V}{s_{11}}w$	$F_b = \frac{d_{15}V}{s_{55}}\frac{lw}{t}$
Stiffness	$K_m = \frac{lw}{s_{33}t}$	$K_m = \frac{wt}{s_{11}l}$	$K_m = \frac{lw}{s_{55}t}$

S_{ij} is the actuator compliance constant (m^2/N), equivalent to the inverse of its Young's modulus. It has different properties if measured with the electrodes in short circuit or open circuit. V is the input electrical field (in V). Virtually any piezo manufacturer (for example [28-30]) will provide catalogs with a small piezo tutorial to explain the different piezo properties for a specific piezomaterial characteristic, often designed for a specific application (ultrasonic motors, actuators, transducers, etc.).

A stack piezoactuator range is quite limited: for low voltage multilayer axial piezos (up to 200V), it is approximately 1μm per millimeter in length. Its stiffness and driving force are proportional to its cross-section. Thus, few square millimeters of ceramic have a high stiffness (several N/μm) and a driving force of several Newtons.

These actuators have a very quick response and are very sensitive to variations in the input electrical field. This makes it convenient for micro/nanopositioning systems, and can be found in diverse configurations, for example in [31-33]. Nevertheless, there are some important drawbacks. The relation between applied voltage and displacement has typically 10-15% of hysteresis that can only be solved through feedback control or charge drivers [25], although the last option is not suitable for quasi static applications. Creep, as the name suggests, is a slow and gradual change of the displacement in function of time, decreasing as the time passes. Both of these phenomena have been discussed elsewhere [27] as topics with the objective to use Piezoactuators in open loop to avoid costly electronics. Today the safety solution still uses control feedback.

Axial and shear actuators will be, in this work, constantly be mentioned as driving principle for nanopositioning. Additional properties or relations will be provided on demand, as it will be easy to explain them with direct examples.

Nanoindenters from Hysitron and Csiro [34] are two examples of devices that use piezoactuator for indentation. The Hysitron Triboindenter uses a piezo for its high load option indentation head (0.5 – 5N, 80μm range, sub nanometer resolution). Csiro "Umis" uses a piezo actuator to drive the tip, using a specially designed spring. Measuring the spring deflection gives the applied load as well as the penetration depth. The maximum load (50mN for 2μm range or 500mN for 20μm range) is more a function of the spring than a limitation of the piezo driver. An additional module is, for example, available for smaller loads or for loads up to 5N and 40μm indentation range.

Piezos are good solutions for SEM indenters. They allow a fine displacement and are stiff and compact. Nevertheless, they must be shielded to avoid electromagnetic perturbation. The drawback is the short range. Thus, a coarse displacement system

must be added. To bypass this, another class of piezo actuators will be presented in this paragraph; the piezoelectric motors.

The actuators described up to now are just a few examples of what could be used as a driving principle. Adapted from Smith and Chetwynd [25], Table 2-2 gives a brief overview of several actuators, as intended to be used for micropositioning.

Table 2-2: Small overview of actuators often used in micropositioning systems

Actuator	Force/size	Range (sensitivity)	Stiffness	Linearity
Piezoelectric	very good	µm (nm)	high	poor
Electrostrictive	very good	µm (nm)	high	poor
Micrometer	good	mm (µm)	medium	moderate
Friction drive	medium	mm (nm)	medium	moderate
Magnetostriction	poor	µm (nm)	high	poor
Magnetoelastic	poor	µm (nm)	high	poor
Shape memory	poor	mm (µm)	high/med	poor
Voice coils	poor	mm (nm)	-	good
Electrostatic	poor	µm (nm)	-	square law
Hydraulic	medium	mm (nm)	high	good
Poisson's ratio	poor	µm (nm)	high	good

The fact that an attribute is defined as "good" or as "poor" depends on the adopted configuration, as well as on a subjective evaluation, considering it in an open-loop operation. Force/size means that either the size needs to be strongly enlarged to increase the driving force (ex. voice coils) or, even if it is very compact, the provided force may not be as strong as an actuator with similar dimensions (example; memory shape alloys/bimetallic strips compared with piezos). In this case, the sensitivity is more connected to the actuator's internal limitation. This means, that it will rather be constrained by the driving electronic resolution than by internal aspects.

2.3.4 Piezoelectric motors

How can a larger range be obtained with piezo actuators? If the idea is to increase the original range a few times, the mechanical amplifiers, like levers or bimorph actuators, are a common technique. Nevertheless, if the desired range is in the mm to cm range, a piezoelectric motor is the solution. The piezoelectric motor is a current subject in actuator researches and already many products are available. As the goal of this work will be focused on stick-slip actuators, examples will be narrowed to commercial available versions.

2.3.4.1 Ultrasonic motors

Available in rotary and linear mode. The piezoelectric element creates an ultrasonic wave that travels along the mobile - motor contact surface, often in resonance mode. A minimum configuration of one actuator and one driving channel is necessary to create each degree of freedom for displacement. Ultrasonic motors are found in two types:
Traveling wave: The piezoelement is excited to bend in a synchronized way, producing traveling waves. The contact between the motor and the carrier is done

simultaneously in several points. Two channels and two actuators are the minimum configuration. Figure 2.8 shows this principle as well as a commercial version [35, 36].

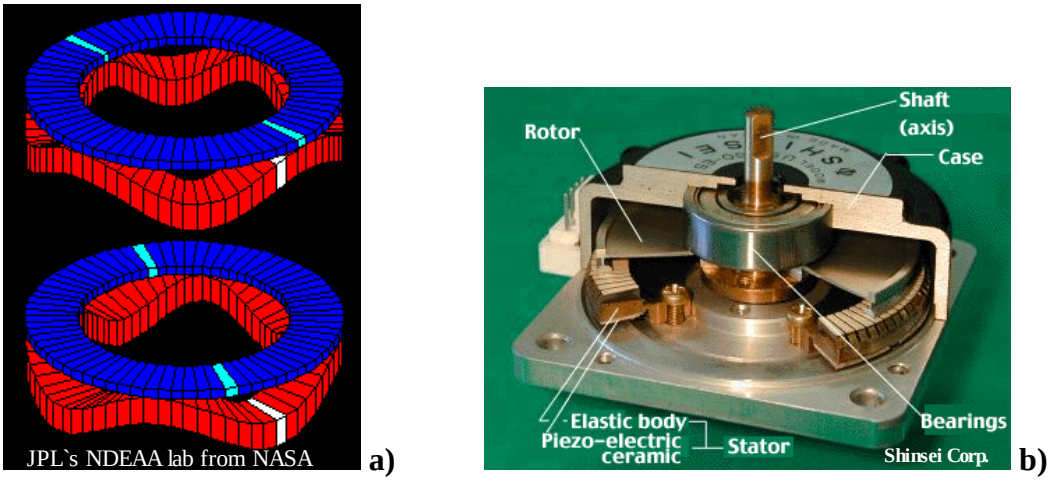

Figure 2.8: Traveling wave ultrasonic motors. a) Video sequence of a traveling wave principle, b) Components details of a commercial traveling wave ultrasonic motor

Standing wave: A vibrating element pushes/pulls the driven member (carrier) through a frictional contact. It is less complex than a travel wave and has the status of being less reliable or having short life (related to wear). However, new designs have found their way to the market. UDP by Cedrat, Flexmotor, Elliptec, Squiggle, etc. are some available brands [33, 37-39]. Figure 2.9 (a video's frame sequence[12]) shows how some commercial actuators explore different ways to use standing wave technology.

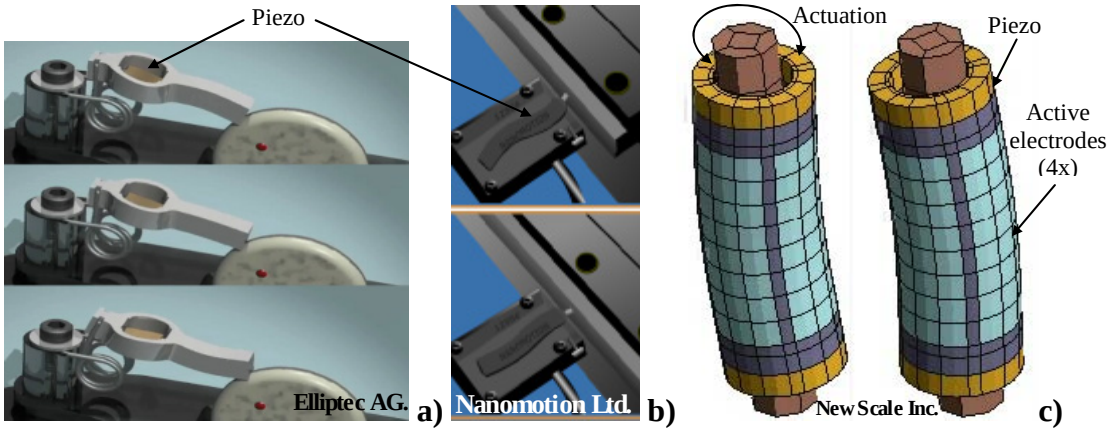

Figure 2.9: Video sequence working principle of commercial stand waves actuators: a) Elliptec, b) Nanomotion, c) Squiggle ™

2.3.4.2 Sequential based motors (multiphase system)

The full step is reached after a sequence of leg movements.
Type clamp/unclamp and expand. The most well known is the " Inchworm" actuator [40] with a minimum configuration of three actuators and three driving channels. Its principle is presented in Figure 2.10a.

[12] The original videos are found on each one manufacture's home page.

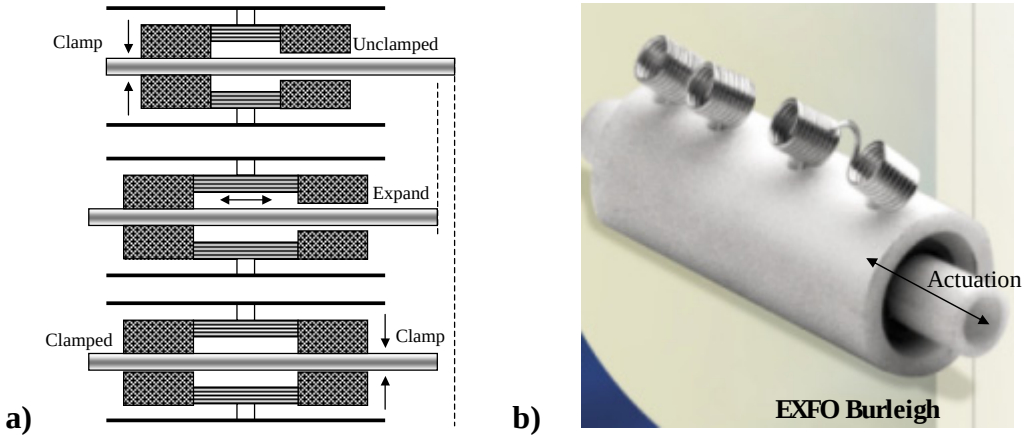

Figure 2.10: Inchworm actuator: (a) Principle of its working sequence. b) A commercial Inchworm actuator (for UHV) [40]

Walking mechanisms: Similar to the "inchworm" principle, since each leg partially releases the carrier contact in each step. Commercial versions (Figure 2.11 [41]) explore shifted sine waves to drive the carrier. Two channels are needed to drive one leg.

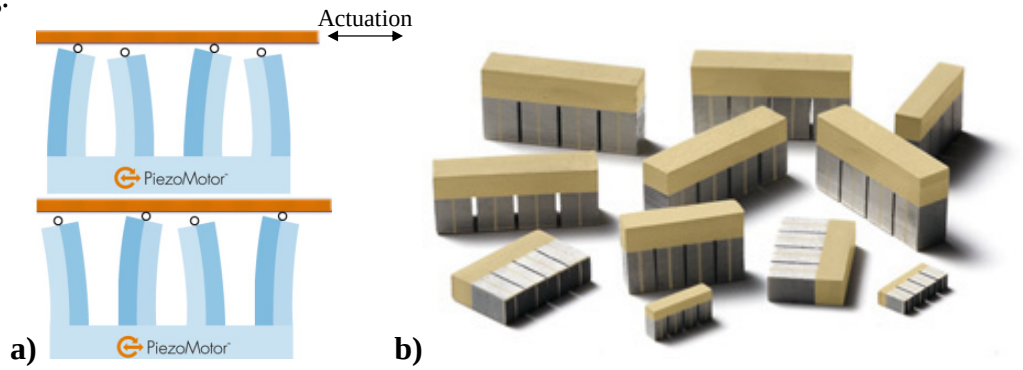

Figure 2.11: Walking principle using two pairs of bending piezos. a) Video sequence of its motion principle. b) An example of commercial 'walking type' piezoactuator [41].

Inertial actuators: One drive channel and one actuator are necessary to drive the carrier. Impact drivers and stick-slip actuators are common examples (Figure 2.12).

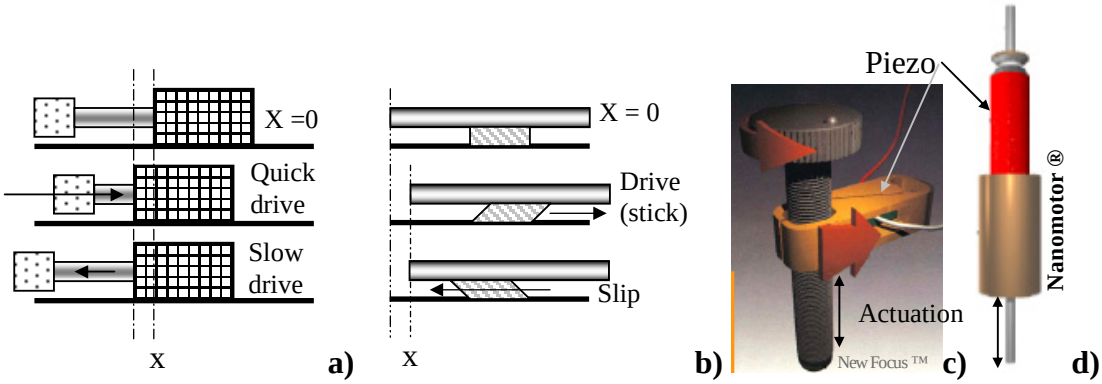

Figure 2.12: Working principle of an impact drive (a) and stick- slip actuator (b). Examples of commercial versions that uses these principles (c, d) [42-44]

Some common characteristics claimed in all those technologies, are:

- High driving force at low velocities (if compared to magnetic based motors)
- Velocities from nm/s up to cm/s
- Sub μm step size
- Self blocking (holds position)
- Compact
- Free of magnetic field
- Better energetic conversion
- Reliable operation
- Long durability

Although some companies sell its actuators as real options to replace more traditional ones, like step motors or DC motors, most of the models shown here are focused on a market that needs positioning at sub micron resolution, but yet large range, as for example the coarse-fine operation. Since "positioning" is the main application for these devices, the search of high driving forces is not a common issue, except if the setup needs to be lifted (and kept in position) or if very high accelerations are needed. Therefore, it is not a surprise to find that each actuator illustrated above has a very customized and proprietary driver, which represents the main knowledge of each company. Hence, because of its complexity, the system is tuned for specific condition. For example, a change of external reaction force over the piezoelectric motor is harder considered. Thus, the behavior of each motor in these conditions is not well documented or not even available.

Piezoelectric motors and specifically stick-slip actuators may be a very good choice for a SEM indenter, as stated below.

- Several actuators are easily found in UHV (ultra high vacuum) version or already tailored for SEM applications.
- They are originally high-resolution actuators in a compact form, what makes them easy to be integrated in a material test device.
- They combine high range and sub-micron resolutions (step mode) or sub-nanometer resolution (scanning mode); the final setup can be simplified (and again more compact) from sample setup/positioning up to the test execution.
- They are easy to control and do not need power to hold its position.

In a first moment, it is difficult to justify that a stick-slip actuator is the best principle for indentation or scratching, when many of the presented actuators are already available out of the shelf. The clue is: it depends on the chosen configuration to obtain a smooth indentation or scratching. If this can be reached with the simplest configuration (channels and actuators) available for each type of the presented actuators, stick-slip is far from being the one that can provide easier integration in a more reduced package. Another advantage is the step or scanning mode as typical actuation. If the stick-slip complexity needs to be increased for a proper execution of its tasks (ex. low jump-back size), the choice of stick-slip will have fewer advantages. This topic will be explored in Chapter 4 and 5.

2.4 Tip geometry and the indentation graph

Instrumented indentation testing (IIT) still uses most of the tips developed for traditional hardness measurement. IIT/nanoindentations are performed with pyramidal, spherical and conical indenters. They are preferably made of diamond, because of its high hardness and elastic modulus that minimize the interference of the tip over the measurement.

2.4.1 Types of indentation tips

Pyramidal indenters: Knoop, Cub-Corner, Vickers and Berkovich are the most common shapes in this class. The Knoop[13] tip has been developed as an alternative to Vickers tip microindentation in hard material. Its special shape (rhombohedral) leaves a very shallow print that is still easily measurable by optical microscopes. Since for IIT a print measurement is not an issue, Vickers has been kept as a traditional tip in nanoindentation. Its four sides can never be merged in one point. Hence, a small plateau is left over (chisel edge). For this reason the three-sided Berkovich is preferable in nanoindentation. It has the same depth-to-area relation as Vickers but a real edge with a tip radius from 50-100nm [6]. The Berkovich tip is the standard tip in nanoindentation.
The cube corner is also a three-sided tip, but its angles produce much higher stress and strain near the contact. It acts more like cutting the sample. Its shape can produce small but well defined cracks around the material and this is thus useful for measuring fracture toughness at very small scales. On the other hand, as the load increases, the failures around the material do the same, making the tip calibration more difficult to realize.
However, it still can be used for performing nanoindentation (although less common) and because its acute sides, it lets a good observable area for in-situ indentation and scratching without the need of highly tilted samples (Figure 2.13c, Figure 2.14b). As a sharp tip, it is also a good tip for "machining" materials.

Spherical indenters: This is a popular choice for soft material. At small loads, it produces mainly elastic deformation. As the penetration increases, an elastic-plastic transition occurs, which in theory could be used to exam yielding, work hardening and recreate the entire uniaxial stress-strain curves from a single test [4, 45]. The spherical tip is often shaped at the end of a conical base. If sharp conical angles and small radius are used, it becomes easier to observe indentation with this kind of tip. Difficulties to manufacture high-quality small spherical indenters (diameter below 1μm) are reported to be the main constraint for the use of this kind of tip and for this reason the preference is to use bigger diameters or blunted Berkovich tips, even if they cannot be truly used to investigate elastic-plastic transitions at the nanoscale [4].

Conical indenters: Their simple cylindrical symmetry makes them popular for modeling indentation as the complications related to the stress concentration on the edges (as pyramidal indenters have) do not exist. It is a standard shape for studies and allows interpreting IIT results based on indentation models. However, it is not so common to use it for real tests. It is considered difficult to get high quality diamond and sharp conical indenters for nanoindentation. Once solved some of its manufacture problems, it will be more common to use spherical and conical indenters, which could be shaped in an angle that provides a free view during in-situ indentation.

[13] A four-face tip characterized by a long diagonal nearly 7.1 times as long as the short diagonal.

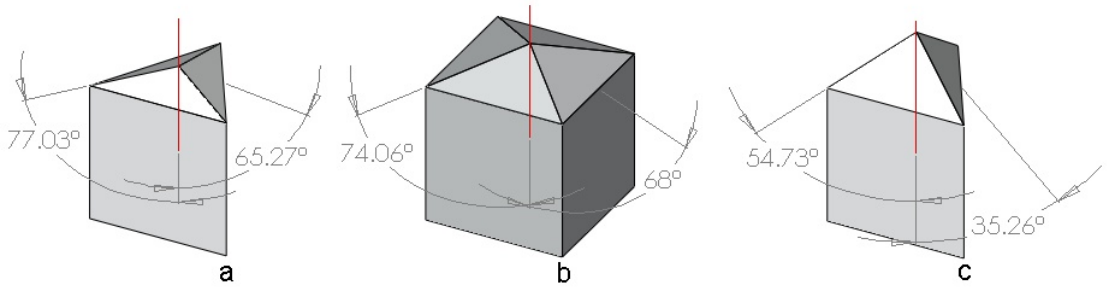

Figure 2.13 : Face and edge construction angles of three typical indenters: a) Berkovich, b) Vickers, c) Cube-Corner

2.4.2 Tip main parameters

Table 2-3 and Figure 2.13 show the main parameters of these tips. For observation purposes, the semi angle θ is a very important parameter. The other ones, as for example ε (ratio between elastic deformation above and below the contact area) and β (a correction for non-rotational symmetry shape of pyramidal indenters) will be detailed later. These parameters will become necessary to describe the indentation graph (the P x h curve) but they are already included in this table for commodity, since they are related to the tip geometry.

Table 2-3: Some important parameters related to the indenter geometry [6]. The definition of each term will be gradually presented.

Indenter	Projected area	Semi angle θ°	Effective cone angle α(°)	Interceptor factor ε	Geometry correction factor β°
Sphere	$A \approx 2\pi R h_p$	-	-	0.75	1
Berkovich	$A = 3\sqrt{3}h_p^2 \tan^2\theta$	65.27°	70.3°	0.75	1.034
Vickers	$A = 4h_p^2 \tan^2\theta$	68°	70.3°	0.75	1.012
Knoop	$A = 2h_p^2 \tan\theta_1 \tan\theta_2$	θ_1 = 86.25° θ_2 = 65°	77.64°	0.75	1.012
Cube-Corner	$A = 3\sqrt{3}h_p^2 \tan^2\theta$	35.26°	42.28°	0.75	1.034
Cone	$A = \pi h_p^2 \tan^2\alpha$	α	α	0.727	1

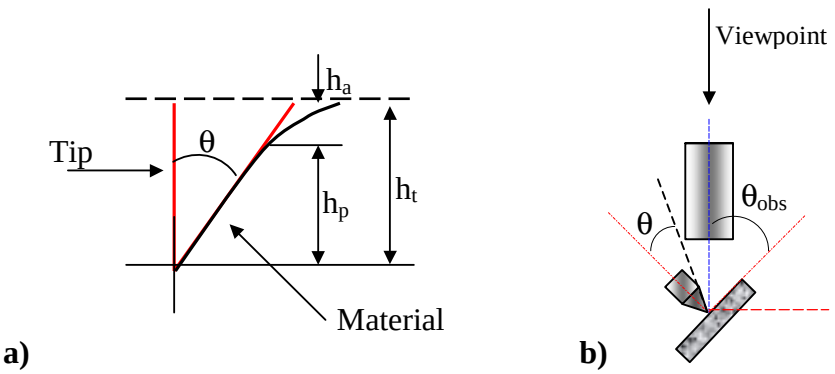

Figure 2.14: a) Geometry of contact with a general indent (see also Figure 2.15b for more details). b) Observation of the tip-sample contact in a SEM in function of the tip's semi- angle

The semi-angle θ° is measured between the face and the central axis of the indenter, as presented by a general conical indenter (Figure 2.14a). Together with h_p (depth of penetration), it is possible to determine the projected area of contact between the indenter and the material.
For observing indentation, the tip face or the edge must be tilted toward the observer viewpoint (coincident to the electron beam column). As the tip center axis is **always** positioned perpendicularly to the sample, the viewpoint angle θ_{obs} is an angle between $0 < \theta_{obs} < 90° - \theta$, where θ is the face or edge angle (Figure 2.14b). Orienting an edge related to the SEM viewpoint exposes two of the tip faces. This can be a good setup to see a crack generation made of a Cube-Corner tip or to visualize the material's behavior in front of the edge during scratching. Table 2-4 summarizes the range of θ_{obs} for these three indenters. For conical indenters, θ_{obs} is related to the cone angle. Acute (sharp θ) cone angles improve visualization, as they reduce the visualization gap between the material under the tip and around it. Spherical tips follow similar visualization rules as conical indenters since the sphere is created at the end of a conical base. On the other hand, the visualization around the contact region is difficult. The bigger the sphere radius is, the more difficult is to observe the material's behavior at early depth of penetration.

Table 2-4: Observation angle as spotting the tip face-sample or tip edge-sample region

Tip	Range θ_{obs} (face)	Range θ_{obs} (edge)
Berkovich	0° - 24.73°	0° - 12.97°
Vickers	0° - 22°	0° - 15.94°
Cube-Corner	0° - 54.74°	0° - 35.27°

As θ_{obs} goes towards 0° (sample parallel to the beam), fewer electrons will be detected by SE and BSE detectors. In addition, more depth of focus will be necessary for a good observation, which is not always possible at high magnification. The possibility to tilt the sample up to θ_{obs} can be limited by the indenter device size and its disposition inside the SEM, as it might touch the electron beam column or any sensor inside the chamber. This is clear why Cube-Corner tips as well as sharp conical or spherical tips provide easier in-situ observation and better image quality.

2.5 The indentation graph

Because its properties measured at a determined crystallographic orientation and the type of tip utilized, each material will provide a characteristic Force (*P*) x Tip penetration (*h*) curve when a diamond tip is pressed against the sample. Figure 2.15a for example, shows some ***P x h*** curves based on materials hardness (*H*) and Young's modulus (*E*), while Figure 2.15b shows the typical output of an indentation curve. More specifically, on Figure 2.16a, it is possible to observe the loading curves for different materials at same maximum load (with a Berkovich tip). Figure 2.16b shows unloading curves plotted based on the difference in indentation depth at maximum load and completely unload (h_t-h_e = h_r).

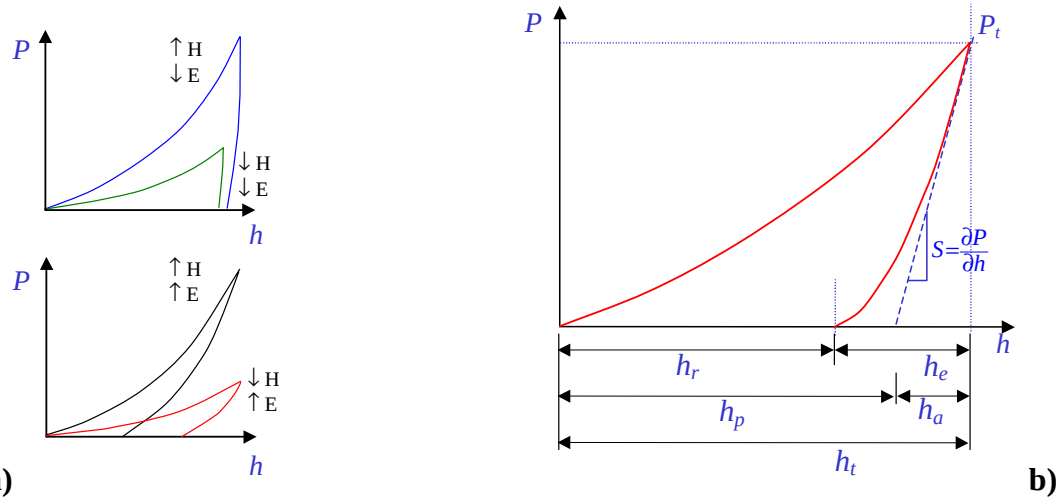

Figure 2.15: (a) Shapes of indentation curves as a result of *H* and *E* [5], (b) Indentation curve output. *S* - material unloading stiffness, h_r, h_p - size of the residual imprint, h_e, h_a - size of the imprint elastic deformation, h_t total tip penetration depth.

It is clear that the tip actuator will face a high variation of forces when indenting different materials (ex. Figure 2.16). This means that in few micrometers a high load is reached (ex. indenting sapphire) that can be interpreted as a **reaction force**, acting against the tip's actuator. For the unloading process, these large variations in force will also depend on the elastic-plastic properties of each material, but now the material's elastic response is acting in favor of the tip actuator as it is retracting. Materials with high elastic recovery (h_e) have a force that changes "slowly" compared to a material with high plastic deformation (given by a high h_r), where the unload force drops abruptly during unloading and the tip looses quickly contact with the material.

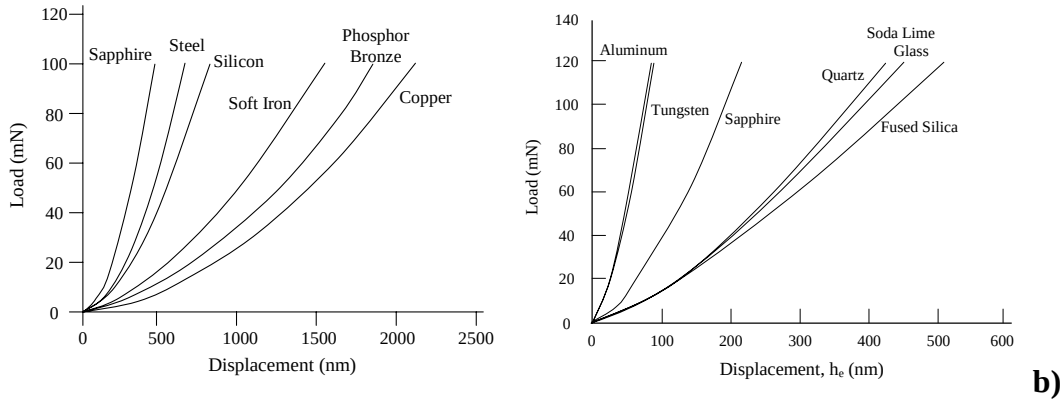

Figure 2.16: (a) Berkovich loading curves at same maximum load [46], (b) unloading curves based on h_e, the difference between displacement at maximum loading and complete unloading [47].

To have an idea about the force generated during indentation of diverse materials using indenter with different frame compliance[14], analytical models describing the loading-unloading curves have been implemented in Matlab®. These simplified models can provide a good approximation of real values obtained during indentation. An introduction of these models is now presented.

[14] The compliance related to the machine considering a force loop that starts on the sample holder, passing by the machine body, finishing at the tip holder (see Figure 2.17).

2.5.1 Loading and unloading curves in instrumented indentation testing (IIT)

All the models to be presented **have been mainly developed for indentation with Berkovich tips**. As explained before, this is the standard tip for nanoindentation, what makes it easier to obtain calibrated data for several materials. Different analytical models will be presented. Each one has a particularity, going from straightforward implementation to results that are more accurate. With some modifications, other indentation tips could be adapted into the models.
The indentation models describe the tip penetration **only**. They do not consider the instrument influence, being based on a corrected indentation graph and not on raw data. Typical measurement influences are not included as:

- drift (creep related to indenter frame thermo expansion or material creep)
- penetration depth correction. In a real situation, it is not easy to determine *h* (from the moment that the tip touches the surface - P≠0). The models thus consider that the indentation starts always exactly on the sample's surface.
- instrument compliance (subtraction of the system compliance over the indentation depth)
- The need of a correct tip calibration (the real area function).

However, they can be incorporated in a larger model: The *indenter* model. This is the case of the frame stiffness, which will be here presented (also in Paragraph 3.3).

A raw data (h_{raw}) means that values are the ones directly measured by the indenter that includes the instrument and environment influences over the *P x h* graph. Indentation models are based on corrected data. Thus, the simulated *P x h* can be compared with corrected indentation results obtained with any calibrated indenter.
Drift and the determination of the initial penetration depth can shift the graph (shifting h_t.) The procedure to correct drift or to determine the correct initial *h* can be found in diverse literatures [4-6, 47] and it is done semi or automatically by the Indenter instrument. For simulation purposes, the indentation starts "exactly" on the surface and thermo drift is not considered. Every movement of the indentation head is directly proportional to the indentation depth (Figure 2.17). The parameter h_{t_raw} (that is h_t plus the frame compliance) is measured through the difference between the two reference lines: h reference *head* and *indentation*.
Without indenter frame compliance[15], the tip displacement *h* could have been completely converted in penetration ($h_{t\_raw} = h_t$). As any indenter has a limited stiffness, a correction must be made, and this will be explained below, in the *instrument compliance* section.

The area of contact (*A*) at a given penetration *h* is assumed to be found directly by the means of a perfect tip geometry (Table 2-3). A perfect tip does not exist (the tip will wear and become blunt). Thus, corrections must be made, applying a correction factor over the area function values. These corrections, as well as the procedure for tip calibration is part of any commercial nanoindenter package.
Imperfections in the tip calibration have more impact over the result if the indentation load gets lower. As low loads (mN or lower) are **not** the focus if this work and for simplification purposes, a perfect tip is considered during simulations.

[15] Actuator, load cell, tip, sample holder, etc. are also part of IIT devices' frame stiffness.

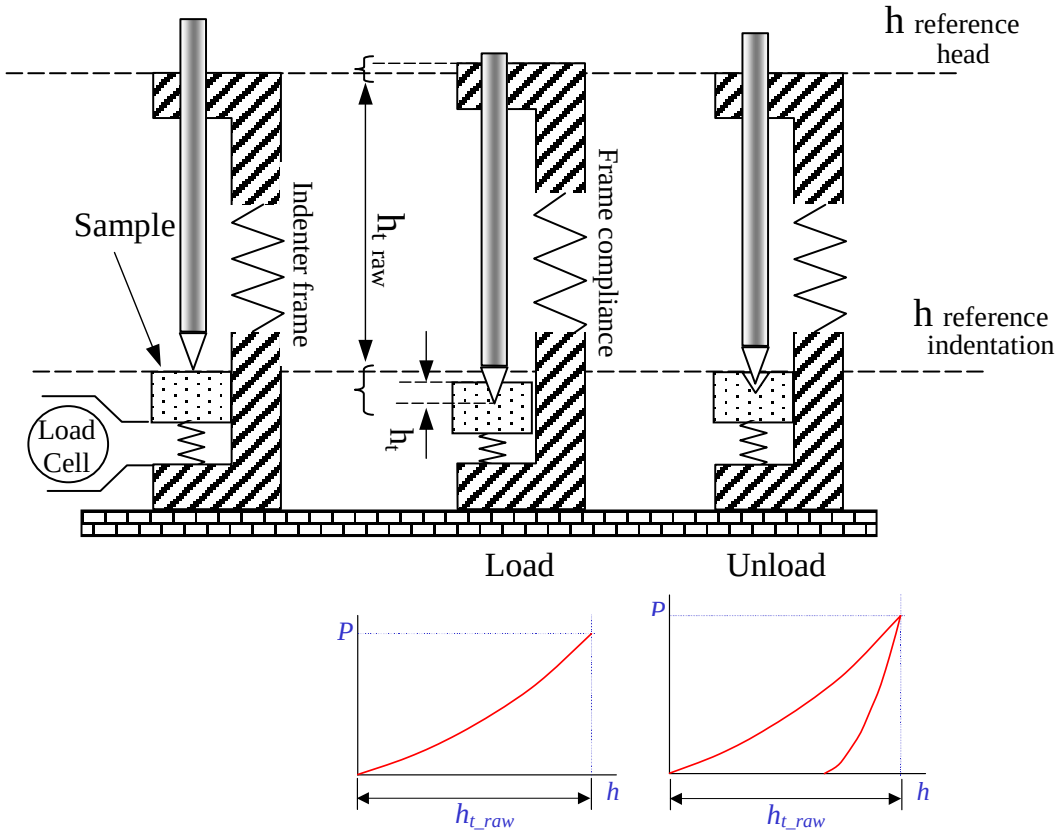

Figure 2.17: Sketch of an IIT device (including frame compliance) and its references. The inset graphs show output parameter *P* and *h* during loading and unloading .

The **instrument compliance** (or frame stiffness) also changes the indentation curve. Reaction forces shifts the sample and are measured as indentation depth. This parameter could also be ignored if the applied indentation force is very low and the frame stiffness very high (range of N/µm). Nevertheless, here the interest is more on the influence of higher loads. Compliance has thus been included in the simulation to evaluate the contribution of the indenter frame to the tip-sample interaction and afterwards to use it for dynamic analysis, when using stick-slip indentation.
Frame compliance (C_f) is simply the frame deflection divided by the applied load. The frame compliance acts like a spring during loading/unloading. If the load P and the raw depth (h_{raw}) are known, the corrected depth (h_c) can be determined by the means of the following equation:

$$h_c = h_{raw} - C_f \cdot P \qquad \textbf{Eq. 2.3}$$

The instrument compliance must be determined before any other material characterization. Tip calibration and frame stiffness is made using standard materials (known H and E). An interactive process is necessary to correctly determine these parameters. After an initial calibration A and C_f does not need to be evaluated again very often. Thus, only the remaining parameters have to be estimated after each

indentation, apart of specific material responses as pile-up or sink-in[16] and influence of the surface roughness.
Therefore, it is expected that for the simplifications mentioned here, the chosen models cannot output the same values as measured during real nanoindentation and will diverge even more at very low loads (μN range). They will nevertheless be useful to describe loads up to 0.5-1N, which is often the maximum value available on commercial IIT devices for nanoindentation. Moreover, as mentioned before, the interest of this work is more on high loads.

The Loading–unloading equations have originally been formulated to provide displacement (*h*) in function of an input load (*P*). This makes the formulation easier and more logical, as most of the indenters (based on voice coils, electrostatic actuators) have force as their input parameter. However, piezos and stick-slip actuators can be considered as displacement input. Hence, those equations had to be modified for having displacement as input. This has provided a better integration with the stick-slip model (that will be presented in Chapter 3), which is generated from displacement out of friction forces.

2.5.2 Loading curve

2.5.2.1 Hainsworth equations

The loading curve can be, for simplification purposes, be approximated as a parabola. It depends on a combination of *E* and *H*, as shown in Eq. 2.4. It has been proposed by Hainsworth et al [46] as a refinement of the work previously presented by Loubet et al [48] for Vickers tip. The goal of the Hainsworth study has been to propose the loading curve as an option to find *H* and *E*, in the case one of these two terms is known.

$$P = K_m \cdot h^2$$

where

$$K_m = E\left(\phi\sqrt{\frac{E}{H}} + \psi\sqrt{\frac{H}{E}}\right)^{-2} \qquad \textbf{Eq. 2.4}$$

P is the load (N), *E*, Young's modulus (GPa), *H*, hardness (GPa) and *h* the real displacement inside the sample (in *m*).
The constants ϕ and ψ (respectively **0.194** and **0.930**) have been determined through testing with Berkovich tips and several materials (Figure 2.16a) with properties known in advance. Hainsworth reports that the model is imprecise at very low loads, since at this scale the tip geometry can be better described as a sphere than as a general conical indenter. In this case, traditional Hertz theory provides a safe start to correlating *P* and *h*.
Maltzbender and With [49] report different values for ϕ and ψ (respectively **0.202** and **0.638**-), calculated (using Eq. 2.5) for an ideal Berkovich tip rather than obtained by a specific calibrated tip.

[16] When the indentation involves plastic deformation, the material may sink-in or pile-up around the print. In this case, the parameter h_p can be wrongly determined and consequently outputting a wrong contact area *A*.

$$\phi = \sqrt{\frac{1}{A}}$$
$$\psi = \varepsilon\sqrt{\frac{\pi}{4}}$$
Eq. 2.5

Note that A and ε are obtained from Table 2-3 ($A_{Berkovich}$ = 24.5). At that time, the geometric constant ε utilized has been 0.72, the theoretical value for general pyramidal indenters. Actually, the value ε = 0.75 has been found to better represent these tips in real indentation and has thus been adopted as a standard value.

2.5.2.2 Zeng and Chiu equations

Zeng and Chiu [50] have also made an extensive load-displacement curves analysis (on 13 different materials) in nanoindentation. The goal has been to study a new way to determine elastic-plastic properties, combining information coming from unloading, and the loading curve. Hence, Young's modulus, strain-hardening and yielding stress could be determined.
The equation used to describe the load has been originally developed by Larsson and Giannakopoulos [51] who has used finite element analysis and experiments to build up the equation:
For a elastic materials and Berkovich tip, the loading can be determined trough Eq. 2.6:

$$P = 2.1891(1 - 0.21\nu - 0.01\nu^2 - 0.41\nu^3)\cdot\frac{E}{1-\nu^2}\cdot h^2$$
Eq. 2.6

And for elastic-plastic materials (and Berkovich tip) using Eq. 2.7.

$$P = \frac{1.273}{(\tan 24.7^\circ)^2}\left(1+\frac{\sigma_u}{\sigma_y}\right)\left(1+\ln\frac{E\cdot\tan 24.7^\circ}{3\sigma_y}\right)\sigma_y h^2$$
Eq. 2.7

Where ν is the Poisson's ratio, σ_y (GPa) is the yielding stress, σ_u (GPa) is the stress at 29% strain and the ratio σ_u/σ_y is used to represent the strain-hardening property of the material.
As it can be seen, the equation for elastic-plastic materials is more complex than the one proposed by Hainsworth et al. and slightly more difficult to use. σ_y and σ_u *@29%* are not so straightforward to find in tables as *H* and *E*, which are standard output from IIT. Nevertheless, the materials tested by Zeng and Chiu can provide enough information[17] to verify the best equation for testing material with very different values of *H* and *E*.

2.5.2.3 A loading equation for a generic conical indenter

Finally, Eq. 2.8 is a general equation describing the loading curve for (that includes pyramidal indenters) [6].

[17] Their work provides additional parameters for correcting *h* caused by pile-up of sink-in.

$$P = \frac{E^* \cdot h^2}{\left[\frac{1}{\sqrt{\pi} \cdot \tan\alpha}\sqrt{\frac{E^*}{H}} + \varepsilon\sqrt{\frac{\pi}{4}} \cdot \sqrt{\frac{H}{E^*}}\right]^2} \qquad \textbf{Eq. 2.8}$$

E^* is the combined tip and sample Young modulus, calculated as:

$$\frac{1}{E^*} = \frac{\left(1-\nu_{tip}^2\right)}{E_{tip}} + \frac{\left(1-\nu_{sample}^2\right)}{E_{sample}} \qquad \textbf{Eq. 2.9}$$

α is the effective cone angle(Table 2-3)[18]. This equation has been later on adapted [52] to consider the effect of pile-up and sink-in (not discussed here).

As additional references, loading curve equations can be obtained in works of Venkatesh et al [53], made for Vickers and Berkovich tip and considering pile-up and sink-in. Gerberich et al. [54] have studied nanoindentation with spherical tips in elastic loading over rough surfaces, based on standard Hertz equation.

2.5.3 Unloading curve

Literature shows that the studies of *P* x *h* curves are more focused on the unloading part, since it is from there that traditionally *H* and *E* are calculated. Oliver and Pharr have developed the idea from previous works involving the study of indentation diagrams as mentioned in [4, 47, 55] to develop what is today the standard procedure to characterize a material using IIT.

The shape of the unloading curve generally depends on the stress-strain properties of a general elastic-plastic material, as presented in Figure 2.18 [50]

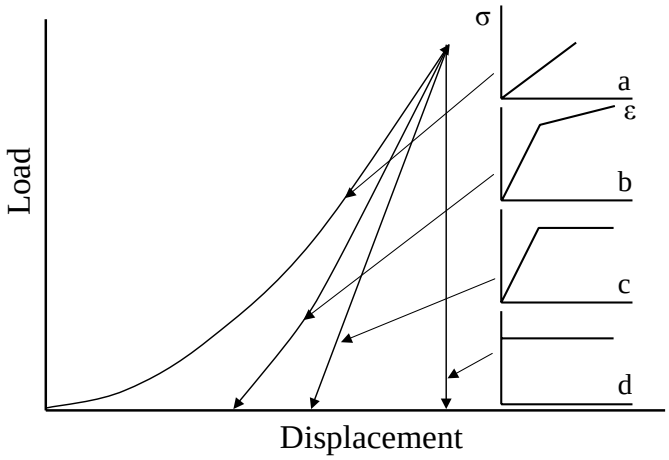

Figure 2.18: Stress-Strain characteristics to the unloading shape: a) Elastic, b) elastic-plastic, c) elastic-perfect plastic, d) rigid plastic

[18] Except for Knoop, reported by Maltzbender and With, that changes *tan* α to $\sqrt{\tan\theta_1} \cdot \sqrt{\tan\theta_2}$

2.5.3.1 Oliver and Pharr (O&P) equations

Eq. 2.10 (a power law function) can completely describe the shape of an unloading curve. However, Eq. 2.11 is the starting point to create an unloading curve, point by point, having *H* and *E* as known parameters.

$$P_u = B(h_u - h_r)^m \qquad \textbf{Eq. 2.10}$$

$$\frac{\partial P}{\partial h} = S = Bm(h_t - h_r)^{m-1} \qquad \textbf{Eq. 2.11}$$

Where P_u is the unloading force, h_u (nm) the displacement during unloading (from the maximum load) and h_r (nm) is the final displacement at complete unloading (P = 0), see Figure 2.19. Values for ***B*** and ***m*** are fitting parameters for each material and for a specific tip shape [47, 55]. P_u can be generated changing the value of h_u in the range of $h_r \leq h \leq h_t$. As the fitting parameters should describe the unloading curve at any given P_u, $\boldsymbol{h_r}$ can be determined through Eq. 2.11 if ***S*** is known. ***S*** can be obtained using $\boldsymbol{P_t}$ and $\boldsymbol{h_t}$, as to be presented.
Another possibility, without using the fitting parameters, is to use ***S*** to partially describe the unloading curve as it can be obtained from the tip geometry and the materials mechanical properties (Eq. 2.14).

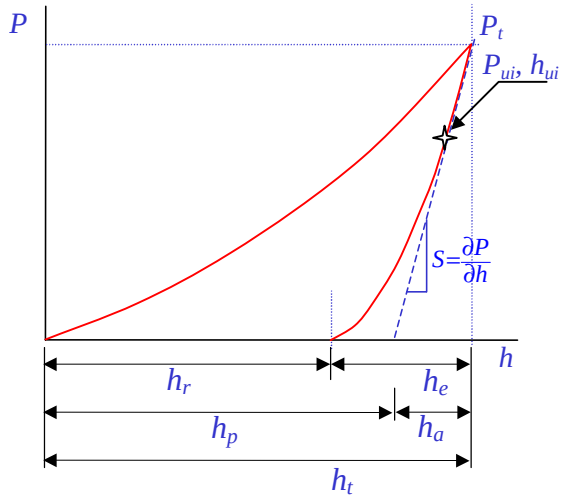

Figure 2.19: P x h graph and its components calculated during unload

The drawback is that the original method focuses only on the linear unloading to calculate ***S*** (the elastic response, situated somewhere between 30 and 80% of the unloading curve). As a result, the "elbowed" end part has not being considered and will not appear. For some materials, a substantial part of the unloading curve will be represented in a linear instead of an elbowed way (Figure 2.15b).
The *S* approach to represent reaction forces through simulation is thus more conservative. It describes the unloading forces and the plastic deformations higher than in a real indentation.

The relations determined from the Oliver and Pharr methods are presented from Eq. 2.12 to Eq. 2.14.

$$H = \frac{P_t}{A} \qquad \textbf{Eq. 2.12}$$

$$E^* = \frac{S\sqrt{\pi}}{2\beta\sqrt{A}} \qquad \textbf{Eq. 2.13}$$

$$\mathrm{S} = \frac{\partial \mathrm{P}}{\partial \mathrm{h}} = 2\beta E^* \sqrt{\frac{P_t}{\pi H}} \qquad \textbf{Eq. 2.14}$$

Note: In the original O&P publication [47] β has not been included (although it appears later in [55]). Its values (as presented in Table 2-3) are not standard as they depend on the elasto-plastic behavior of the material. Reported options are not to use β or to attribute 1 (one) to it. However, to agree to the main literature used in this chapter, values from Table 2-3 are used.

For describing the unloading curve (based only in *S*) the calculation of *P* during unloading (P_u) as the tip withdraws (h_u) still has to be obtained through Eq. 2.15 to Eq. 2.17. The mathematic procedure to obtain the $\mathrm{P_u}$ points considering h_u as a given input is presented in Eq. 2.16 and Eq. 2.17.

$$\partial \mathrm{P_u} = 2\beta E^* \sqrt{\frac{P_t}{\pi H}}\, \partial \mathrm{h_u} \qquad \textbf{Eq. 2.15}$$

$$\begin{aligned} P_{u1} &= P_t - \partial P_{u1} \\ P_{u2} &= P_{u1} - \partial P_{u2} \\ &\vdots \\ P_{ui+1} &= P_{ui} - \partial P_{ui+1} \end{aligned} \qquad \textbf{Eq. 2.16}$$

And for $\delta \mathrm{h_u}$,

$$\begin{aligned} \partial h_{u1} &= h_t - h_{u1} \\ \partial h_{u2} &= h_{u1}^{'} - h_{u2} \\ &\vdots \\ \partial h_{ui+1} &= h_{ui} - h_{ui+1} \end{aligned} \qquad \textbf{Eq. 2.17}$$

As presented, O&P could be used to quickly describe the unloading curve as a function of the sample stiffness *S*. In a more complete way, together with the fitting values *B* and *m* to calculate h_r in Eq. 2.11 and finally the real unloading curve through Eq. 2.10. However, *B* and *m* are values that are very specific for a given curve (obtained through measurements). Therefore, a general value for *B* and *m* does not exist, except if the curve (at a given load) is previously available.

2.5.3.2 Field and Swain equations

Field and Swain have presented a simple model where the entire indentation graph for a spherical tip can be predicted from the material and indenter properties [45]. This

work has been later on compiled and adapted [6] in order to describe the unloading curve for the Berkovich indenter and the so called "Single point unload method" (Eq. 2.18). This uses a single unloading point rather than *S* to determine h_r and h_p based on Hertz theory, as the first unloading point is purely elastic.

$$h_u = \left(\frac{P_u}{P_t}\right)^{1/2} \cdot \left[h_r\left(\left(\frac{P_t}{P_u}\right)^{1/2} - 1\right) + h_t\right] \qquad \textbf{Eq. 2.18}$$

P_u and h_u are the points that describe the unloading curve (Figure 2.20).

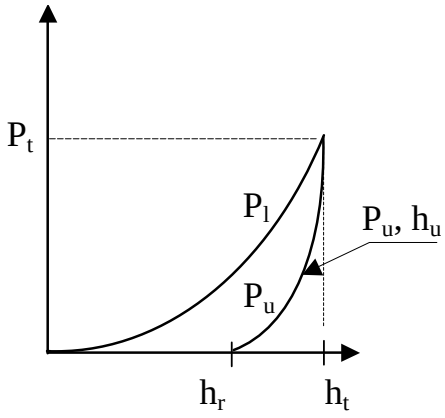

Figure 2.20: Indentation graph with the main parameters for F&S method.

P_t and h_t are obtained by the loading curve. Finally, h_r is obtained through Eq. 2.19.

$$h_p = h_t - \left[\frac{\pi - 2}{\pi}\right] \cdot h_t + \left[\frac{\pi - 2}{\pi}\right] \cdot h_r \qquad \textbf{Eq. 2.19}$$

h_p can be found using Eq. 2.12 and Table 2-3. For the Berkovich tip

$$A = 24.5 h_p^2 \qquad \textbf{Eq. 2.20}$$

$$h_p = \sqrt{\frac{P_t}{24.5 \cdot H}} \qquad \textbf{Eq. 2.21}$$

Rearranging Eq. 2.18 for P_u, Eq. 2.22 is obtained.

$$P_u = \left(\frac{\sqrt{P_t} \cdot (h_u - h_r)}{(h_t - h_r)}\right)^2 \qquad \textbf{Eq. 2.22}$$

2.5.3.3 Zeng and Chiu equations

Zeng and Chiu [50] have also analyzed the unloading curve, based on previous works (as described in their analysis of the loading curve) and measurements of different materials. The unloading equations, obtained for a Berkovich tip are presented from Eq. 2.23 to Eq. 2.26.

$$P = (1-\theta) f(\nu) E h_u^2 + \theta S (h_u - h_p) \qquad \textbf{Eq. 2.23}$$

Where

$$f(\nu) = \frac{2.1891(1 - 0.21\nu - 0.01\nu^2 - 0.41\nu^3)}{1 - \nu^2} \qquad \textbf{Eq. 2.24}$$

$$\theta = \frac{\sigma_y}{\sigma_u} \qquad \textbf{Eq. 2.25}$$

$$S = 2\sqrt{\frac{24.5}{\pi}} \frac{E}{1-\nu^2} h_p \qquad \textbf{Eq. 2.26}$$

The material properties H, E, σ_y, σ_u @29% strain utilized on the experiment can be found in the Zeng and Chiu paper [50]. Again, h_p can be calculated as Eq. 2.21. Note that the equation still uses the notion of sample stiffness *S* to guideline the unloading curve, but it now includes θ (strain-hardening parameter), balancing plastic/elastic behavior. Changes in θ will make the unloading shape to change in a more or less parabolic shape, depending on the material properties.

For those interested in unloading analysis including pile-up, sink-in or for different tips, references [50, 51, 55] are a good start.

2.5.4 Models overview

Indentation models for loading and unloading have been presented in this chapter. The goal has been to describe the loading and unloading and later, to use them to determine the reactions forces over the indentation tip and consequently by the tip actuator.

The Hainsworth model has easier implementation, as it needs only the material's properties *H* and *E*, virtually obtained in any IIT test. For the same reason, the Field and Swain equations are also easy to be implemented and able to describe the entire unloading curve, including a kink (elbow) shape. However, as it will be shown in Chapter 3, its representation is more conservative and (example for Fused Silica) this model does not agree so well on the representation of $\boldsymbol{h_r}$. The Oliver and Pharr method (using unloading stiffness ***S***) has also an easy implementation, but it gives a linear unload. For partial (but not strong) unloads during the loading phase, the ***S*** approach fits well, as an elastic-plastic material has a purely elastic response during initial unload. In the same way, the entire unloading curve will have a nearly linear unloading in the case of materials with low elastic response, as for example Aluminum or Tungsten (see Figure 2.16).
The main difficulty for unloading is to estimate the point of $\boldsymbol{h_r}$ from a given $\boldsymbol{P_t}$. In some tests with IIT devices, the sample is tested at several ranges of maximum loads. One possibility is to take a similar experiment to plot $\mathbf{h_r}$ in function of $\mathbf{P_t}$. Since at this point the values are independent from the indenter frame stiffness (as is the point where the tip leaves the sample), a general function could be generated, adding more accuracy to the unloading description. The disadvantage is again the need to have the curves for a given material in advance.

2.6 Conclusions

This chapter has introduced some relevant points of an in-situ indentation and scratching device. An overview of a SEM is necessary in order to explain the operational conditions of an ITT device and its interaction with the electron beam. For the same reason, selecting an actuator that could be, or is used in nanoindenters, implies that it must be compatible with a SEM environment. The indentation tip is important for design considerations, as it determines the operational position of the indenter (necessary tilting), to get a full view around the tip-sample interaction. In addition, the tip-material interaction during indentation will output a specific reaction force. This force, explained through the P x h graph, will be used to visualize the actuator response (that drives the indentation tip), as the reaction force increases. The implementation and integration of those models into a model of a stick-slip actuator will be presented in the next chapter.

Blank page

Chapter 3

Simulations of Stick-Slip Actuators for Indentation and Scratching

3.1 Introduction

In this chapter, the use of stick-slip actuators for indentation and scratching is demonstrated.
This includes a more detailed description of this kind of actuator, with emphasis on a dynamic model to describe its behavior. This model, originally presented by J-M. Breguet [56], has been integrated with the indentation models previously described and a model describing the indenter reaction (frame stiffness, damping, etc.). The full model has thus been implemented by the means of a simulation software (Simulink®, a Matlab® package [57]). Hence, not only the full indentation behavior can be better visualized, but also individual points (as changes in friction, frame stiffness, normal load, etc.) can be easily changed to better understand the actuator influence on the indentation curve.

3.2 Implementation of the indention curves

The indentation equations presented in Chapter 2 are implemented through *Simulink*. The resulting graphs from a simulated Berkovich indentation are thus compared to a real indentation graph.
Indentation equations have been prepared to have a penetration depth *h (meters)* as input and load *P (Newtons)* as an output. This modification makes it possible to match the stick-slip model (already available in Simulink). This model uses the indentation force as a reaction force over the actuator.
Describing the indentation force in terms of an input displacement *h* is quite unusual. As presented in Chapter 2.3 – Actuators, most of the presented actuators have load as input. Entering load on the equation and getting *h* is more straightforward and it is easier to determine h_r (related to plastic deformation). Stick-slip actuators and Piezoactuators are displacement input. Force is only obtained when the movement is constrained. For example, driving it against a spring. In this case, the material stiffness during loading-unloading, plus the frame compliance will be the springs acting against the piezoactuator or carrier. Thus, for a given displacement, a reaction force is obtained.
The loading-unloading equations must take into account some real behaviors. The loading equation (called here P_l) will output a P_t and an h_t *(registered max force and depth).*
The unloading equation (P_u) is valid from $h_r \leq h_u \leq h_t$ and $P_u = 0$ if $h_u < h_r$. If h_u (displacement during unloading) reaches h_r (correspondent of the material plastic

deformation), the contact will be lost, and the generated forces during unloading will be zero.
Force during unloading is only generated if the elastic component (h_e) is still present. As presented before, (Figure 2.15), h_e is simply h_t - h_r. A flowchart describing this procedure is presented in Figure 3.1.
Finally, if the unloading stops at any point before h_r, ($h_u \geq h_r$) and changes direction (now loading), the equation utilized will be the same as P_u until h_u is again higher than h_t when the equation to describe the loading switches again to P_l.

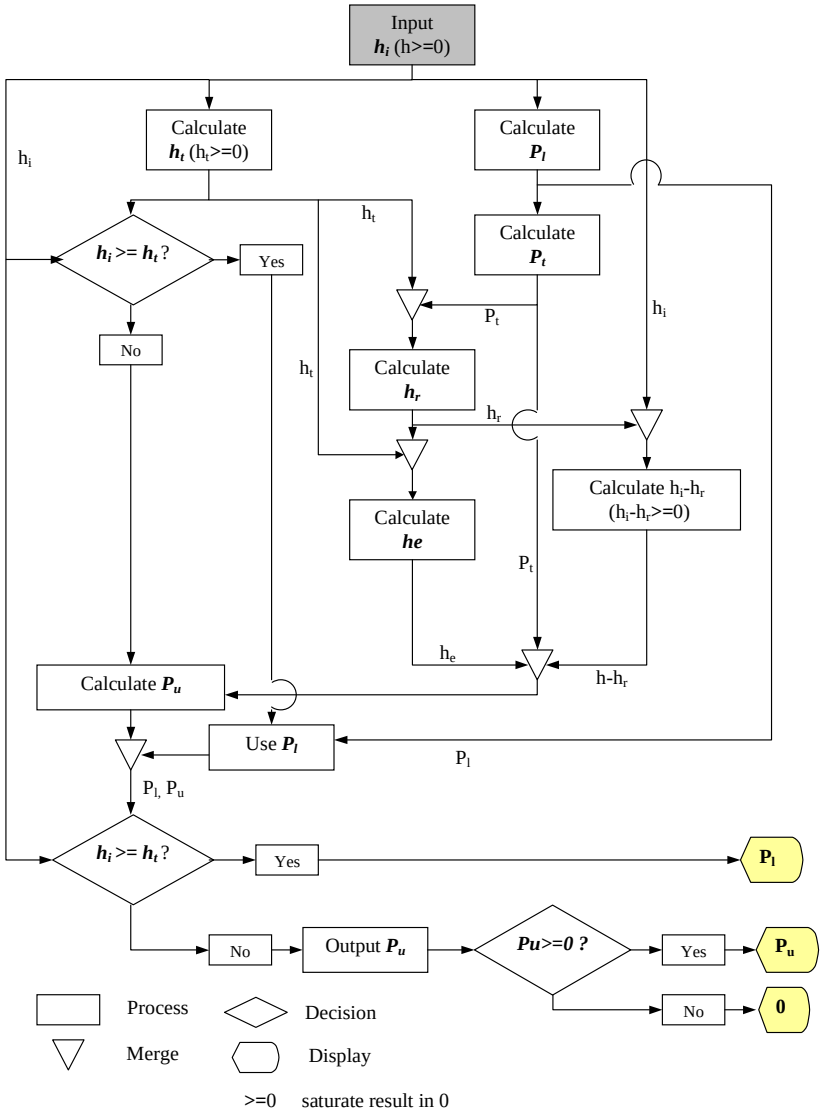

Figure 3.1: Flowchart of the loading-unloading calculation.

An indentation graph with partial unloads is shown in Figure 3.2. A full implementation using Simulink is presented in Annex I.

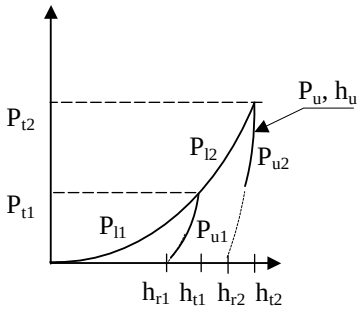

Figure 3.2: Indentation graph with partial unloads

3.2.1 Evaluating the indentation model.

Following the described procedure, the two loading and the three unloading models have been implemented using Simulink. The results are compared to real indentation curves (*P_mts*) at two different maximum loads. A good material to start with is Fused Silica, often used as a standard material to calibrate indenters. The result can be observed in Figure 3.3.
P_mts is the reference curve, measured through a commercial instrument (MTS XP). *P_hainsworth-orig* uses the constants ϕ and ψ, respectively **0.194** and **0.930**, obtained through calibration of a specific tip, as reported in the original paper [46]. *P_hainsworth-corr* uses ϕ and ψ, respectively **0.202** and **0.638,** calculated for an ideal Berkovich tip, as mentioned in Maltzbender and With's paper [49].

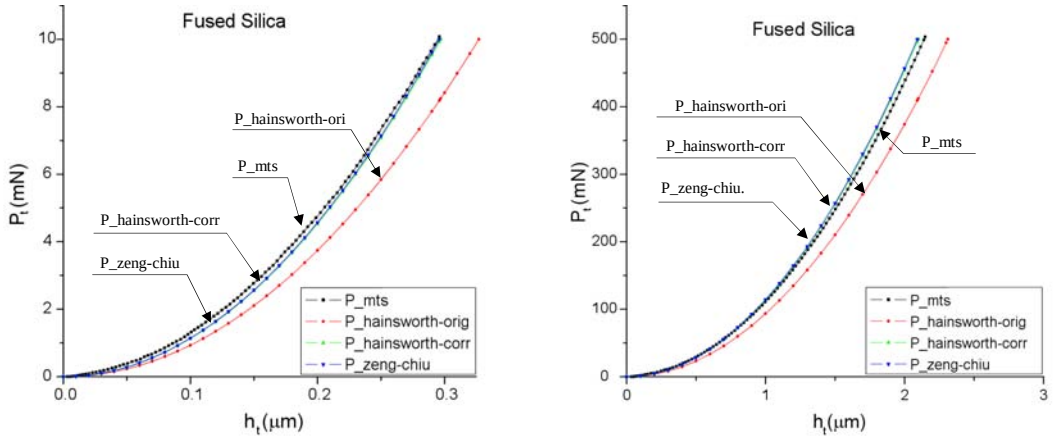

Figure 3.3: Comparison of loading models in fused silica at two different maximum loads, 10mN and 500mN

Finally, *P_zeng-chiu* used the model described by Zeng and Chiu. This uses the strain-hardening property of the material. Input terms hardness (*H=9GPa)*, Young's modulus (*E=72GPa)* and Poisson's ratio (ν*=0.17*) have been obtained from the reference curve and the strain-hardening parameter (θ*=0.49*) has been obtained directly from the work by Zeng and Chiu.
As can be observed, there are good agreements between *P_zeng-chiu*, *P_hainsworth-corr*. and the real curve, at least for Fused Silica. In this case, it is easier to use the Hainsworth model (considering a perfect Berkovich tip), since it depends only on the material property *H* and *E*, which is easier to find than the strain-hardening parameter.
For the unloading part, the overlapping is not as good as during loading, as can be observed in Figure 3.4.

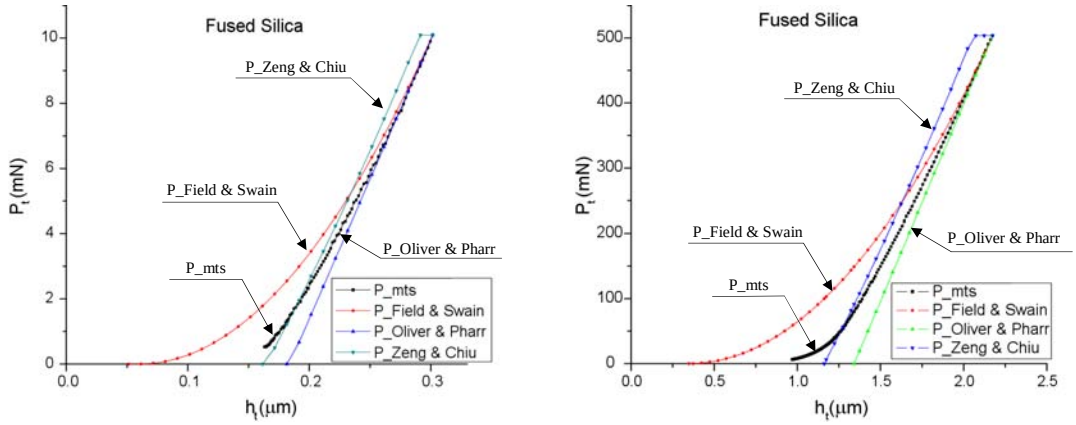

Figure 3.4: Comparison of unloading models in fused silica at two different maximum loads, 10mN and 500mN. The flat region (saturation) that appears in the P_Zeng & Chiu model is discussed in the text.

Once more, *P_mts* is the reference curve. The maximum loads P_t and displacement h_t have been obtained from the reference curve and have been input as initial point on all models. The Field and Swain model can output a more evident kink, although it does not completely agree with the real unloading curve. The Zeng and Chiu model has initially output the first unloading points higher than P_t. However, for simulation purposes, P_t is the maximum value allowed (saturation point). This model uses a linear unloading plus the strain-hardening parameter to balance the elastic/plastic characteristics to describe the unloading phase. Still, the result also does not represent the final section of the curve. As expected, the Oliver and Pharr method matches well the initial unloading section. This has been expected as the utilized *H* and *E* have been obtained through this model. An option to include the kink on the Oliver and Pharr method is to use the relation $P_u = B(h_u - h_r)^m$. The *B* parameter (fitting parameter) is not the same for all loads, but *m* is very similar. It is important to highlight that the fitting parameters are obtained considering only the initial part of the unloading curve. Once more, the final part of the curve will not be described. Yet, the unloading curve will not be linear.

Table 3-1 shows the calculated parameter *B*, h_r and *m* for the *P_mts* curves presented (considering the first 80% of the unloading curve), as well as the values found in the Oliver and Pharr paper [47, 55].

Table 3-1: Table of unloading power law curve fitting values

Curve	B (mN/nm^m)	h_r (μm)	m
O&P[19] = 120mN	0.05	0.50	1.25
P_mts = 500mN	0.46	1.11	1.22
P_mts = 10mN	0.11	0.15	1.26

As can be noticed, a value of 1.25 for *m* (case of Fused Silica) could be used as a constant, although it is still necessary to obtain *B* and h_r. The Field and Swain method provides a way to estimate h_r. Therefore, it could be combined with the Oliver and Pharr method (based on the unloading stiffness *S*), in an interactive way to find *B* and finally plot the entire unloading curve. This is left as an idea (as has been the P_t x h_r

[19] Estimation taking as example *Fig 8* in the O&P paper, showing a 120mN indentation in Fused Silica.

function proposed at the end of Chapter 2). The main interest of this work on these graphs is to have a good idea about the indentation forces acting on the actuator.
In case of a stick-slip, this means increasing its jump-back during loading but decreasing it during unloading.
The final graph section is quite difficult to represent (and consequently to find h_r). It also has little significance for the calculation of *H* and *E*. For this reason, only the initial part is considered, varying from 30 to 80% of the unloading curve, depending on the material analyzed (the procedure is described in ISO 14577).
For stick-slip indentation, the interest in h_r (where also P_u=0) is, that it can reveal how many times the tip will completely unload the sample after partial unloads created during the slip phase. A partial unloading is not a common procedure, although it is a known process. It can be used to verify changes on the material properties in function of the applied maximum load or to study material creep. However, a complete unloading and to use afterwards the same print to continue indentation is something not usual.
Consequently, the main question to be answered (and one of the goals of this thesis) is if the conventional procedures to determine the material's mechanical properties can be influenced by a P x h curve obtained through a stick-slip indentation.
If the material has a more elastic-perfect plastic or rigid plastic behavior (Figure 2.18), it is expected that the unloading equations will have a better agreement, since the kink will not be so pronounced. On the other hand, materials with a more prominent plastic deformation have $h_r \approx h_t$. In this case, the tip easily loses contact with the sample.
During indentation (acquiring raw data), the instrument frame stiffness can play an important role. A low frame stiffness may contribute to avoid complete unloads even in very plastic materials. Unfortunately, low frame stiffness is not a desirable characteristic in nanoindenters, since it triggers a low dynamical response and a difficult displacement measurement, because the real penetration depth (h_{corr}) must be determined from the raw data.

3.2.2 Selecting a loading-unloading model

An evaluation of loading and unloading models has pointed out a better implementation using a Hainsworth model with a perfect Berkovich tip to describe loading and the Field and Swain model to describe unload. The justification is that both models need as an input only the material hardness (H_GPa) and Young's modulus (E_GPa). The appearance of a more evident kink (instead of a straight line) has also been considered. It represents a non linear unload, although this implies in a more conservative h_r (tip will need more redraw until it reaches a complete unload).

3.3 Indenter frame model

When an indentation force is applied, it will follow a path that starts from the sample, goes through the force transducer, indenter frame, tip actuator and finally ends at the contact between the tip and the sample (Figure 3.5a). This can be approached as a series of springs, where the more compliant point will overcome the other ones. The total stiffness is called frame stiffness (K_{inst}).

This is a simplified assumption that works well for indentation depth correction. However, the real instrument dynamic behavior is a combination of *n* mass-spring-damp systems found in the instrument's frame stiffness loop (indenter frame, sample holder, load transducer, etc.). This creates a system with a same number of natural

responses but dominated by the lowest natural frequency. For modeling purposes and computational speed, the *Indenter model* has thus been simplified to a first plus second order system (Figure 3.6).

Burnham et al. [58] presents a model that can be described as a single universal linear model for quasi static and dynamic responses for depth-sensing indenters (instrumented indentation testing - IIT), atomic force microscope (AFM), surface force apparatus (SFA) and their relations. In the text, they are generally called mechanical properties nanoprobes (MPN). Figure 3.5b shows the frame main components, the reference (zero), a place where displacement is applied, two different ways to input force and three different ways to detect displacement. Often, in IIT devices, a very stiff frame is desired, which includes in this case the instrument head, the base and the force transducer.
The design of the indenter frame can assume different forms. This is also the case for the points where force and displacement can be acquired. Figure 3.6 shows a simplified free body diagram of the Figure 3.5a indenter frame. In this case, a sample and a holder with a combined mass ***m*** are held by a frame with equivalent (total) stiffness and damp.

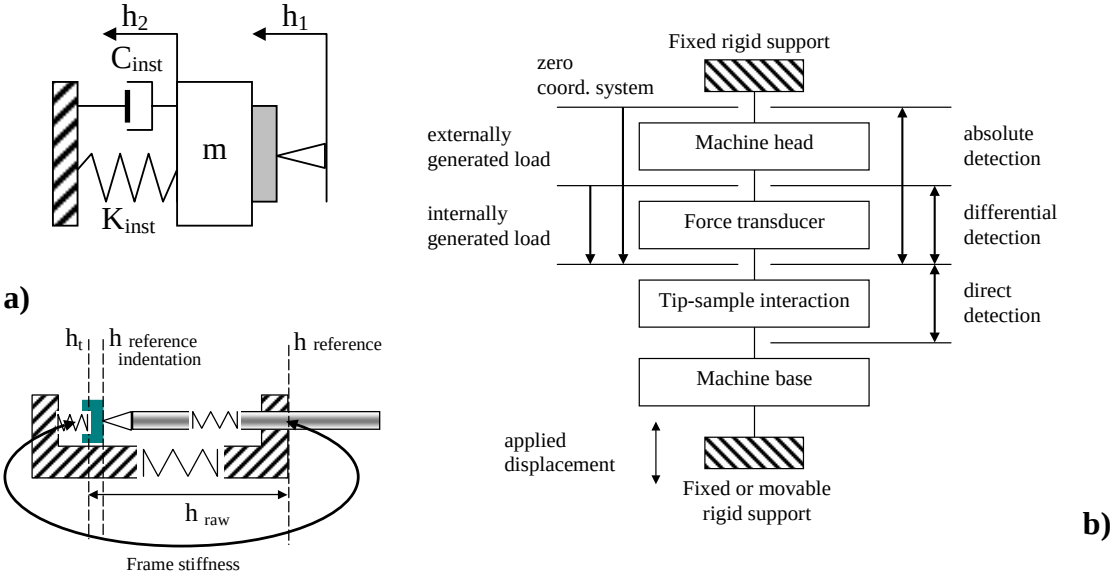

Figure 3.5: a) Frame overview, b) diagram of a universal frame and its components.

In this model, the frame stiffness (combined stiffness - K_{inst}) has a linear behavior, but the sample stiffness (K_{spl}) can be approached as a non-linear spring containing hysteresis. This can be obtained directly from the loading–unloading model (input displacement, output force) described in Paragraph 3.2. A *Simulink*® implementation is shown in Annex I.

The indentation models presented in Paragraph 2.5 have displacement as input (indentation depth). The presented models have been originally developed with ***P*** as input. The complete equations are found in the references of each of the loading-unloading models.

One variant of the model (not implemented in the simulations) is to place the load cell between the tip and the carrier, letting the sample in a rigid frame (Figure 3.7). The

input ***h₁*** is displacement (given by the carrier) and the output is the force ***P*** over the sample.

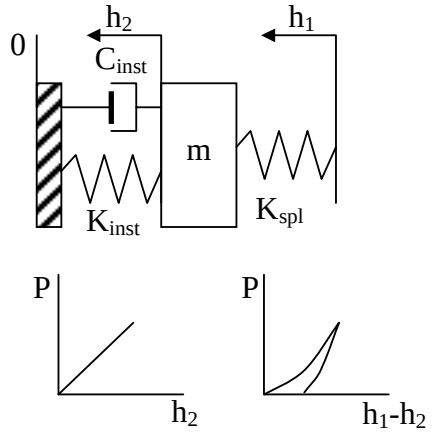

$$\sum F = m\ddot{h}$$

$$K_{spl}(h_1 - h_2) - K_{inst}(h_2 - 0) - C_{inst}(\dot{h}_2 - 0) = m\ddot{h}_2$$

K_{spl} , Described by P_l and P_u
K_{inst} , Combined instrument stiffness
m, combined mass (sample+holder)

Figure 3.6: Free body diagram of Figure 3.5a. The P x h inset pictures represent K_{inst} as linear spring while K_{spl} as a non liner spring containing hysteresis.

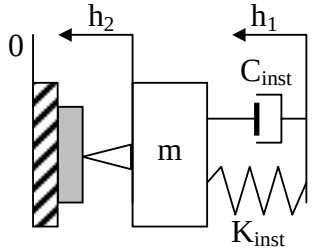

Figure 3.7: Model of the indenter body diagram having frame stiffness placed between the tip and the carrier.

3.3.1 The SEM indenter frame description

A standard design approach has been utilized to build up a SEM indenter (or SEM IIT). It utilizes a combination of sliding and flexure mechanisms to provide a coarse and fine tip-sample approach, a stack piezo actuator (type d_{33} piezoactuator) to drive the tip into the material and a load cell, to hold the sample and recording force. The stack piezoactuator has a built in strain gauge used as a displacement transducer. Facilities for sample positioning can be used for sample scratching (as the Y-stage, using stack piezoactuators or stick-slip actuators). The instrument is shown in Figure 3.8. Details about it are found in [16, 18] and in Chapter 5.

The comparison of this design with the universal frame (Figure 3.5) makes it possible to identify the fixed rigid support, that is the L shape part that holds the X and Y stage and the dovetail that holds the linear stage. The force transducer is the load cell that, in this case, stays referenced with the instrument bases instead of the instrument head[20]. The instrument base, in this design, is the tip holder plus the flexure (in charge of providing a linear movement with high lateral stiffness). The piezoactuator is fixed in one extremity on the linear stage. It can be considered here as the movable rigid support. As the displacement sensor is on it, it is easy to make the zero coordinate

[20] In some IIT machines, the indenter tip is installed over the load cell (Figure 3.7). The load cell also moves toward the sample during indentation. The reading force is the reaction force over the tip.

system matching its rigid base. The measurement is thus of an 'absolute type', being necessary to know the instrument frame stiffness (starting at sample, finishing in the tip holder) to determine the true indention depth. A direct detection, in this design, can be obtained by measuring the distance between the *sample* and the *tip holder*, from the moment when a force is detected in the load transducer.

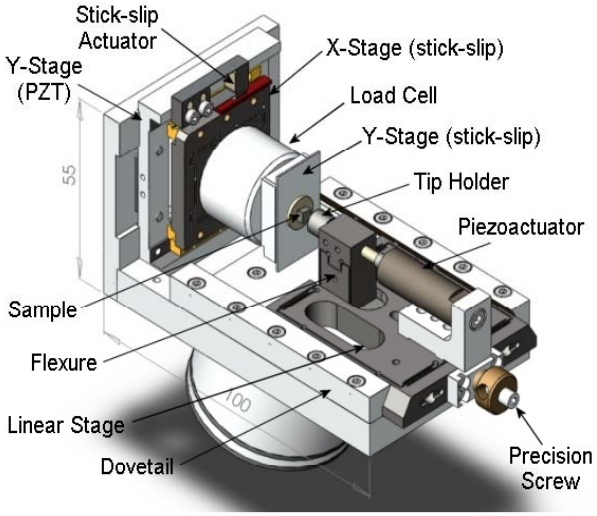

Figure 3.8: The SEM indenter (main components). Details are presented in Chapter 5.

The frame design implemented in the simulation follows the design of the presented SEM indenter (presented in Figure 3.6). The frame has a characteristic stiffness and damping. The load cell is modeled in series with the frame and is often the most compliant part of the system[21]. The sample, with a given mass, will be placed over the load cell. The linear stage plus the piezoactuator and the flexure is combined as spring in series. For simplification purposes, all those components in series are represented by a combined stiffness and damping.
Specifically in the case of a stick-slip indentation, the linear stage (including piezo and flexure) is modeled as a mobile carrier that holds the tip. This *carrier* is schematized in Figure 3.9.
The instrument will be used later on to show the differences among a number of ways to drive the tip (for indentation), as the stack piezoactuator can perform both cases (continuous displacement or simulating jump-backs related with stick-slip) keeping all the parameters.

3.4 Stick-slip model

3.4.1 Introduction

A dynamic model of a stick-slip actuator (Figure 3.9) has been presented by Breguet [56] and it has originally been developed in cooperation with a work presented by Altpeter [59] in the field of friction modeling. Both works have been specifically developed for stick-slip actuators, although with a different focus.

The contact model (between the foot and the carrier) considers different and complex friction models, involving negative viscous friction, Coulomb (sliding) friction and a

[21] The load cell is a spring system. Strain gauges are glued over a set of flexure disks. Normally more sensitive is the load cell, less stiff are these springs.

viscous friction model (Stribeck friction). The combination of these models is necessary to describe the transition between static and dynamic friction, which is not instantaneous (Figure 3.10c).

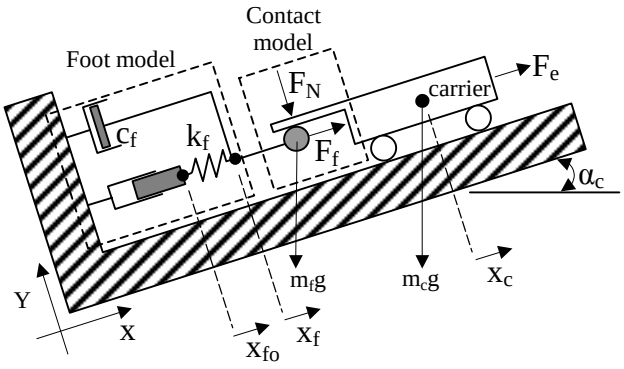

Figure 3.9: Stick-slip actuator model, including the foot model and the contact interface

The Stribeck effect is known as a destabilizing influence on control systems [60] and is related to displacements at very low velocities (occurring near the transition of static and dynamic friction). For this reason the stick-slip **effect** is more known as a problem that impedes a system to be driven over small distances with accuracy. One should notice that, in this work, stick-slip **actuators** denote the opposite. It is a method to drive small distances with high accuracy.
A transition from positive to negative motion is presented as a vertical line in Figure 3.10. During this transition, the friction forces are described by the *Dahl effect*.

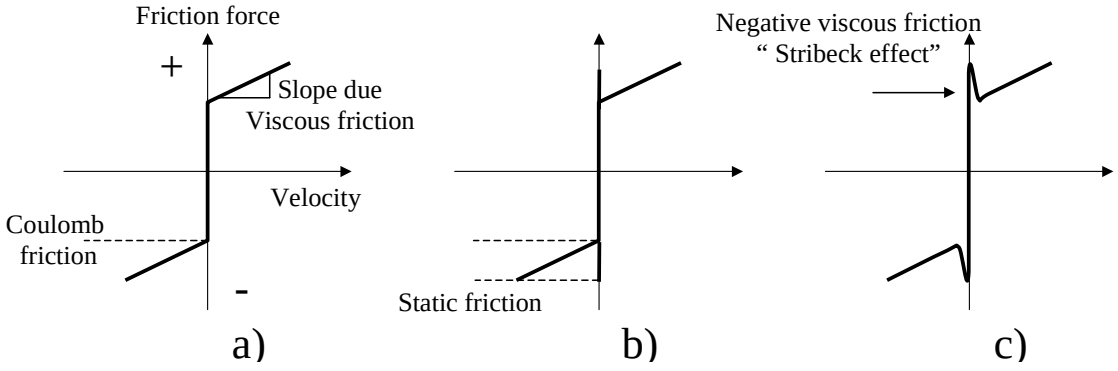

Figure 3.10: Representation of friction forces. Common models: a) Coulomb+Viscous, b) Static+Coulomb+viscous, c) Negative viscous+Coulomb+viscous (Stribeck effect) [61]

When friction forces change direction, there is a delay until the system reacts (a memory effect). This is not only caused by mechanical plays on the entire system but it happens also on the interface between bodies that are under the influence of external forces. Two bodies stay in contact through a series of points, called asperities (Figure 3.11a). Asperities deform (plastic/elastic) to generate a contact area necessary to afford the applied normal load (F_N). They will also have an initial elastic deformation when in presence of a lateral load (F_t), creating a pre-sliding displacement. Thus, any interface has a normal and a lateral compliance (Figure 3.11b).

This lateral displacement is approximately a linear function of an applied tangential force and is called tangential contact stiffness. If a tangential force is applied and removed (Figure 3.11b), without reaching the maximum static friction, the interface

recovers. Each asperity can indeed deform plastically, what is connected with the rising force detected in the static friction region. If the tangential force continues to increase, a breakaway will occur, and the body will slide; but this does not happen at once. Johnson [62] has used the term micro-slip to design the transition between elastic contact and sliding. As he has once observed, the sliding starts first at the ends of the junction width (boundary), propagating toward the center. This implies that a part of the contact is under compressive stress, while the opposite side will be under traction and this changes each time the tangential force changes direction. This denotes how complex the interface mechanism is and why there is no sharp transition toward sliding[22].

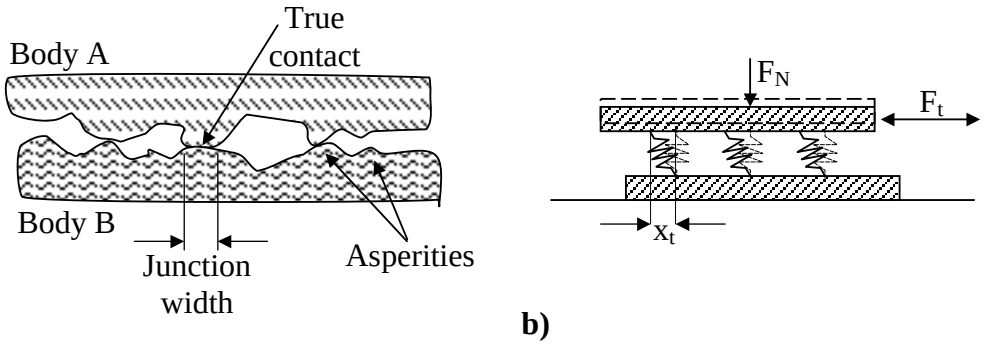

Figure 3.11: a) Scheme of two bodies in contact, b) Compliance between junction bodies

Tangential stiffness is a function of the asperity geometry, material elasticity and applied normal force [61, 62]. For formulation purposes, the normal force is considered static. Modeling the tangential stiffness is in itself complex and the simplest model (and the one implemented on the stick-slip driven model) is the sphere-plane contact. Mindlin [63] has presented a literal solution for it, that helps a more straightforward implementation within the stick-slip actuator model. A more complex contact interface geometry (elliptic, angular, etc.) increases the number of considerations (boundaries). The implementation is more difficult, without improving substantially the stick-slip model [56].

3.4.2 Model description (equations)

Starting with the scheme presented in Figure 3.9, the foot model is described by Eq. 3-1.

$$m_f \ddot{x}_f = k_f \left(x_{f0} - x_f \right) c_f \dot{x}_f - F_f + m_f g \sin \alpha_c \qquad \textbf{Eq. 3-1}$$

The foot is in charge of driving a carrier through a friction force F_f (N). The components m_f, k_f, c_f are respectively the foot mass (kg), foot stiffness (N/m) and the foot damping (kg/s).
The component x_{f0} and x_f are the foot reference and the final foot displacement, while $\dot{x}$ and $\ddot{x}$ are the foot velocity (m/s) and the acceleration (m/s^2). The foot is also under gravity acceleration (g, in m/s^2), and its vector force is calculated in function of the tilted angle α_c (degrees).
The force balance over the carrier is described by Eq. 3-2.

[22] A sharp transition could increase the performance of a stick-slip actuator, as part of the displacement will not be stored in the foot-carrier interface. Static friction is considered as a force of constraint as there is so sliding movement.

$$m_c\ddot{x}_c = F_f + F_e + m_c g \sin\alpha_c \qquad \textbf{Eq. 3-2}$$

Component descriptions are the same as the ones used for the foot. F_e (N) is the external force acting on the carrier. It could be, for example, the reaction force arising from indentation.
The friction model between the foot and the carrier (F_f) is given by:

$$F_f = \sigma_0 z + \sigma_1 \dot{z} + \sigma_2 \dot{x} \qquad \textbf{Eq. 3-3}$$

This is the starting point used by Breguet-Altpeter which have been based on a model initially presented by Canudas - de-Wit [64] that is a modification of the Dahl model including the Stribeck effect.
The subcomponents of Eq. 3-3 are presented from Eq. 3-4 to Eq. 3-10.

$$\dot{z} = \dot{x} - \frac{|\dot{x}|}{g(\dot{x})} z \qquad \textbf{Eq. 3-4}$$

$$\sigma_0 g(\dot{x}) = F_{col} + (F_{sta} - F_{col}) e^{\left|\frac{\dot{x}}{v_s}\right| \cdot \frac{\dot{x}}{v_s}} \qquad \textbf{Eq. 3-5}$$

Where $\dot{x}$ (m/s) is the relative velocity between foot and carrier, the variable $\boldsymbol{z}$ (m) denotes an average deflection of the asperities between foot/carrier. $\boldsymbol{\sigma_0}$ (N/m), $\boldsymbol{\sigma_1}$ (kg/s) are the contact stiffness and the damping coefficient of the contact. $\boldsymbol{\sigma_2}$ (Ns/m) is the viscous friction coefficient. The function $g(\dot{x})$ describes the Stribeck effect and $\boldsymbol{v_s}$ (m/s) is the Stribeck velocity. F_{col} and F_{sta} (N) are the Coulomb and the static force and are given by:

$$F_{col} = F_N . \mu_{col} \qquad \textbf{Eq. 3-6}$$

$$F_{sta} = F_N . \mu_{sta} \qquad \textbf{Eq. 3-7}$$

$\boldsymbol{F_N}$ (N) is the normal force and $\boldsymbol{\mu}$ is the friction coefficient (static or Coulomb).

The tangential contact stiffness ($\boldsymbol{\sigma_0}$) for a simple sphere-plane contact has been presented by Mindlin as:

$$\sigma_0 = \frac{1}{\frac{1}{8 \cdot a}\left(\frac{2-\upsilon_f}{E_f} + \frac{2-\upsilon_c}{E_c}\right)} \qquad \textbf{Eq. 3-8}$$

$\boldsymbol{\upsilon_f}$, $\boldsymbol{\upsilon_c}$, $\boldsymbol{E_f}$, $\boldsymbol{E_c}$ are the foot and carrier Poisson coefficient and the Young's modulus (GPa). The term $\boldsymbol{a}$ (m) is the radius of the contact interface, calculated as:

$$a = \sqrt[3]{\frac{3 \cdot F_N \cdot R_f}{4E'}} \qquad \textbf{Eq. 3-9}$$

R_f (m) is the foot radius and $\boldsymbol{E'}$ is the combined Young's modulus.

$$E' = \frac{1}{\frac{1-\upsilon_f^2}{E_f} + \frac{1-\upsilon_c^2}{E_c}} \qquad \textbf{Eq. 3-10}$$

With those equations, it is possible to describe dynamically the friction contact between the driving foot and the carrier, as well as the carrier displacement. This model has a good agreement with a real system as presented elsewhere [56]. A simplified friction force block diagram is shown in Figure 3.12.

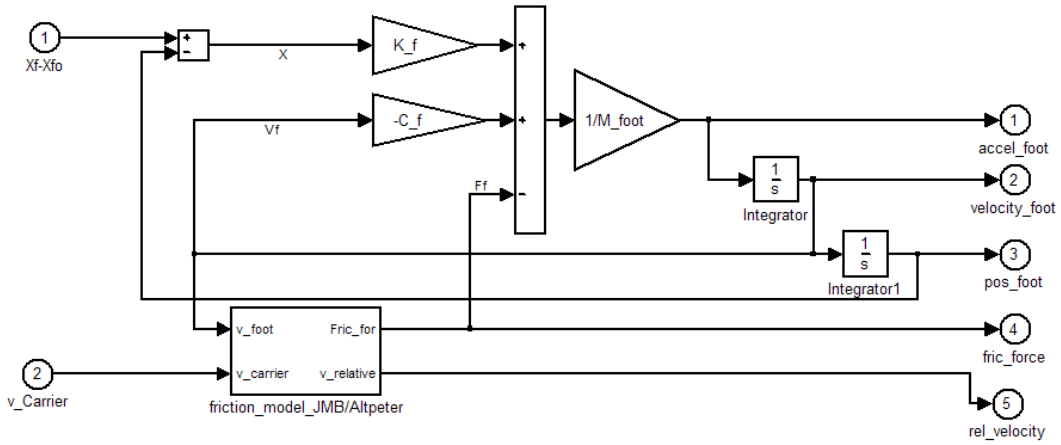

Figure 3.12: Friction force block diagram. Sub-system *friction model* contains Eq. 3-3.

This finishes the dynamic model of a fix driving foot (a half sphere) contacting a mobile carrier (having a flat contact).
Stick-slip actuator is a specific case of inertial driver. Thus, it is necessary a carrier with a certain mass (ideally higher than the foot system) and a foot with high backward acceleration do create the slip phase. A standard input shape to drive the foot is the sawtooth signal (a slope followed by a quick redraw).

3.5 A complete model of a stick-slip indentation

Finally, all presented models are incorporated in a single system called stick-slip indentation (schematized in Figure 3.13).
A foot excitation signal (sawtooth) creates the foot movement. The driving friction contact model is presented by the ***Foot Model*** block. This block contains essentially Eq. 3-1 and outputs the friction force $\boldsymbol{F_f}$. This force, plus an external force $\boldsymbol{F_e}$ and a constant force actuating over the carrier (vector weight) $\boldsymbol{F_g}$ are resulting forces - the carrier input force. The external force $\boldsymbol{F_e}$ will always be in opposition to the driving force, although weight can be a positive or a negative force, depending on how the system is tilted.

The ***Carrier Model*** block has as an input the resulting force over the carrier. As the carrier has a mass, acceleration can directly be determined and further integrated. The first integration provides velocity and the second, displacement (presented as ***x_c***).
In this configuration, the indentation tip is attached to the carrier, sharing the same movement and reaction forces. The carrier output displacement ***x_c*** is a raw displacement and cannot be used directly as penetration depth for the indentation model because frame stiffness is present.

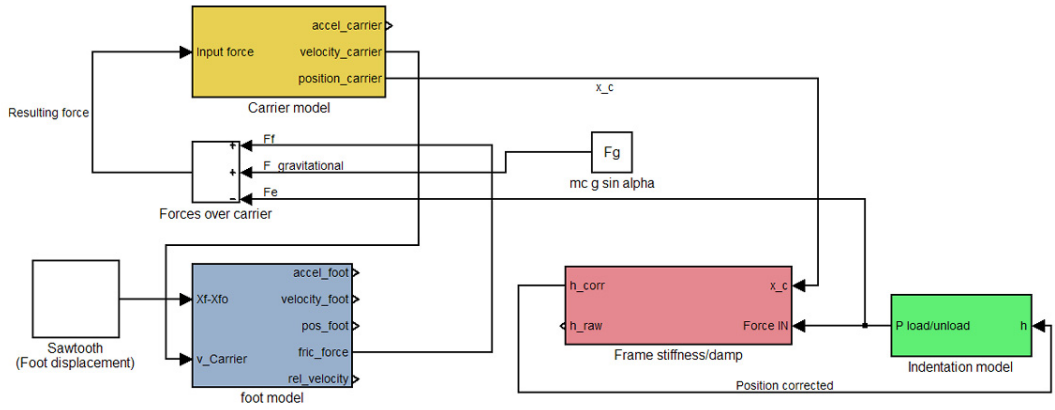

Figure 3.13: Block diagram[23] of an indentation with a tip driven by a stick-slip actuator

The ***Frame stiffness/damp*** block has as an input the (reaction) indention force. This force will deform the frame and the displacement will later on be subtracted from the carrier displacement. The difference is the corrected displacement and that it is the real penetration depth. As this block includes a sample plus a sample holder with a given mass (combined load), the acceleration can be obtained as well as velocity and displacement. The model includes damping that will generate a force that is proportional to the sample velocity. The complete model is useful to analyze the phase between the driving force (indentation) and the system reaction force (mass-spring-damp system), and the influence of secondary vibrations over the tip-sample contact.
Finally the ***Indentation Model*** block uses the corrected indentation depth (***h_corr***) as input for the loading-unloading model selected in paragraph 3.2.2.

3.5.1 Application examples

Figure 3.14 shows a Fused Silica simulated graph (P_sim) compared to a measurement using the SEM indenter (P_meas). The graph is based on h_{raw} (without frame stiffness correction). The indentation model, including frame stiffness, is set to a value that matches the SEM indenter frame stiffness.
Figure 3.15 presents a simulation of Fused Silica 250mN indentation with a Berkovich tip. The corrected and the raw data are shown. Frame stiffness has been set as 1N/µm, which gives a shift of 0.25µm between the raw and the corrected data at maximum load.

The combined model between stick-slip indentation and the Instrument model is used to determine the influence of several factors for example as frame stiffness, damping, and microvibrations or jump-back movement over the tip-sample interaction.
All this information can be used to help the indenter design, to customize the actuators (numbers, total driving force) as well as to have a good idea about how severe the jump-back and the microvibrations over a certain type of sample can be.
Figure 3.16 shows an example of these studies. Only the frame stiffness parameter has been changed (from 1 to 5N/µm) and the tip sample interaction observed.

[23] Some items have been removed to provide a better visualization of the main blocs interaction.

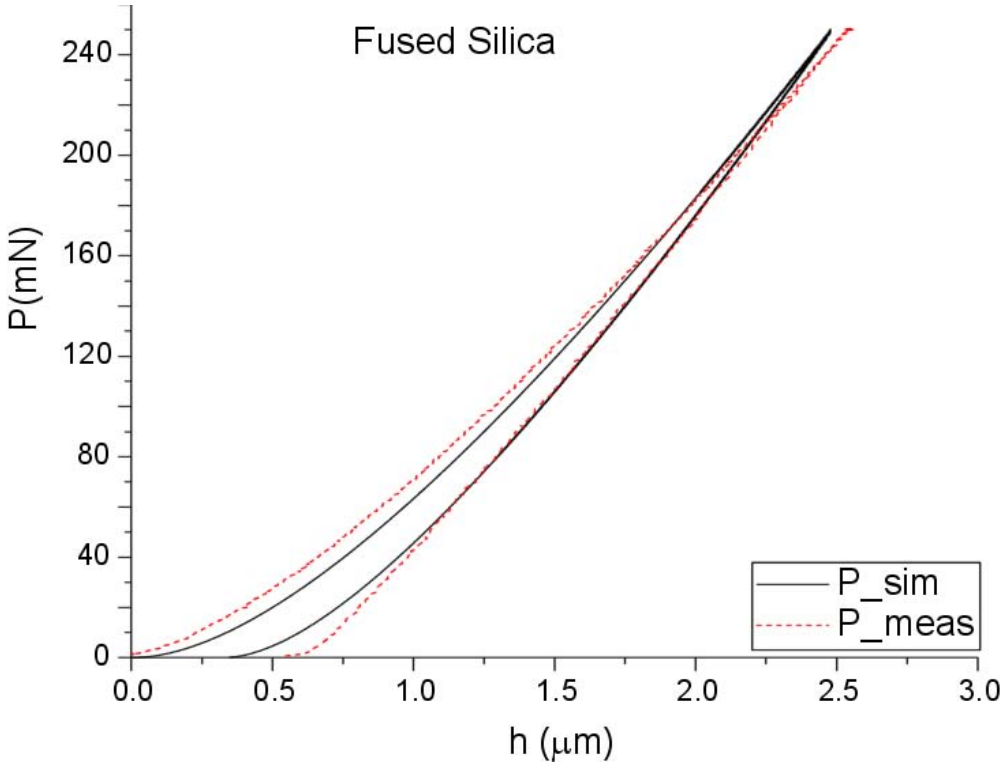

Figure 3.14: Indentation using the SEM indenter (P_meas) compared to the model (P_sim). The calibrated SEM indenter frame stiffness has been input into the model. The graph is based on the raw displacement (no frame stiffness correction),

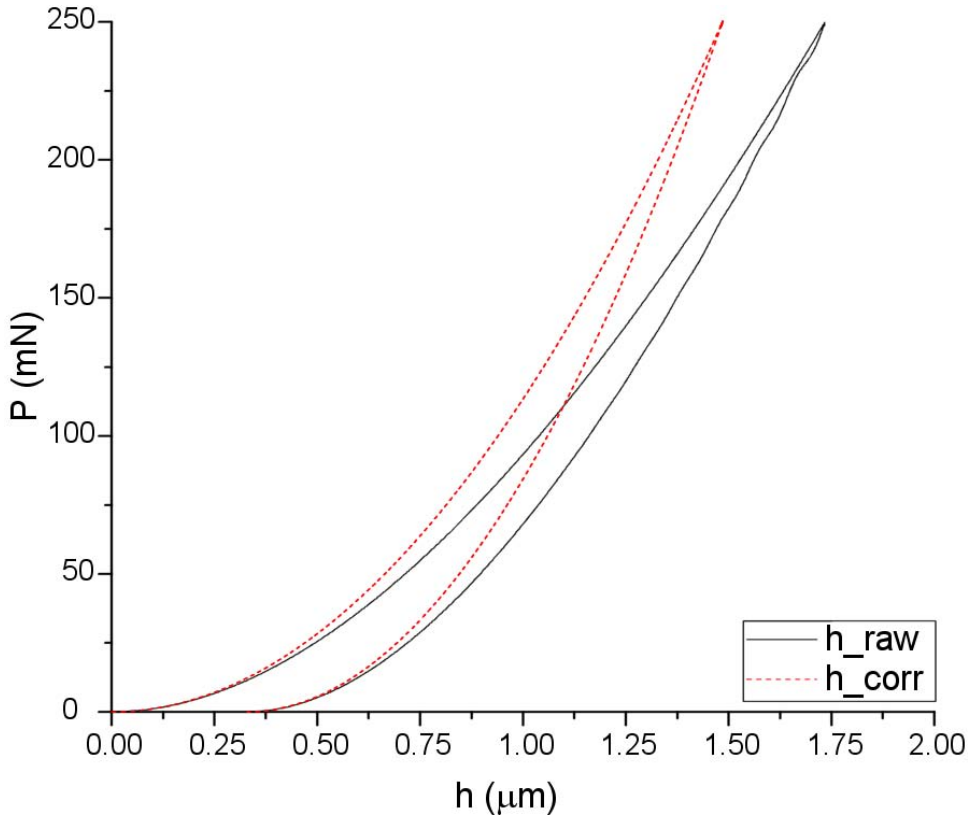

Figure 3.15: Simulation of a Berkovich indentation in Fused Silica. Graph compares the raw (h_raw) data with the corrected one (h_corr). The frame stiffness has been set as 1N/μm with a 15 Ns/m damping. Combined mass is 10g. Natural frequency of the instrument is 1.6kHz

Simulation has shown that increasing the frame stiffness does not have a substantial impact on the jump-back. High frame stiffness has the advantage of fewer steps before reaching the set load, as the frame deforms less. This is observed in Figure 3.16. Unloads have occurred later (more *h* between the next slip phase) with increasing of the frame stiffness.

Low frame stiffness (less than 0.5N/μm) gives simulations with excessive vibration in the system and even instabilities at higher loads (not presented here). The processing time has been highly excessive because of the time spent analyzing the system's behavior after each slip phase (as the software was automatically adapting the simulation to not miss quick events, as the vibrations after each slip). The models still must be tuned with the appropriate damping and simulation parameters.

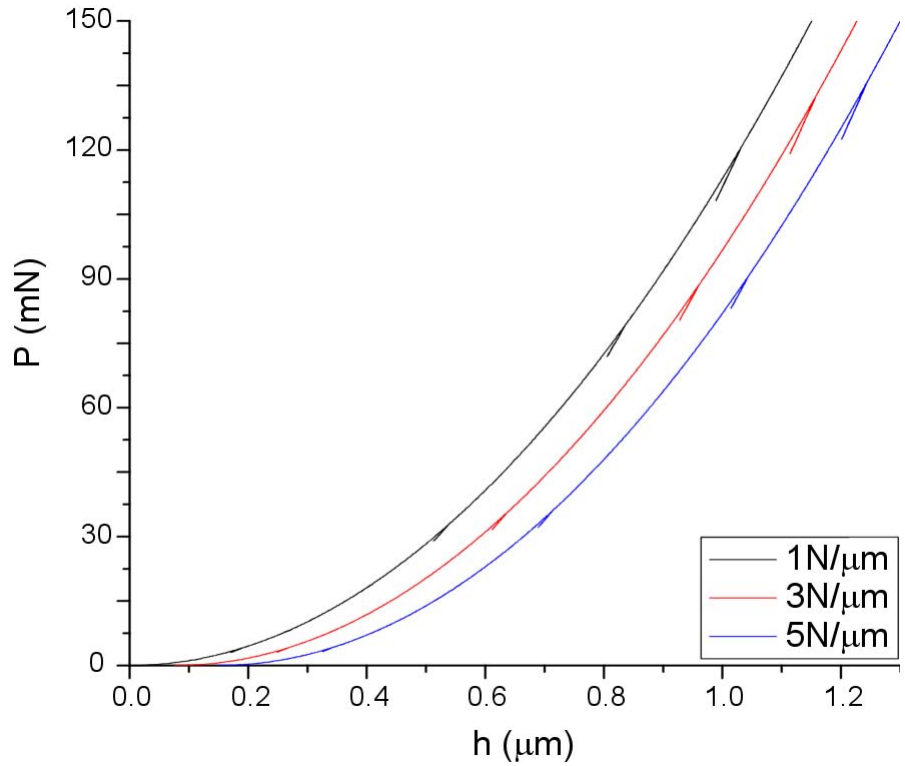

Figure 3.16: Simulation of Berkovich stick-slip indentation in Fused Silica with different frame stiffness. Graphs are based on corrected data and have been shifted in 0.1μm for a better visualization. From left to right: 1, 3 and 5N/μm.

3.6 Conclusions

Indentation models have been implemented in a computational package (Simulink) and compared to graphs obtained during indentation (Fused Silica at 10 and 500mN max load).

The models of Hainsworth with a perfect Berkovich tip for loading and the Field and Swain for unloading have been chosen due to the facility to represent any material. Both models require as input only ***H*** and ***E***. The Hainsworth loading model has a good agreement with the measured curve (as exemplified here with Fused Silica). For stick-slip indentation, the load increases jump-back but the unloading compensates it. For this reason, an accurate representation of unloading is not as essential as for loading. Nevertheless, it is still important to determine the situations where complete unloads happens during the slip phase (tip backward). The Field and Swain method is more conservative, since the forces generated during unloading are smaller. It

represents less jump-back compensation but at the same time it leaves more time for a complete unload.

The instrument frame stiffness has also been presented and integrated into the indentation model. Finally the stick-slip indenter model has been completed, including the model originally presented by Breguet [56].
These models will be used in Chapter 5 in order to study the behavior of jump-back size during stick-slip indentation under different tip driving conditions.

Chapter 4

Stick-slip Actuators for Indentation and Scratching

4.1 Introduction

The goal of Chapter 4 is to study the effect of a stick-slip driven tip on the material during indentation or scratching. The comparison will be made through visual inspection (to verify remarkable differences between driving modes) and an analysis of the corresponding P x h curve.
In order to characterize the differences, three setups have been utilized.

- The first one is the SEM IIT (Instrumented Indentation Test device – Figure 3.8), from now on called SEM indenter. It utilizes a commercial stack piezoelectric actuator for indentation. This method of actuation is here called *continuous mode*.
- In the second setup, the SEM indenter has been programmed to create a periodic jump-back through its piezoactuator. The size of this backlash has been kept constant during the entire indentation time. No jump-back has been imposed during the complete unloading phase (continuous unload). The driving mode in this configuration is called *stick-slip mode with the SEM indenter*.
- Finally, the third setup was a modification of a stick-slip linear actuator built at EPFL [65] (Figure 4.1, Figure 5.1), creating a veritable stick-slip IIT, meaning a variable jump-back size. It is here called *stick-slip Indenter* and the indentation mode is named *stick-slip mode with the Stick-slip indenter*.

The SEM indenter has also been used to realize scratching in both modes (continuous and stick-slip) since it has also a build in piezoactuator to realize scratching in the Y direction (vertical - toward the observer). As the instrument does not have the capability to register neither lateral force nor displacements, only a visual inspection has been realized.

4.2 Partial reloads in indentation

The procedure to unload and reload the material several times before the effective unloading is a usual procedure in the Instrumented Indentation Technique (IIT). It is used to verify the reversibility of the deformation and to assure that the unloading graph being used for mechanical characterization is mostly elastic.
Oliver and Pharr [47] describe a procedure to loading and unloading the specimen three times (up to 10% of P_{max}) before finally obtaining the effective unloading curve. This procedure has been reported in very different type of materials. The unloading curve has not been changed, but its reversibility (overlapping of the unloads) has been

different depending on the materials. Sapphire, Fused Silica and Quartz have had a good reversibility. Aluminum and Tungsten have presented a shift in the maximum displacement after each reload (material creep). The O&P experiment has been made with Berkovich tip and controlled unload/reload (following a given load rate). This makes it not completely similar to unloads found when using stick-slip actuators. However, similar characteristics have been found during stick-slip indentation.

Nevertheless, there are still some concerns about what could be the influence of a stick-slip indentation over a visual inspection (imprint analysis) and over the P x h curve.

A **review of partial unloads effects** in indentation is presented in Annex II and briefly summarized here.

Stick-slip indentation is a series of loading-unloading steps. This means that the average indentation velocity has included the necessary time for the actuator return to the set point after each jump-back. Higher is the jump-back, faster the actuator must move forward to keep the same average velocity.

- **Material Creep**: Material creep depends on the indentation velocity. In stick-slip indentation an oscillatory (yet small) indentation velocity will be present as the tip backlash is compensated by the IIT control system.
- **Constant load/displacement rate**: To keep a constant load (or displacement) rate may be thus a problem and have direct influence over *strain rate sensitive* material and *material hardening*. However, this can be previously evaluated and in mostly cases, the influence may be small (see Annex II for details).
- **Holding period**: It is a typical procedure applied at the maximum load to minimize material creep. A stick-slip actuator can work in *step* and *scanning mode*. Thus, if creep is small, the indenter can hold the load (or displacement) as any indenter device that uses a continuous actuator. However, if the creep is higher than the step size, a step has to be applied, inducing new stress in the material. The holding period may be thus higher than usual.
- **Crack formation**: It is well known that cracks can be formed or propagated during loading or unloading (a more concerning situation for brittle materials). Stick-slip actuators generate a succession of load-unloads. This may have influence in the generation of more or longer cracks, material chip-out and so on. Sharp tips (as Cube Corner) are the preferable ones for in-situ indentation, but they also easier generate cracks. Brittle materials and stick-slip indentation still will need a wider study, yet, as going to be shown in this chapter, no direct influence of the driving mode has neither been observed over the P x h graph nor in the imprints in the test conditions here applied.

4.3 Overview of the instruments and test procedures

4.3.1 The Instruments

4.3.1.1 The SEM indenter

The SEM indenter that has shortly been presented in Chapter 3 (Figure 3.8) is fully detailed in Chapter 5. For the experiments, the important part is the indentation head, containing the piezoactuator and that the tip holder can be programmed to simulate a stick-slip movement. The Y-Stage (PZT) also contains an integrated stack

piezoactuator, which has been used to simulate a stick-slip scratching. However, for scratching, the instrument has neither displacement nor lateral force measurement. Thus, the applied normal load has been the unique parameter that monitored during scratching test.

4.3.1.2 The stick-slip indenter

Figure 4.1 shows the actuator converted into an indenter that uses stick-slip actuators during indentation.
As the setup is assembled outside the SEM, there is no need for a SEM compatible design. The test device shares the same load cell and the tip holder of the SEM indenter. The displacement system is a laser interferometer from SIOS GmbH [66], targeting the carrier directly where the tip holder is fixed. The carrier, a shaft with 10mm in diameter and 60mm in length, is made of hardened steel. Four legs (shear piezos and 3mm diameter half spheres in Sapphire) are placed in a V shape, holding the carrier kinematically through four contact points. More details about the instrument are provided in Chapter 5.

For indentation, the depth penetration (***h***) is obtained measuring the displacement of the carrier through the interferometer. A turning stage has been added between the sample and the load cell to facilitate the sample displacement for new test. The sample is rotated and not translated.
The load and the displacement acquisition are not perfectly synchronized, which could result in a small delay (few msec) between the reading of the load and the displacement. Due to the small indentation velocity and the acquisition rate (5Hz), this is not a concern[24].

The device has provided a good contribution to better visualize real indentation in stick-slip mode and as a tool to characterize stick-slips in different conditions.

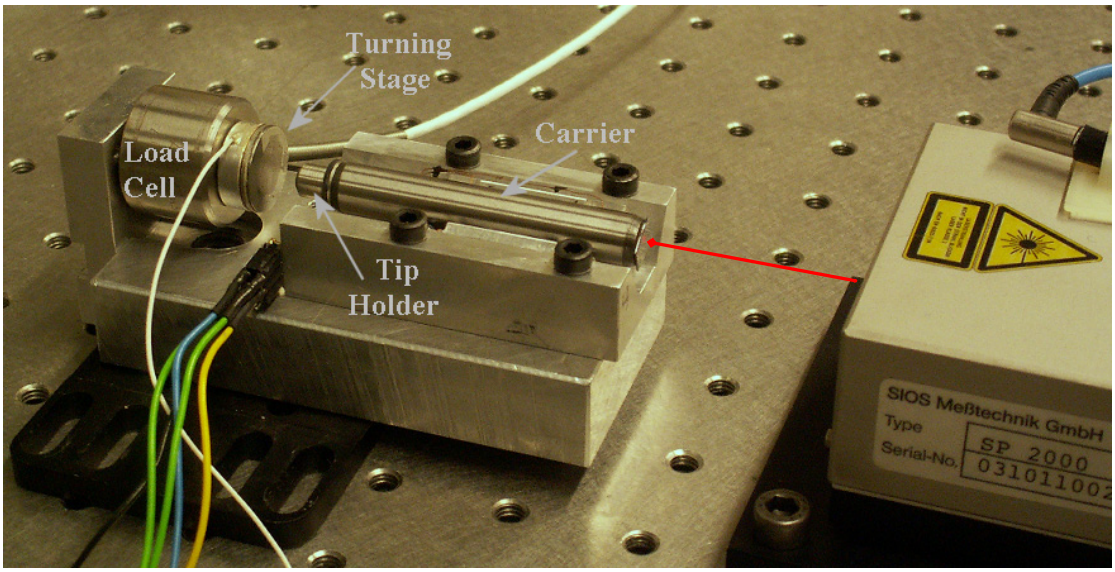

Figure 4.1: Picture of the stick-slip indenter and its main components

[24] This could be nevertheless the case, if the objective is to analyze the sample/tip micro vibrations after each slip phase. In this case a measurement must thus be realized at high measurement sample rate (over 5kHz).

4.3.1.3 The measurement system

The 150g range load cell, from Sensotec [67] (model 31) has been calibrated using standard dead weights. The same load cell has been used in both setups. Nevertheless, SEM indenter and the Stick-slip indenter do not share the same acquisition system (bridge feed voltage, amplifier gain, AD converter). Thus, a calibration procedure had to be executed separately for each instrument. The built-in displacement sensor (a strain gauge) at the piezoactuator indentation head has been calibrated with a laser interferometer. The stack piezoactuator is exclusive of the SEM indenter instrument. The stick-slip indenter had an external laser interferometer to register the carrier displacement (Figure 4.1) and consequently the penetration depth.

Two different programs for instrument control have been made using LabView, because the tip driving signals are different (a ramp for stack piezoactuators and a sawtooth for the stick-slip actuator). In the case of stick-slip simulation with the SEM indenter, the utilized program has been the same for the *continuous* and the *stick-slip* mode, as the amount of jump-back is the only variable parameter analyzed. Therefore, the setup conditions are identical.

4.3.2 Description of the jump-back generation (piezoactuator setup)

The jump-back size is arbitrarily defined in terms of a given step size (Figure 4.2). If a step of 400nm is chosen as the step size, each time that an increment equivalent of a step is reached, a certain percentage of the step is removed, creating thus a fast backward movement (jump-back, backlash). The jump must be as quick as possible to reproduce the real situation found in stick-slip devices. Thus, the system has been operated in open loop, avoiding unexpected interferences over the driving signal.
Consequently, the driving mode is directly through the voltage. For that reason, the equivalent step size and jump-back have been converted in Volts[25] (Figure 4.2c).

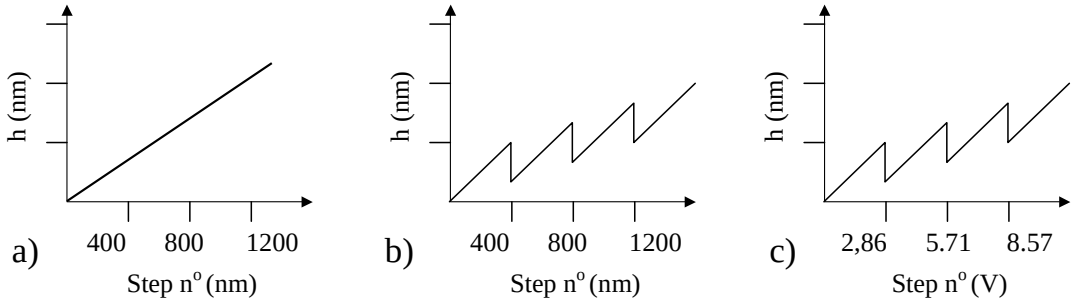

Figure 4.2: Jump-back definition. a) 0% jump-back at each 400nm step, b) 50% jump-back at each 400nm step, c) 50% jump-back having Voltage as input (equivalent to a 400nm step).

Having the piezoactuators a high driving and blocking force, the influence of the indentation reaction forces is unlikely to change the programmed step size. On the other hand, hysteresis and creep have much more influence on the step behavior.
In any case, the average size of each backlash should be very similar during the entire indentation and this can actually be observed. The real step size, as well as the backlash size has been determined using the data files. The effective step and jump-back size have been at the end 30 to 40% smaller than planned (400nm), but it remains very similar during the entire test.

[25] The conversion has been made simply dividing the maximum piezo displacement (21μm) by the maximum applied voltage (150V).

The main reason for this difference has firstly been due to the piezo hysteresis. Secondly, measuring the displacement through the data file also implies to analyze filtered signals (by averaging). The acquisition rate has also been set to low rate (5-10Hz). This is low to visualize quick changes but enough to observe a global change in the graph shape rather than to characterize the step size.
One advantage of having a constant backlash size is that it can provide a periodic signal with the same amplitude, creating thus a pattern that is easier to identify.

One should note that, in a real situation, the size of the backlash increases as the stick-slip actuator faces more reaction forces arising from indentation. If a periodic pattern is left in the imprint, the difference between one step and another will become smaller, until a complete overlapping (no more displacement, saturation is reached)[26].
As the jump-back increases, more steps are needed to drive the tip to a same set load. The setup has no speed compensation. Thus, the higher is jump-back; the lower is the average indentation velocity.
In experiments that have used the SEM indenter to simulate stick-slip, a holding period has been introduced at maximum load. Because of the piezo creep, the final load values are not identical but matches within a range of 5%.

4.3.3 Description of the test procedure

The maximum normal load (for the SEM and the Stick-slip indenter) has been chosen such that several steps during indentation could be observed. The load applied over each material is presented in paragraph 4.3.6.
Low normal loads have not been chosen for this analysis, as they make the experiments unnecessarily difficult for the following reasons:

- The maximum load can already be reached before the first step[27]. In this case, the indentation is simply realized in a continuous way, as through a standard piezoactuator.
- The fact that are only a few steps makes it difficult to visualize or identify a pattern in the image, or to observe a modification in the P x h graph.
- Very low loads might produce shallow imprints of difficult visualization, and a very high magnification will be necessary to search for differences.

The drawback is that for some combinations of tip geometry and sample, higher loads increase the damages around and inside the imprints. This makes a clear visualization inside and around the indentation difficult and adds new events to the P x h graph (as pop-ins) that could be related or not with the chosen driving mode (continuous or stick-slip).

The indentation has been made in open-loop and applying a same stick-slip driving frequency (steps per second). This implies in a nearly constant indentation velocity, but slightly different maximum loads (< 5% of the maximum load). However, no procedure has been adopted to compensate the displacement lost during each jump-back. As the jump-back increases, more time and steps are necessary to reach the set maximum load. For example, a test with 50% jump-back size takes 50% more time to reach the set load than a test with 0% jump-back. This relation is better observed on the inset graphs presented in each picture of paragraph 4.4.

[26] Figure 5.4 in Chapter 5 exemplify this behavior.
[27] Usually from 300-500nm, depending on the piezomaterial.

The complete unloading rate has been kept the same for all cases, as no jump-back has been introduced in this phase. In the SEM indenter, a small holding load time (usually less than 10s) has been applied at the maximum set load.

Finally, the same indentation tip and the same sample have been used in both instruments (SEM indenter and Stick-slip indenter).

For scratching, a similar procedure has been adopted. The input has also been given in voltage, sharing the same characteristics as previously described for indentation. The particularity is that in this case, the number of steps has been kept constant. The unique parameter being controlled has been the applied normal force. Thus, for a zero jump-back, the scratch length has the same maximum displacement length available on the Y-axis piezoactuator (21μm). As the jump-back percentage increases, the maximal indentation length decreases nearly[28] at the same proportion. The procedure utilized has been first to apply the normal set load and then to start the scratching.

4.3.4 Description of stick-slip scratching test

The stack piezoactuator is mounted behind the vertical Y-axis. Thus, the scratching direction is toward the observer viewpoint (coincident with the SEM column). First, the tip has been driven up a determined set load and only after the scratching has started. The normal load control has not been used. The set normal load has been kept by manual intervention acting directly over the piezoactuator voltage input through a precision potentiometer. Because of the sample slope and the piezo creep, the normal load has reached a value of 20-30% higher than the set load. However, it has not been necessary to make more than few interventions during the test (20μm range scratch)

During the in-situ scratching, only the features in front of the tip edge could be observed, as the direction of the scratching has been toward the observer viewpoint. The tip obstructs the scratched surface until a complete tip withdrawal. Since the objective of the test has been a comparison between different amounts of backlash, only the Y stack piezoactuator has been utilized. The main visual analysis has been performed observing regions inside and around the scratch using a High Resolution SEM.

The amount of jump-back has been set of a percentage (0%, 20% and 40%) of an arbitrary step size. It has thus been kept the same in all the tests. A maximum number of steps have been programmed for each case. Because of the amount of displacement lost in each slip phase, the final scratch size has been reduced approximately proportional. For example, a 0% of jump-back and fifty steps produce the longest scratch while 40% jump-back and the same fifty steps produce a smaller scratch (see Figure 4.24).

4.3.5 Description of the test analyses

The analysis of the jump-back size over the sample has been made through the Load – Displacement curves (the P x h graph) and through visual inspections.
Residual imprint analysis have been made using of a high Resolution Cold Field emission SEM. High magnification pictures have been made showing details inside

[28] Hysteresis is always present during the forward-backward displacement.

and around the imprint. The goal has been to detect events that could be related to the tip being driven in different modes (stick-slip or continuous).

4.3.6 Description of the utilized materials and experimental parameters

For indentation, two different tip geometries (Cube Corner and Berkovich) and three different materials have been used: Fused Silica, Bulk Metallic Glass, and Gallium Arsenide.
In scratching, only Cube Corner tip has been used. The tested materials have been AlCu alloy, Zr-BMG and GaAs.

The choice of the materials (except for Fused Silica) is related to their distinct mechanical properties, availability and knowledge support[29]. External knowledge is important to help to identify unusual features in the Load x Displacement graph or through visual inspection.

Table 4-1 summarizes the main experiment parameters when testing a material with the SEM indenter in stick-slip mode or with the Stick-slip indenter. Details about the experiment parameters are presented after the table.

Table 4-1: Summary of the experiment parameters using stick-slip indentation.

Instrument	Material	Max Load (mN)	Jump-back size (%)	Runs	Analysis Berko. tip	Analysis CC tip	Remarks
SEM-Indenter	FS	250, 500 (Berks.) 250 (CC)	0, 20, 50	3	P x h graph SEM image	P x h graph SEM image In-situ indentation	a
	Zr-BMG	200, 500 (CC)	0, 20, 40	3	-	P x h graph SEM image In-situ indentation	
	GaAs	200, 500 (CC)	0, 20, 40	3	-	P x h graph SEM image In-situ indentation	b
Stick-slip Indenter	FS	100, 150, 200, 250, 500 (Berk0)	Variable	3	P x h graph	-	c
a), c) – A graph comparing both instruments is also presented b) – A measurement involving a maximum load of 600mN with 60% jump-back is also presented							

Fused Silica (FS) – H=9GPa, E=72GPa, ν=0.17 – is commonly used as a reference material in instrumented indentation testing and the main material utilized for charactering the stick-slip mode with the SEM indenter and with the stick-slip indenter.

Zr-BMG – Vitreloy-105 – H=6.3GPa, E=107GPa (details about the material can be found in [17]) shows a very specific type of plastic deformation, characterized by shear bands around the imprint. It has low plastic recovery, making it interesting to analyze the effect of different tip driving modes.

[29] From researches at EMPA-Thun

GaAs is an important semiconductor for optical end electronic devices and its mechanical properties depend strongly on its crystallographic orientation[30]. For the experiments, an arbitrary position has been chosen and has been kept the same for each replication (run). GaAs is a brittle material and cracks and chips-outs are easily produced during indentation.

Indentations using Zr-BMG and GaAs have been realized only with the SEM indenter and using a Cube Corner tip.

SEM stick-slip indentation in Fused Silica has been realized with Berkovich and Cube Corner tip. For Berkovich, two maximum loads[31] have been used – 250mN and 500mN. For Cube Corner, only 250mN has been applied. Each set of jump-back size (0, 20 and 50%) had three runs (replications) for each of the set loads. In-situ indentation (with video) has only been performed with Cube Corner indentation.

SEM stick-slip indentations in GaAs and Zr-BMG: Maximum loads have been set to 200 and 500mN. The test has consisted of three jump-back sizes (0, 20 and 40%), having three replications (runs) for each jump-back size.
Only a Cube Corner tip has been used with these materials.

With the ***Stick-slip indenter***, only ***Fused Silica and a Berkovich tip*** have been used in this test. Five maximum loads have been set: 100, 150, 200, 250 and 500mN (based on a 100g – 1N conversion).
The measured actuator step size (max amplitude) has been 550nm for an input of – 200V to + 200V in the stick-slip actuator.
No control system has been used to create a constant load or displacement rate during the test. In the moment that the setup reaches the set load, the actuator legs changes direction. Because the stick phase behaves as a continuous movement, it is possible to change direction in a smooth way (what is called scanning mode in stick-slip actuators). No holding time at maximum load has been applied for tests done with the Stick-slip Indenter.

The scratching test has been made in AlCu alloy, Zr-BMG and GaAs. As the SEM indenter does not have the capability to measure neither lateral force nor lateral displacement during scratching, only the normal load could be set. The procedure and utilized programs have been the same described when simulation stick-slip movement with the indentation head. The stack piezoactuor using in scratching has a maximum range of 21μm.
The choice of the materials has been the same as described for indentation. AlCu alloy have been chosen to represent a very ductile material.

[30] Available values (obtained at EMPA-Thun) for the tested sample are H=8 GPa and E=111 GPa for the <110> direction. Sample is a Si doped GaAs Wafer.
[31] 1N is equivalent to 100 grams, as *g* has been rounded to 10m/s^2 (measured values have been acquired in grams and after converted in Newtons).

4.4 Indentations analysis (results)

If a difference in the indentation caused by the stick-slip driving mode exists, then it should be possible to detect it in the Load – Displacement curve analyzes (P x h) or in the SEM images and pictures.
For all experiments, the P x h overlapping among runs has nearly been perfect, showing a very low data dispersion (using Berkovich or Cube Corner tip).
Each run had the same graph envelope, but the curves did not have each of them the slip phase exactly at the same ***h*** (indentation depth).
For this reason, instead of making an average of the three replications, it has been opted to choose one of the runs to be represented (thus, it is represented as raw data).

4.4.1 Fused Silica (FS) indentation

4.4.1.1 Berkovich indentation in FS using the SEM indenter

The graphs in Figure 4.3 and Figure 4.4 are measurements with different jump-back sizes for two maximum loads 250 and 500mN, using Berkovich tip.

All graphs show a good agreement for these high loads. No difference between stick-slip and continuous indentation has been found.
The inset graph shows the intensity of dropping in load as well as the number of unloads in each case. The latter increases as the amount of jump-back increases.

SEM images of the Figure 4.3 and Figure 4.4 experiments are shown in Figure 4.5 and Figure 4.6. To avoid charging effect, the sample has been coated with a thin layer (few nanometers) of Gold-Palladium before the test inside the SEM. Part of the layer has been removed during the indentation (probably stuck in the tip), creating the dark-light difference at the bottom of the imprint, as well as highlighting the cracks.

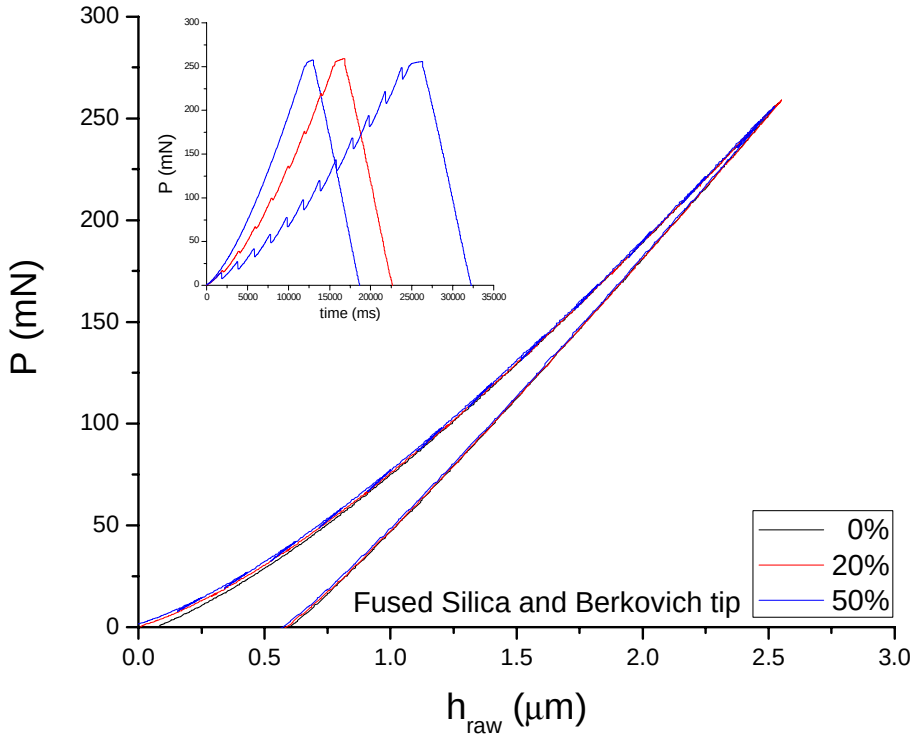

Figure 4.3: Influence of the jump-back size over a 250mN Berkovich indentation in Fused Silica (raw data). Inset graph shows the drop in load and number of unloads in function of percentage of jump-back.

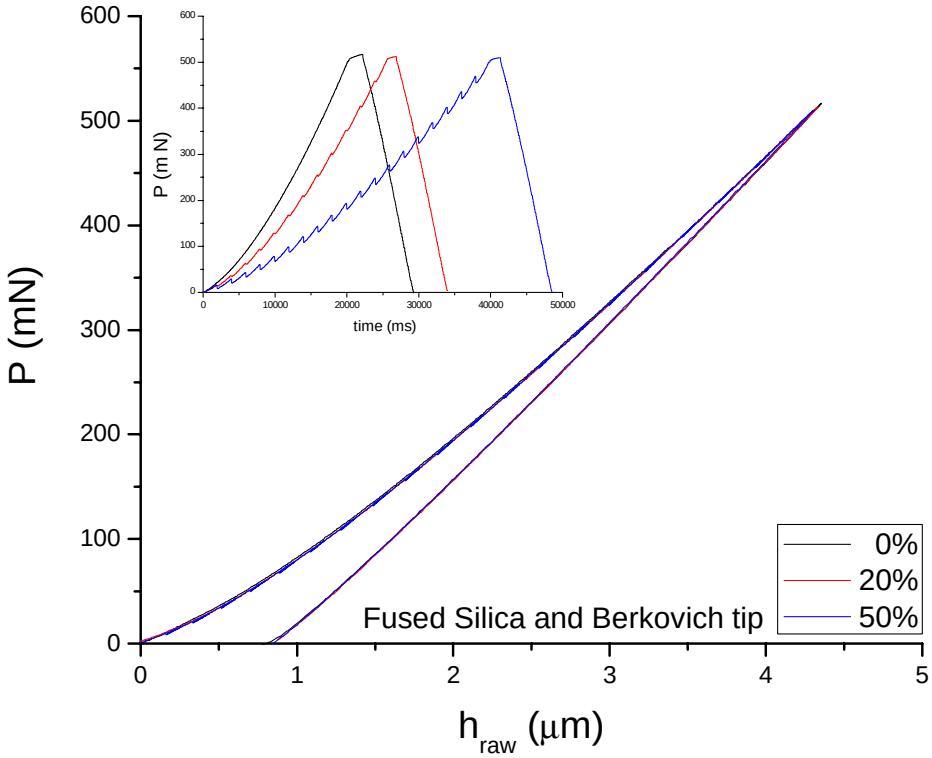

Figure 4.4: Influence of the jump-back size over a 500mN Berkovich indentation in Fused Silica (raw data). Inset graph shows the drop in load and number of unloads in function of percentage of jump-back.

4.4.1.2 Berkovich imprints SEM observation in FS - around the imprints

Providing a better visualization, Figure 4.5c shows an imprint at 50% unload. Even the experiments with the highest amount of jump-back have not shown any particular features inside or around the imprint. All the nine imprints (three for each percentage of jump-back) have presented common features. Cracks arising and connecting each imprint are not originated from the driving mode, but due to the fact that the indentations have been placed close to each other.

The imprints from Figure 4.4 (500mN normal load) are shown in Figure 4.6. One radial crack (Figure 4.6a) has been the unique particularity found on the nine observed imprints and it has happened with 0% unloading. As for the 250mN normal load, no particular features have been found as belonging of a specific set of jump-back size.

4.4.1.3 Berkovich imprints SEM observations in FS - inside the imprints

In the case of an in-situ visualization using the SEM, the visible points are only those around the indentation tip. To complement the visual inspection in the vicinities of the imprint, the same types of observations have been carried out inside the imprint. This post imprint analysis has been used to verify any visual pattern that could be related to the type of stick-slip movement.

For the combination of Fused Silica and a Berkovich tip no pattern have been found, at least up to a magnification of 130.000 times (in this case, visualizing the region that had the gold-palladium coating removed). Figure 4.7 shows the region inside the imprint in more details (20.000 times magnification). The imprints are the same as the ones presented in Figure 4.6*a* and *c*.
None of the imprints analyzed (three for each jump-back size) have shown anything atypical or that could be correlated to the amount of jump-back applied.

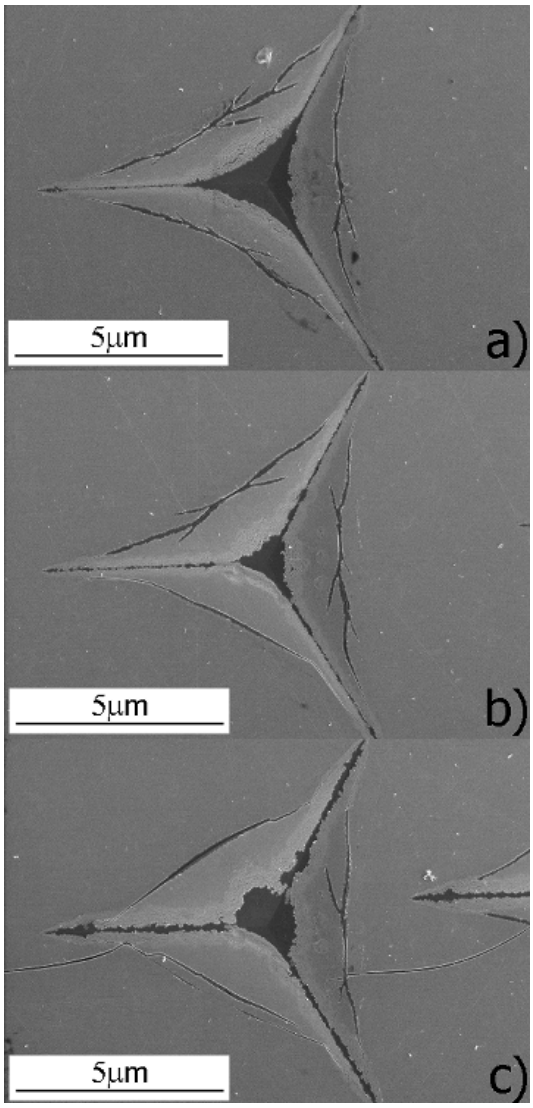

Figure 4.5: SEM pictures of the 25omN Berkovich imprints in Fused Silica at 0% (a), 20% (b) and 50% (c) unload

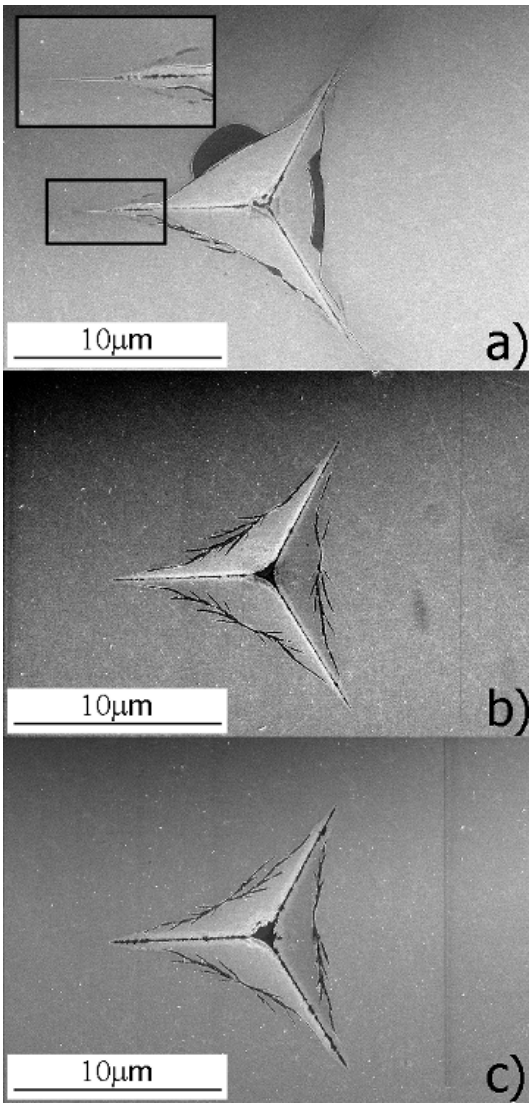

Figure 4.6: SEM pictures of the 500mN Berkovich imprints in Fused Silica at 0% (a), 20% (b) and 50% (c) unload

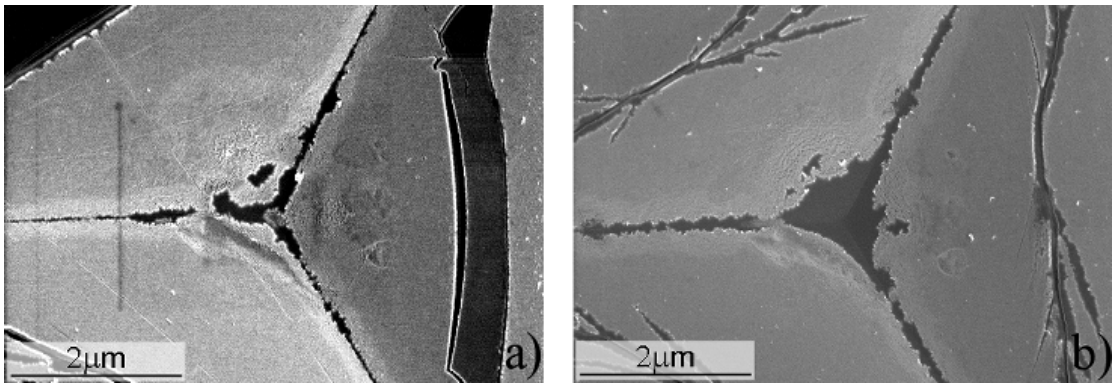

Figure 4.7: Detail of two Berkovich 500mN imprints in Fused Silica. a) with 0%, b) with 50% unload. The dark region inside the imprint is the Au-Pd coat removed during indentation. The sample has been previously coated to improve the SEM visualization during in-situ indentation.

4.4.1.4 Berkovich indentation in FS using the stick-slip indenter

Figure 4.8 provides an overview of the measurements. Now, each jump-back has a different size. The inset graph gives a better visualization of the drop in load, as the indentation load increases. When the reaction forces over the actuator are getting higher, the size of the jump-back movement becomes higher.

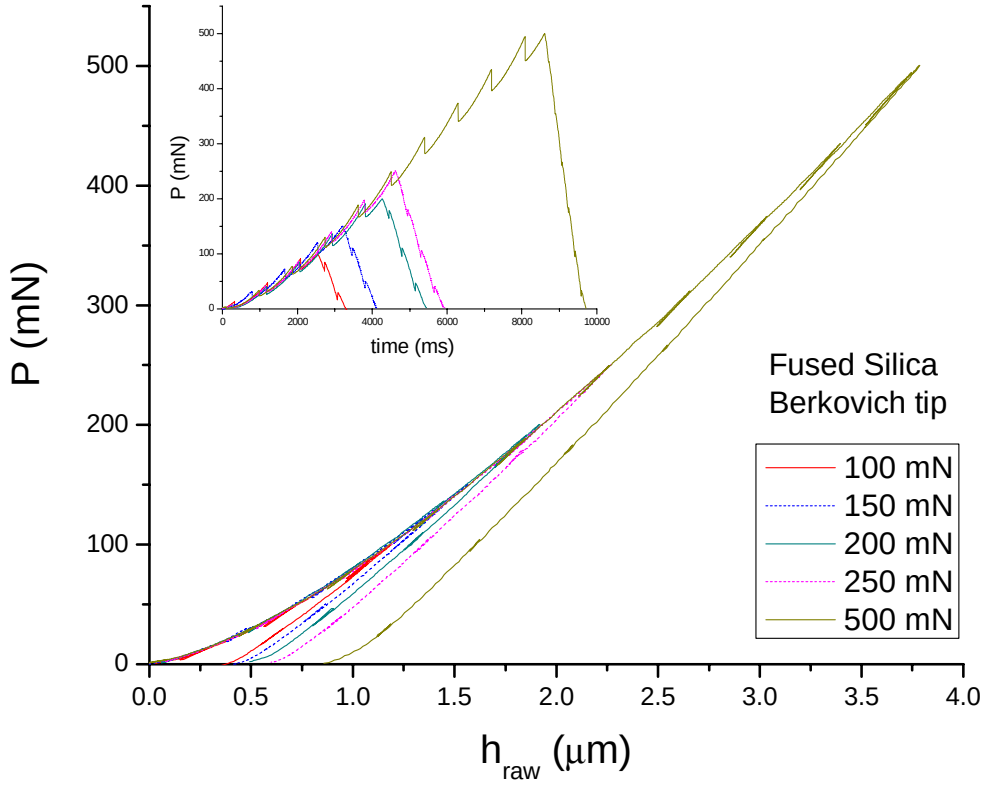

Figure 4.8: Stick-slip indentation experiments performed at different maximum loads (raw data). Inset graph shows the drop in load and how the jump-back size increase with the rising of the normal load.

The unloading phase helps the tip movement, as it almost compensates the forces generated by the leg during the slip. This is more evident in the 500mN maximum load graph. The firsts two unloading steps have been almost fully compensated (giving a max of 30nm backlash size instead of the 230nm measured at 490mN in Figure 4.8).
Tests made at different maximum loads show a good overlapping loading graph.
The increasing size and number of jump-back has not influenced the P x h curve, confirming what has already been observed with the SEM indenter (Figure 4.3 and Figure 4.4).

4.4.1.5 Comparing Berkovich continuous and stick-slip indentation in FS – a two instrument output analysis

For a more precise comparison between the two driving modes, measurements coming from the SEM indenter (continuous mode) have been compared to the Stick-slip indenter (stick-slip mode). As it has been described in paragraph 4.3.1.3, both instruments use the same load cell, indentation tip and sample, but each one has its own frame compliance. Figure 4.9 shows the P x h graph of both instruments.

The observed shift is related to the different frame stiffness of each instrument. This is clear, as for both instruments; the depths where the tip completely unloads the sample (at P = 0N) are coincident in all the three cases (100, 250 and 500mN).
To facilitate a comparison of both graphs (overlapping), one of the frame compliances (C_f) has been compensated in order to match the other instrument[32]. It has been chosen to change the more compliant frame. Thus, the SEM indenter measurements have been compensated to match the Stick-slip indenter at 500mN maximum normal load. The same value has thus been used for the 100 and 250mN data. The value of C_f is obtained using the value of $h_{stick\text{-}slip}$ and h_{SEM} at the same 500mN and Eq. 4.1.

$$h_{stick-slip} = h_{SEM} - C_f \cdot P \qquad \textbf{Eq. 4.1}$$

With the same C_f, all h_{raw} from the SEM indenter have been translated (Eq. 4.2) for a same frame stiffness of the Stick-slip indenter. The result is shown in Figure 4.10.

$$h_{corr} = h_{raw} - C_f \cdot P \qquad \textbf{Eq. 4.2}$$

The raw data obtained from both instruments shows a good P x h overlapping in the tested maximum loads in both driving mode.

The raw data can also provide information about the curve's similarities. Thus, a fitting curve function has been utilized to compare the unloading curves.
A power-law fitting curve has been proposed by Oliver and Pharr as the best function to describe the unloading curve. The function described in paragraph 2.5.3, is presented again.

$$P_u = B(h_u - h_r)^m \qquad \textbf{Eq. 4.3}$$

For better visualization, the data from Figure 4.10 has been plotted showing only the unloading part. The power-law fitting parameter ***m*** has thus been used[33] to verify possible differences among the same set load in continuous (Con) or stick-slip (S-S). The resulting graph is shown in Figure 4.11. Confirming the first impression, there are no evident differences between the driven modes. This can be verified by the *m* value, summarized in Table 4-2.

Table 4-2: Fitting unloading parameter *m* for both driving modes.

Load (N)	*m* value continuous	*m* value stick-slip
0.10	1.151	1.140
0.25	1.103	1.105
0.50	1.086	1.094

[32] Overlapping graphs can provide a quick and direct visualization of any differences from each curve.
[33] Calculated from the first 90% of the unloading curve. Calculation has been made using the software Origin v.7.5 and the *power* fitting function *Belehradek*.

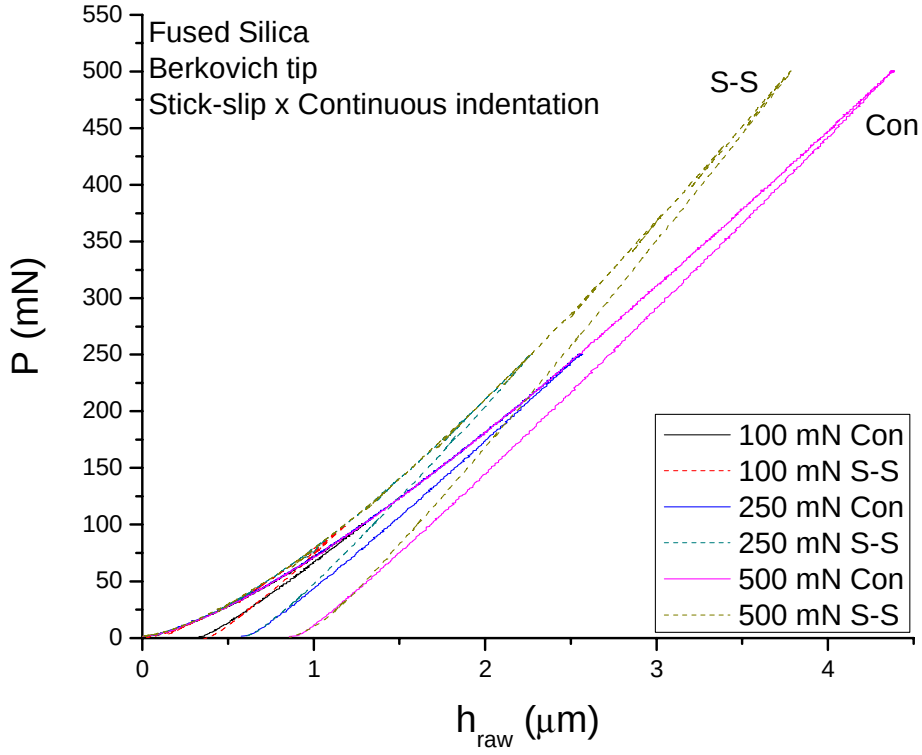

Figure 4.9: Comparison of Berkovich indentation in Fused Silica using stick-slip (S-S) and continuous indentation (Con) at three normal loads. Graphs present original (raw) data. The difference between both tip driving modes graphs is due to the frame stiffness of each instrument; the SEM indenter and the Stick-slip indenter.

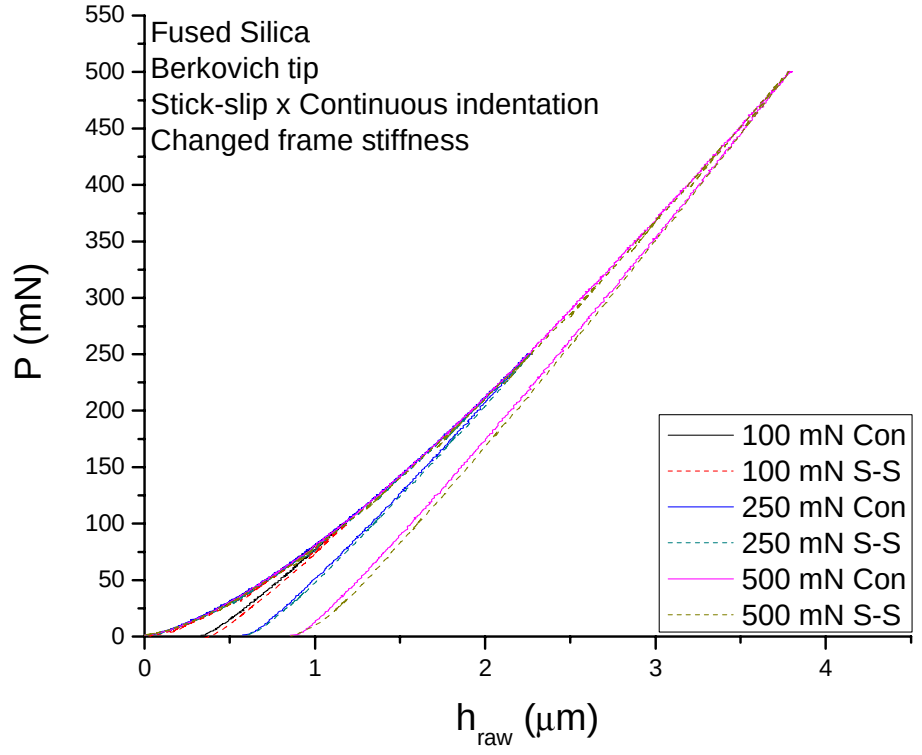

Figure 4.10: Results with same frame stiffness in both instruments. The graph is the same presented in Figure 4.9. Using frame stiffness correction, the data from the SEM indenter (Con) has been translated to mach the Stick-slip indenter (S-S). See text for details.

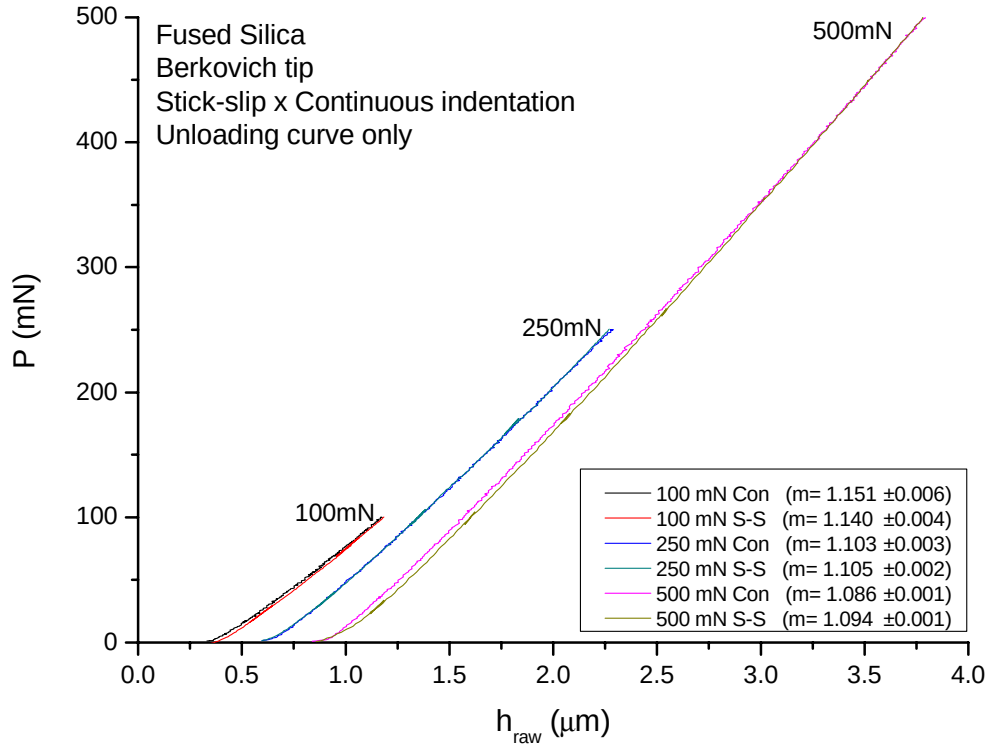

Figure 4.11: Unloading curve in continuous mode (Con) and stick-slip (S-S) for Fused Silica. The power-law fitting parameter *m* shows that the unloading curves are basically the same independently of the tip driving mode utilized.

4.4.1.6 Cube Corner indentation in FS using the SEM indenter

The test with CC has additional contributions in in-situ indentation. It is easier to observe the indentation, cracks are easier generated and visualized as it displaces more volume than the Berkovich under similar loads (creating thus higher stress around the imprint) and there is more pile-up formation (good opportunity for those interested in tip calibration).

Figure 4.12 shows the P x h graphs for a 250mN Cube Corner indentation in Fused Silica. All graphs (using raw data) have a good overlapping during loading and unload.
The unique remarkable difference has been the drop in load (pop-in) at the end part of measurement. This may be related to a material break located behind the Cube Corner tip (a video taken during the test has not shown any irregularities during those tests). A small chip out can be seen in Figure 4.13, on the imprint under the tip (related with 50% backlash size). As a first glance, the material break seems to occur earlier when the jump-back size is increased (and consequently the number of total load-unloads).

However, a new experiment (Figure 4.14) has shown that any correlation is not so obvious. A graph showing the location of each pop-in in function of the amount of jump-back is shown in Figure 4.14. For 0% jump-back, five tests have been realized and all of them have shown a distributed drop in load (pop-in).
For 20% jump-back, seven tests have been made and only one did not present a pop-in. The events are also distributed.

Finally, for 50% jump-back, five experiments have been realized, with one occurrence without pop-in. All events have been detected at loads very close to each other and in general just after a jump-back.

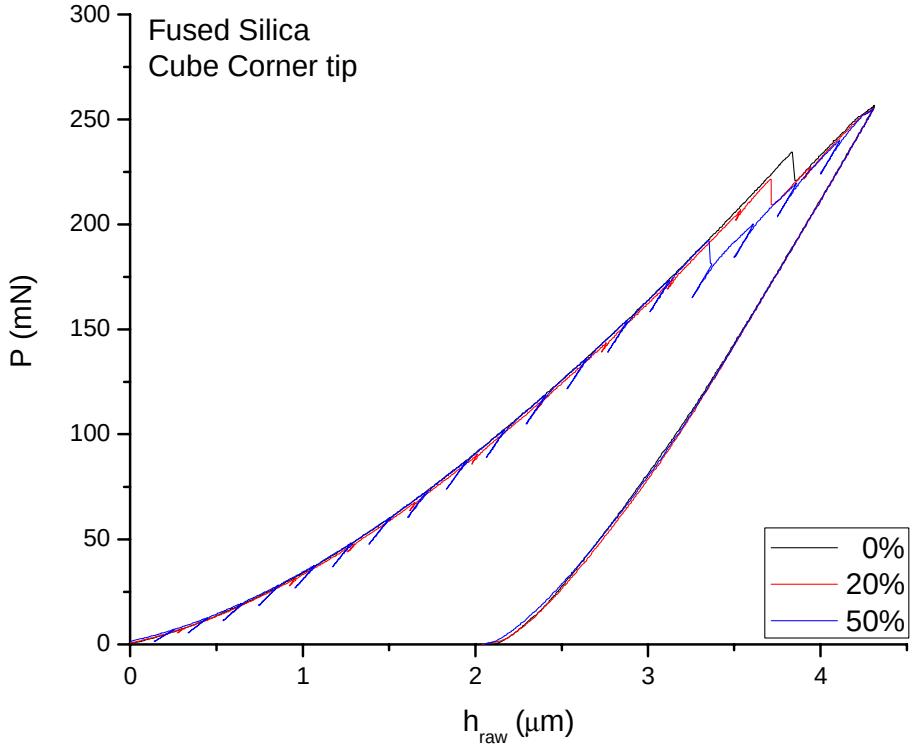

Figure 4.12: 250mN Cube Corner indentation in Fused Silica with 0, 20 and 50% jump-back size.

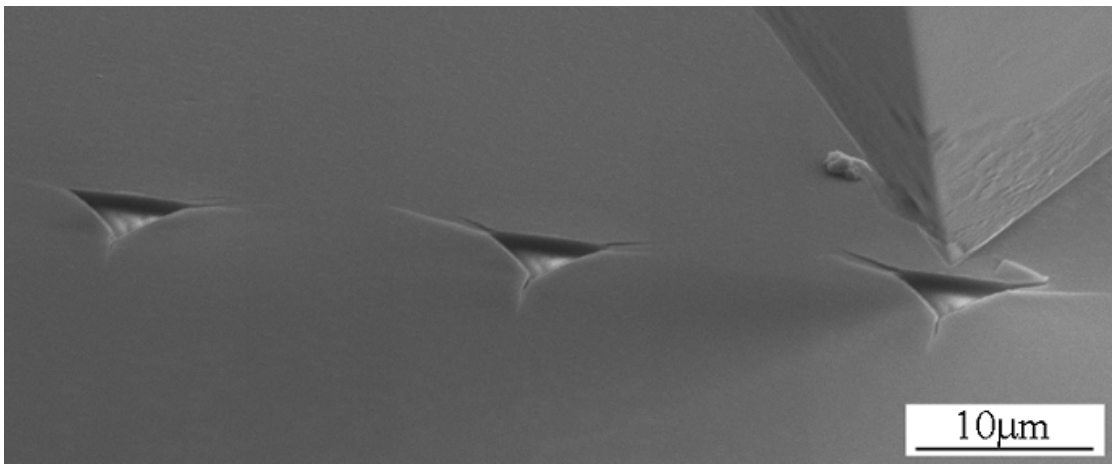

Figure 4.13: SEM indentation pictures based on Figure 4.12 test. From left to right: 0, 20 and 50% jump-back size

In the end, the experiment has raised more (good) questions than it has given answers to the original question – Can the jump-back anticipate the event of a pop-in? The pop-ins at 0% have been well distributed. Nevertheless, they have mostly appeared at middle – high loads. Generally speaking, the 20% jump-back has not shown many differences from 0%. The 50% jump-back has had a good reproducibility, with pop-ins around 130mN. The fact that each drop has been detected very near a backlash can be related to the fact that at 50% jump-back, the steps are closer to each other.

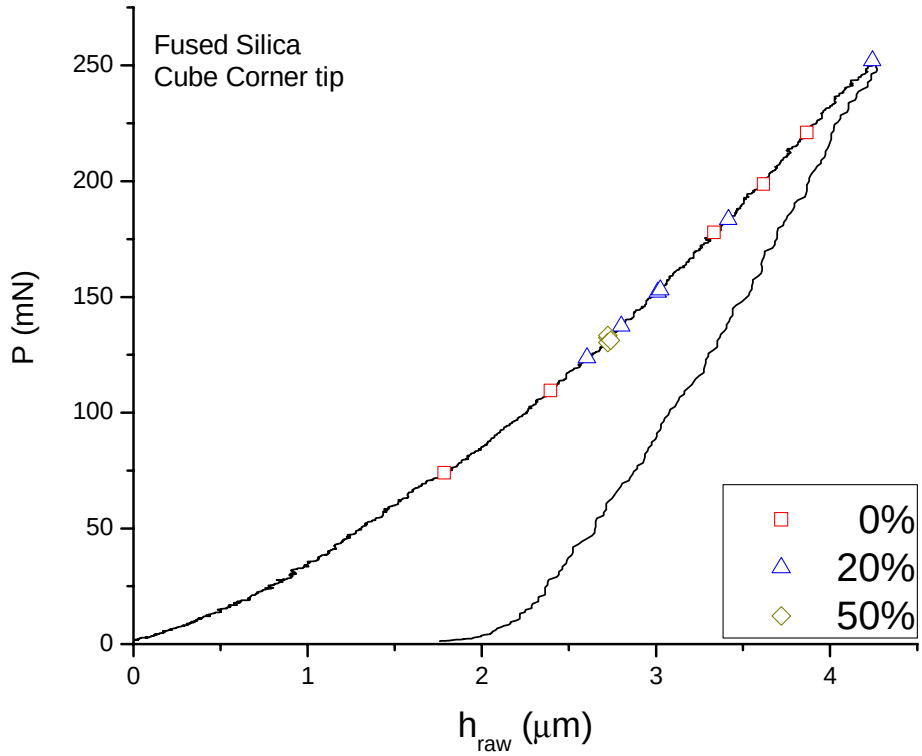

Figure 4.14: Pop-ins detection during CC indentation in Fused Silica with different amounts of jump-back. The indention rate (step/s) has been left the same for each test. Due to the amount of jump-back, the effective penetration rate is different for each experiment. Base indentation velocity (at 0%), 0.1µm/s

4.4.2 Bulk metallic glasses (BMG) and Gallium Arsenide (GaAs) indentation

4.4.2.1 Cube Corner indentation in Zr-BMG

For the experiment shown in Figure 4.15, the continuous indentation mode took around 9 seconds to reach the maximum load of 200mN (penetration velocity equivalent of 0.4µm/s). The drop in load, obtained directly from the P x h curve, has an average of 8mN for a 40% unload. Note that the acquired signal has been previously filtered and averaged and that the acquisition rate is low (5Hz) to characterize high-speed changes, as is the slip phase.
The agreement between the curves at different jump-back sizes is good, showing that the applied reloads have not modified the curve envelop.

The same good agreement can be observed in the case of 500mN normal load in Figure 4.16. Note that, as the sizes of the jump-back have been left the same, the ratio loading-unloading reduces, while the load is increasing (up to 500mN). Thus, the worst situation is at small normal loads, when almost a complete unloading exists.

The graph presented in Figure 4.17 shows different combinations of maximum load and jump-back sizes. The loading has a good coincidence, independently of the maximum load or jump-back size (40 or 60%). The inset graph for 60% unloading shows that the sample has been unloaded 40 times before the complete continuous unload.

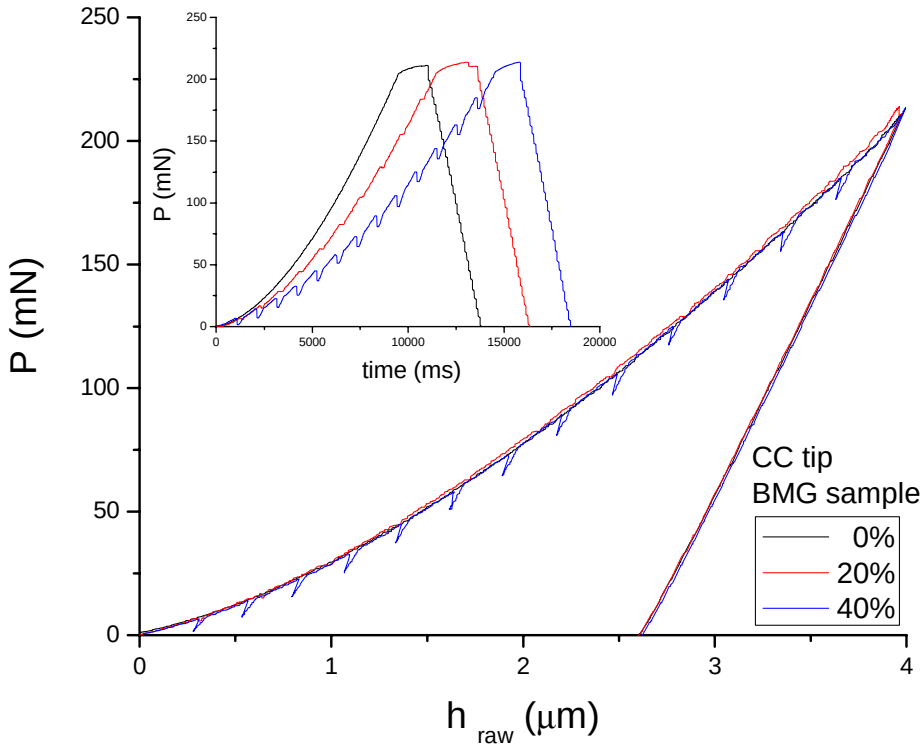

Figure 4.15: 200mN Cube Corner indentation in Zr-BMG with 0, 20 and 40% jump-back size. Inset graph shows the drop in load and number of unloads in function of percentage of jump-back.

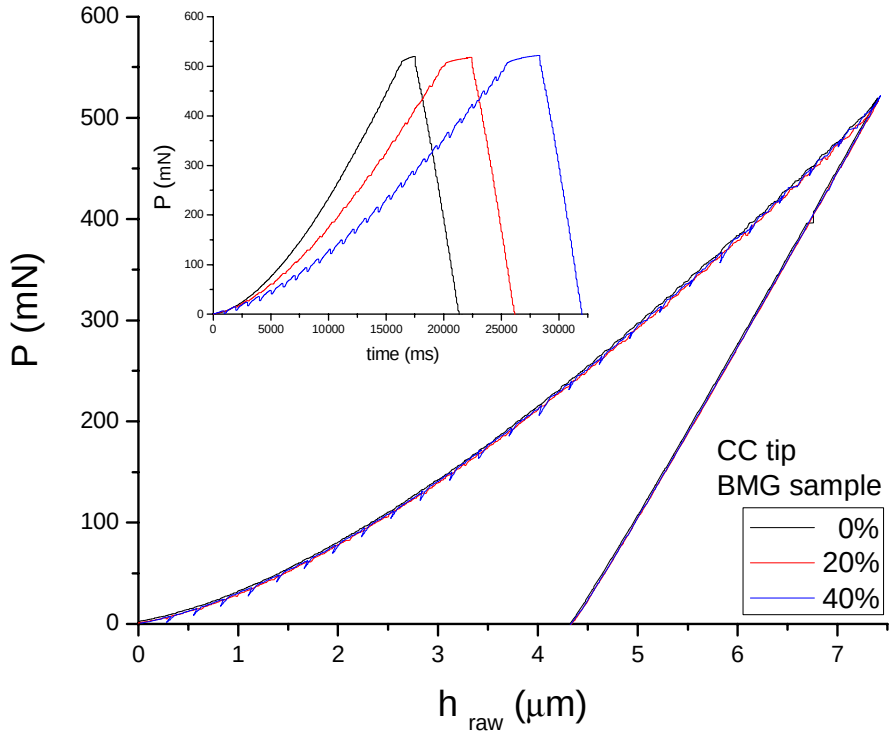

Figure 4.16: 500mN Cube Corner indentation in BMG with 0, 20 and 40% jump-back size. Inset graph shows the drop in load and number of unloads in function of percentage of jump-back.

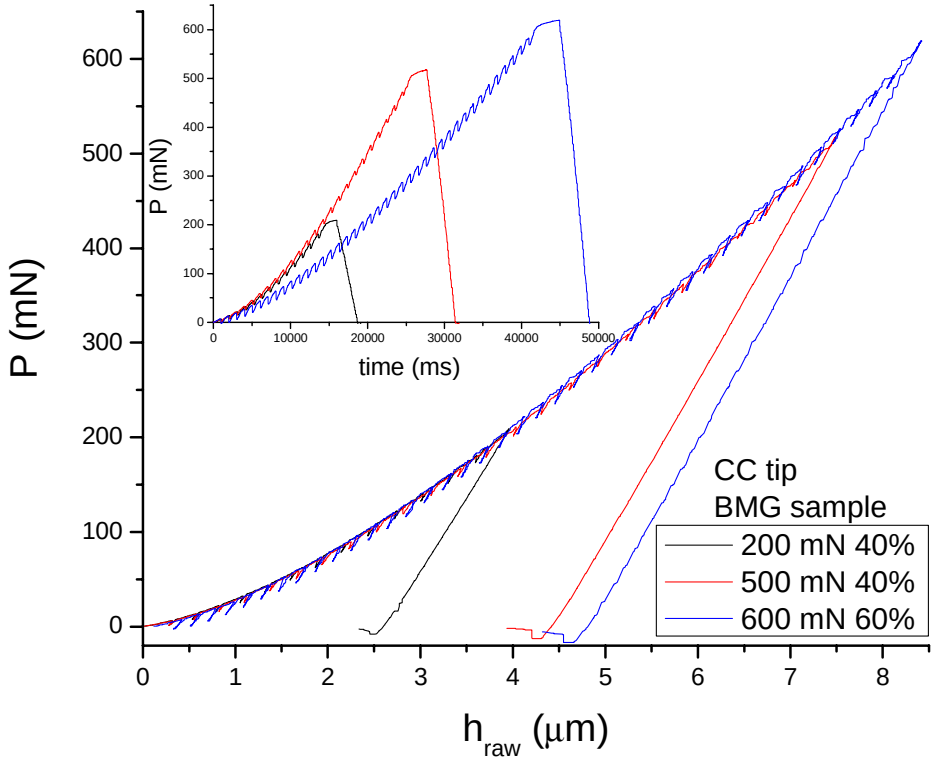

Figure 4.17: Graph comparison between different maximum load and jump-back sizes using Cube Corner indenter in Zr-BMG. With increasing of the jump-back, the average indentation velocity reduces.

4.4.2.2 SEM observation of Cube Corner imprints in Zr-BMG

Some SEM pictures from the experiment presented in Figure 4.15 (CC indentation at 200mN with 0, 20 and 40% jump-back) are shown in Figure 4.18. The particular behavior of its plastic deformation has left a very rough surface inside the imprint. None of the observed imprints have been found to have any indications that could be related to the amount of jump-back utilized. The shear bands around the imprint have not shown differences concerning the % of jump-backs. The dark transparent spots around and inside the tip are organic material deposited over by the material during storage.
Figure 4.19 shows two pictures of Zr-BMG, taken at higher loads. Figure 4.19a is a 400mN indentation with 0% jump-back. Figure 4.19b is a 600mN indentation with 60% jump-back. The 600mN imprint is the same represented in the graph shown in Figure 4.17

Again, even at higher loads and jump-back sizes, no visual difference has been observed as been related with the utilized tip driving mode.

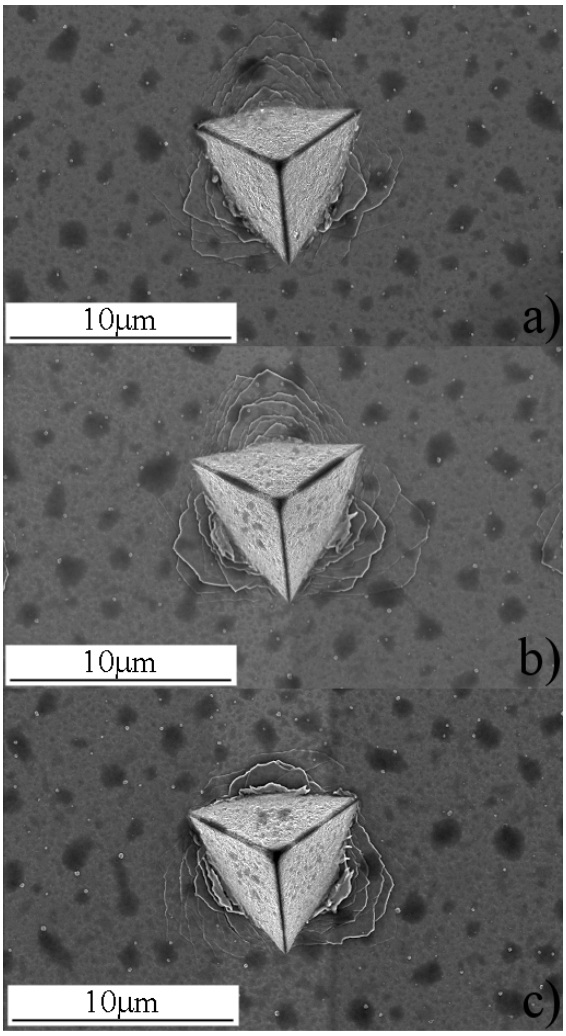

Figure 4.18: Cube Corner indentation in Zr-BMG, 200mN load at 0% (a), 20% (b) and 40% (c) unload.

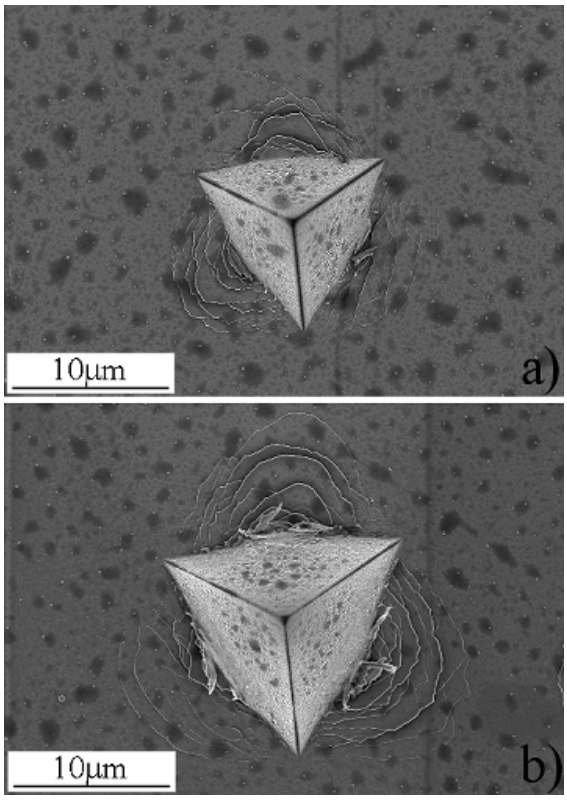

Figure 4.19: Cube Corner indentation in Zr-BMG. a) 400mN 0% unload, b) 600mN 60% unload.

4.4.2.3 Cube Corner indentation in Gallium Arsenide (GaAs)

Figure 4.20 shows the result of a SEM stick-slip indentation in GaAs. The test, for 0% the jump-back took nearly 8s to reach the set load of 200mN, which gives an average velocity of 0.42μm/s. Unloading has been made in 2.8s (the same for all three cases).

No noticeable difference has been observed among the different jump-back sizes. The envelope overlapping of the graph during loading and unloading are nearly the same (the match has been made using maximum load).

Figure 4.21 represents the GaAs test at a higher maximum load (500mN). SEM images have revealed a high amount of damage around the imprint. However, the agreement between the curves at different levels of jump-back is still good, as detected for the 200mN experiment.

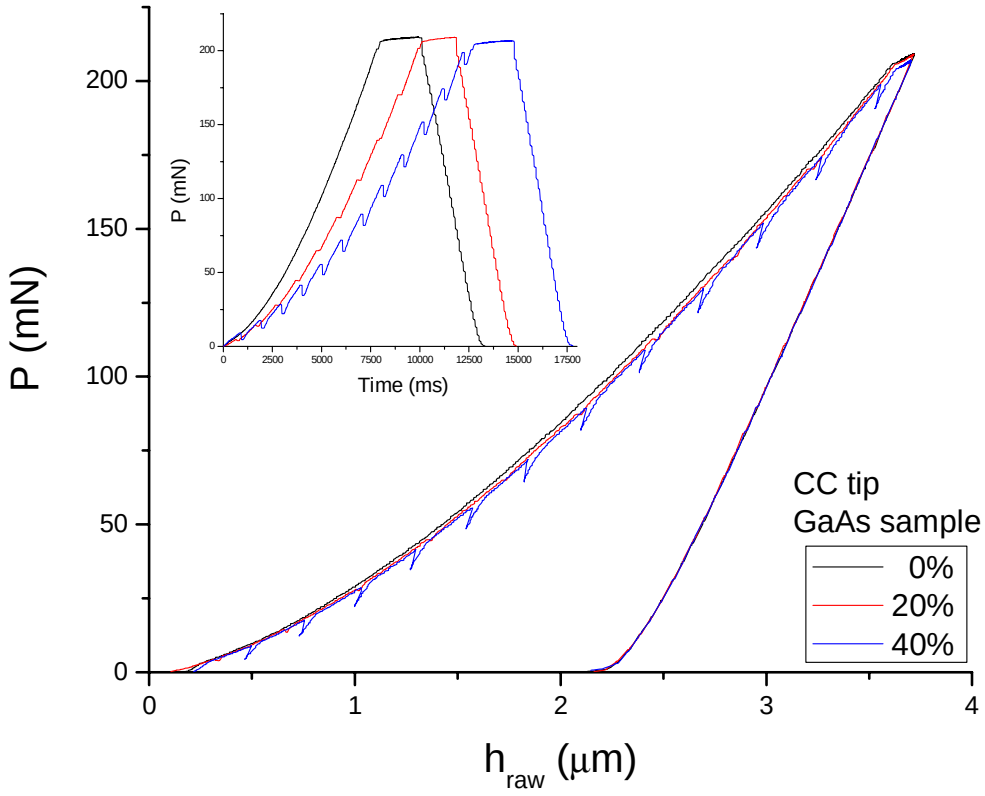

Figure 4.20: 200mN Cube Corner indentation in GaAs with 0, 20 and 40% jump-back size. Inset graph shows the drop in load and number of unloads in function of percentage of jump-back.

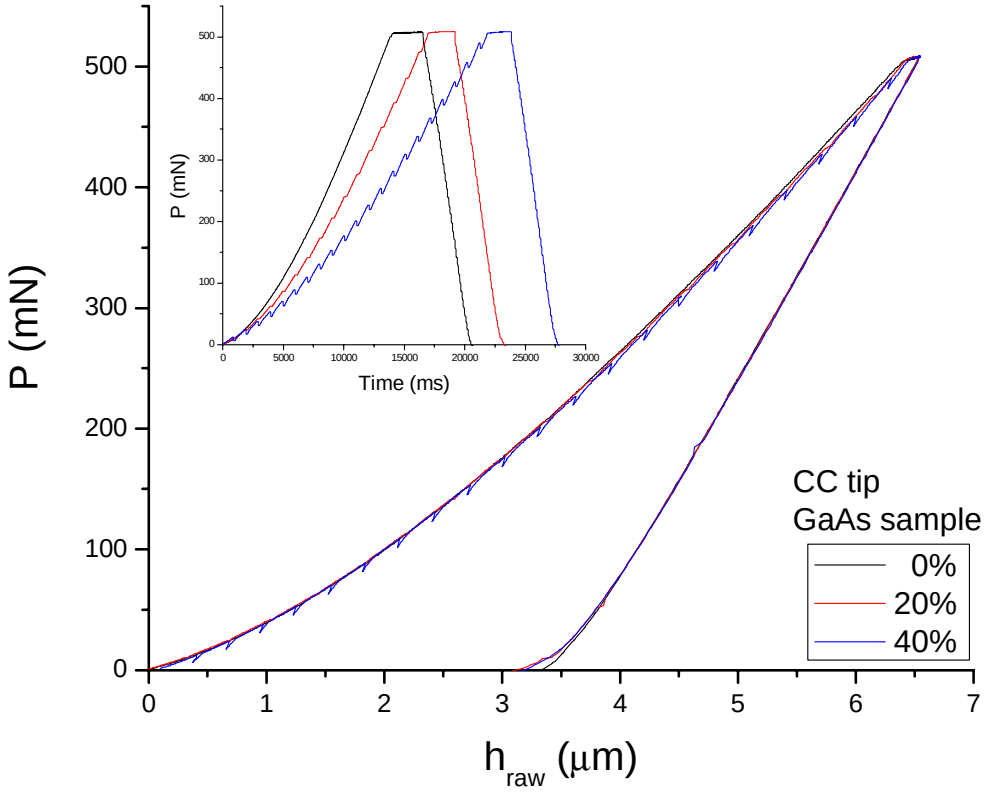

Figure 4.21: 500mN Cube Corner indentation in GaAs with 0, 20 and 40% jump-back size. Inset graph shows the drop in load and number of unloads in function of percentage of jump-back.

4.4.2.4 SEM observation of Cube Corner imprints in GaAs

A post visual inspection has been carried out to observe if there have been noticeable differences inside the imprint or anything else that could indicate differences between the amounts of jump-back. Figure 4.22 shows the details around the imprints taken after the experiment presented in Figure 4.20 (200mN maximum load).

High magnification (25.000 times) pictures have been realized inside the imprint. No specificity has been found as being characteristic of a certain amount of jump-back, as can be observed in Figure 4.23

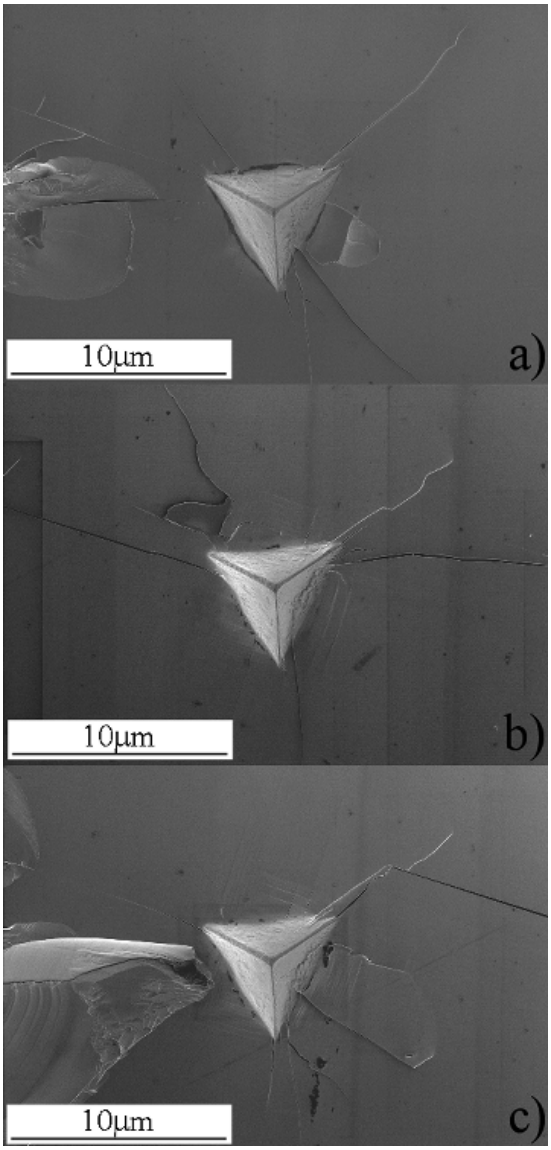

Figure 4.22: SEM Pictures of the 200mN CC imprints in GaAs at 0%(a), 20%(b) and 40%(c) unloads

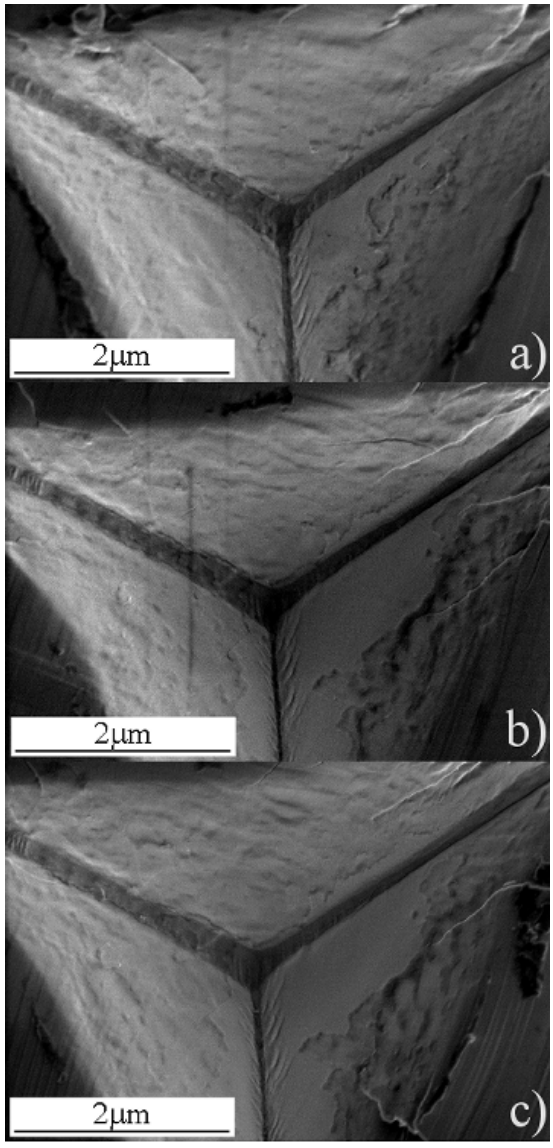

Figure 4.23: Inside imprints details of the same imprints presented in Figure 4.22. a) 0%, b) 20% and c) 40% unload

Crack formation is a statistical event. A detailed analysis of the cracks formed around the indent, as well as their interpretation is a difficult task and goes beyond this work. A brief introduction about types of cracks and what the impact of stick-slip actuators over its formation could be is discussed in Annex II, *Brittle materials* section. Here,

the main goal has been to identify something that clearly could be related to the actuator slip phase.

Compared with Berkovich tip, a Cube Corner tip induces high amounts of stress under and around the tip. Chip-out have been observed around each imprint. Imprints have also had their material removed by the next indentation, even exiting a gap of four to five times the indentation size.
Nevertheless, the P x h graph obtained through the SEM indenter has not shown a drop in load associated with the cracks. The unique detected drops have been those connected with the jump-back phase.

4.5 Stick-slip scratching analyses (results)

The influence of jump-back size has also been studied for a scratching test using the SEM indenter. The samples and adopted procedures have already been discussed on Paragraph 4.3.4.
Figure 4.24 shows the SEM pictures of an AlCu scratching using CC tip. The number of applied steps has been left constant (50 steps) but the amount of jump back has been changed. The scratching length reduces as the jump-back size increases.

In all tests, the observed results have been similar. During the test, no evident features could be observed in front or around of the scratch that could easily be related to the applied driving mode (0, 20 and 40% jump-back size).

On the other hand, a post analysis of the scratch has revealed a pattern, which gets more pronounced as the amount of jump-back increases. Moreover, this has been verified in the three materials tested (AlCu, Zr-BMG and GaAs).
At 20% unload, a weak pattern has sometimes been observed inside the trace. However, for this case, the visualization has required magnification higher than necessary to visualize the pattern cause by a 40% unload. An example is the inset picture of Figure 4.24c, which has been taken with a magnification of 40.000 times.

The fact that sometimes the pattern appears clearer could also be correlated with the manual intervention to compensate the set load. As the piezo drift gets smaller, the contact should be kept constant, even during the slip phase.
When scratching with an edge first, the jump-back phase will scratch back the sample with tip face. Any oscillation at the normal load, just prior to the slip phase could create a new scratch when the sample moves back. In this sense, it is expected that the slip phase will always create a pattern, but the latter will not always be easily visualized.
Figure 4.25 shows a test in Zr-BMG. At 20% unloading it is possible to see a pattern with magnification of 20.000 times. The inset picture has been taken with 40.000 times magnification.

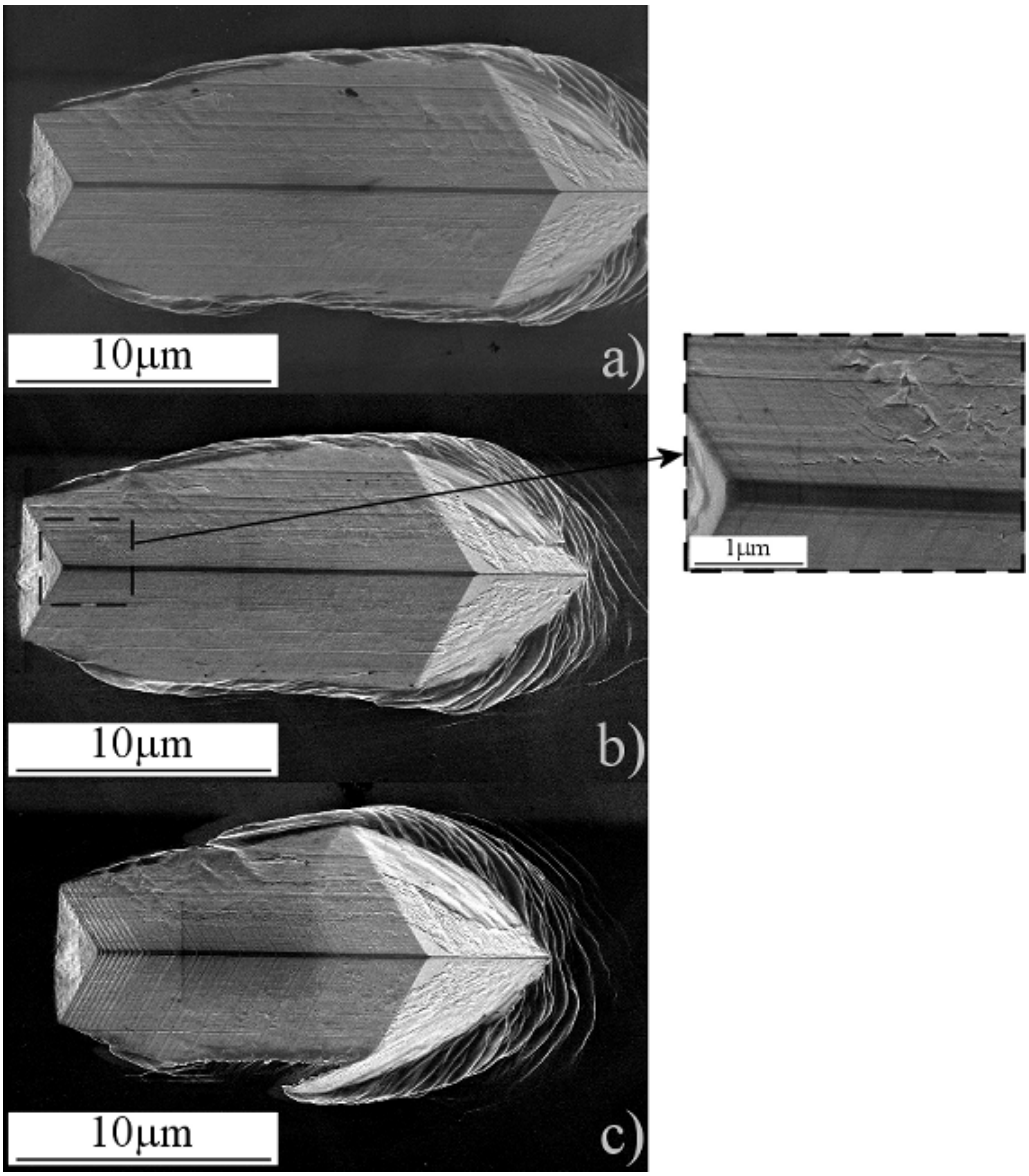

Figure 4.24: AlCu scratch (10mN) with CC tip with different jump-back sizes: a) 0%, b) 20% and c) 40%. Inset picture (40.000 times magnification) shows the pattern related with the stick-slip actuator having 20% of jump-back. The pattern is more evident at 40% jump back (fig c).

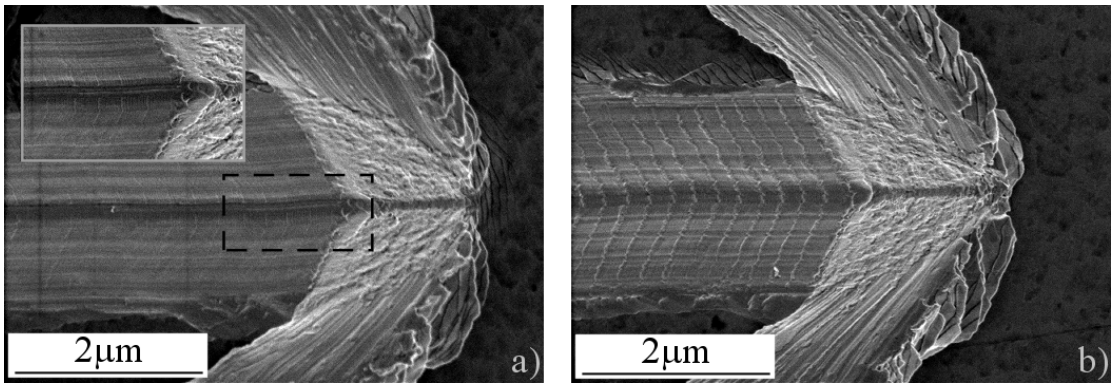

Figure 4.25: Zr-BMG scratching with CC tip at 10mN normal load. a) 20%, b) 40% jump-back. A pattern is difficult to spot at 20% jump-back size (inset picture) but is evident at 40%. In figure b, fifty steps have been found inside the entire scratch. This is the same number of steps set for the piezoactuator during the test.

Scratches in GaAs (Figure 4.26) have shown the similar results. At 20% jump-back, the pattern is visualized with only the help of high magnification (not shown). Externally and around the scratch, there is no evident feature correlated to the driven mode.

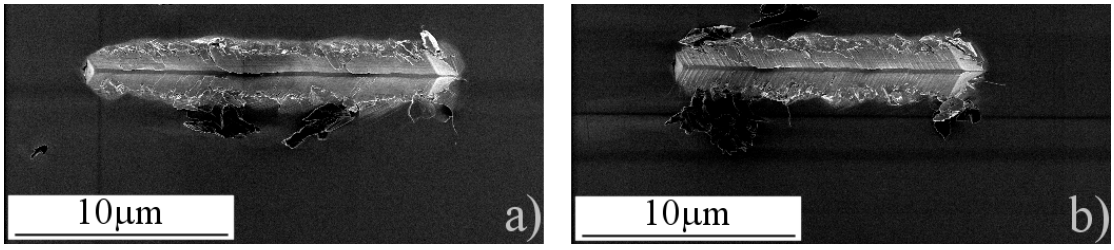

Figure 4.26: 10mN normal load scratch in GaAs with CC tip. a) 20%, b) 40% jump-back size. No differences have been observed around the imprints that could be related with the set amount of jump-back. A pattern caused by the tip driving mode is evident when using 40% jump-back.

As shown before, a more evident visual correlation has been noticed inside the scratch. With the help of an image analysis program and the scale bar, it has been possible to measure the jump-back size (space between marks) and to count the number of marks. For 40% unload, there is a stronger pattern. Thus, it has been easy to count 50 steps; corresponding to the number of steps applied during the experiment. This confirms that the patterns have been related with the amount of generated jump-back.

4.6 General comments

4.6.1 Indentation

Surely, the first question is how much the loading-unloading movement could influence the results, for example, modifying the imprint or the P x h graph. For the test here presented, it has been difficult to find any clear correlation or to have a general conclusion. These graphs have shown virtually no differences and have had a good agreement of the curve envelop. As the P x h graph is the starting point for material characterization, it can be expected that mechanical properties obtained from these curves will be similar. The fitting value ***m*** obtained during experiments in Fused Silica has shown that this is possible. The amount of jump-back has not changed the shape of the unloading curve.

The drop in load detected in the Fused Silica Cube Corner indentation demands more experiments. The numbers and type of the performed tests have not been enough to point out a correlation between the jump-back size and the occurrence of the observed pop-in.

Visual analysis of the indentation imprints have not shown a pattern inside, contrary to what has been observed during scratching. High loads (up to 500mN) have been applied to assure the occurrence of a certain amount of partial unloading during the loading phase (as the unloading has been left continuous). Fused Silica, Zr-BMG and GaAs have a very different elastic-plastic behavior, but also no extra marks or patterns have been left inside as observed with resolution limit of the SEM.

As can be observed in the P x h curves, the initial unloading part is mainly elastic (the contact area is constant during the first part of unload). In this phase there is no movement relative between the tip and the material.
An explanation to how a material behaves around the indentation tip during reloads has been provided by Pharr et. al. [68] and schematized in Figure 4.27.
Unloading and reload processes are elastic. A reload is the reverse of what has happened during unloading. A continuous decrease in the contact area happens as the contact impression peels away from the indenter.
The "peeling", as mentioned in [68], is easier to be observed in materials with smaller *E/H* ratios, as hard metals, ceramics or glasses. There is no real slide movement, except if the sample cannot follow the quick redraw of the tip (ex. as a result of the frame inertia).

Even in case the tip unloading could be fast enough to be followed by the sample's material, the next reload should erase part of the previous indentation, as the material starts to deform again. Soft metals will not have a high elastic response during indentation, as a result, a small unloading should completely release the tip. In this case, the contact is still kept by the frame stiffness.

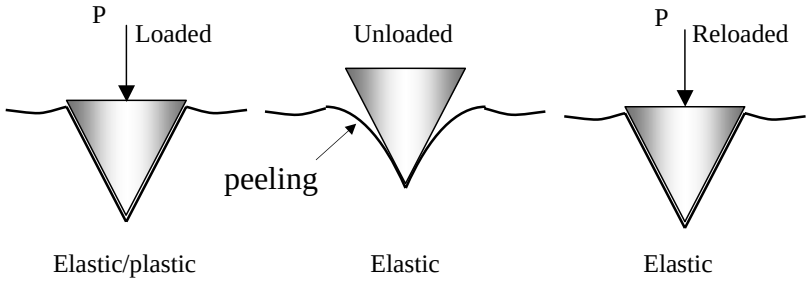

Figure 4.27: Schematic representation in a reload of a conical indenter

If there is an imprint pattern related to a stick-slip driven tip, it will have more chance to be found during unload. However, the unloading path is shorter than followed during load. Also, the reaction force from the indentation compensates partially the jump-back. Consequently, the jump-backs during unloading are smaller and they will happen in small amounts. This will make it more difficult to be noticed.

Analysis of the cracks around the imprints may lead to more concrete answers about stick-slip in indentation. However, to formulate a conclusion just considering the amount of jump-back is not possible. Cracks are complex to analyze and are influenced by material, indenter, maximum load, environment or a combination of these parameters [69].
A small discussion of what could be related to partial unloads in glasses and ceramics is presented in Annex II as well as for metals and polymers.
This discussion has the goal to create a conscience of precaution when conducting a test that uses a driving principle with similar characteristics of stick-slip actuators. It will also be used as a project guideline. The actuator can be tuned up to a level that the slip phase will be considered "harmless" to any characteristic that has been studied during in-situ indentation. Some techniques that could be used to reduce this backlash are presented in Chapter 5.

Finally, it is possible that a complete elimination of the jump-back is not necessary or even possible (the increasing in complexity to do this became too high). However, in

any case, reloads related to the slip phase should not be easily visualized or identified in a P x h graph. The final P x h graph should only show events originated from the tip-sample interaction and not from the type of actuation.

4.6.2 Scratching

Even if for several materials a sequence of partial reloads has proved to not change anything, the fact that there is a pattern will simply distract the observer and make it more difficult to have a general overview of the scratch.
It exists a threshold (the maximum jump-back amplitude) that no pattern is left in the imprint. The maximum allowed pattern could be defined as having a size that can pass unnoticed for most standard magnifications used during in-situ indentation or scratching.

4.7 Conclusions

So far, the experimental results have not shown a situation that restricts the use of a stick-slip actuator for indentation and, in some extension, for scratching as long as the amount of jump-back keeps below a certain size. Jump-backs as big as 150nm have been detected during stick-slip indentation. However, what must be considered is the size and the amount of unloads. And this will depend on the indenter frame stiffness; the tested sample and the indentation tip type. The key is to find the 'tolerance' of each material.

Materials with a high elastic response and that are free of creep or strain hardening should not face problems from the jump-back movement. A sensitivity test (changing the average indentation velocity) should be able to warn the indenter user if using stick-slip with strain sensitive material will bring too many differences, at least when the device is being used for exploratory purposes and not for absolute measurements.
Brittle materials and wide-angle tips will face fewer problems than materials tested with acute tips, although sharp tips are by far the best ones to be visualized during in-situ indentation or scratching.

Further investigations and tests are necessary to determine how much cracks may be influenced by small unloads. Visual analysis and the comparison of graphs are difficult because of the high dispersion of the results. The measurement is quite sensitive to small changes in the experiment conditions or simply the graphs do not register any event.

The literature review (Annex II) could not point out the limits of reloading the material (amplitude and number of reloads). However, it seems very probable that reloads may generate more cracks. In a simplified explanation, cracks are formed (and expanded) during loading or unloading if the limit load of each material is reached (what also will depend on the tip type). The started cracks might at the end join, creating thus a chip out.

A quantitative study is necessary to determine its limits (size) and quantify the allowable amount of jump-back (as a fatigue test), overall in brittle materials.
It will depend also on the type of material studied. An extension of the present study, however, is beyond the scope of this thesis.

Chapter 5

Instrumentation for Materials Characterization

5.1 Introduction

This chapter is an application of the work developed in the past chapters.
The first part shows some techniques to reduce the amount of jump-back related to each actuator slip phase. It contains results obtained through simulations and experiments. In this first proposal, the solutions are focused on the leg movement (combinations) driven independently by one channel each. After that, a more mechanical than electronic solution will be proposed.
Later on, the focus will be on the indenter/scratch itself. The design of the actual instrument will be reviewed and modifications will be proposed after all the feedback taken from material science researchers (end users), as well as from new ideas that have appeared later on.
The chapter will be completed by a small, but valuable review on how to design instruments to work inside a Scanning Electron Microscope; most of them acquired designing nanopositioning systems.

5.2 Techniques to reduce the amount of jump-back (backlash) during the slip phase

As shown in Chapter 4, a certain amount of jump-back can be present during indentation or scratching, with more or less intensity, and still not changing the measurements result (visually or through the P x h curve).
The slip phase is inherent of the stick-slip actuator in order to have a step movement. The abrupt foot recoil generates a force against the movement (based on the dynamic friction coefficient). It also acts as a mini step response to the system, exciting several frequencies that can be observed as vibrations after each step. The amount of jump-back reduces the efficiency (as part of the displacement is lost). The microvibrations after each step limit the maximum driving frequency, since there is not enough time between the steps to damp these microvibrations. Therefore, the vibrations of a previous step will be present in the next one. The interaction of these vibrations will thus create an uncontrollable movement of the carrier.
Vibration control, jump-back reduction and driving force are no new topics in the case of stick-slip actuators. It has already been discussed by Breguet [56] and Bergander [27]. A part of this work will follow some of the ideas present in Breguet's work, although with more emphasis on how to have the same reduction and still have enough driving force.

5.2.1 The carrier-foot contact considerations

Stick-slip actuators have a better performance with stiff legs (actuators) and stiff contact.

Material: The leg stiffness is a function of its dimension and its material. A shear piezoactuator (ex. a PZT type C-82 from Fuji Ceramics [29]) has shear Young's modulus (Y_{55}^{E}) around 2.2GPa in the direction of the movement. It is a property that does not significantly change between different types of PZT.

Assembly: Compliance is also introduced in the leg assembly. The sapphire foot is glued over the piezoactuator with epoxy glue[34] and then the piezo leg is glued to the instrument frame by electric conductive epoxy glue (Figure 5.1a). Assembly stiffness is improved when low viscosity glue and few stacked assembled parts are used.

Contact: The carrier-foot contact is matched through asperities contact (Paragraph 3.4.1) and it can be improved through material selection and finishing. A lower friction coefficients induces less vibrations and lower jump-backs ([56] p. 68). However, more normal load will be necessary to keep up the same driving force.

Material selection: A good material selection (foot-carrier) can be used to optimize[35] the actuator in terms of performance (effective step size) and driving force. For example, Bergander [27] has explored different combinations of materials[36] contact (steels, hard coatings and ceramics) for stick-slip applications focusing on wear resistance.

Interface: A correct selection of the interface geometry limits contact pressure. High contact areas or increasing the numbers of contact points is preferred. The challenge, then, will be in how to do this without over constraining the actuated part.

5.2.2 The linear test stage – a measurement procedure review

5.2.2.1 Stage components and characterization

The linear stage utilized for the tests is the same as the one presented in Chapter 4 for stick-slip indentations. The mobile shaft (carrier) is actuated by four legs (shear piezo actuators) as can be seem in Figure 5.1a. The legs, having each a ∅4mm half sphere in sapphire, are assembled in pairs forming a 120^{o} V shape. Each foot-carrier contact creates a unique contact point, as shown in Figure 5.1c. The mobile shaft (carrier) is made of rectified hardened steel (hardness 62 HRC) and has 10mm in diameter

A steel sphere has been glued on one extremity of the carrier in order to provide a contact point on a flat platform placed over the load cell (Figure 5.1b). The carrier displacement is measured through a laser interferometer (Figure 5.2) and load is measured by a 10N range load cell (Figure 5.1b). The normal load F_N is given by placing magnets under the steel shaft. This configuration, with four contact points permits a kinematic coupling. This makes the jump-back analysis easier, as the normal load is equally distributed over each contact. The friction coefficient (Coulomb) has been experimentally determined as μ=0.13.

Measurements have been taken at sample rate of 2500Hz for load and displacement. The data coming from the interferometer has been taken at an internal rate of 10kHz

[34] Epsilon 2103 from *Abatech*: Viscosity 0.25Pa·s, H=80 Shore D, shear resistance 15Mpa. Electric conductive glue *Epo-Tek* E4110, characteristics: 10 Pa·s, H=80 Shore D, shear 6.9MPa

[35] Through the amount of applied normal load

[36] The basic shape has been a 1.5mm sapphire half sphere contacting a flat plane.

and averaged four times before being uploaded to the computer. The load cell has been read using a 12bits[37] A/D card from National Instruments. The signal coming from the load cell has then been amplified[38] before going through the acquisition board. Interferometer and load acquisition systems have been synchronized by an external trigger on its start.
The step amplitude has been measured applying a low frequency sinusoidal signal (no slip) over the legs (from –200 to + 200V), without reaction force (not contacting the load cell) and reading the shaft displacement through the laser interferometer. The calculated and averaged value peak to peak of 13 periods has been measured as having 560nm.

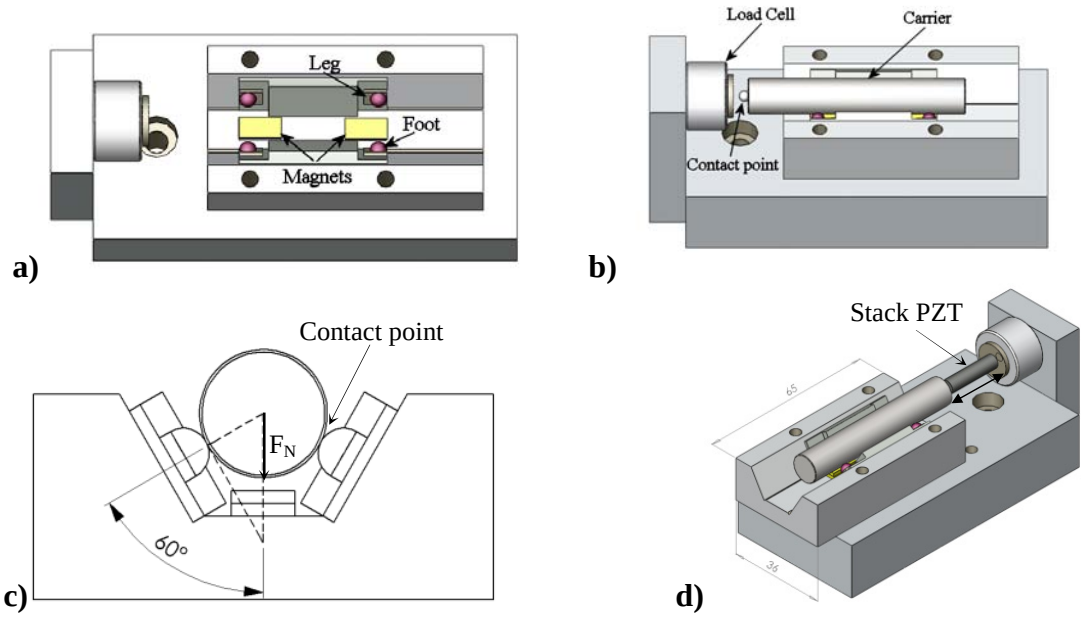

Figure 5.1: Scheme of the linear stage utilized for the stick-slip test. a, b and c) General scheme of the actuator. d) Actuator with a stack piezo actuator placed between the load cell and the carrier.

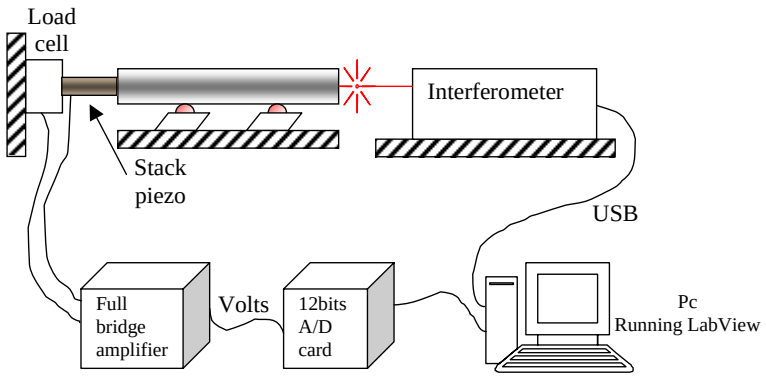

Figure 5.2: Scheme of the measurement system used during the movement characterization

The tangential force has been measured by placing a stack piezoactuator (range 21µm - Figure 5.1d) between the load cell and the carrier. The displacement measurement has been recorded simultaneously from the carrier (interferometer) and from the built-in piezoactuator strain gauge (Figure 5.2).

[37] From –10 to +10V. Range could not be changed.
[38] The amplifier had a built-in high frequency filter (capacitor) set for 2500Hz.

This has been a simple way to determine the linear stage stiffness (reading the piezo displacement and the load) and the tangential stiffness, reading the shaft displacement before or after it starts to slide. Figure 5.3 shows the measurements (replications) of five runs to estimate the friction force and carrier tangential stiffness (the base has been bolted with four screws M3).
Table 5.1 shows the linear stage mechanical characteristics at two loads (with 4 magnets and with 2 magnets) [39]. Frame stiffness and tangential stiffness have been obtained through a linear fitting function applied during unload. Friction force has been measured taking the average force of the five measurements[40].

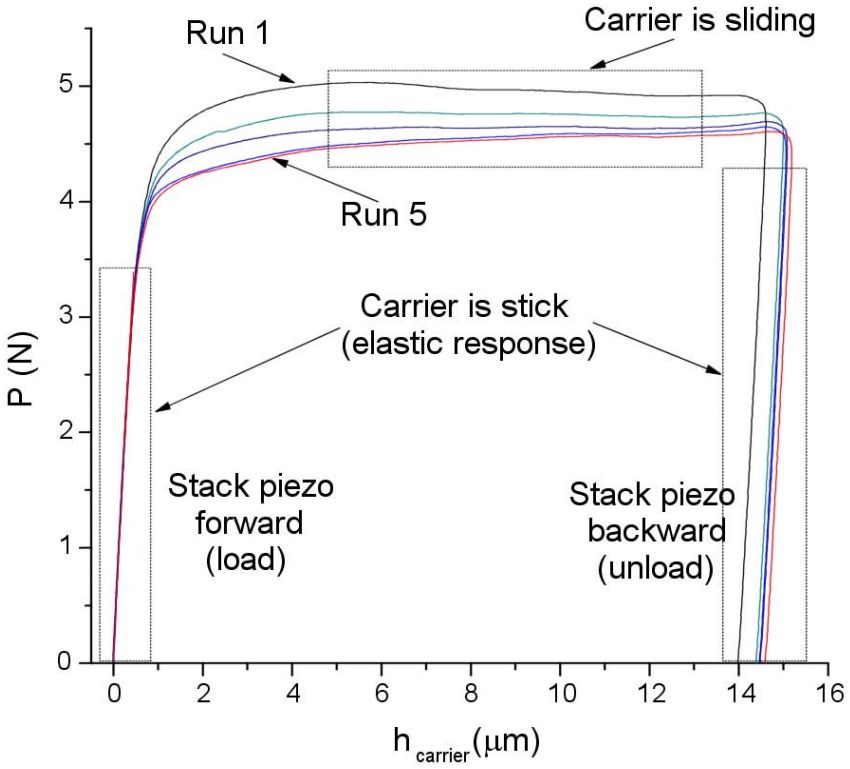

Figure 5.3: Linear stage characterization at high load (carrier measurement). Main phases.

Table 5.1: Linear stage mechanical characteristics

	Friction force (F_{dyn})	Tangential stiffness	Frame stiffness	F_N Total
4 magnets	4.69N	7.4N/μm	0.71N/μm	36N
2 magnets	1.01N	5.7N/μm	0.69N/μm	7.8N

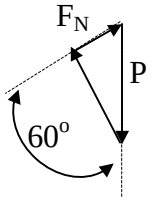

$$F_{dyn} = \mu_{coul} \cdot F_N \qquad \textbf{Eq. 5-1}$$

$$P = \frac{F_N}{\cos 60^\circ} \qquad \textbf{Eq. 5-2}$$

The normal load over the four contact points could not be directly measured. It has been calculated through Eq. 5-1 as being 36N with four magnets installed, and 7.8N

[39] The first set has been placed under each leg pair. The second set of magnets is placed over the original set.
[40] Using the software Origin 7.5 function 'Average multiple curves'.

with two magnets. The four magnets have created a total down force *P* of 72N (Eq. 5-2) and with the two magnets configuration, a down force of P = 15.6N.
It can be noticed that the tangential stiffness changes as the normal load increases. This is caused by a compression of the contact interface (asperites). The gap is smaller. Thus, more asperities are brought in contact (increasing the contact area – Eq. 3-9) and the radius of the already contacted asperity increases. Therefore, the tangential stiffness increases with preload.

5.2.2.2 Measurement outputs of stick-slip test

A typical result of the measurement is presented in Figure 5.4. The carrier can starts at a few micrometers from the load measurement system. For some steps, there will be no change in load (inset picture in Figure 5.4b). These few steps (inset graph in Figure 5.4a) can be used to evaluate the jump-back size before the action of an external load. The load starts to change when finally the carrier touches the load cell (signalized as 'contact' in Figure 5.4a).

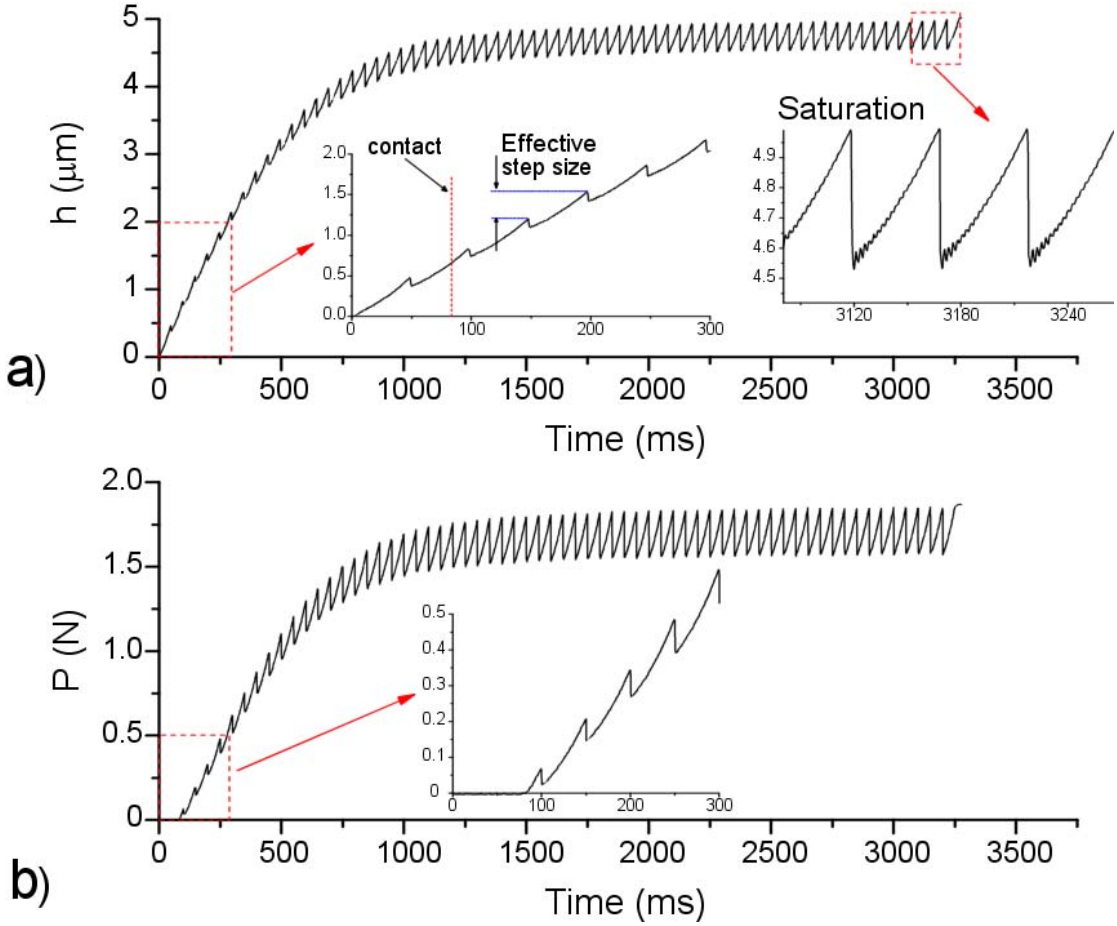

Figure 5.4: Typical displacement (a) and force (b) graphs obtained when driving the carrier up to its saturation in displacement. Inset graph shows in details the drop in displacement and load at different points of the test (at the beginning and during saturation).

The jump-back increases with increasing of the reaction force. The effective step size (Figure 5.4a) reduces, until the system is saturated. Saturation, in this case, means that the displacement in the stick phase is completely taken back during the slip phase.

5.2.2.3 Measurement procedure

The driving force of a stick-slip actuator relies on two main parameters: Normal load and the friction coefficient (static and dynamic). The linear test stage (Figure 5.1) has had an additional degree of freedom unconstraint, which is the ability to turn around its axis (roll). During the experiments, the normal load has been guaranteed by the gap between the magnets and the shaft (carrier). As the cylinder has been contacting each leg in a single point (kinematic coupling), the distance between the shaft and the magnets have not changed each time that the cylinder had to be removed.
On the other hand, a new contact line has been formed each time that the shaft has had a small rotation and starts to run again. In addition, the environmental conditions have been not controlled. Contaminations at the foot-carrier interface (as oxidation of the metallic shaft, moist) can change the friction coefficient.
One procedure adopted before each measurement has been to make the carrier run several times against the load system (until the saturation position) to reduce measurement dispersion during the first measurements (see also in Figure 5.3 how the graphs behave after each replication). The graphs presented in paragraph 5.2.3 are an average of five measurements (five runs[41]) for each case.
To complement the test, simulations[42] (as presented in Chapter 3) have been used to better understand a result using a 'virtual environment', as a single parameter can be effectively changed.

5.2.3 Feet in phase

Working with the feet in phase[43] has been pointed out in [56] as being an effective way to reduce the amount of jump-back. Figure 5.5 shows four combinations (modes) utilized for testing. Here, one period is described by 100 points in volts over the piezo leg (from –200 to +200V, after amplification). In terms of a set driving frequency (20Hz), 100 points are updated in 50ms.
Each step (independently of leg combination) has been driven at 20Hz and the load has been measured at a scan rate of 2500Hz.

- The reference driving mode is Figure 5.5a, where all the four legs are driven synchronized.
- Type *b)* needs two channels to be driven, but can work with only one channel, simply assembling one leg inverted.
- Type *c)* uses four channels. Each leg is driven after a delay of 25% of the full period.
- Type *d)* also uses four channels. All legs are driven together and returning one by one. Note that for this last mode, because a software characteristic, the period is four times longer than the other modes. This means that, at the same driving frequency, the carrier displacement is slower in this mode.

Figure 5.6 and Figure 5.8 show the main results of the test. Each graph is the average of five runs (replications).

[41] A 'run' is the same as one replication of the test, keeping the same parameters.
[42] The main difference here is that the modeled foot-carrier contact is a half sphere in a plane and not a half sphere against a cylinder. However, for an observed tendency, results are not significantly influenced for this reason.
[43] It also has been applied for a patent in by CSEM - Centre Suisse d'Electronique et de Microtechnique SA (EP0750356, 27.12.1996). The patent has been ceased in 14.02.2003

In Figure 5.6, the full graph shows the saturation point of each condition, while the inset graph, in each case, shows the drop in load of reaction forces from 0 to 0.5N.

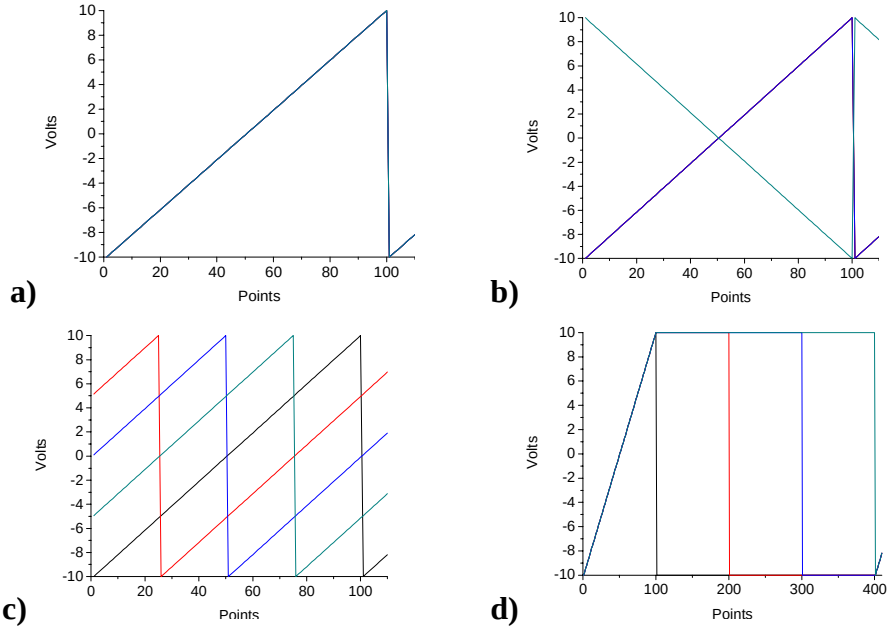

Figure 5.5: Driving signal (in volts) for each of the four analyzed leg phase condition. a) reference signal (all 4 legs together), b) one leg inverted, c) legs with 25% period shift, d) one by one back.

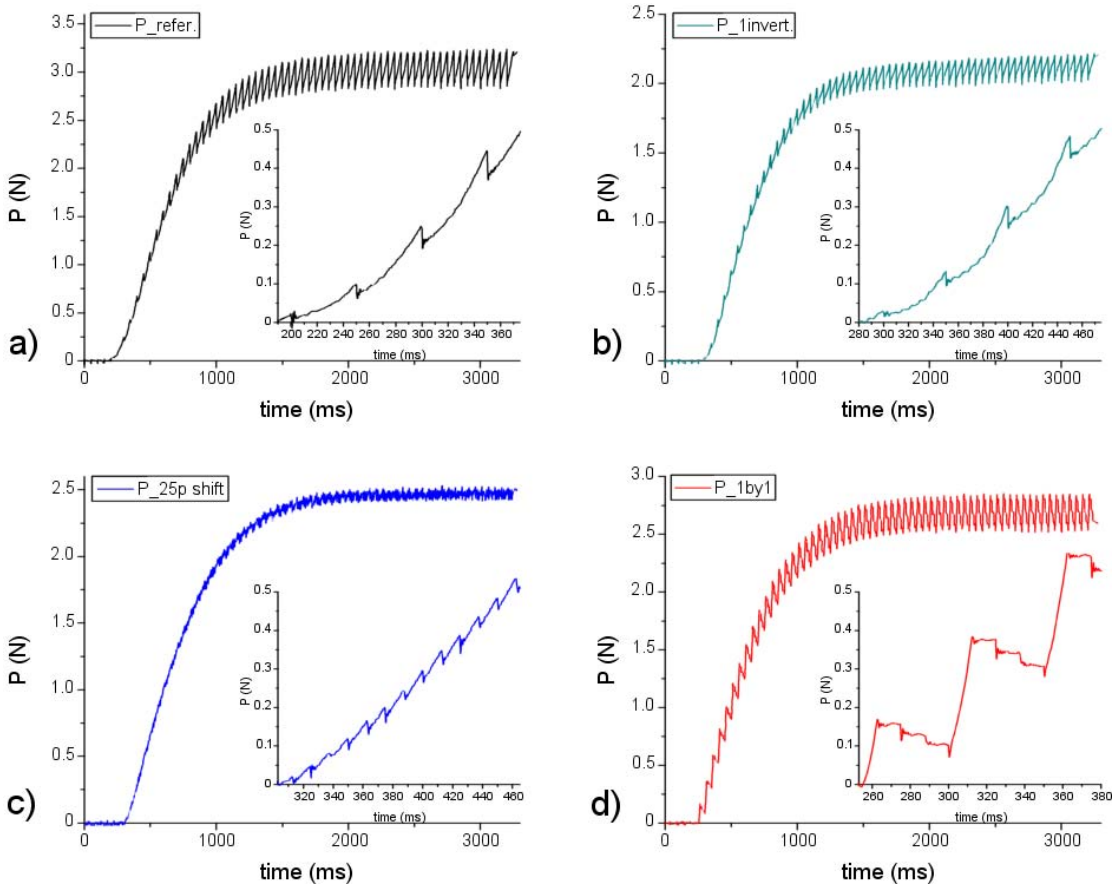

Figure 5.6: Load response as combination of leg movements. a) All together (reference), b) one leg inverted, c) phase shift between legs, d) legs return one by one. Inset graphs show the carrier behavior before face a reacting force. Inset graphs are at the same scale, all graphs are an average of five runs.

The saturation load is defined as the average load (a middle value of the slip phase) measured with the last 20 steps at the end of the graph. The result is presented in the following table.

Table 5.2: Average saturation load (equivalent to the middle of the slip phase) for each of the presented conditions in Figure 5.6.

Driving mode	a	b	c	d
Saturation load	3.0N	2.1N	2.5N	2.7N

The interferometer has a better resolution, sample rate and filtering than the load measurement systems. The output signal is clearer than the one obtained through measuring load, and is thus better for analyzing fast events, as the slip-phase.
The results are summarized in the next two figures. Figure 5.7 shows an overview of the jump-back behavior before touching the load cell up to its saturation (measuring the carrier displacement). A detailed view of two regions of interest is presented in Figure 5.8. The main graph shows the step behavior at the saturation point, while the inset graph shows the step size from 0 up 0.5N reaction load.

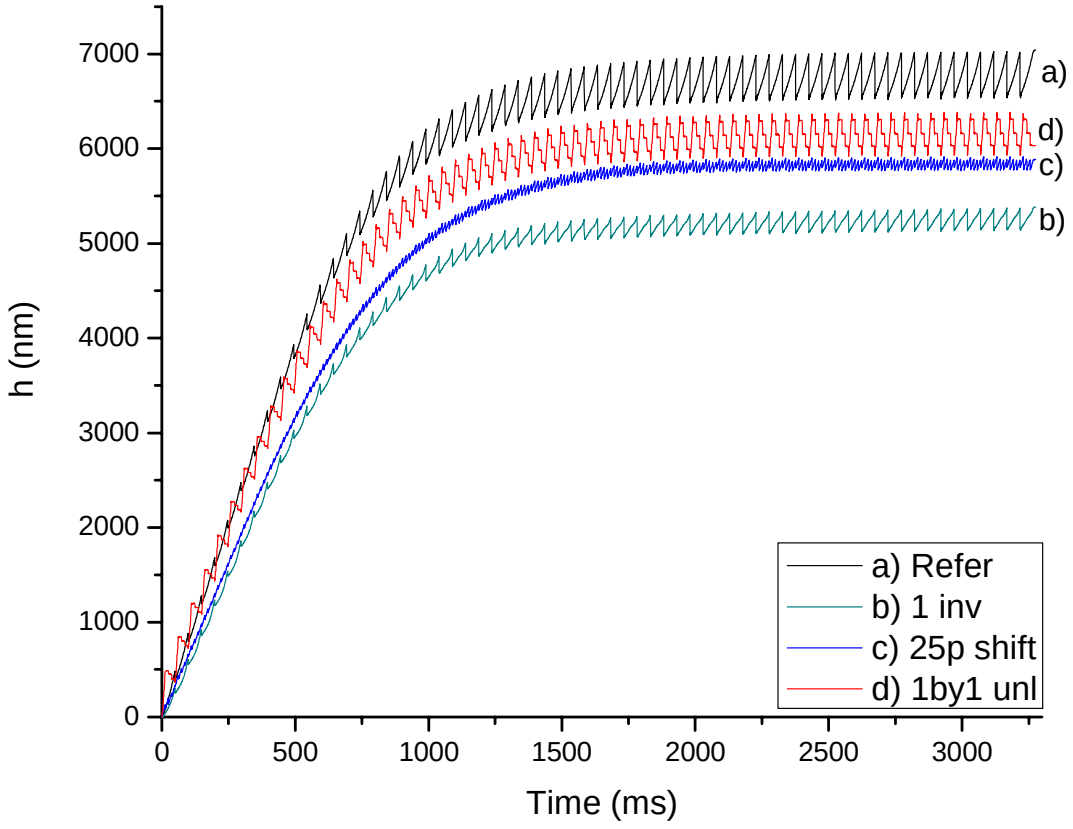

Figure 5.7: Step behavior for each of the conditions (from no reaction force to saturation)

Table 5.3 gives a quantitative way to visualize the jump-back size at saturation point.

Table 5.3: Average Jump-back size measured at saturation point[44]

Driving mode	a	b	c	d
Jump-back size (saturation)	477nm	195nm	77-134nm	448nm

[44] The measurement just after the slip phase includes a region with vibration.

It is clear that when the legs are driven at 25% shift between each other, the reduction is higher than the reference mode. A good result has also been obtained with one inverted leg.

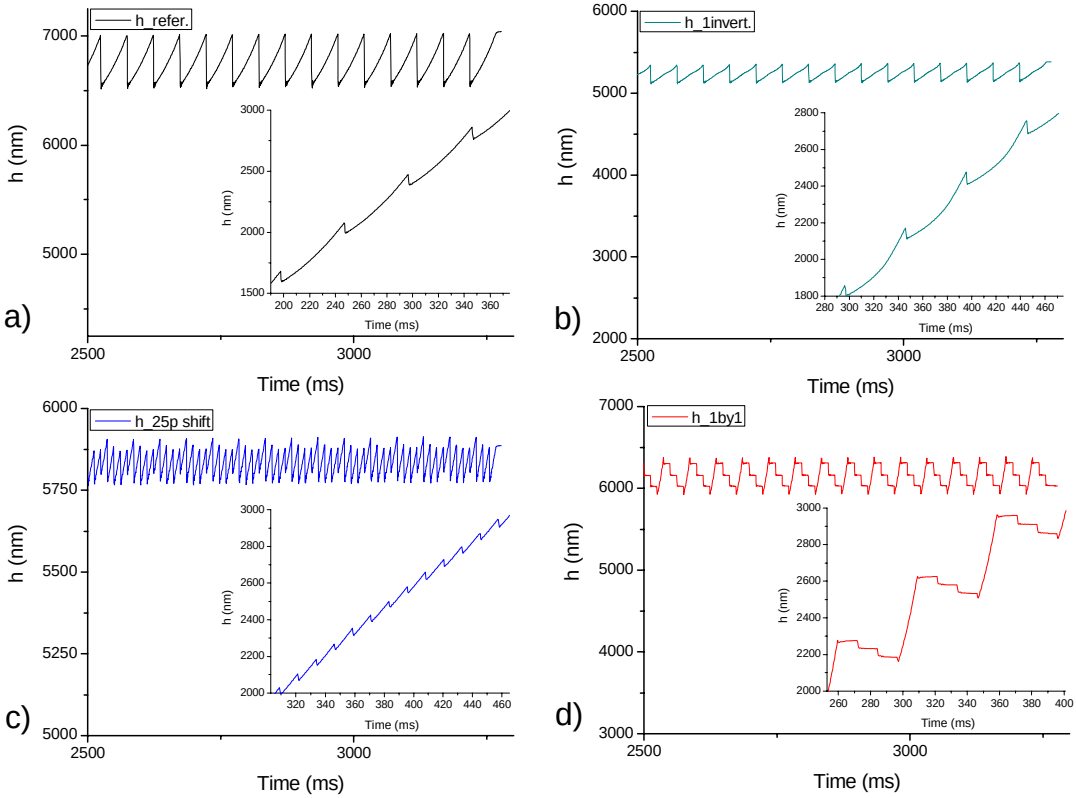

Figure 5.8: Details of carrier displacement behavior for the four modes. Main graph shows the saturation point. Inset graphs are taken from 0 to 0.5N reaction load. (Not in the same scale)

5.2.3.1 Simulations and Measurements – Understanding the jump-back phase

Simulations of a carrier being driven against a spring, using the same driving modes as presented before, have also been realized.
Figure 5.9 shows a simulation of the two best driving modes observed during the measurements (25% shift and 1 leg inverted).
The simulation has confirmed the differences between the two best driving modes. It has also shown that each leg has equally contributed to a partial unload. This homogenous unloading can be easy seen in the 25% shift or, more evidently, in the one by one unload driving mode (not shown in Figure 5.9).
However, analysis of the measurements, even before the carrier touches the load cell, shows a non-uniform displacement – as it is the case for the one by one unload. The measurement in Figure 5.10, with two different normal loads, shows this behavior.

- One possibility is that each leg has not had the same contact characteristics. This can be verified changing the actuation order and compare results. The procedure has been adopted and no different behavior has been observed.
- It is known that the leg stiffness plays a big role in the jump-back size (the stiffer, the better). Through simulations, setting the leg stiffness to higher values (as 9N/µm) has considerably reduced the jump-back size at the same normal load (in any drive combination). Stiffer legs should provide more homogenous unloading when driving the legs in phase.

- The combination of leg stiffness and normal load can store energy in the piezo (that has a nominal stiffness) and in the foot-carrier interface. An explanation is provided now.

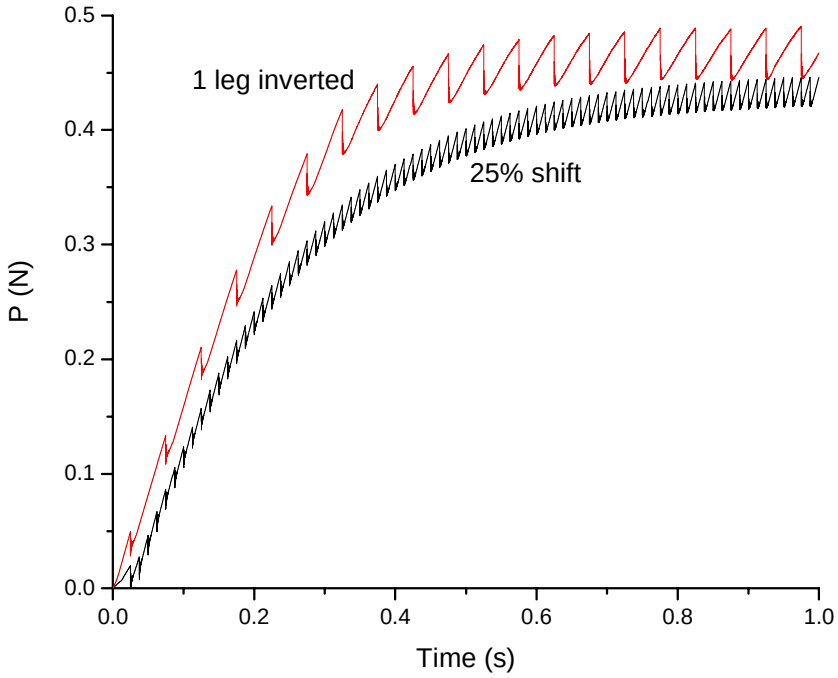

Figure 5.9: Simulation of two driving modes. The carrier is driven against a spring by 4 legs. Conditions: Spring stiffness, 0.31N/µm. Normal force (over each leg), 2N. Static friction coefficient , 0,15. Dynamic friction coefficient 0.1. Step size, 400nm. Driving frequency, 20Hz, carrier mass, 30g.

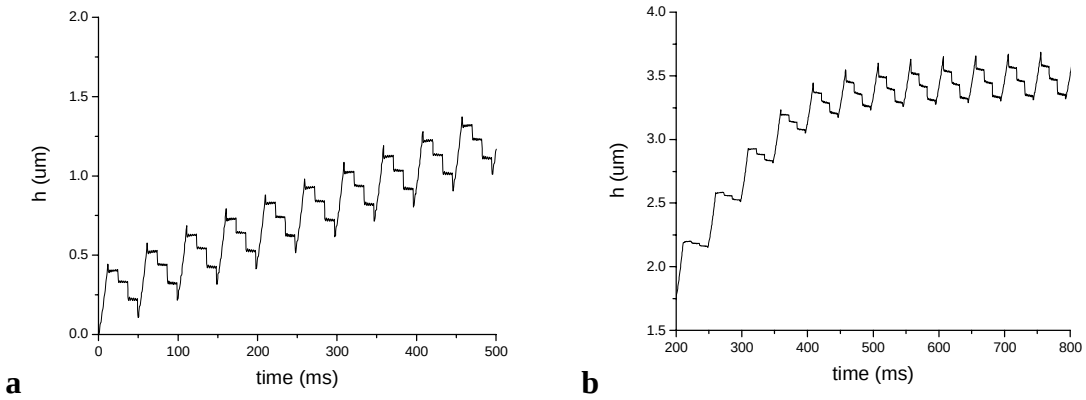

Figure 5.10: Measurement of 1by1 unload mode. a) High normal load, b) low normal load

The jump-back is measured targeting the carrier displacement. As schematized in Figure 5.11, when each leg returns, a friction force is generated and retained by each piezo leg and foot-carrier contact (each one has a certain stiffness). As more legs are going back, more internal forces are actuating over the carrier (and constrained by friction). Once the last leg returns, all the internal forces are released. The carrier thus goes partially in the opposite direction, compensating thus the jump-back from the last leg. This can help understanding why the first and the last jump-backs are smaller. The first one is held in position by the remaining legs. The last one is compensated by releases of the internal constrained forces of the remaining legs, when it finally slips.

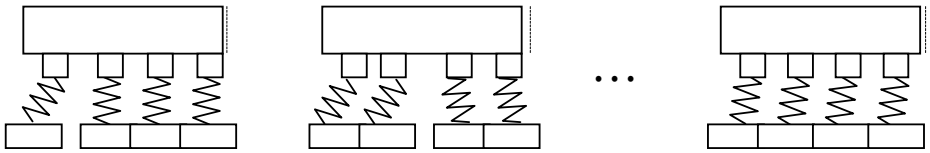

Figure 5.11: Scheme of internal feet-carrier compliance over the carrier displacement. The stiffness in each leg influences the carrier displacement at each slip phase. See text for details.

In this case, it is expected that a partial actuation (reload) of each leg after each slip phase will compensate these excessive jump-back movements. This may be what happens when legs as driven in shift mode, as shown with 25% phase difference.

5.2.3.2 Results overview

Using legs in phase is a straightforward solution as the actuators are a part for the instrument for indentation and/or scratching. On the other hand, to increase the number of drive channels will increase costs and complexity. Legs in phase need one amplifier and one wave generator for each leg plus an equal number of power lines inside the instrument and consequently through the vacuum chamber. As the necessary electronic gets more complicated, the commercial actuators (Paragraph 2.3.4) nowadays available will be more attractive. For instance, inchworm actuators will need three channels, while Piezolegs will need two.

Phase shift also means that more steps will be necessary to reach a target load or position. The drop in load reduces but now the steps are closer to each other. This can be similar to an actuator working in Continuous Stiffness Mode (CSM) described in Annex II. Considering the simulation present in Figure 5.9, reaching a load of 0.4N has required 28 steps using the 25% legs shift mode. This means that a sample has been reloaded 28 times during the loading process, instead of only 7 times with one inverted leg. The number of reloads starts to be a source of concern in the case of the material behavior.

One inverted leg has provided good improvement at low loads and it is even better at higher loads (ex, comparing the saturation point). The implementation of this driving mode is easy and can be done without adding a new channel for the driving axes.

As conclusion, the driving mode can be an option to reduce the jump-back for positioning, indentation or scratching. However, it should not be used alone. The first step should be the normal force optimization, as presented now.

5.2.4 Optimizing normal load[45]

The application of the correct normal load depends on the desired target force. This force is simply the reaction force over the actuator. This can be a variable force, as faced during indentation, scratching, or simply the necessary force to lift a mass against gravity.
An over preloaded system does not mean an available driving force up to its friction static force ($\mu.F_N$). As it has been shown for the Figure 5.1 device, its measured friction force has been nearly 4.7N (with 4 magnets). However, the maximum driving

[45] Considering the actuator working horizontally and against a spring. An actuator working against gravity, without any other external force acting against its movement and keeping a same F_N, will have its minimum jump-back increased almost linearly in function of weight.

force (all legs together) had a maximum of 3N (Figure 5.8a). The step saturates before reaching the maximum friction force.

Increasing normal load also increases the amount of jump-back and the microvibrations amplitude that follows each slip phase. These microvibrations limit the maximum driving frequency and contribute to the leg saturation as the next step occurs inside a not fully damped region. For this reason, a small step amplitude is easier to saturate when facing opposite forces.
Minimum step amplitude is defined as a limit value where, below it, the carrier just swings. Normal load (F_N) has a direct effect on it.
The minimum leg amplitude can be calculated by the following equation.

$$x_{\text{lim}} = \frac{\mu_{sta} \cdot F_N}{\sigma_0} \qquad \textbf{Eq. 5-3}$$

σ_0 is the tangential stiffness, which for a contact between a sphere-plane, can be calculated using Eq. 3-8 to Eq. 3-10. The behavior of the jump-back size in function of an applied normal load can be visualized in Figure 5.12.

The observed characteristics from simulations and experiments of high-preloaded stick-slip actuators being driving against an opposite load, are now presented:

- The size of jump-back (keeping the same friction characteristics) depends on the normal load and the direction of the force acting parallel to the carrier movement. It is independent of the leg amplitude. A small step does not lead to smaller jump-back.
- The smaller the step size is, the easier it is to reach the saturation region and the lower will be the maximum driving force. Higher leg amplitudes are better. They bring also higher driving forces, as for example, when working in scanning mode.
- Through simulations, it has been observed that the best normal load could be determined setting the saturation point to match the target force (maximum driving force). The best result is found matching the slip phase. Matching the slip phase is slightly better than matching the maximum load, with the advantage of providing a power reserve for driving.
- It is important that the contact pressure between foot-carrier stays below a certain limit[46] (below the maximum Hertzian contact), to avoid excessive wear or permanent deformation of the interface.
- To reach the targeted driving force, one option is to increase the number of actuators or the leg movement amplitude.

The last presented item is difficult to be implemented once the device is built. Therefore, a stick-slip model, as presented in Chapter 3, helps to verify if the actuator will fulfill the project requirements. Determine or set the best-driven characteristics for the actuators can be done experimentally if the normal load can be changed.

[46] For a contact point (sphere - plane), an easy calculation is to stay at 35-40% of the Brinell hardness.

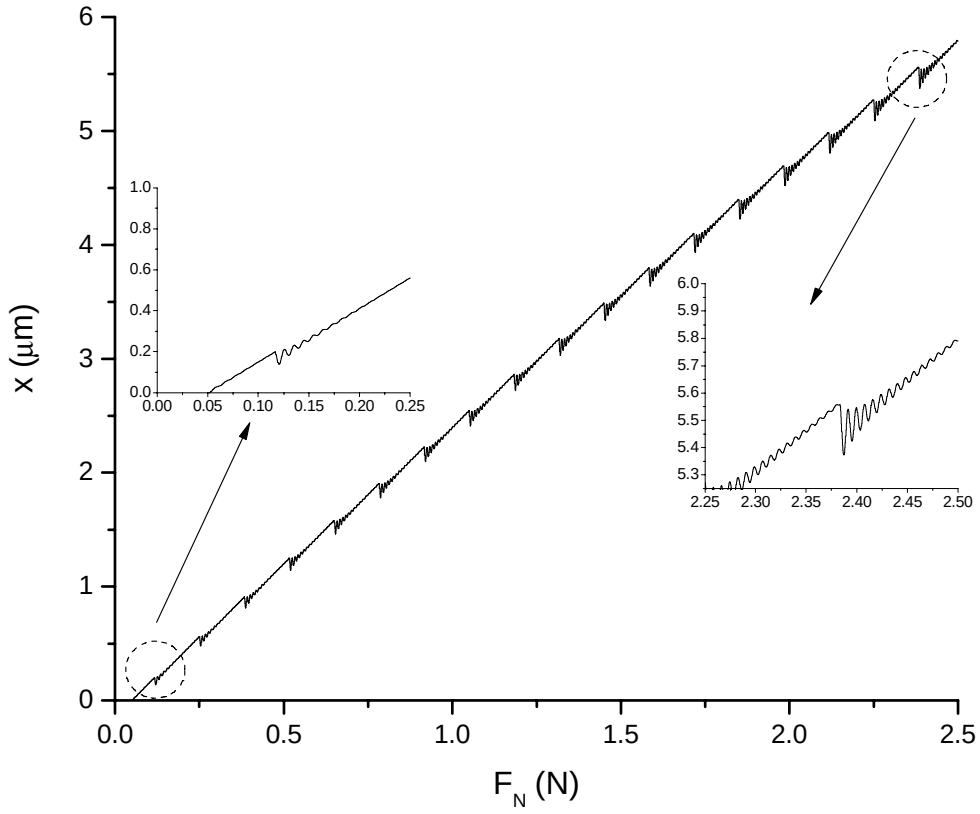

Figure 5.12:Simulation of the jump-back size in function of an increasing normal load.

The interaction between normal load and jump-back is complex, making difficult to find a single equation that can output the best normal load for a desired driving force.
The simulation presented in Figure 5.13 helps to understand how a one-leg system[47] behaves as the normal load is increasing monotonically in function of time and the carrier is under action of a crescent external force (as a spring).
If the static friction is not high enough, the carrier will start to slide already during the stick phase (beginning of the graph). In this case, the driving load stays constant and equals to the F_{coul}.
The best maximum driving force, for the simulated conditions, is obtained with a F_N around 1.5N. This means that the maximum driving force for this system should not be more than 0.17N (F_k read at the slip phase when F_N = 1.5N).

5.2.4.1 Finding optimal conditions through simulations

However, the test above is not a handy simulation for finding the maximum driving force with minimum jump-back, as it will depend on the simulation conditions and since the F_N rate (linked with the variable time) and the K_{spring} must first be determined.

An optimization model requires testing several F_N up to their saturation point (K_{spring} is kept constant) and observing the maximum driving force. The higher slope will be detected under the condition with less jump-back. Unfortunately, this method requires several tests (interactions) until reach the optimal parameter.

[47] 2mm radius sapphire leg against a steel flat plane – μ_{stat} 0.3, μ_{coul} 0.1

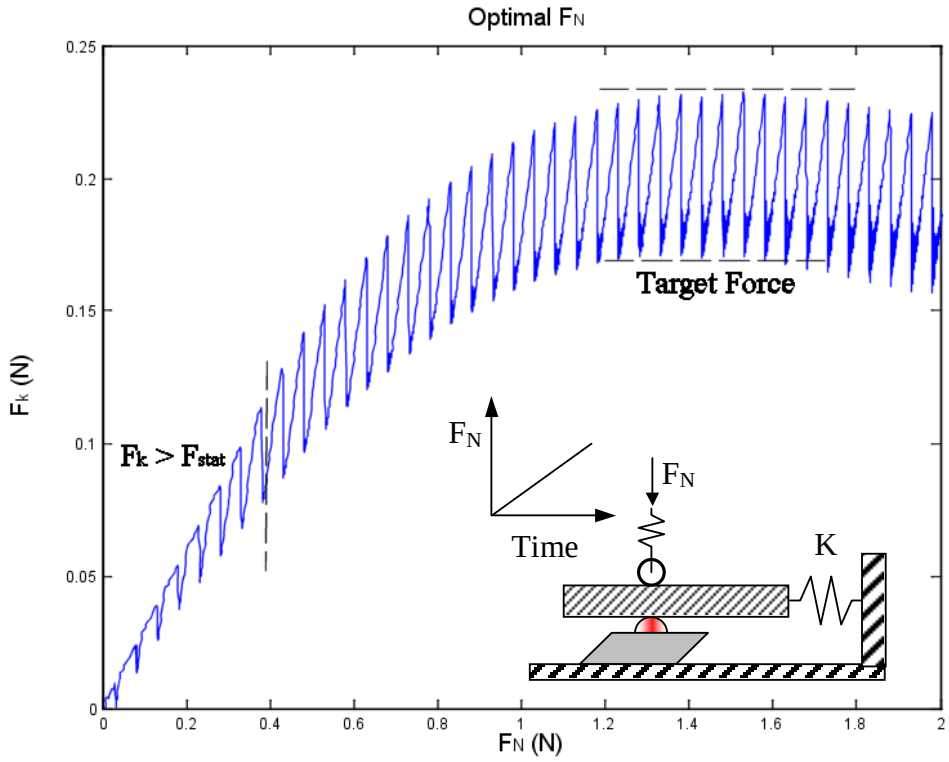

Figure 5.13: Drop in load as F_N increases. Simulation conditions. 100Hz driving frequency, $_{spring}$: 0.2N/µm, Leg amplitude: 400nm, F_N rate: 5N/s

The procedure has been performed manually, using a K_{spr} = 0.2N/µ for the same conditions as in Figure 5.13. The maximum driven force with smaller jump-back has been found at F_N=1.2N. The driving forces, at the saturation region, have been calculated as 0.17N for the slip phase and 0.23N during the stick phase.

The simple model utilized in Figure 5.13 cannot output an optimal value as F_N has been left to increase in function of time. Thus, if some constraints are applied (F_N tested one by one), the model can find the optimum parameter.

If the system already exists, it is possible to obtain experimentally the optimal F_N.
However, at the design stage, it is necessary to verify first if the setup can reach the target load. Only after, an optimization can be performed. Frame, Sample stiffness (or the combination of both) and the target load are simulation inputs.
In addition, increasing the system's stiffness decreases the leg amplitude (as the piezo acts against a spring). If the stiffness is known in advance, the effective leg displacement is calculated as:

$$A_{leg\_k} = A_{leg} \cdot \frac{K_{piezoleg}}{K_{piezoleg} + K_{spring}} \qquad \textbf{Eq. 5-4}$$

For simplification purposes, the leg amplitude has not been dynamically compensated during the simulations above (making the verification of the results easier). The piezo stiffness is calculated in function of its physical dimensions ($w_x l_x h$) and its parameter S^E_{XX} that in reality is the inverse of the actuator Young's modulus measured in the displacement direction. The specific stiffness equations are found on the manufacturer of each piezoactuator. For example, for shear piezoactuators, it is calculated as:

$$K_{shear} = \frac{wl}{S_{55}^{E} h}$$ **Eq. 5-5**

An optimization example in indentation

A perfect indenter system (no frame compliance), working horizontally, has been simulated (Figure 5.14). Reaction force arises exclusively from the sample. The target material is Fused Silica. The indenter uses four legs working in parallel, each one having the same characteristics as presented in Figure 5.13. The target indentation force is 0.5N.
For a driving force of 0.5N, each leg has been set to provide a maximum force of 0.125N in saturation mode (slip phase). Through simulation, an optimum F_N around 0.7N over each leg has been determined.

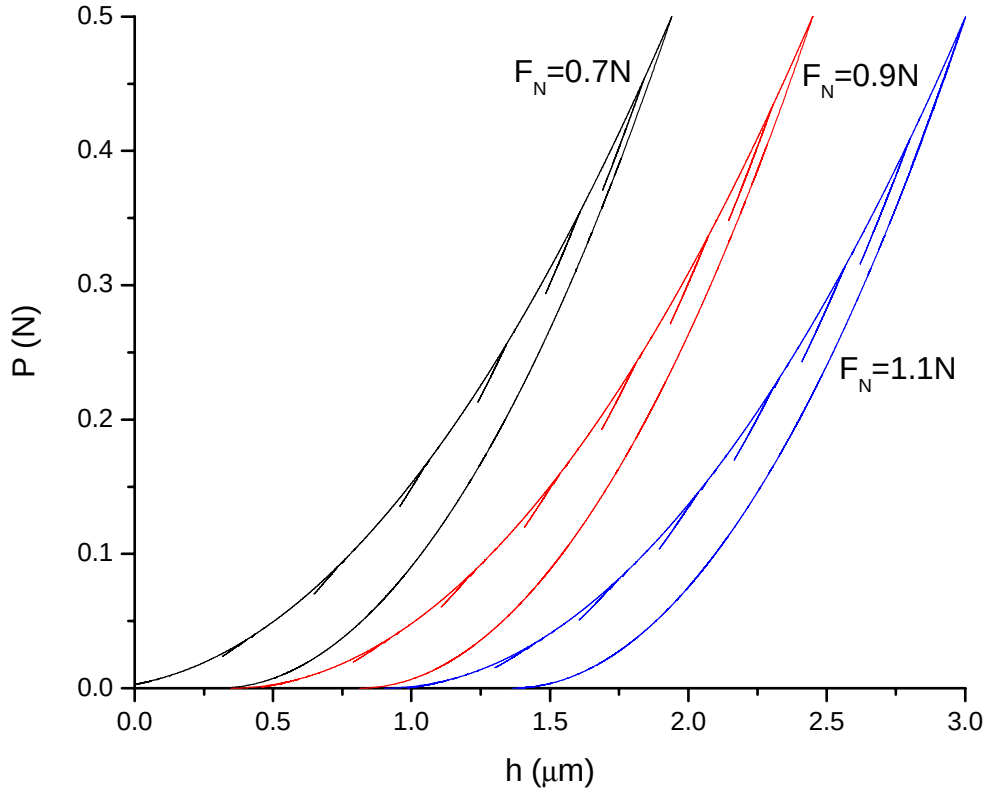

Figure 5.14: Simulation of a Berkovich FS indentation with F_N varying from 0.7N (optimal) to 1.1N. Curves are shifted to provide a better visualization of the jump-back.

A close analysis of the P x h graph and the *h* x *Time* graph (not presented here) has shown that the jump-back has increased in function of F_N. At F_N = 1.1N, one step more than the first situation has been necessary to reach the 0.5N load.
As an additional information, a F_N=0.6N has output results similar to the optimal F_N. The jump-back increases up to a F_N around 0.4N where the carrier could not reach anymore the target load (0.5N).

5.2.5 Using an external force

The third method to reduce the jump-back during indentation requires a more mechanical approach, as it relies on externally generated forces.

For in-situ indentations, it is necessary that the indenter stays tilted, related to the SEM column, to provide a view around the indenter tip. For each type of tip, there will be a minimum tilted angle (face or edge) for visualization (see Figure 2.13 and Figure 2.14b). As the carrier has a mass, a part of the weight will be used to balance the reaction force.
The force generated is calculated by $m_c g \sin\alpha$, where m_c is the total carrier mass and α is the tilted angle ($0 < \alpha < 90° - \theta$). θ is the tip face or edge construction angle (Figure 2.13). The gain is, however, not high. For the example mentioned before (a 20g carrier) and a Cube Corner tip, a tilted angle of 20^o will output a constant force of 68mN to be used during indentation, compensating in 13% the indentation load.

A more active solution is to apply an external load to compensate the reaction forces arising from indentation, for example.
Tunable springs are normal solutions to compensate weight in actuators that need to move a mass against gravity. To design a system that can store enough energy to compensate the maximum applied load (even as simple as a screw-spring system) is not so trivial, if the reaction forces change. An excessive stored energy will make the carrier jump forward at the beginning of the indentation and finally the unloading will contain the jump-back.
This last drawback has attenuations. Unloading is elastic and reloads in this phase seem to be less problematic and will occur less often, as the unloading path is smaller due to the plastic material deformation. Traditionally, the unloading phase is also faster than the loading. This solution needs different external loads being applied during the entire test.

A possible concept is to use a double carrier connected through a flexible joint. This elastic connection contains elements that can store energy for the main carrier and could have damping elements to suppress vibrations arising from the main carrier (Figure 5.15). Ideally, each carrier is driven by one channel (a passive system is possible but less efficient). If a load measurement system is present in this connection, an active compensation system can be implemented.

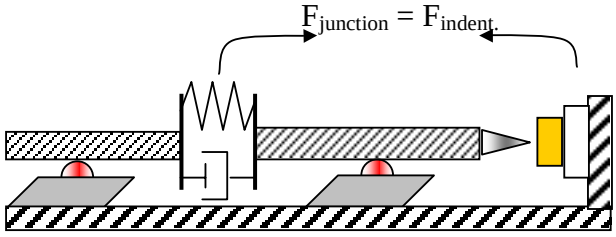

Figure 5.15: Concept of double carrier and active compensation

This solution goes beyond stick-slip optimization, adding more complexity onto the system. The fact that it will need two channels is not the main concern, but rather the need of an active control and more sensors. The idea can be simplified if the goal is a partial, rather than a complete compensation.
As an example, a first indentation can be realized with both carriers at (nearly) the same speed to analyze the size of the jump-back at the maximum indentation load. After that, a simple calculation is done to determine how much the spring between both carriers must be compressed for compensating the load during the indentation time. Thus, a ramp velocity is applied on the second carrier during the next indention.

The end of each indentation is the input parameter for the next one. The setup realizes a post-processing of the measured conditions and is not in real-time. The implementation is simpler but less efficient than a real-time system.

5.2.6 Using an extra actuator in series

If an extra actuator (as a stack piezo) is placed between the indenter tip and the carrier, the jump-back can also be minimized. This is an option that does not require a new driving channel if the extra actuator amplitude is left constant, making it an option for systems where the jump-back size does not change considerably (as positioning objects). This concept is demonstrated in Figure 5.16 and Figure 5.17.

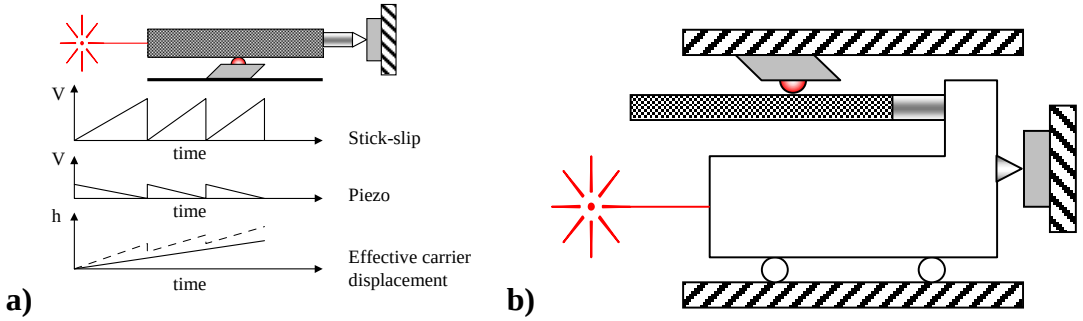

Figure 5.16: Concepts of an extra actuator in series

For a dynamic compensation (as during indentation), a second channel is required to increment or reduce the amplitude of the serial actuator.

If the measurement system targets the carrier (Figure 5.16a), it does not measure the effective tip displacement, as the carrier displacement is partially subtracted by the actuator retraction. Except if it the serial actuator has its own measurement system. On the other hand, if the measurement system and the tip are placed in a secondary carrier (Figure 5.16b), the serial actuator does not need to be instrumented.

Figure 5.17 shows the result of an experiment using a stack piezoactuator in series with the carrier (as present in Figure 5.1d). The maximum applied voltage has been left constant during the entire test. Measurement shows that the carrier movement has not been affected during the jump-back of the intermediate piezo (not shown in the picture). The inset graphs show details from the saturation region. Most of the load registered in each compensated jump-back (P_Comp) has had its origin from the intermediate piezo vibration and there has been a possible delay between charge/discharge of the stack and the shear piezo. Suppressing this high amplitude and frequency component could reduce four times the unloading size during slip (as measured from the graph at the saturation region), showing thus the good potentialities of this compensation. More work is still necessary to verify the best procedure for this option of compensating jump-back.

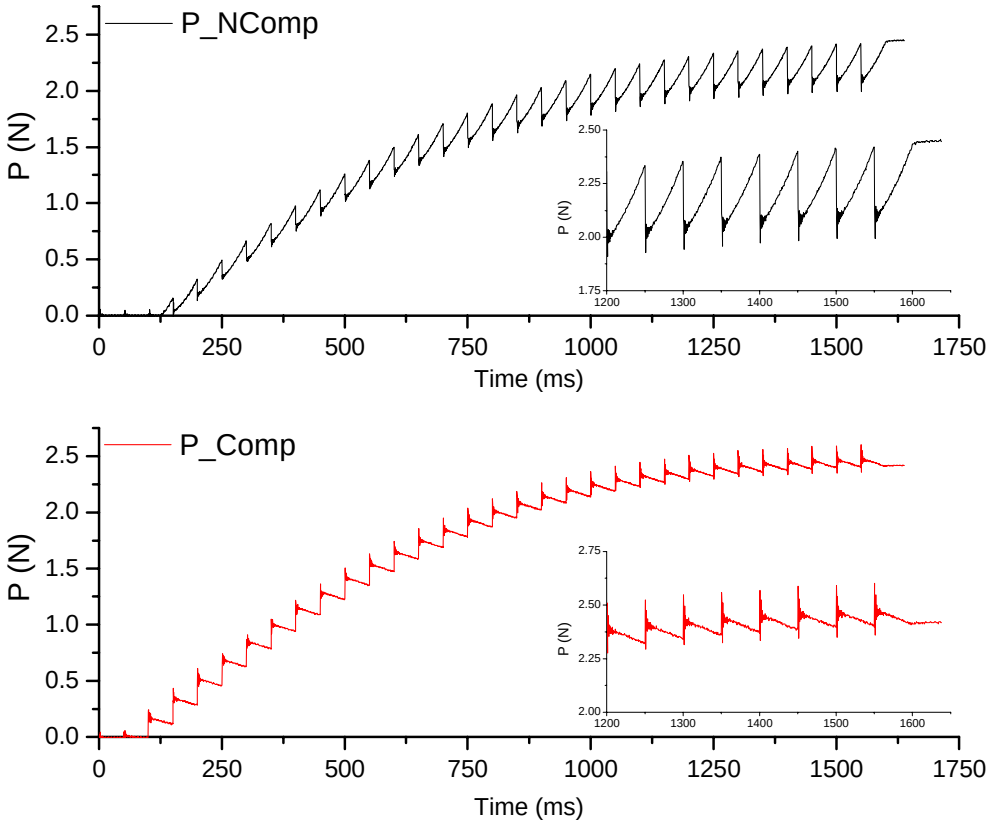

Figure 5.17: Measurement without (P_NComp) and with (P_Comp) jump-back compensation through a serial actuator. Inset graph shows with more detail the drop in load at displacement saturation.

5.2.7 Conclusions about the presented techniques

Four techniques to reduce the amount of jump-back present in stick-slip have been presented. The focus has been rather on the compensation of variable forces acting against the driving force than on the compensation of constant loads, as for example lifting a weight.

The first technique is to apply the correct normal load over each actuator. This also implies a determination of the correct foot-carrier contact (material selection). Lower friction coefficients are also preferable, as the x_{lim} is lower (Eq. 5-3) and induces fewer vibrations. However, this also means that a higher F_N will be necessary to reach a set driving force. However, there are more gains reducing the friction coefficient (results observed during simulations).

The models can indicate the maximum driving load with smaller jump-back or they can show the maximum driven load where the amount of jump-back is be too high for a given application.

Legs could be set to work in phase, following one of the driving modes presented in Paragraph 5.2.3. This implementation only needs changes on the driving circuit, without any major design modifications. After that, an optimization can be realized to fine tune the carrier driving.

Actuators in series could compensate the displacement or generate an external force for complete or partial suppression of the jump-back. An external force is also generated by the gravitational vector, but its contribution is small. An active compensating system can be implemented. However, an additional effort in control system developments and design changes will be needed. As mentioned before, the more system gets complex to bypass the feeble points of using-stick-slip in indentation/scratching, the more attractive other actuators will be.

Figure 5.18 shows a simulation[48] of Fused Silica indentation with a Berkovich tip in two conditions. Condition *a)* has F_N over the actuators optimized for a target load of 0.5N. Condition *b)* Optimal F_N plus using two pairs of legs (2+2) driving with 50% shift to each other. The indenter has also been tilted in 20°. The combination of reduction techniques shows a visible reduction of the load drop associated to each slip phase.

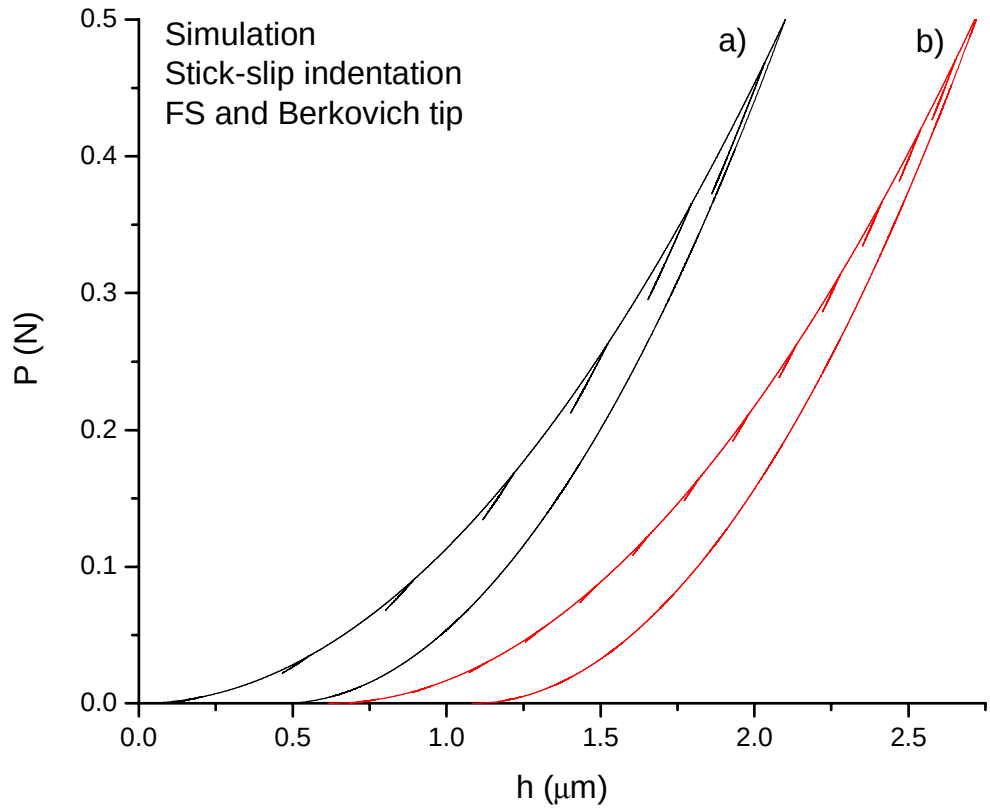

Figure 5.18: Simulation of Fused Silica indentation using stick-slip. a) F_N set for optimal conditions (for a max 0.5N load). b) The indenter has been tilted in 20° and each pair of legs has been driven with 50% phase shift. Curves have been shifted for a better visualization.

[48] Same setup as Figure 5.14.

5.3 A compact test platform for in-situ indentation and scratching

In this chapter, the design aspects will be studied, from the specifications up to a catalogue of solutions, the step just before the final design. However, a particular approach is utilized. As the instrument has been designed at early stage of this thesis, a best approach now is to discuss the utilized solutions, its evolutions and finally to propose new ideas. Valuable feedback from material science researches, as well as new fields where the SEM indenter has been applied, have originated new ideas and improvements, since the instrument has been put in operation at EMPA-Thun.

5.3.1 User requirements

The compilation of project requirements is based on the client needs. The 'client'[49] is a designation of those involved with the 'product'. The case of the compact platform includes the final instrument user (called external client) and those involved in the instrument design, production and integration (called internal client).
The compilation has been realized at an early stage of the thesis, during ROBOSEM project [15]. The requirements below have been obtained through material researchers experienced in nanoindenter devices (operation) and SEM users.

- Compatible with the available SEM
- Easy installation
- Easy Operation
- Manual or Automatic operation
- Good sample positioning
- Compact
- Possibility to use *MTS* tips
- Working with load or displacement control
- Ability to work with different samples sizes

The initial requirements have been found to be very similar as the ones desired for any other indenter. This effectively speeds up the important process of understanding and interpreting the needs of the *external clients*. The wish was to have a small version of an indenter working inside a SEM, with similar performance and operation as a commercial indenter.

External clients have had no tight requirement for manufacture. The instrument has been left free to be produced in different places. Nevertheless, special attention has been given to some design parts. Examples are moderate fabrication tolerances, affordable costs and the use of direct-from-the-shelf parts. To improve the integration and speed up the design phase, existing equipments available at the installation place (EMPA) have been utilized. This has been the case for electronics and sensors from other material characterization instruments (as the Push-Out device, tensile and bending tests).

Once the most important points for the end user have been identified, the next step has been a more tangible description of each term. In this stage, the specifications have been quantified as target values (project specifications).
Important points have been the compatibility with the target SEM and the facility to reach precisely any point of a sample to realize the test. Operational flexibility has

[49] For this case, the external clients have been the researchers from the Nanomechanic group at the EMPA-Thun, while the internal clients have been those involved during the design and integration phase – The Laboratory of Robotic System (LSRO) at the EPFL.

been more important than setup, test speed or ability to realize several tests in sequence (test automation).
Yet, the first specifications (obtained during the ROBOSEM project) have still been based on the specifications[50] of commercial nanoindenters, as can be seen in Table 5.4.

Table 5.4: Project Specifications

Sample positioning (coarse) •Range: X: ± 10mm Y: ± 10mm Z: 30mm	Scratching •Normal force: 1mN – 100mN (50nN resolution) •Lateral force: 10% of the N. Force range •Depth: 15μm (1nm resolution)
Sample positioning (fine) •Resolution: X,Y: 5nm	•Scratching length: 10nm - 100μm •Scratching direction: X-Y
Indentation	Max sample size/weight:
•Force: 10nN – 100mN (1nN resolution) •Depth Range: 15μm (1nm resolution) •Velocity: 1nm/s - 1μm/s	•10x10x10mm – 20g

These requirements have later on been modified, not only due to the difficulty to find small and SEM compatible sensors (at that time) that have been able to reach the project specifications but also due to the difficulty to visualize dynamic tests (in-situ indentation and scratching) at very low loads. Thus, the load resolution has changed to μN at the same time that the range has been increased, taking profit of the load cells available for the design.
The actual specification of the SEM indenter is summarized below, based on the noise floor level values.

Standard configuration

- *Indentation force*: 0.5, 1.5, 10, 20N (changing the load cell).
- *Load resolution*: 0.1mN up to 1mN.
- *Max indentation depth*: 20μm.
- *Indentation resolution (Piezo)*: 20nm (Close loop), 7nm (Open loop).
- *Frame stiffness*: 0.2 up to 1.5N/μm (depend on the load cell).
- *Sample positioning range*: X: 10mm, Y(PZT):20μm.
- *Sample position resolution (Op. loop only*): X: 100nm, Y (PZT):7nm.
- *Max Sample size*: 15x15x10mm.
- *Max Sample weight*: limited by the load cell range.

With Y-stage (stick-slip)

- *Sample positioning range:* 6mm.
- *Sample position resolution (Op. loop only):* 100nm.
- *Max Sample size:* ∅ 8mmx5mm - *Max Sample weight:* up to 10g.

With turning stage:

- *Sample positioning range:* 360°.

[50] A good compilation for specifications of nanoindentation test instruments is found on Chapter 11 of the Fisher-Crips book [6].

- *Max Sample size:* ∅: 10mmx5mm - *Max Sample weight:* up to 10g

5.3.2 The SEM indenter, a design review

The first design has taken in consideration some of the systems available at the end-user place (EMPA-Thun). This has included the SEM (A tungsten filament Zeiss DSM 962 model) and its chamber accessories, the load cells and the acquisition system.
The available chamber size, the electron column design and the built-in sample positioning systems have been the physical constraints. The ambient conditions (type of vacuum) and electromagnetic considerations has been the following step to correctly select the construction materials and the sensors/actuators. A virtual model of the SEM chamber and the instrument is presented in Figure 5.19. The first version had limited sample positioning characteristics. A manually operated *X* axes, using an available feed-through actuator (a knob) installed in the SEM door and a *Z* axes operated using the Push-Out[51] instrument [9]).
A first modification has been the installation of a stick-slip actuator (a single leg) over the X axes to replace the knob-based actuator. The knob actuator has then been used to drive the *Z*-axes (a spring preloaded flexure table). Removing a Z-axis actuator has improved the instrument frame stiffness and shortened the working distance, as the instrument can be placed close to the SEM objective lenses. This has improved the image quality. This modified version is shown in Figure 5.20.

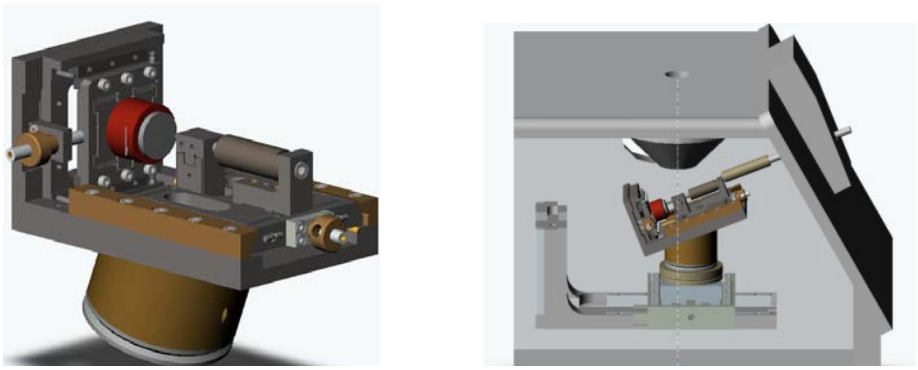

Figure 5.19: First operational version of the SEM indenter.

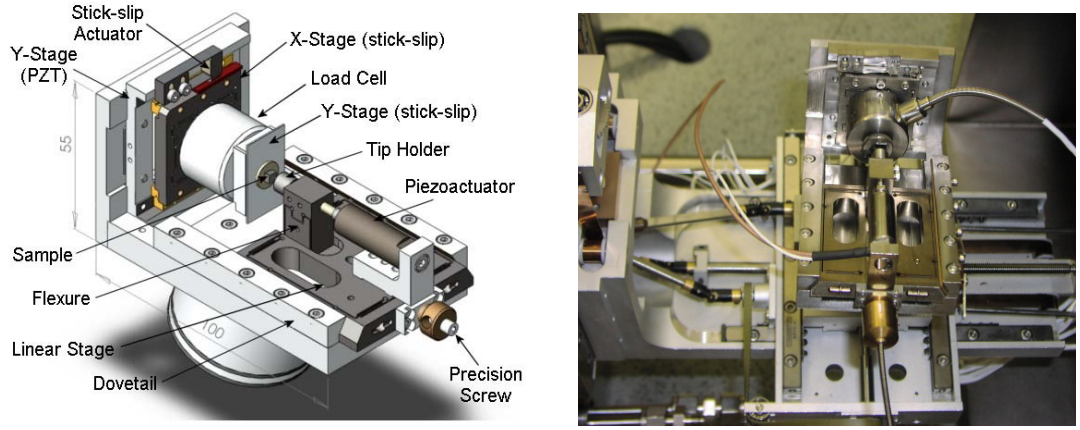

Figure 5.20: Actual SEM indenter and a picture of it installed in the Zeiss DSM 962 SEM

[51] The Push-out test instrument has been developed by Touchstone labs. The tip, used to characterize fibers bonding resistance is driven by a lead-screw connected to a step motor located outside the chamber having a theoretical step resolution of 0.06 μm with a maximum 20lbs driving force.

5.3.3 Instrument subsystems

The main function of any indenter can be summarized in one single action:

- To drive a tool into a specimen

And for scratching

- To drive a tool into a specimen and to create a relative movement between both

It is not surprising, that this function, called *global function* in the design stage, can be shared with very distinct devices, as for example a machine tool[52]. The *global function* is the most abstract function that describes what the device needs to do.
The next step is to divide the main function in sub-functions as:

- To install the instrument
- To install the tip and the sample
- To setup the instrument
- To test the sample

Those sub-functions help to translate the main function in a less complex system and then to use a catalogues of solutions – a set of solutions able to fulfill a specific demand (as to hold the sample, to fix the tool, etc).

Each subsystem must be related to one part of the indenter.

- The instrument frame: Holds the remaining subsystems and provides fixation within the SEM.
- The sample positioning system: In charge of holding and position a sample. It also includes the scratching system.
- The indenter head: Holds the tip and provides the mechanism to drive the tip against the sample.
- The measurement system: Can be in combination with one of the subsystems above.

5.3.4 The indenter frame

The frame design is an interactive process, as it will depend on the available size inside the SEM chamber, the desired working distance (WD), and finally how each subsystem is placed over it. Figure 5.21 presents three frame concepts. They should be analyzed in their operational position (tilted).

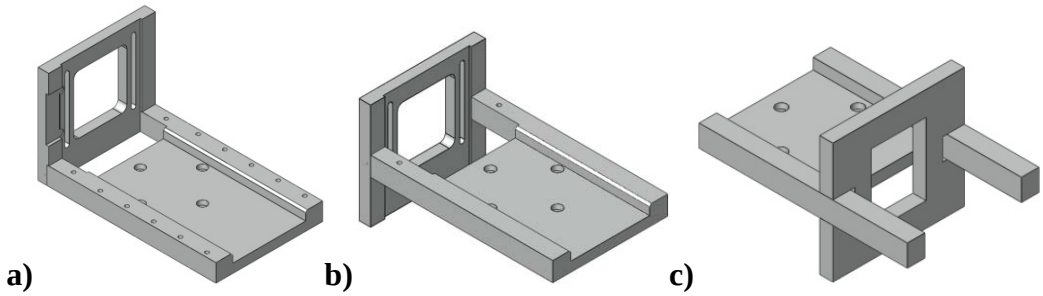

Figure 5.21: Frame conceptions. a) 'L' shape, b) 'T' shape, c) 'X' shape.

[52] And indeed a nanoindenter can be used to crate micro machined structures.

The advantages and disadvantages of each configuration are summarized below, while some conceptual designs are shown in Figure 5.22.

'L' concept	**'T' concept**	**'X' concept**
+ Easy to implement	+ More compact than L	+ More possibilities to place subsystems
+ Free base to install the several subsystems	+ Design more symmetrical	+ More flexibility to integrate subsystems
+ Easy reconfiguration	+ Higher frame stiffness	+ Easy reconfiguration
+ Provides short SEM WD	+ Provides short SEM WD	+ Provides short SEM WD
- Higher frame compliance	- Difficult to add new components	- Higher frame compliance
- Space occupied by the subcomponents	- Difficult retrofitting (subsystems are more integrated in the frame)	- A more complex design than L or T concepts.
- Subsystems are closer to the SEM column		
- More chance of mechanical and electromagnetic interferences		

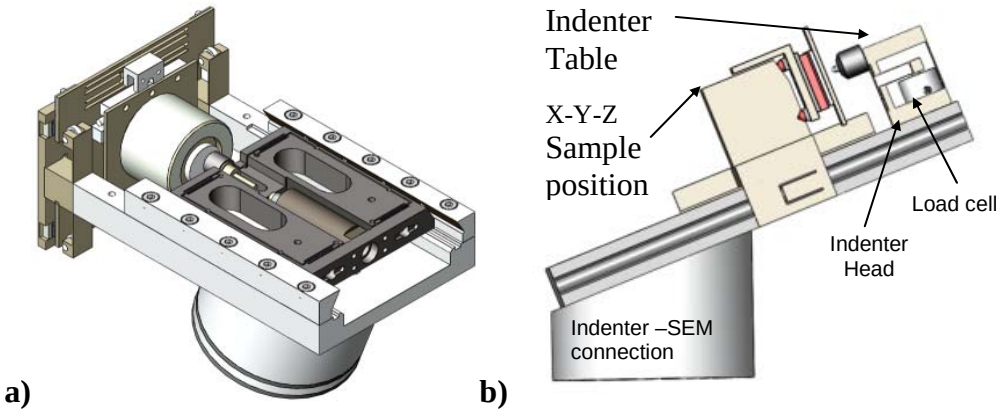

Figure 5.22: Concept of a SEM indenter in: a) type 'T' frame, b) type 'X' frame

These are surely not all the existing frame configurations. Inspiration sources, as an example for brainstorming, are the Coordinate Measurement Machines frames.

5.3.4.1 Frame design and SEM working distance

The indenter frame design can improve the frame stiffness but it will not be alone responsible for the available working distance. Visualizing the 'L' and the 'T' conception inside the SEM shows other constraints (Figure 5.23).
For conception *a)*, the working distance limit is given by the stage that holds the tip (part of the indentation head). Reducing space between the tip and the sample positioning (as using a smaller load cell) shifts the physical interference to the sample positioning system (Figure 5.23c). Configuration *a)* increases the frame compliance (as the path force between the tip and sample is longer), although permits shorter SEM work distances.

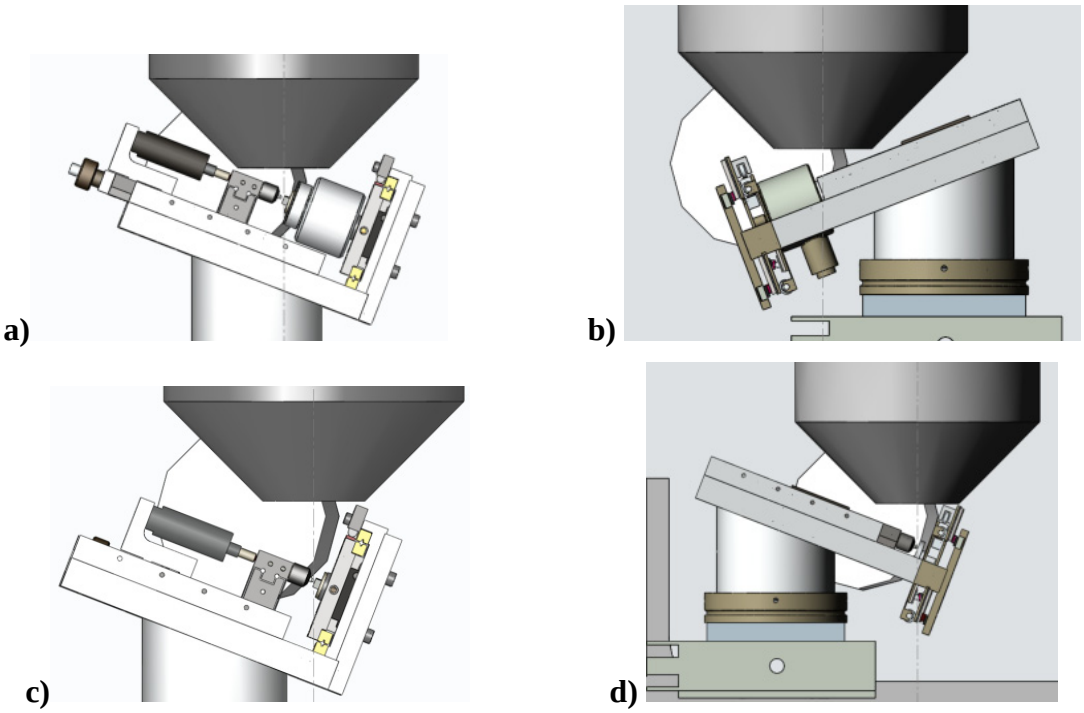

Figure 5.23: Working distance and mechanical interferences as function of frame design

Configuration *b)* has similar constraints. The indentation head physically limits the working distance. Reducing the space between the sample stage and the tip causes mechanical interferences between the SEM column and the sample positioning system. Therefore, the 'L' and the 'T' frame shape have similar constraints. The working distance will depend on the SEM lenses shape and size as well as the size of the sample positioning system. The visualization of the constraints using the 'X' frame shape is more difficult, as it will depend on how the sub-systems are arranged.

5.3.5 SEM indenter fixation

The built-in SEM stage often provides a good degrees of freedom (DOF) to manipulate the samples (Figure 5.24). The standards are X-Y-Z (Z = height) plus theta (rotation around Y axes) and phi (rotation around Z axes). For the case of the DSM 962, the theta range is from 5^{o} clockwise up to 90^{o} anti-clockwise.

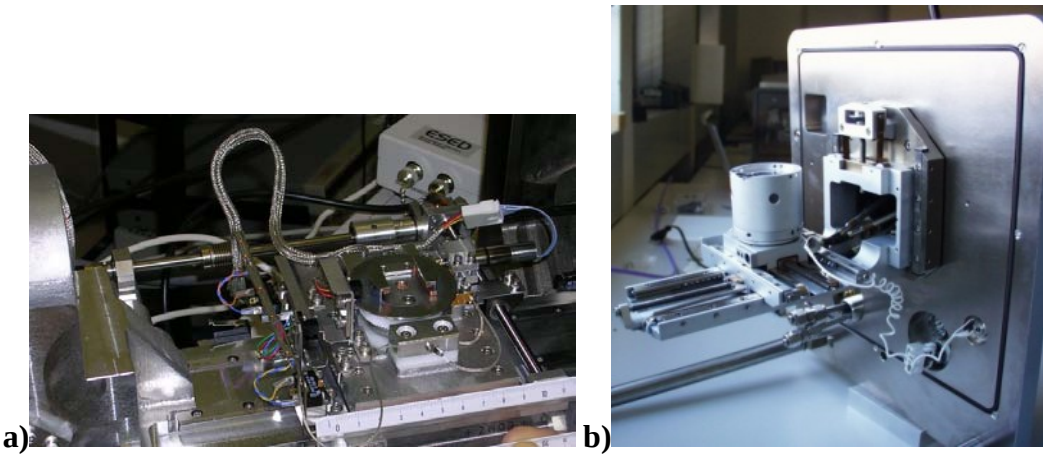

Figure 5.24: Two examples of SEM stages. a) Hitachi S-3600, b) Zeiss DSM 962

The range is mainly guided by the position of the electron detectors placed inside the chamber (most of them at the left side). Tilting the sample is used to improve the sample surface contrast. For the case of the SEM indenter, it is necessary to visualize the tip-sample interaction (the tilted angle will depend on the tip shape).
One solution is to add an intermediate component able to freely tilt the indenter without the need to use the original SEM stage. This can be done by modifying the part that connects the SEM indenter with the SEM stage (Figure 5.22b). The new holding part can be setup to visualize different tip geometries.
The stage coupling part can differ quite a lot from one model to another (disks, V groves, etc.) as well as the range of each DOF. A small stage range limits the physical size of the instrument that can be fit inside the chamber. The working volume (as well as the maximum allowable weight) of the stage must also be considered. Alternatively, it can be completely replaced by a customized stage. This is not a rare situation (as it simply means to change the SEM door), yet expensive, as some manipulators will still be necessary to move the tip under the view region.

5.3.6 The sample position system

A precise sample positioning has been pointed out by the end-user as an important function, as it can take profit of the SEM vision system as a feedback. This means searching for an interesting region with high magnification and then to test it. The visual feedback has partially explained the reason why a built-in sensor has not been considered as a fundamental requirement. However, this has compromises some of the instrument requirement, as for example when it is used for scratching. Controlling the velocity is easier through displacement sensors than by image feedback.
However, the presence of a sensor in the sample position system also means an additional complexity for the design. It increases size; demands more noise consideration (thermo and electric), cabling and so on.

The X-axes of the SEM indenter has followed a standard design (placed over a linear bearing), since it has been decided to place the sample holder and the load measurement system over the sample positioning system. For the same reason, the Y-axes have been designed to be semi-mobile (accessed by screws). The linear bearing has had an easy integration and compatible to be driven by a stick-slip leg. Nevertheless, it has also contributed to add more frame compliance.
To compensate this lack of mobility in Y, a Y flexure table has been included in the X-axes. This table is driven by a stack piezoactuator (20μm range) that is strong enough to lift the load cell and the sample and to realize a scratch in the Y direction.
As the types of material testing got more complex, it became necessary to have more DOF and range for positioning. The next step has been to develop small positing tables to be placed over the load cell. Conceptions of stick-slip driven tables are now presented.

5.3.6.1 X-Y tables.

There are three starting points for designing a table: Range, force and stiffness. The Range will delimit its size; the force is related to the capability to scratch or to drive the sample (or other systems placed over the table). The stiffness is related to the indenter frame.
A kinematic design for a stage means to avoid unnecessary constraints to provide the desired movement.

A stage that respects this rule (Figure 5.25) needs less fabrication tolerances, is easier to assemble and provides a smother movement. If a table has less degrees of freedom (DOF) than necessary, it is said to be under constraint. An under constrained linear axis means that it can have undesirable DOFs.
In the opposite case, an over constrained table has more DOF than necessary. It becomes more difficult to assemble, more dependent on fabrication tolerances and easier to jam. The positive aspect is that it can be stiffer if well designed and that it affords more loads.

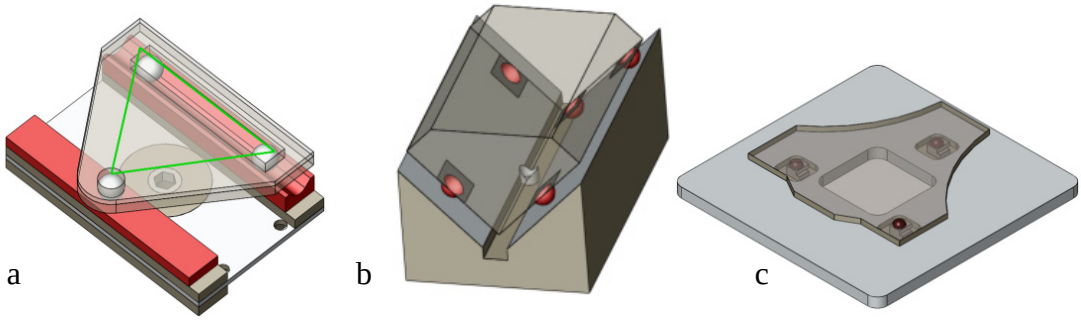

Figure 5.25: Example of kinematics tables. a) two spheres in a V groove and the third one over a flat plane. b) Prismatic base contacted by three spheres in one face and two on the other one. c) Three legs contacting a plane

Figure 5.25*c* shows a 3DOF stage. This is a typical example of how stick-slip actuators can be combined to create a multi DOF stages. Combined XY actuators, as a new kind of push-pull stick-slip actuators [27, 70, 71] developed at the LSRO, can create a flat stage. Placing X-Y sliding bars under the carrier creates a 2DOF stage.
An example of a system with a certain degree of over constraint is shown in Figure 5.26. This solution has been adopted in the SEM indenter for creating a small, yet stiff linear table, placed over the load cell. The main compliance here is through carrier bending and Hertzian contacts in the region of the legs. Therefore, stiffness can be customized through the material (using high Young's modulus materials), thickness and contact interface. X-Y tables are simply built placing both axes perpendicularly to each other.

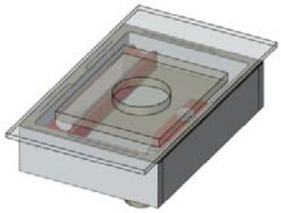

Figure 5.26: A quasi kinematic solution – contact points replaced by a line

5.3.6.2 X-Theta table

A turning stick-slip stage has been designed to provide more measurement options, since turning the sample permits easily to test anisotropic materials. A X-Theta positioning system is not as easy to use as a Cartesian table, but it is more compact. To reach a certain point of a sample, it is necessary to place the tip as close as possible to the table's center of rotation (Figure 5.27). The combination between the Theta and the X axes means that only half of the sample needs to be above the tip. To reach a region at the bottom of the sample, it is not necessary to move it upwards. This creates

a design that places the tip-sample closer to the SEM lenses, improving thus the working distance.

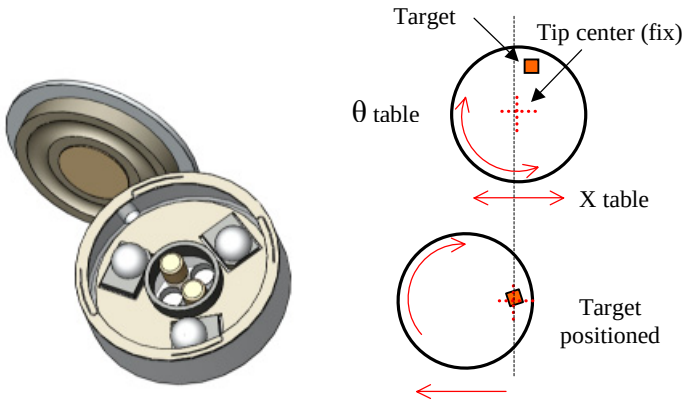

Figure 5.27: Miniature turning stage and principle of operation of a X-Theta table

The kinematic adopted here can be integrated into the table as described in Figure 5.25*c*, creating a compact (and flat) solution.

5.3.7 Scratching table

Reviewing what has been presented in Paragraph 4.5, the stick-slip movement can leave a pattern in the scratch (although observed only inside the wear) that may interfere with the results' interpretations. However, below a certain jump-back level, it is very difficult to spot any pattern. The positioning table must be stiff toward where the indentation force is applied (justifying the adopted design). This also means that the indentation force will be a part of the normal driving force, increasing the friction forces. The two forces will be coupled, thus being a problem to set the optimum driving force (F_N).
Nevertheless, the applied loads in scratching are not so high as used for indentation. Furthermore, the scratching forces are usually a percentage (10 to 50%) of the applied indentation load. As verified, a small variation in F_N (as shown in Figure 5.14) does not change too much the optimal condition. The horizontal stage (X-axes) can thus be left optimized for a given scratching condition.
Finally, the Y-stage can make use of the sample weight to compensate jump-back. If the tip edge or face is set towards the observer, the sample must be driven downwards to provide a free view of the scratching. The backlash movement is thus partially compensated by gravitational force. A scratching stage design does not need to be different to those designed for sample positioning.

5.3.8 Sample fixation

The sample holder must be carefully considered to not add frame compliance. One of the most common fixation methods in commercial nanoindenters is gluing. Thermo glue[53] is often used, as it is easier to remove the sample simply by heating it up. The excess is cleaned up with solvent, as acetone. If the sample cannot be heated, quick glue (Cyanoacrylate) is another option – however removing will demand more time, as letting it in acetone, or, when possible, hitting the sample mechanically.
In the case of the SEM indenter, samples are thermo glued directly over the Y or Theta stage, or over a sample holder that is later on screwed over the load cell. This

[53] Crystalbond[tm] from Aremco Poducts, Inc

last option makes it easy to fix and transport the sample from one instrument to another. Nevertheless, screwing also means an additional difficulty to position the sample correctly, especially when a specific crystallographic orientation is required for the test.

5.3.9 Indentation head

The indentation head (Figure 5.28) is the instrument subsystem in charge of holding and driving the tip. In the present SEM indenter configuration, it is the system with more potentiality in size reduction, if exclusively stick-sip actuators are used to drive the tip.

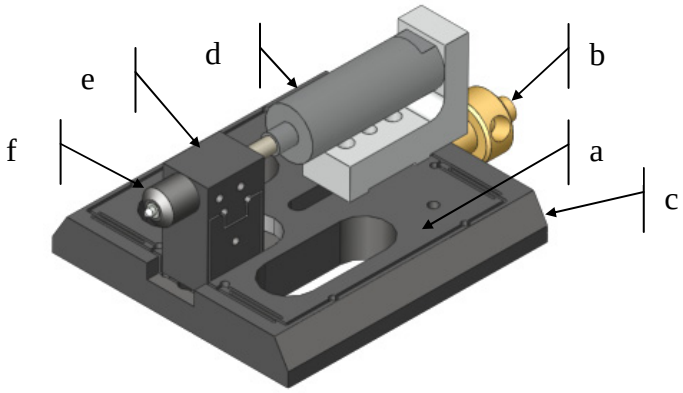

Figure 5.28: Subsystem indentation head

5.3.9.1 Subsystem description

The main subcomponents of the indention head (see also Figure 5.20) are the linear stage (*a*), driven by a precision screw (*b*), the dovetail frame (*c*), the piezoactuator (*d*), the flexure driving tip (*e*) and the tip holder (*f*).
The dovetail shape of the base permits to slide the entire indentation head over the indenter frame. It has been necessary to compensate different heights due to the load cell, the table placed over the load cell and the different sample sizes.
The linear stage (a monolithic flexure based linear table) is thus utilized to make the fine approach of the indentation tip-sample. This inner table is preloaded against the dovetail frame through springs placed internally in the table (not shown). This has increased towards displacement as the precision screw can only push the linear stage.
The precision screw is turned through a flexible cable (yet rigid in torsion) connected to a knob placed at the SEM door. The fine approach is made to let the tip as close as possible to the sample, as the range of the piezoactuator is only in the µm range. This is a difficult step and made by using the SEM image as a feedback.
The piezoactuator is placed between the tip flexure table and the base. The original design has predicted that the piezo could be replaced in order to provide more range. Therefore, an additional mechanism has been included to hold long piezos.
The indenter tip should not be placed directly over the piezo actuators (the moving part of the actuator has low lateral stiffness). A flexure driving tip table has been designed to hold the tip and to provide lateral stiffness.
A simple parallelogram table (*e*) provides a compliant movement in the direction of the actuator and high stiffness in the remaining directions. On the other hand, a parasitic movement is present. As the parallelogram is traveled forward, it will also have a small movement in height (Figure 5.29).

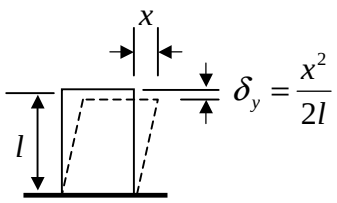

Figure 5.29: Parasitic movement in a parallelogram table. Input *x* creates a movement in height

The tip holder (*f*), adapted to hold MTS® nanoindenter tips, is placed in front of the flexure table. The holder can be turned for setting up the tip orientation related to the sample or the observer (placing the tip face or edge horizontally or vertically). Two screws are used to fix the holder.

5.3.9.2 A stick-slip tip-driving table

The design of a tip-driving table should present similar characteristics as presented in the sample positioning tables. Thus, a kinematic approach will bring the same benefits. Stiffness in the movement direction is very important. Lateral stiffness is thus important when scratching a sample.
The additional component is the indentation force, making it necessary to know where the tip holder must be placed to create an equal force over the feet.
If each foot generates the same driving friction, it is better to have the indentation tip placed at the center of gravity of the forces that, in this case, coincides with the middle of the carrier (Figure 5.30*a*). In the case of asymmetric driving forces, it is necessary to determine the position of the new center (Figure 5.30*b*).

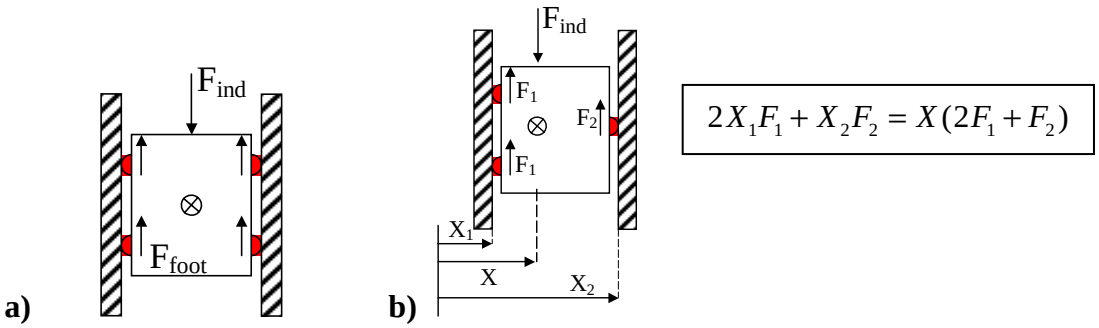

Figure 5.30: Schemes for the reaction force position over the carrier

To receive the force at the correct place minimizes the moment generated over the table. This can induce parasitic movements as jig during the displacement. Making the carrier longer than wider provides a better driving characteristic.
Often it is desirable to explore symmetries during the design. Taking as example the Figure 5.25a, the tip should be placed near the V groove. However, this creates an asymmetric design over the entire indenter, which adds more design restrictions. Still, two simple design modifications can be used.

- The feet must be placed in a way that the friction force at each foot forms a wide base in length and a short width (the log slider principle [72]). This makes the carrier less sensitive to external forces.
- The position of the preload friction force (F_N) has to be placed in a point that generates approximately the same friction forces over each leg.

These are simple options, as kinematic linear tables can face different driving conditions at each set of legs.

To design perfect kinematic and symmetric stick-slip tables is a time demanding task. However, some solutions are directly applicable. One is clearly the linear axis (Figure 5.31*a*) that has served the base for the stick-slip indenter. Note that the **unconstrained DOF** can be utilized for **turning the indentation tip**. For this, it is only necessary to use a combined X-Y leg or to place two shear piezoactuators at 90^o under each foot. For a pure translation the turning DOF can be blocked through the addition of one leg in a V groove made over the cylinder (Figure 5.31*b*). This leg can also be utilized, through a spring system, to apply the necessary preload over the system (see section 5.3.11), replacing magnetic preload.

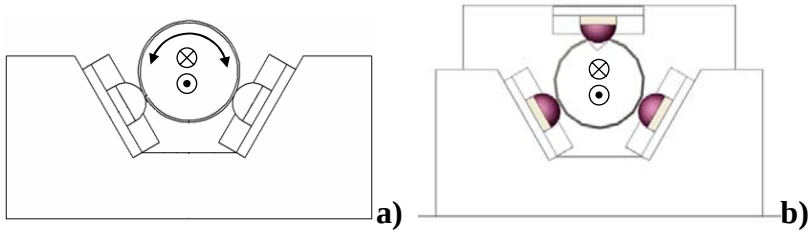

Figure 5.31: a) Kinematic 2DOF axis (4 legs), b) Kinematic 1DOF axis (5 legs)

5.3.9.3 Hybrid designs

A hybrid design means the combination of more than one type of stage or actuation to execute the same movement. An example is a stick-slip devices plus stack piezos. This opens a series of conceptions, including high load indenters and a solution where jump-backs cannot be tolerated. The drawback is more complexity and the restrictions to miniaturize the instrument. Figure 5.32 shows two concepts of hybrid design. The first one is the simple addition of stick-slip legs under the linear stage. The second concept is a more integrated idea. It uses a linear table made of flexures and levers to amplify the stack piezoactuator range (indentation). Stick-slip tables are used for sample setups and scratches.

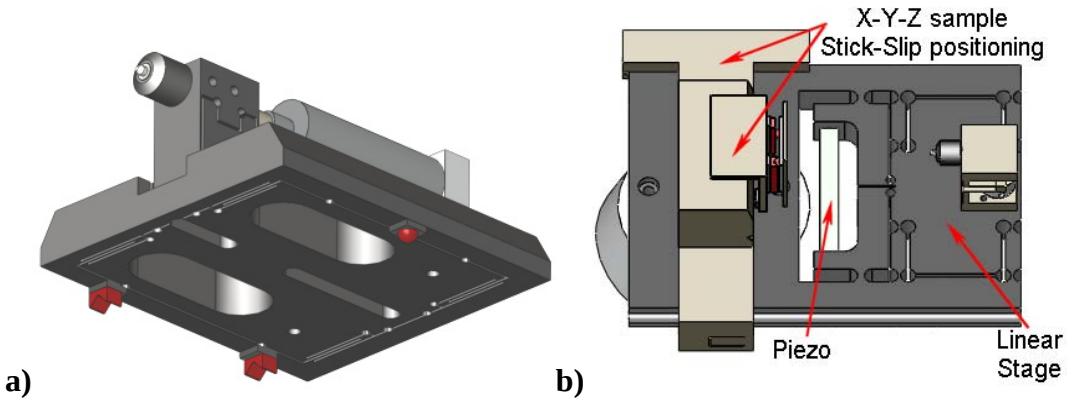

Figure 5.32: Example of combined design. Stick-slip actuators and stack piezo actuators

In a hybrid design (as involving double actuation), the stick-slip actuator is optimized for high holding and driving forces. Jump-back size is no longer an important parameter. For example, the linear actuator of Figure 5.1 has a holding force of 4.7N (Table 5.1) and a maximum driving force of 3N (Table 5.2). This means that the piezo actuator could apply an indentation force of nearly 4.7N over the linear stage before it slides.

Stack piezoactuators and flexure hinges are utilized in micro-nano positioning systems as they can provide resolutions of the movements in the nanometers range. The displacement is still limited by the stack piezoactuator (still it can be amplified several times through special designed hinges). Stiffness and driving forces can be designed to be high (as in the N/μ range and blocking force of several Newtons). Two good references to understand and design flexure hinges are Smith [73] and Henein [74], while the keywords 'Flexure hinges' and 'Nano positioning systems', will provide a good start to find clever designs using piezoactuators and flexure hinges.

Another example of hybrid design is a linear stage (as preloaded linear bearings) driver by an actuator. The guiding and the actuating systems are not part of the same component. They are thus two independent components. The advantage is the use of commercial linear guides (available in several sizes, even vacuum compatible versions) for integration[54] into the system.
Figure 5.33 shows a commercial nanoindenter configuration using this principle. The present SEM indenter X-stage is another example of this design. The piezoactuator is not part of the guiding; it is simply the driving unit.

5.3.10 Load and position measurement systems

5.3.10.1 Load system

In the case of the SEM indenter or any other indenter that has the load-displacement system decoupled, the place of the load system can impose substantial difference in the instrument design.
In the case of the SEM indenter, to leave the load cell and the sample holder as part of the sample positioning system has been a choice because of:

- The size of the load cell. Placing it at the tip table reduces the SEM work distance (due to mechanical interference). In addition, the load cell body blocks the indenter viewpoint. A long shaft to hold the tip is hence required.
- Frame stiffness. The load cell construction is a double plate spring system. This is claimed by the manufacturer to be very stiff for out of plane loads. However, if a long shaft is used, any lateral force will be amplified by the arm moment.
- Sensitivity. Placing the load cell between the piezoactuator and the tip table improves stiffness and shifts the load cell out of the viewpoint region. However, the load cell measures also the tip table stiffness. This value must be used to correct the raw load value. This reduces the load sensitivity. The load system needs to detect the sample response among the force generated when deflecting the tip table.

To place the tip directly over the load cell has been the original solution proposed by Touchstone Research Laboratory [9] in its SEM Push-out device delivered to EMPA-Thun. A commercial nanoindenter from Micro Photonic (*Nanovea* series [75]) is another user of the same principle (Figure 5.33).
High sensitivity load cells are often not very stiff. This contributes to frame with a low stiffness. In addition, the choice where to place the load system makes difference

[54] As Schneeberger small *R type* for integration or the full preload set type ND.

for some applications involving the indentation instrument[55]. Figure 5.34 shows the main difference.

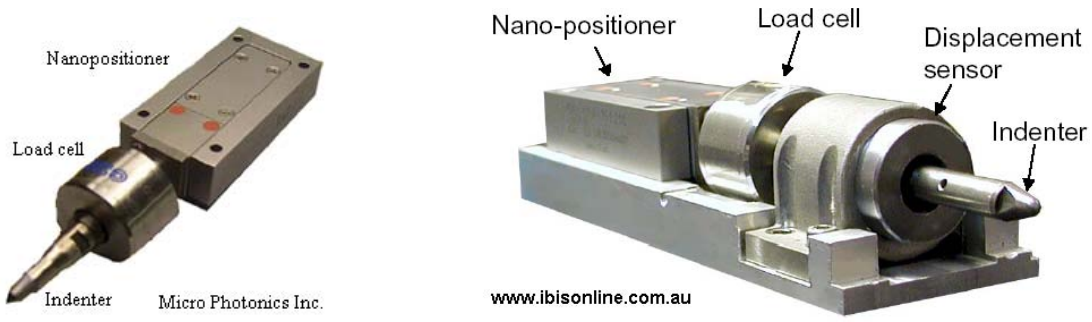

Figure 5.33: Example of Nanoindenter with a tip coupled directly over the load cell

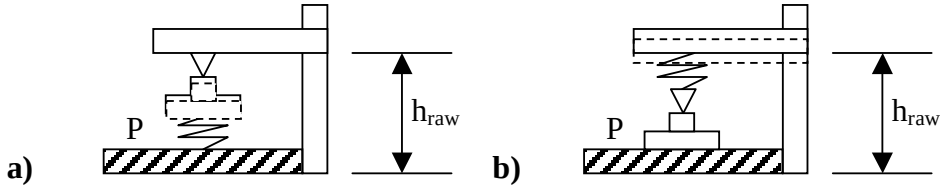

Figure 5.34: a) Load system in the sample system, b) load system in the tip system

In configuration *a)*, the sample is over the load cell (a compliant system). As the indentation is carried out, the sample displaces in the same direction of the tip movement. During a SEM indentation, a repositioning of the view field (using the SEM stage) can be necessary to bring the interest region back to the center of the screen.
If the indentation tip is placed just before the load system (case *b)*, the region being observed is not affected by the load cell compliance and an image correction is not necessary. Note that the measurement reference does not change in both layouts.

To place the load measurement in the indentation head has the following advantages.

- The sample has less compliance under it. More stable platform for visualization during SEM indentation.
- The sample positioning system does not need to hold the load cell. The design gets more balanced as some of the functions are transferred to the indentation head.
- Tips have a standard size and the same sample holder. Samples can have several shapes and sizes. Sample size or weight is not limited by the range of the load cell, as it is today the case with the SEM indenter. It will only be limited by the sample positioning system.
- The indentation force is always measured at the same point. Placing the sample over the load cell can lead to off-axis errors if the force is applied out of the load cell center. The entire load-displacement measurement chain can be located on a single line.
- Placing the lateral measurement system at the indentation head (scratching force) can have easier calibration as the distance between the tip and the measurement system does not significantly change.

The advantages to have the load cell under the samples are:

[55] As for example, micro-pillars compression, as it will be presented in Chapter 6.

- The load system works under gravitational preload. A compression load cell is enough.
- Load is not induced when the tip is being setup (being moved, as example using stick-slip actuators). The systems only start to register load when the contact occurs.
- The indentation head can be built as a very stiff part and the load cell can have a different stiffness depending on the load range or the necessary sensitivity.
- There is more space and less physical constraint using the sample positioning system to hold the load cell.

Designing the indenter head integrated with the load measurement systems brings on average more advantages. To have a stiff indentation head (in any direction) and still keep up the required load resolution, can be achieved if the load system is a part of the body. Thus, the head is designed including the best place to install the strain gauges (metallic foils or semi-conductor types), which will be used to measure load.
Another option is to use a specific (commercial) load cell and try to integrate it into the indentation head. Figure 5.35 illustrates the concept.

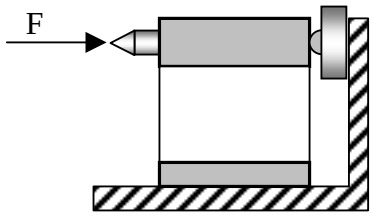

Figure 5.35: Concept of a load measurement system

As the flexure table is driven against the sample (it is a passive component), the reaction force will make the flexure parallelogram move backwards, compressing the load cell. An immediate advantage is the significant reduction of the parasitic movement described in Figure 5.29.
However, now the load cell loses sensitivity as it acquires the force after a spring system (the flexure table). In this example, sensitivity will be recovered lowering the flexure table stiffness in the direction of the movement. The final head stiffness is a combination of the table coupled with load cell (as they work in parallel). Unfortunately, the final solution will not be as simple as represented in Figure 5.35. Some important details must be taken into account. The connection between the load cell and the table must be as stiff as possible. Inside the SEM, the head works downward (Figure 5.23). The combined tip and table weigh and the stiffness of the load cell will determine the dynamic of the indentation head - an important consideration if the entire head is driven by a stick-slip actuator (similar as presented in Figure 5.32*a*). As can be observed, the conception of the load system will have and will influence the design of other indenter systems.

5.3.10.2 Position system

The place of the measurement system has a direct influence on the instrument's performance. Ideally, it should follow the Abbe principle[56] and be insensitive to the instrument frame stiffness. The best place to measure the indentation depth is placing the scale and the reading between the sample and the tip. An example of this

[56] The measured length and the measured scale should lie on a single line.

implementation is the reference ring of the CSM Instrument nanoindenter [76]. This secondary measurement system contacts the sample, providing a differential measurement. Frame compliance and thermo drift are then subtracted from the raw data.
The measurement system from Ibis/MicroPhotonics (Figure 5.33) is another example. It is susceptible to the influence of the frame stiffness. However, the compliance of the load cell does not interfere with the depth measurement.
Figure 5.36 shows another design with displacement compensation. The UMIS nanoindenter [77] uses two LVDTs to measure force (through calibrated leaf springs) and penetration depth. The compliance of the force sensor is decoupled from the displacement. Furthermore, this configuration also follows the Abbe principle.

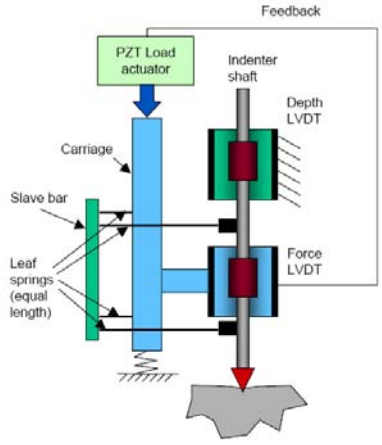

Figure 5.36: Example of decoupling displacement from the load compliance (UMIS nanoindenter)

The actual design of the SEM indenter has the measurement system placed inside the piezoactuator, meaning that the displacement is read in the same line on which the displacement is applied. This follows the Abbe principle, although still includes the instrument frame compliance. For the SEM indenter, a high amount of frame compliance can be decoupled, measuring the deflection of the load cell.
High frame stiffness improves the measurement system. Depth measurement better represents the tip penetration as the frame deformation has a smaller contribution (that can be approached as a noise). The measurement is thus clearer. However, there is still a doubt if the gain in measurement performance is high enough to justify an additional sensor an all the complexity to measure a load cell deflection.

5.3.11 Preload systems

Weight, spring and magnetic forces are the basic systems used to increase normal forces in stick-slip actuators.
A coupled stick-slip system means that friction, inertia and natural frequency cannot be changed independently. Adding mass to a carrier placed over stick-slip legs and working horizontally, increases friction forces, inertia and decreases the natural frequency of the system (more vibrations after slip phase). Normal force can be built to be independent and thus creating a decoupled system. Henceforth, the meaning of coupled or decoupled systems will be used to indicate systems that can have the friction force set independently from the carrier weight.
Some applications (or environments) require completely non-magnetic materials, which makes automatically impossible to use electromagnetic preloads. In this case, a

mechanical preload must be utilized (or, if possible, other non interfering forces, as electrostatics).
A mechanical preload system is built out of springs. A preload part can be active, when it includes an active leg (Figure 5.37*c*), or passive, when it includes a low friction component (Figure 5.37*b, d*). Mechanical preload integration is more complex as it demands more parts and assemblies. Yet, it can be made very compact[57].
Figure 5.37*a* shows a concept of a hybrid preload system where weight and flexures are used together. This concept replaces the SEM indenter X-stage linear bearing and improves its stiffness. Weight gives nesting and preload forces, complemented by mechanical preload through a rolling element placed over flexures (acting as a spring). A strong carrier is required to hold and move the heavy load cell.

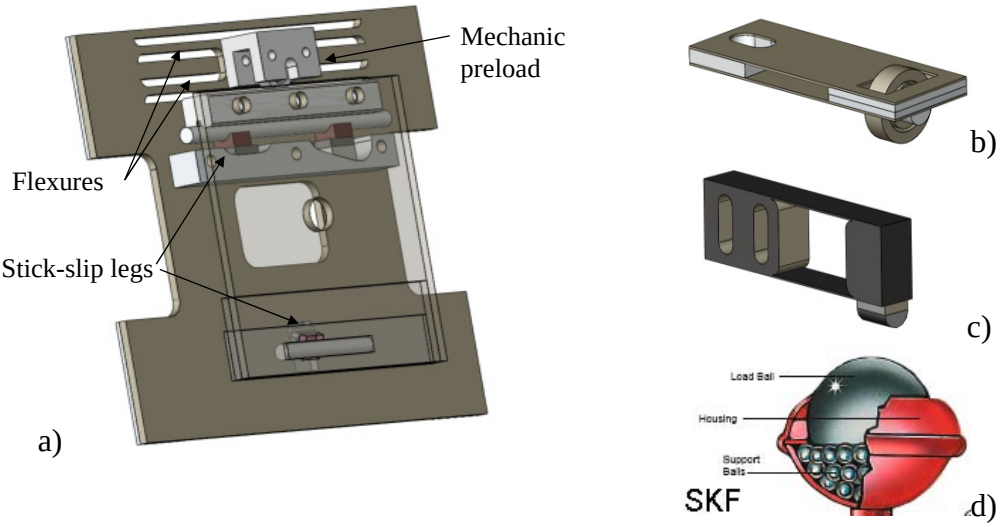

Figure 5.37: a) Hybrid preloaded system. Gravity plus spring preload. b) rolling element over flexures, c) stick-slip actuator over flexure, d) miniature ball transfer (360°)

If some electromagnetic interference can be tolerated, the use of electro or magnetic forces for preload can reduce design and assembly complexity, as well as size.
The easiest way is to make use of permanent magnets. Permanent magnets have been the adopted solution for preloading the small positioning tables placed over the load cell (Figure 5.26*a*, Figure 5.27). As the sample is placed directly over it, a magnetic shielding had to be created.
The magnet preload had to provide enough driven force to lift or turn a sample (jump-back size has not been an issue) and not to interfere with the image quality (being necessary to shorten the magnetic field).
This has been obtained combining two solutions, using magnet with different polarities and making use of materials with high magnetic permeability. How to confine a magnetic field is presented in section 5.4.5.

[57] The HiFla actuator [8] is an example of keeping the preload system as part of the actuator kinematics

5.4 Design for the SEM environment

The term SEM compatible means that a component or entire equipment should work without problems inside the chamber. Without be disturbed by the operational environment (vacuum) or by the electron beam. The reciprocity is also necessary. The device inside the SEM should disturb neither the SEM environment nor the electron beam.
This short review (including Annex III) has as function to help guideline designs for SEM. It mixes information from designs focusing on vacuum environments and practical experiences collected during the development of nano positioning systems and instruments developed to work inside the SEM.

5.4.1 Vacuum level

As the operational environment inside a SEM is vacuum - from $1.33x10^{-3}$ Pa (High vacuum - HV) to $1.333x10^{-6}$ Pa (very high vacuum - VHV), some design aspects must be respected.
The first aspect is related to the vacuum generation – the instrument should not compromise the vacuum level. The second aspect is that the vacuum should not interfere with the instrument's performance. Some design points are now presented.

5.4.2 Outgassing

The outgassing rate[58] is more important in UHV systems ($1.333x10^{-9}$ Pa and beyond) as it can effectively increase the amount of time necessary to reach this level of vacuum. For this reason, UHV compatible components have very particular materials, storage conditions and specifications. This includes, for example, the possibility to bake the entire device under vacuum conditions in order to remove any material adsorbed in the equipment that can contribute to increase the outgassing rate. Equipment designed to target UHV systems are thus more difficult to accomplish.
However, a careful cleaning and correct clean storage does not bring a noticeable improvement for reaching the start operational pressure of a SEM (ex. 0.1 Pa for the Zeiss 962). Yet, following similar procedures in devices to be installed inside a SEM still brings advantages that can be noticed in two different forms.

The first contribution will be to short the time necessary to reach the HV-VHV range (what, anyway, will still take hours), but the main contribution will be for the SEM itself. The materials molecules released during outgassing will be deposited over the SEM vacuum chamber, creating thus a log term contamination (taking more and more time to reach HV-VHV). These molecules (hydrocarbon) dispersed over the vacuum chamber are also broken by the electron beam. Thus, a region being visualized receives layers and layers of impurities, covering details and decreasing the contrast of the image. This situation alone justifies the correct use of low outgassing materials and a design that allows a good instrument cleaning.

5.4.3 Friction changes in stick-slip actuators

In his work, Bergander [27] has studied the friction changes (due to wear) in stick-slip actuator. Using a device developed to study friction in this type of actuator (at normal

[58] See Annex III – Vacuum section, for a definition of outgassing and http://outgassing.nasa.gov for a list of outgassing rate of different materials (adhesives, lubricants, cables, electronic components, etc.)

atmospheric pressure), he has pointed out that the observed wear in the actuator-carrier interface has been a mix between wears originated from sliding and fretting.

Changes in the operational environment, as vacuum instead of normal pressure, can considerably change the wear rate and consequently the friction coefficient. Two basic mechanisms are briefly presented in this paragraph, focusing the foot (actuator) - carrier interface: Molecular attraction between parts and oxide layer formation. More details can also be found in Annex III (*Friction changes in Vacuum*).

It has been shown in paragraph 5.4.2 that equipments for UHV environment need to be backed in order to minimize outgassing rate. An 'atomically cleaned' surface (no adsorbed material) has higher molecular attraction at its surface. Adhesion and cold welding are easier to occur. Thus, if two surfaces are in a relative movement, the UHV increases the friction coefficient and wear rate because the molecular lubricant layer has been removed. This problem is reduced if the vacuum level is not so high, as the case of the one found in the SEM chamber (HV – VHV). Now, the surface is not atomically cleaned. Yet, the lubricant layer degasses, gradually reducing its lubrication characteristics in the foot-carrier interface.
However, the reduction of the interface's adsorbed lubricant layer may not be the main mechanism for changing the friction characteristics. The nature of contact (localized pressure) and the thin layer of lubricant permit a close contact between the surface of the actuator and the carrier. In this situation, the resistance of the oxide layer is more important. For the case of one or more metallic sliding pairs, the oxide layer present in one (or both parts) usually protects them against wear [78]. Each time that the layer is broken, a fresh exposed material re-oxides.
The oxidation velocity depends on the amount of oxidant material present in the environment. It has been shown, for example in [79, 80], that the amount of vacuum changes the properties of the oxide layer (for instance in steel) and consequently the friction. Less oxygen created a thin but tough layer in fresh exposed metal. As the oxide layer increases its thickness, it also becomes more fragile. Chips are formed feeding the wear trace with hard debris. This complex mechanism is described in Annex III (*High Vacuum*).
It has been observed in [79, 80] that the friction coefficient has been reduced as the vacuum has been gradually increased (from normal atmosphere up to medium vacuum) but after, friction has started to increase again for HV to UHV conditions. This shows the need to select a foot-carrier interface that keeps similar tribologic characteristics when working in normal atmosphere or vacuum.

5.4.3.1 Selection of the correct foot-carrier pair

Working in vacuum brings an additional constraint for material selection. A good pair selection should have the similar behavior in both environments.
As it has been mentioned early in Chapter 4, a lower friction coefficient brings more advantages for stick-slip actuators (less vibrations after a slip). Strong changes in the friction coefficient, as the vacuum increases, compromise the optimization of the jump-back size.
Ideally, the selected contact pair should have very close tribologic properties in air and vacuum. This improves the setup and the actuator's life, as it is not being operated out of its optimal conditions set focusing on air or vacuum.
This pair still needs to be determined, as now there is not much experience or available data involving long-term operation of stick-slip actuators in vacuum.

5.4.4 Actuators and sensors in vacuum conditions

5.4.4.1 Heating

Heating generated inside the SEM must be carefully identified during the design phase. Components that heat up can cause diverse problems, as:

- A thermal distortion of the instrument structure what contributes to jam components (easier for over constrained designs).
- They can create thermo drift in the measurement (as in indentation).
- They can contribute to reduce SEM image quality (the sample is moving).
- Difficulty to carry out experiments (ex. E-beam induced deposition using an input gas. The temperature increases the element's vapor pressure making the gas more volatile and more difficult to be used as a deposition source).
- Self damage of the component (out of the operational temperature).
- Long time for thermo stabilization.
- Etc.

The heat source is generated internally (due to component friction) or intentionally (heating up a sample). However, heating is a side effect of devices that need power to work. Examples are sensors and actuators.

The heat will flow from the high temperature region of a body to the lower temperature region. This transfer is realized by three modes [81]: Conduction, convection and radiation.
All the three modes are viable inside the SEM, being *conduction* the most typical mechanism used to dissipate heating from a device inside the SEM chamber. As a rule, the heating source must be minimized or placed outside the chamber. To create a device insensitive to heat generation is a challenging and time demand task that brings several designs constraints.

The actuator or sensor should generate a low amount of heat, which means that it is necessary to have efficient components. A non-reversible actuator has the extra advantage that it does not need power for holding its position (as stick-slip actuators do), dissipating thus less energy.
If heating is still present, the source must be decoupled from the instrument and from the SEM manipulation stage. Ideally, this part could be placed in the SEM chamber (to change heat through conduction), or outside the chamber. In this case, feed-through will be needed to exchange information (sensors) or to deliver the movement (actuators).

Annex III (*Heat dissipation in vacuum conditions*) provides more details about heating dissipation and a practical example of an excessive hating generation caused by positioning sensors utilized in a SEM nanopositioning stage.

5.4.4.2 Sensor calibration and operation

Does the vacuum change considerably a calibration made in a normal environment?
If a sensor has been calibrated having a gap filled with air, it is possible that the parameter changes as the element changes. Normal temperature and humidity parameters are quite different inside the vacuum chamber. In addition, in the case of a

SEM, the electron beam placed over a certain type of sensor could change its behavior[59].
In the case of the SEM indenter, no noticed discrepancy between the calibrated values and those read during the experiment (load cell and piezo displacement sensors, both based on strain gauges) has been noticed. The comparison has been made indirectly, through the Indentation graph. A good overlap between the reference measurements and a corrected SEM indenter result indicates that the load and displacement sensors are in order.

5.4.5 Magnetic systems in the SEM

5.4.5.1 Permanent magnets

Permanent magnets have been used in several stick-slip positioning systems developed for the SEM indenter. Magnetic fields inside the SEM can easily disturb the electron beam. For this reason a device that makes use of permanent magnets have to be carefully designed. A basic review about permanent magnets, magnetic systems and shielding is available in Annex III (*Magnetic systems in the SEM*).

Permanent magnets can have their attraction forces increased by adding special systems (in soft metals) or configurations able to shape up their flux lines, increasing the number of lines reaching the target material. Table 5.5 shows configurations able to increase the basic attraction force (reference, a single magnet).

Table 5.5: Ferromagnetic systems to increase attraction forces [82].

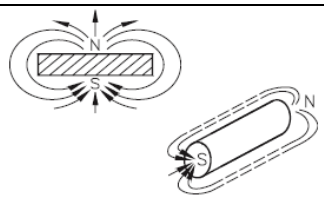 a) Basic configuration F_B=1	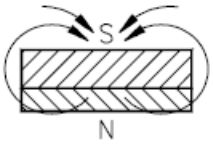 b) Steel pole plate $F = 1.3_xF_B$	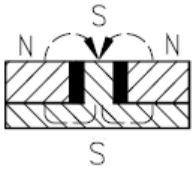 c) Center pole $F = 4.5_xF_B$	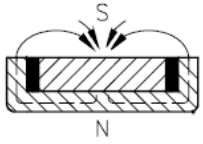 d) Shallow pot $F = 6_xF_B$
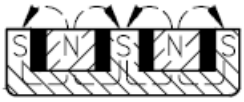 e) Shallow pot with center pole. $F=7_xF_B$	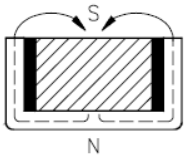 f) Pot $F=7.5_xF_B$	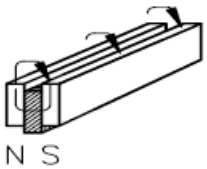 g) Sandwich $F=18_xF_B$	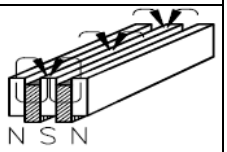 h) Double sandwich $F=18_xF_B$ x each system

5.4.5.2 Target material and shielding

The case study of the mini stages (as the Theta stage - Figure 5.38) can better illustrate the procedures and difficulties of using permanent magnets as a preload.

[59] For example, during the Robosem project, a partner study (IET-Nascatec GmbH) has shown that cantilevers covered with piezoresistive sensors have had different output values if the electron beam has been being placed over it.

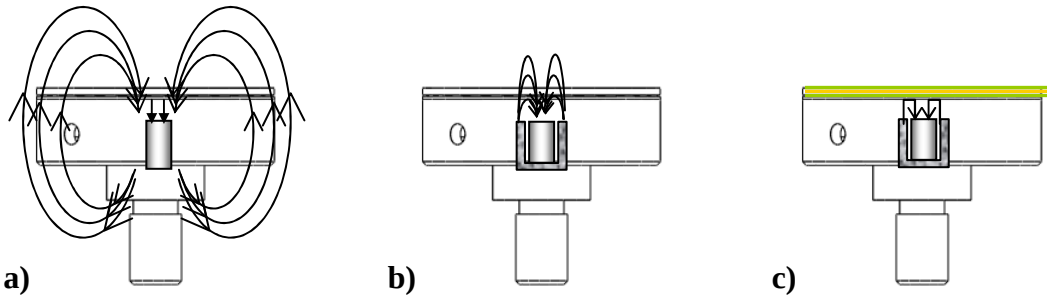

Figure 5.38: Applying magnetic preload over a miniature Theta stage

In Figure 5.38*a*, the magnet is placed inside the stage (body made of aluminum) without any special arrangement. The target material (the turning carrier in steel) saturates and lets some magnetic flux pass. The field at the North Pole (bottom) can cause also some important side effects, as when the stage has been left over the load cell during several days. The magnetic flux has permanent magnetized the load cell, disturbing considerably the SEM image.
In *b)*, a ferromagnetic system (as a pot magnet) redirects the flux lines that now do not pass through the bottom side. The magnetic flux is reduced in size, but the lines are more concentrated and stronger at the top. Shielding became more problematic as the top material can easily saturate. An example is presented in the Figure 5.39 video sequence. It shows the influence of a small and located magnetic field over the SEM image. The Cube Corner tip is fix and the sample is turning. When a small-magnetized region gets near the electron beam, the image shifts.

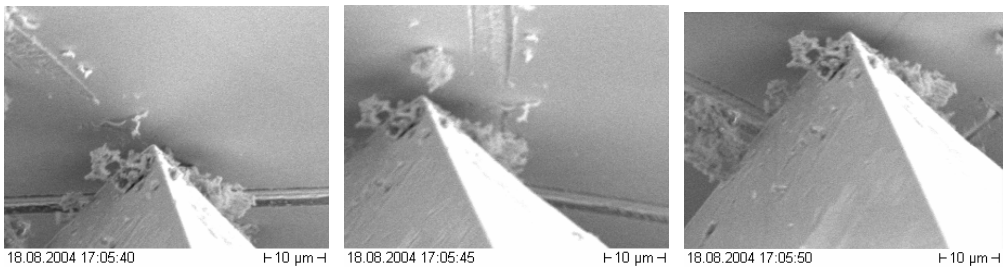

Figure 5.39: Video sequence of a small and located magnetic field influence over the SEM image. The stage is turning and the tip is fixed. A solution has been found adding a thin plate of a high magnetic permeability alloy.

Normal soft metals can be easily saturated, needing more volume for appropriate shielding. Thus, special materials have been selected for this application (Figure 5.38*c*).
Nickel based alloys are good material with high magnetic permeability. High permeability materials means a class of materials able to easily redirect magnetic flux. For field attenuations, materials with high magnetic permeability are desired. Another important parameter is to know the material's saturation (see Annex III, Annex Figure 11). Those two properties are provided by manufactures of these special magnetic shield alloys. Examples are MuMetal [83] and Magnetic Shield Co [84].

So far, the combination of ferromagnetic systems (in the theta stage) and the use of multipole axially poled magnets (in the Y-stage) has been enough to reduce the size of the magnetic flux over the sample or over the load cell. Finally, the introduction of special Ni alloys has improved the attraction forces, as the target material has not been

saturated. This has thus shielded the carrier. The measured flux density at the carrier surface has been mainly inexistent.

5.4.6 Ground and shield

In the same way that the magnetic field disturbs the electron beam, electric pulses can also have the capacity to shift the SEM image each time that they occur. Stick-slip actuators are particularly noisy because the quick change in voltage (usually from +200 to –200V) during the slip phase that generates an electromagnetic pulse. If the actuator is placed close to the beam, the problem is even worse. A non-shielded Miniature Y table (as Figure 5.25*a*) has the power to shift an image several micrometers after each step, if the electron beam is targeting a region near by. On the other hand, the linear actuator presently utilized to move the SEM indenter; the X table (Figure 5.20, Figure 5.37*b*) is not shielded. However, its influence over the SEM image is less perceptible. The reason can be seen in Figure 5.23*a*, in a normal setup of the SEM indenter. The actuator is not located close to the beam; it is behind the metallic electron beam column. The pulse created by the actuator is still strong, but it does not reach the sample with intensity.
The solution adopted for the table has been to create sliding contacts (CuBe compliant contacts). The choice has been to creating a demountable upper part, making it easier to remove for placing a sample.
Care must be taken if the driven force of the stage is low. The contact flexure acts as a spring, compensating a part of the normal force created by the preload system. The friction at each sliding point can also be high (and increases with vacuum). It is important to correctly shape the contacts to provide a good sliding. Electrical conductive lubricants can also be used. Graphite is one example, although its friction coefficient increases in Vacuum. Molybdenum Disulfide (MoS_2) or Tungsten Disulfide (WS_2) can be available also in electrical conductive forms, with the advantage that their friction coefficient is lower under vacuum than in air. The sliding part can receive special selected materials deposited over it (thin films) that act as lubricant and electric contact.
Finally, it is possible to make the foot material with conductive elements. An example is to use electrical conductive Zirconia[60].
To have the stage shielded and grounded is also essential for sample observation. If the electron beam can no longer hit the sample (as it became saturated after a long time exposition to the electron beam), no image can be formed.

5.4.7 Cabling

To provide an easy path for all the necessary cabling for the actuators and sensors is a task that is quite often neglected.
Cables used to connect each instrument subsystem to its connection through the SEM chamber, can hang-up the connector during transport and installation. Damaging a connection is thus easier. Long cables are necessary to freely move the instrument inside the vacuum chamber. This increases the chance to cut or damage a cable when closing the SEM door, as it can lie between the chamber and the door.
Planning the entire cabling path during the design will speed up assembly, connection and reliability of the instrument. Rebuilding connections can require a complete disablement of the instrument.

[60] Y-ZrO_2-TiC composite, from Saphirwerk Industrieproduct AG, Switzerland (www.saphirwerk.com)

Cabling inside the SEM should be shielded. A good shield and ground of data cables will improve the signal to noise ratio and avoid crosstalk. Power cables, as for stick-slip actuators, must also be shielded. The slip phase generates high amounts of electromagnetic noise, disturbing the electron beam (worst if the power line is located close to the sample region). Shielded power cables can be used to pass all data and power channels in a multi-core wire without having crosstalking[61].

A concept to remove wires from the instrument, placing them directly on the SEM stage is shown in Figure 5.40.

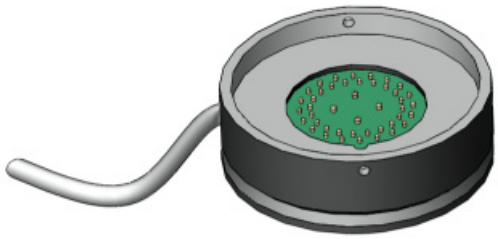

Figure 5.40: Concept of a 'hot-shoe' connection plate located in the SEM stage.

The hot-shoe (term used for the flash connections in photographic machines) is a conception that puts the connections at the base of the instrument. The counterpart is located in the SEM stage. Therefore, the cable goes in a more organized way through the SEM stage, up to a feed-through connector.

The concept of a built-in connector inside the chamber is necessary for those SEMs that do not have the main access through the SEM door but through a side chamber (Ex. Hitachi S-4800 Field-emission SEM). These pre-chambers are utilized to speed up the sample exchange, as the high-vacuum environment is all the time kept inside the main chamber. Only after the evacuation of the pre-chamber, the sample gets access to the main chamber (using a sliding sample exchange). Thus, there is no other way for providing connections between the instrument and the exterior, except if there is a counterpart already installed inside the main vacuum chamber to provide the contact path.

5.5 Conclusions

This chapter has shown that so far it is possible to reduce the amount of jump-back in stick-slip actuators by the means of electronic or mechanical solutions. Optimization of normal load over the feet must be the first step. Working with four legs at 25% shift has dropped the jump-back size nearly four times (taking as an example the saturation region) when compared to the standard stick-slip driving mode. A Piezo placed in series with the actuator has shown good potentialities and easy implementation. However, it still requires better implementation for suppressing the delay and vibrations presented in the test. A compensation of the jump-back through an external load is another possibility.
Each solution has its advantage and its disadvantage. The increasing of complexity over the system is a major concern. If the system gets more complex to minimize the

[61] As the power lines are arranged in a parallel path, there is more chance to create an induced signal from one channel to another.

amount of jump-back, a stick-slip solution becomes less attractive if compared to other piezo-based technologies.

The second part of the work has been focused on the conceptual design of an in-situ Material Characterization device. The basis of the discussion has been the developed SEM indenter/scratch. Explaining its evolutions, as the material tests have been demanded more sample positioning capabilities or instrument performances has been the starting point to introduce new ideas and explain some concepts that can be used to design a new SEM indenter.
These concepts have been divided in two groups: Those completely based on stick-slip technology and hybrid design. This has provided ideas ranging from very compact indenters, completely based on stick-slip actuators, up to high resolution and high force indenters, using a combination of stick-slip actuators, stack piezo actuators and flexure hinges. Some of these concepts have been schematized in the text. Another part of the studies has been dedicated to the load and displacement system, as for example to consider the effect of frame compliance or Abbe error.

General aspects about the design for a SEM environment have also been presented. Topics have included the design for not disturbing the vacuum inside the chamber and operating or designing an instrument to work in vacuum conditions. Magnetic and electromagnetic shields have been another topic with high importance for a correct design, as the SEM image can easily be disturbed by this kind of interference. The last topic discussed has been cabling and connections. It can initially be considered as a superfluous detail. However, it has demonstrated to difficult assemble, installation and it interferes with a good operation of the instrument.

A review of applications in in-situ experiments of the positioning systems here explained is now presented in Chapter 6.

Chapter 6

SEM In-Situ Tests, Conclusions and Future Works

6.1 Introduction

This chapter presents an overview of studies that have applied in-situ material characterization using the SEM indenter.
Following this introduction there is a summary of the contributions of this thesis, for both of the fields that it has been targeted: Material Science and Precision Micro Engineering.
Finally, some suggestions and future works are presented.

6.2 In-situ mechanical tests

Here researches are presented that have been made using the SEM indenter. As new materials and types of experiments have been planned, some modifications and add-ons had to be included in the instrument.

6.2.1 Indenter calibration and Sharp tips indentation

Once the SEM indenter become operational, it has been necessary to verify its results, which have first demanded its calibration (frame stiffness). This phase has involved the indentation of reference materials as Fused Silica and Sapphire, as well as Nickel, Tungsten and Glassy carbon.

A procedure has thus been adapted and implemented by EMPA-Thun in cooperation with ASMEC GmbH [85], using an indentation analysis software (IndentAnalyser®), standard samples and tips.
As an output of the calibration, it has been possible to verify the behavior of each sample during the indentation, especially when using sharp indenters, as for example Cube Corner.

These observations have been later on compiled in a study comparing the different mechanical characterizations through nanoindentation using Berkovich and Cube Corner tips [86].
In-situ indentations have helped to study the sharp indenters/material interaction as pile-ups, sink-ins and chip-outs, which can compromise the correct mechanical characterization of the sample as well as a correct tip calibration.
Figure 6.1 shows some of these features during a cube corner Indentation.

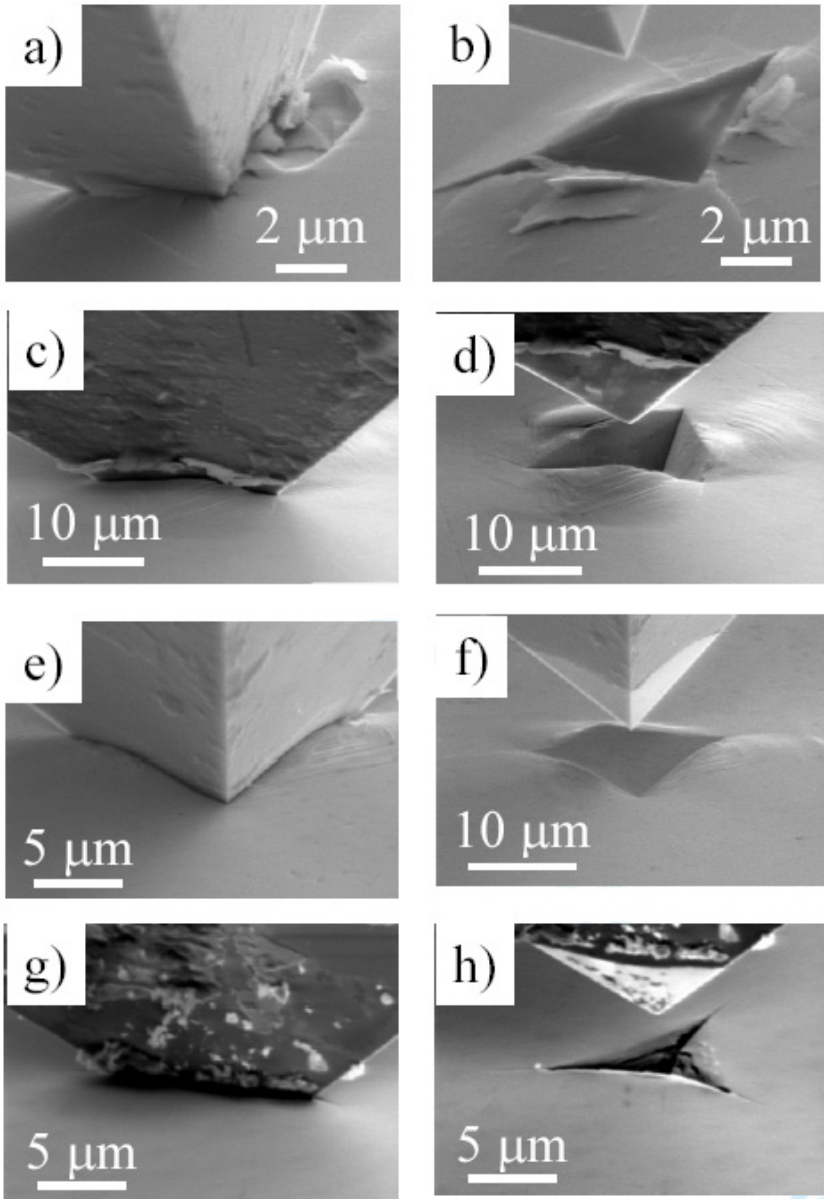

Figure 6.1: In-situ cube corner indentation[62] a-b) Sapphire (max load 981mN), c-d) Nickel (343mN), e-f) Tungsten (982mN), g-h) Glassy carbon (343mN). Ni and W present a high amount of pile-up and Glassy Carbon a strong elastic recover.

6.2.2 In-situ indentation and scratching of hard coatings

One of the first applications of the developed instrument has been to observe the coating behavior during indentation and scratching [16]. This work has been awarded in the International Conference on Metallurgical Coatings and Thin Films (ICMCFT 2004)[63]

Thin films are widely used as protective coatings in tribological applications, like hard TiN/SiNx coatings for cutting tools. Nanoindentation is a current method used to measure hardness, Young's modulus and fracture toughness of thin films while nanoscratching is used determine film adhesion or failure during contact.

[62] Patrick-Schwaller EMPA-Thun, Thomas Chudoba - ASMEC.
[63] Bunshah Award 2004 of the American Vacuum Society at ICMCTF – Best paper in symposium F/E

The SEM in-situ indenter has permitted to visualize some of the know parameters that can interfere with the correct determination of mechanical properties. For example, the formation of pile-up or sink-in during indentation (as can be seem in Figure 6.2) changes the calculated projected area *A* and thus the determination of the correct coating hardness.

Another advantage if in-situ indentation is an easier determination of fracture toughness (K_C) of coatings. In thin films the cracks often appear either at the interface between the coating and the substrate or through the whole thickness of the coating. The extension of the cracks, in particular of median cracks, allows estimating the fracture toughness of thin films.
Cracks can close after unlading what can make them almost impossible to visualize (as it has been observed in Figure 6.2). One should note that typically, the crack extension is mainly measured after unloading. Furthermore, it is not clear at which moment of the loading/unloading cycle the cracks are generated and how they extend during the loading/unloading cycle.
In-situ indentation provides the ideal tool to study crack generation as well as to correctly determine fracture toughness in situations were the length of the crack reduces or even cannot be anymore visualized after unloading.

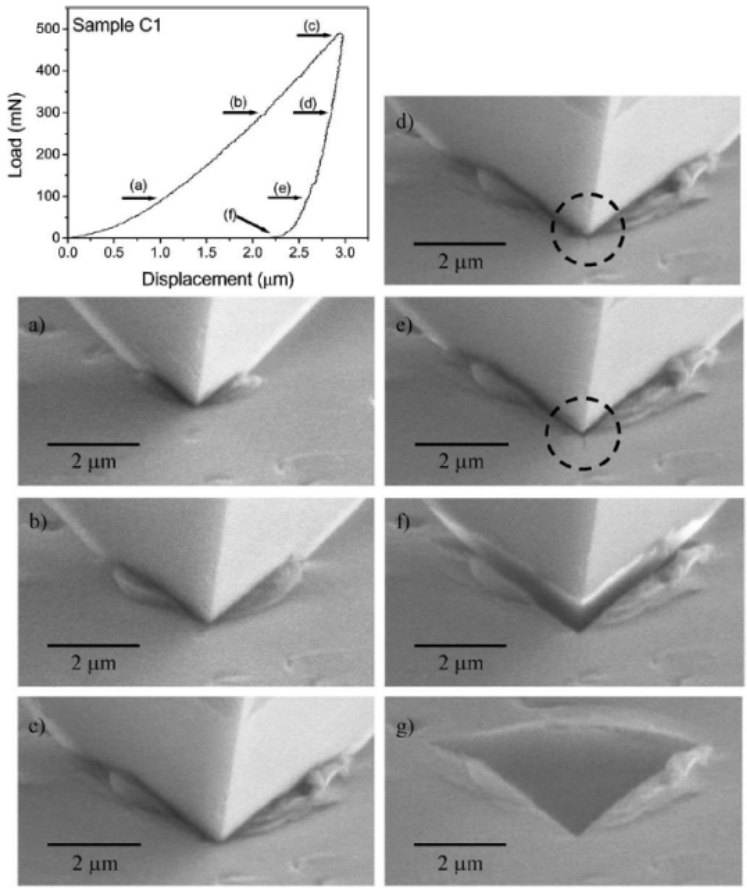

Figure 6.2: Cube Corner indentation on sample C1, a 1.5 μm thin TiN/SiNx coating[64] (H=27.6GPa) deposited on Si. Loading/unloading has been stopped for acquiring the pictures (represented from *a* to *f*). During unloading the formation of a small crack can be observed (indicated by the circle in figures (d) and (e)).

[64] Nanocomposite layers consisting of nanocrystalline TiN grains, which are embedded in a matrix of amorphous SiN_x (Sample C1at 13% Si content is present in the form of SiN_x).

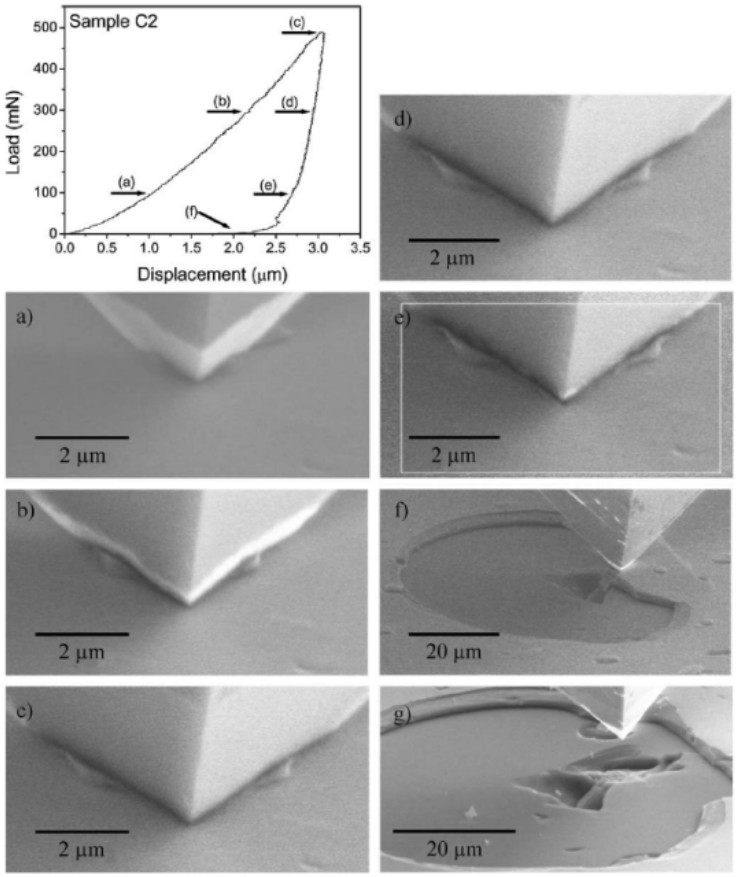

Figure 6.3: Cube Corner indentation made on sample C2, a 1.5 μm thin TiN/SiNx coating[65] (H=24.9GPa) deposited on Si.

Within the sensitivity of the instruments, the test made on C1 and C2 samples (TiN/SiNx) have presented a very smooth and similar P x h graph. The maximum indentation depth is bigger than the film thickness. However, a film-substrate transition cannot be observed in the graph. The small discontinuity in the sample C2 graph (between *e* and *f* as observed in Figure 6.3) can be related with the delamination of a large part of the coating. It is remarkable that such amount of removed material has produced only a small change in the P x h graph.

Indentation made on Si-DLC[66] deposited over a tool steel substrate has shown pop-ins events (sudden increases of the displacement at constant load). These are originated by chipping-out of coating material (Figure 6.4). The main chip-out region could not be seen in Figure 6.4 *a–e* because the indentation tip has masked it. However, a video recorded during the test confirms the chipping-out during pop-ins. A pile-up formation can be observed during unloading. Since the pile-up formation during unloading occurs mainly between loads of 100mN and full unloading, it has been conclude that the pronounced elbow in the unloading curves at loads around 30mN is

[65] Same characteristics as sample C1 but containing 8 at.% Si that is present in the form of SiN_x

[66] A 3-4μm DLC film containing 20 at % Si. A silicon-rich buffer layer of about 50nm thickness was deposited on the tool steel substrate. The subsequent thermal treatment has crated a brittle film, well suitable to be observed through in-situ indentation.

related to this phenomenon. The origin of this pile-up of material may be related to cracking below the surface.

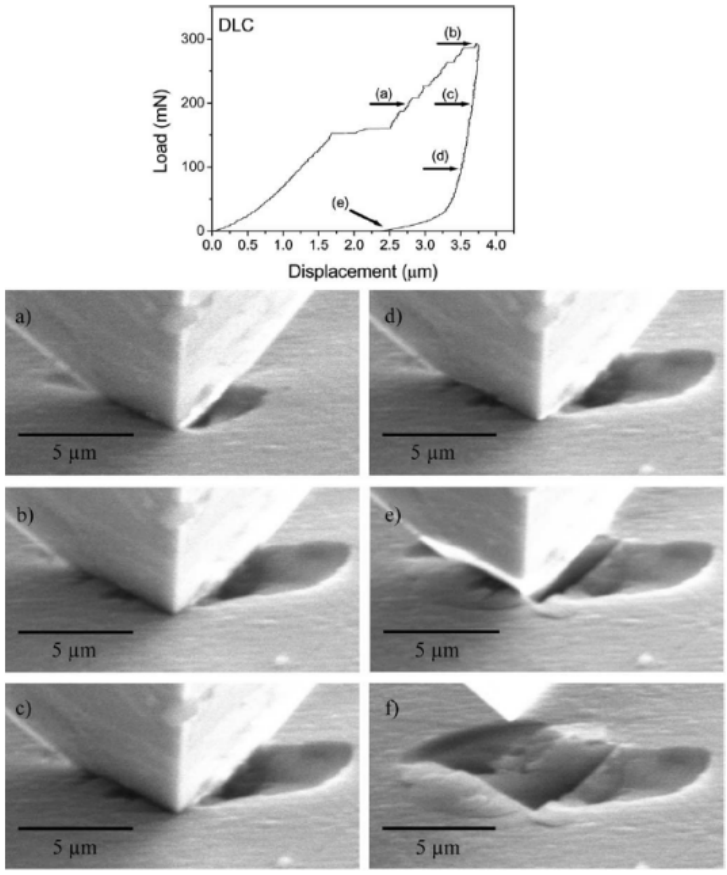

Figure 6.4: Cube corner indentation made on a 3-4μm DLC film deposited over tool steel (see text for details)

Figure 6.5 shows images recorded during the scratches at normal loads of 5mN (a), 10mN(b), and 150mN(c). For the 5 and 10mN scratch, the vertical displacement is below the thickness of the DLC coating. For 5mN applied load there is just minor formation of rather small particles at the rear side of the indentation tip. For 10mN applied load chipping out of larger DLC flakes occurs. Severe coating damage can be observed for 150mN normal load where large parts of the coating are delaminating and the indentation tip penetrates also into the steel substrate.

The experiments on thin TiN/SiNx and DLC coatings reveal that additional information about the material behavior under load (cracks, pile-up, coating delamination) can be gained by in-situ SEM indentation and scratching. Crossing information between the P x h graph and images helps to explain some of the events registered by the graph plus reveals other ones that are not registered by it. In-situ indentation/scratching also shows with details the sequence of the coating behavior (ex. cracks formation, chipping-outs, delamination), a type of information that cannot be revealed by a post-analysis of the sample.

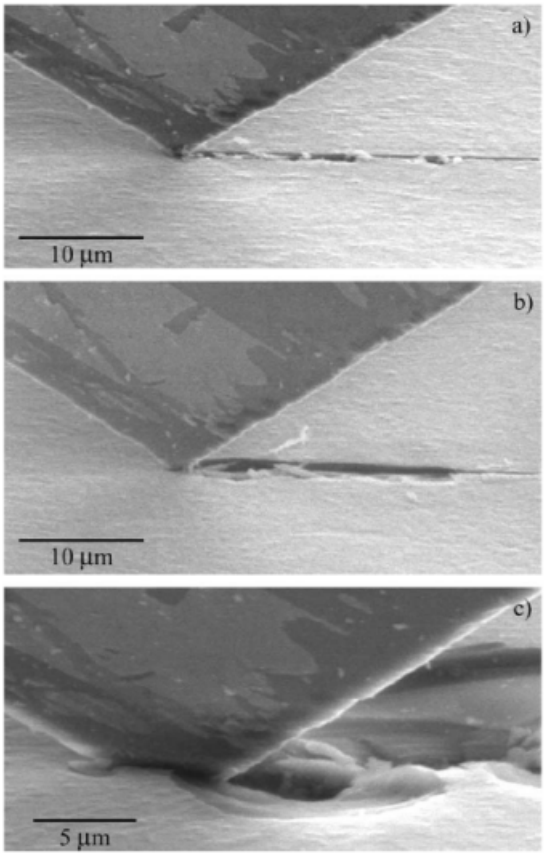

Figure 6.5: Scratches with 5 (a), 10 (b), and 150mN (c) applied normal load on a 3 µm DLC coating on a steel substrate

6.2.3 Correlation between the P x h graph and videos to study shear bands in BMGs

Another awarded work[67] using in-situ indentation has been performed in Bulk Metallic Glasses (BMGs) [17]. Metallic glasses have unique strength and elasticity properties when compared with other materials. Plastic deformation in BMGs is highly unstable and localized inside shear bands. Its ductility is very limited, principally in tension. Shear bands are observed not only during tension but also during compression, bending or indentation. A careful understanding of its plastic deformation is thus necessary to increase ductility in this material. Indenter is one of these methods of study.

Many researches have suggested that the pop-in identified in BMGs P x h graph is related with the formation of shear bands at the sample's surface. However, up to that time, no conclusive evidence had been presented.

With a retrofitted SEM image system (fully customized video options) and a slow indentation rate, high quality video has been synchronized with the P x h curve generated by the SEM indenter, providing a precise observation of the test.

The video-curve correlation has shown that the appearance of a new shear correlates with the pop-in event located in the P x h graph. One example is shown in Figure 6.6. Pictures *A* and *B* have been acquired (from the video) just before and after the pop-in shown in the graph. The appearance of a new shear band is clearly observed.

[67] By Benedikt Moser, winner of a Best Poster Award (Runner-up) - Gordon Research Conference, Thin film and small scale mechanical behavior 2004.

With help of the SEM indenter, for the first time a correlation between shear bands creation in BMGs and the typical events in the P x h graph have been evidenced.

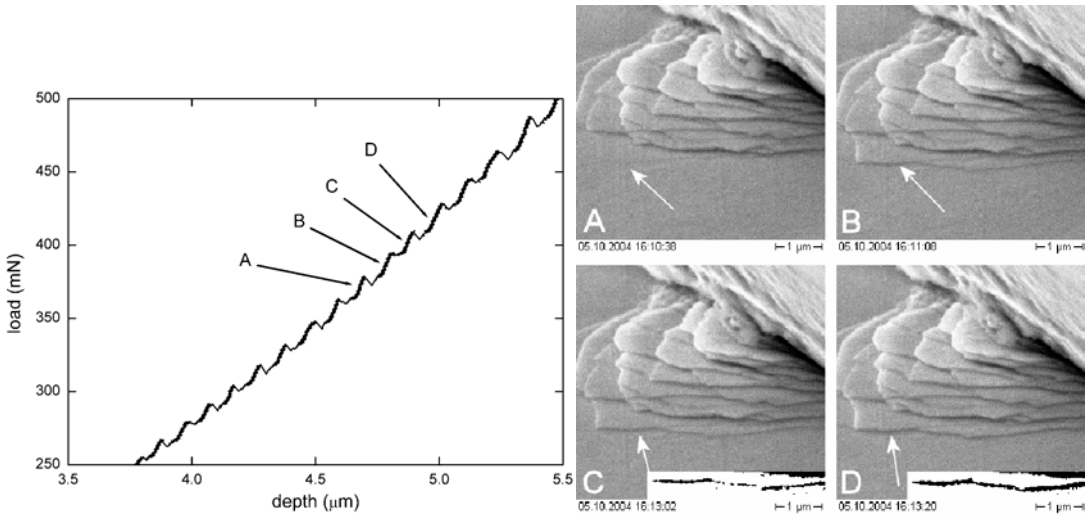

Figure 6.6: Drop in load in the P x h graph and its correspondent images (*A, B*) extracted from a video sequence.[68] Material is Zr-BMG[69] (Vitreloy 105) indented with cube corner tip.

6.2.4 Investigation of wear mechanisms through in-situ microscratching

In this study [18], Fe-BMG, GaAs (<001> type wafer, not doped) and Polymers (thermosetting-based polycarbonate substrate) with a special coating[70] have been scratched with a conical tip (semi angle α 45°, tip radius 1μm). The flow of the material near the indenter (piling-up and sinking-in), the particle formation mechanisms during micro scratching and the crack propagation can be visualized through in-situ scratching.

Scratching test, as already presented in paragraph 6.2.2, is used to evaluate the mechanical properties of coatings, in special the coating-substrate adhesion. Scratching is also used to models experiment to understand the deformation and crack formation mechanism in precision machining as well as to better understand special removal process like grinding, polishing and abrasive wear.

In these experiments, in-situ microscratching has shown good details of chipping and crack propagation as the tip scratches the sample. The test has been complemented using a commercial nanoindenter (Nanoindenter XP from MTS corporation) to performance nanoscratching since the SEM indenter does not have the capability to measure lateral force. Figure 6.7 and Figure 6.8 shows some scratching sequences extracted from the study.

In-situ microscratching (with a constant normal load from 50mN) in GaAs (Figure 6.7*a*) has been performed along the <110> direction. It can be observed that the chip is generated in the back of the scratching tip (tip is moving away from the observer). Two chevron cracks cross-link via a lateral crack that forms at the backside of the moving tip, i.e. during the unloading of the surface. The in situ observations show that cracks extend at speeds similar to that of the indenter, i.e. stable crack propagation takes place related to the scratching speed.

In another test (not shown here, but present in [18]), the tip is driven toward the observer following a normal load ramp from 0 to 100mN. Chevron-type cracks, in

[68] Benedikt Moser – EMPA-Thun.
[69] Measured properties: H=6.4GPa, E=107GPa.
[70] 5μm thick polysiloxane coating containing 20 vol.% colloidal SiO_2 particles.

part together with lateral-type cracks, have been identified to be responsible for chip-outs observed all around the moving tip. In-situ scratching has allowed observing with details the behavior of the cracks and finally chipping-outs.

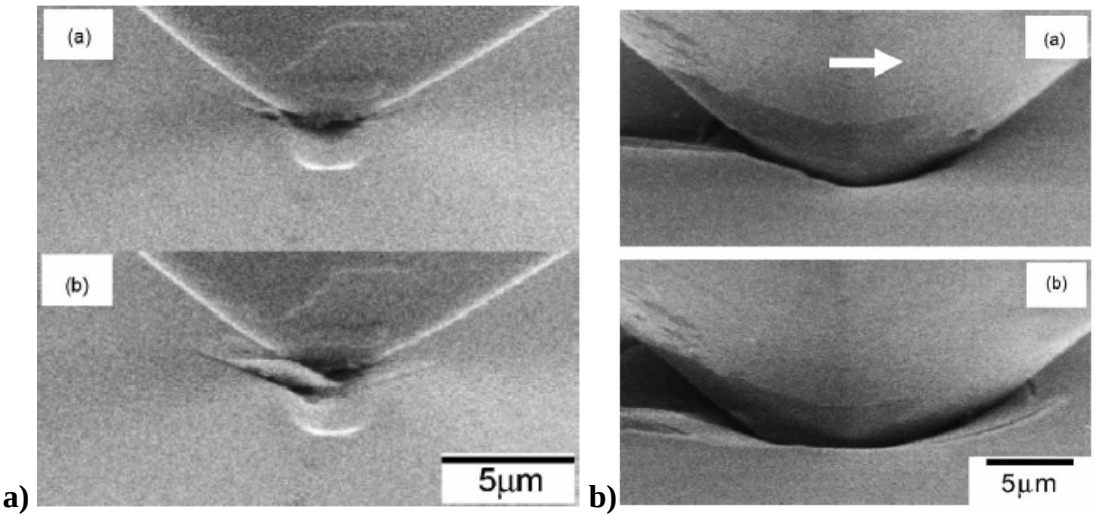

a) **b)**

Figure 6.7: a) Scratching of GaAs at 50mN normal load with 45°, 1µm radius conical tip. b) Video sequence of coated polymer at 120mN (a), 240mN (b). Cracks are forming in front of the tip

Scratching the coated polymer (Figure 6.7*b*) has shown that this highly elastic material tends to think-in around the indenter. A high amount of elastic recover has been observed in the video as the indenter moves from small to large normal loads.
For larger normal loads (picture *b* – at 240mN), the cracks begin to propagate on the sides and to the front of the tip, which causes larger variations in the penetration depth of the indenter (to keep the set normal load).
From ex-situ observations it is not possible to tell when and where (with respect to the moving tip) the cracks appear. This information is important in order to understand the formation of these cracks. Depending on where these cracks appear, different stresses are responsible for their formation, which in turn allows conclusions on the failure behavior of the thin film.
It has been observed that cracks in the wake of the moving tip are probably caused by a tearing action by the tip pulling on the film by friction forces. The progression of cracks via the side to the front of the tip is probably caused by tensile stresses resulting from the bending stresses within the film due to the larger indentation depths

Standard scratching (with a MTS nanoindenter) in Fe-BMG[71] shows the penetration depth (thin line) and the lateral force (thick line) as a function of the applied normal load (Figure 6.8*b*). Up to a normal load of about 120mN the curve is very smooth. Then, a sudden increase in penetration depth as well as in lateral force is observed. At higher normal loads irregular depth variations with amplitudes above 100nm appear. The in-situ scratching has shown that the deformation mechanism at low loads (loads smaller than around 16mN) is a ductile ploughing behavior. Up to this load no chip has been observed. Above this normal load, a chip can be observed as formation of small shear bands in front of the moving tip (Figure 6.8*a*)[72]. The thickness of the chip has increased significantly beyond the transition load (around 150mN) that may indicate a transition from wave removal to chip removal. In-situ scratching has shown

[71] Indentation hardness H=13.9GPa, E=214GPa
[72] The mentioned paper shows a sequence of the chip formation, taken out from a video.

that although BMGs are known to have limited ductility in tension, the chip formation and the residual scratch much more resemble the one of a ductile metal than the one of a brittle material.

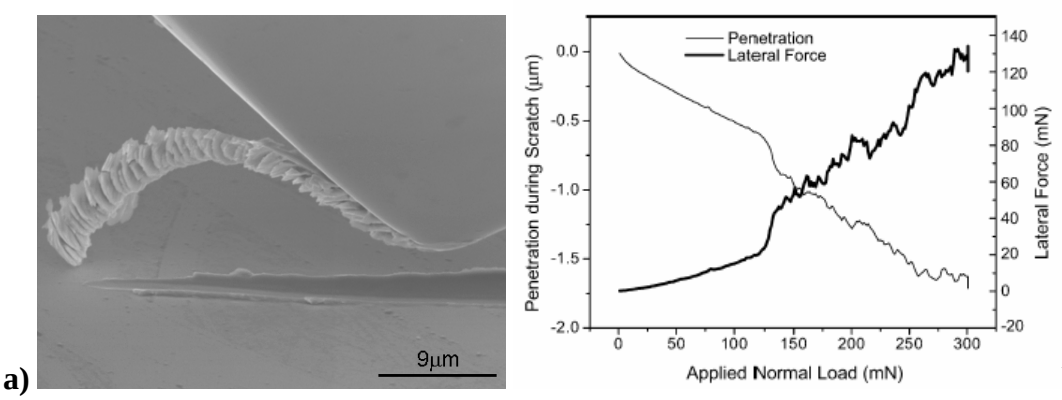

Figure 6.8: a) Final video sequence of a Fe-BMG scratching. b) Fe-BMG scratching graph from a commercial nanoindenter (MTS XP). The SEM indenter video sequence complements the result shown by lateral forces measurements showing when and how the chip formation starts.

6.2.5 Study of crack propagation in semiconductors

The study of crack generation and propagation in semiconductors as GaAs has been an important research field of EMPA-EPFL, having had close cooperation with industrial and scientific partners. This test has demanded most of the sample positioning systems available for the SEM indenter. X-Y tables have been required to precisely place the indenter tip in a specific region, as for example the edge of a wafer. The *theta* table has speeded up the test, as the sample could easily be rotated, providing different crystallographic plane orientations to be indented or scratched.
Figure 6.10 to Figure 6.9 illustrate some of these tests (Source, Cédric Pouvreau, EMPA-Thun – unpublished work).
Figure 6.9 is an indentation made in the edge of a GaAs wafer. It illustrates the difficulty to observe cracks after unloading. Figure 6.9*a* has been taken at full loading whereas the Figure 6.9*b* has been taken after removal of the loading.

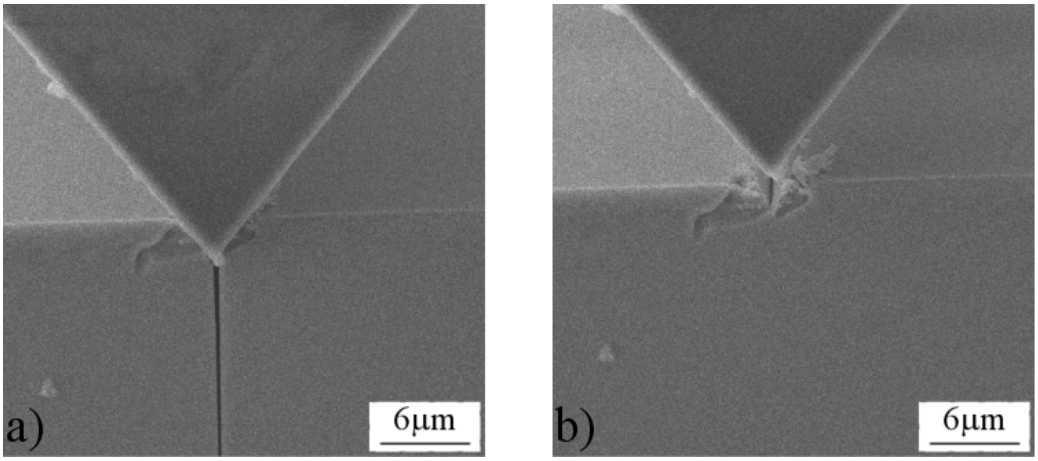

Figure 6.9: Wedge indenter exactly over a cleaved face of a GaAs sample. a) Full loading, b) Completely unloading. The crack completely disappears once the load is removed, being difficult to spot by ex-situ analysis.

These pictures are a good example how in-situ observation makes it easier to observe and measure crack propagation.

With a wedge 60^{o} tip (Figure 6.11), the pop-in event that can be seen (approximately at 350mN) is correlated with the sudden extension of a Half Penny crack at the surface[73].

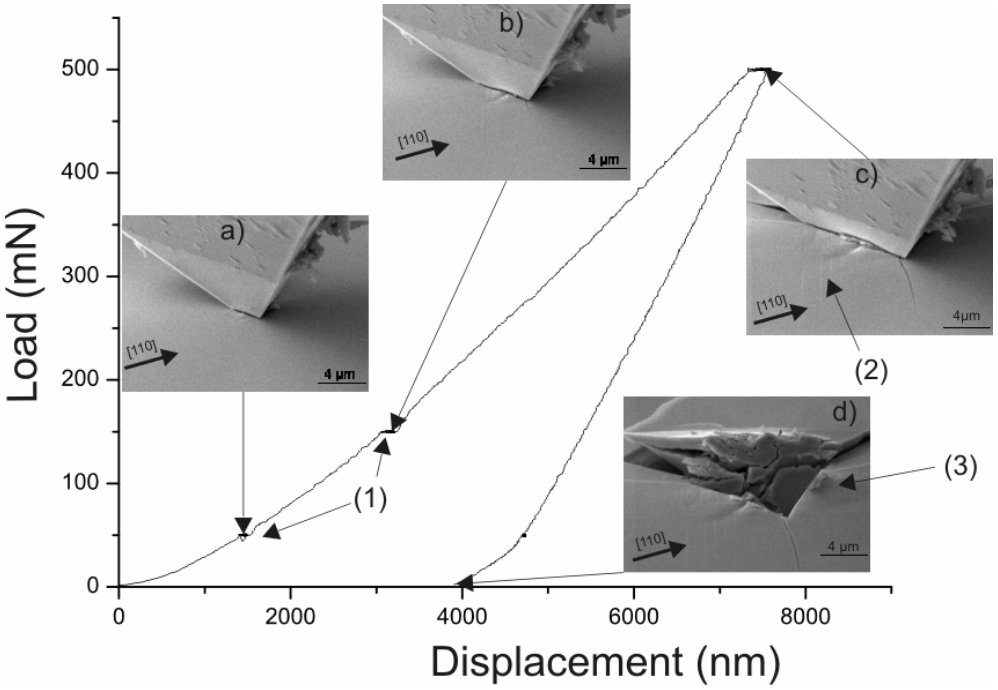

Figure 6.10: Indentation in GaAs with Cube Corner tip. At specific indentation loads, a holding time has been included for taking high-resolution pictures.

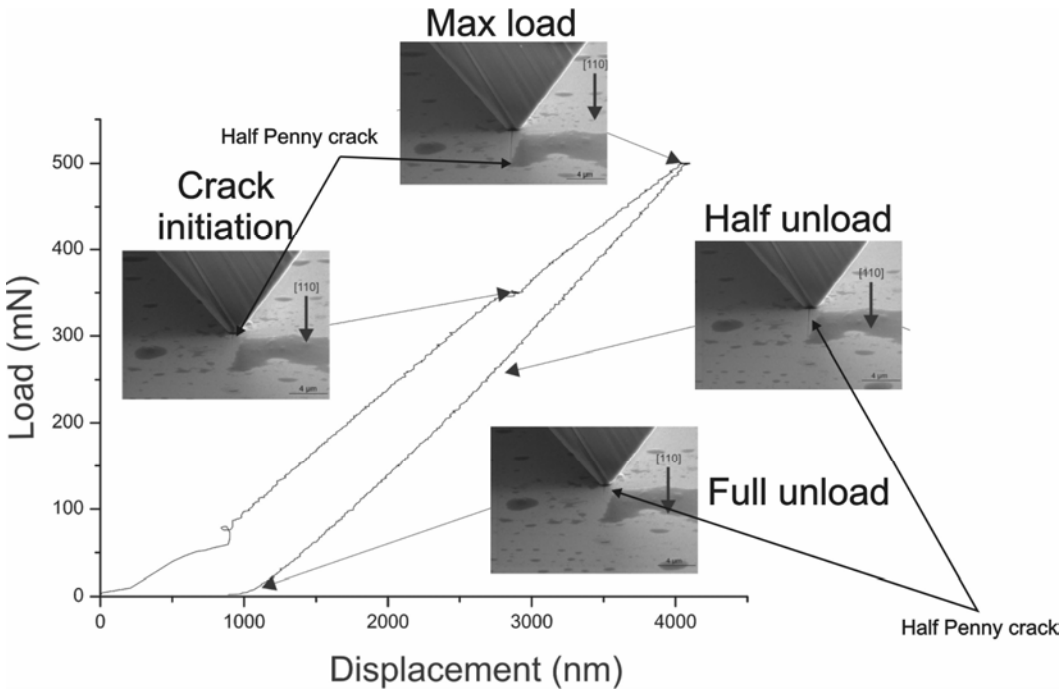

Figure 6.11: Wedge tip indentation in GaAs. The pop-in identified at 350mN is correlated with the extension of the crack. The half penny crack closes considerably during unloading.

[73] A paper has been submitted having the topic 'In-Situ SEM Indentation of Gallium Arsenide'.

6.2.6 Exploratory indentation and scratching

In a first public presentation of the SEM indenter (Euromat 2003 [87]), the advantages of using the SEM capabilities (easy magnification changes, high depth of focus, etc.) together with nanopositioning systems has been shown. The added value has been the possibility to better and easier localize regions of interest and after that to make a precise positioning of the tip over a specific region (ex. Figure 6.12).

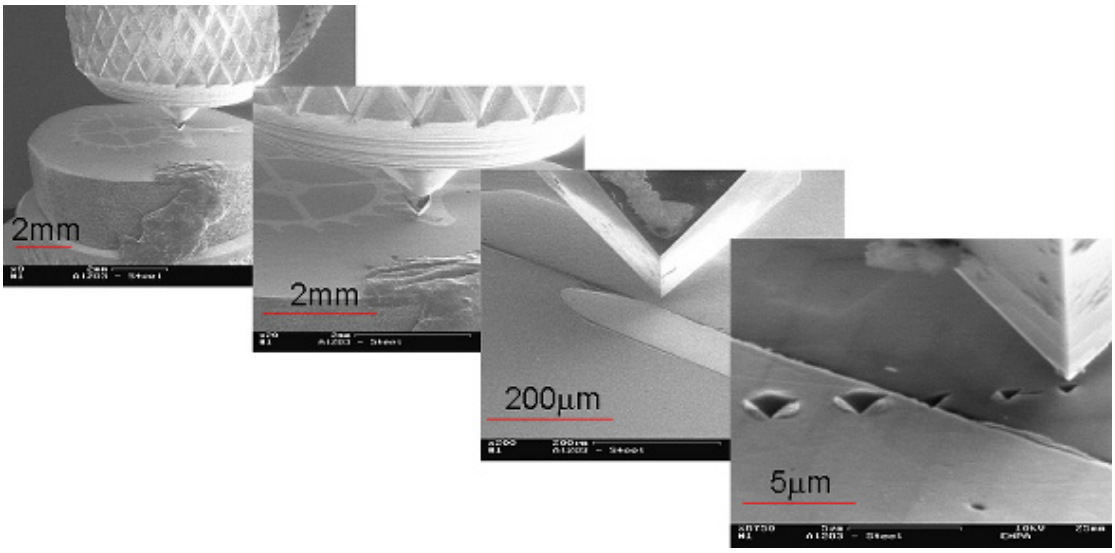

Figure 6.12: Using SEM quick change of magnification to find and test a specific region. For example, a watch part. The material at left is steel, at right ruby – indentation has also been placed at the interface of both materials.

6.2.7 Micropillars tests

Another test that has profited from a SEM indenter has been the compression of micro pillars (Figure 6.13) [88]. Each pillar has few microns in diameter. They are created through Focused Ions beam (FIB) or etching process. Compression is done using a flat tip. The mechanical properties of these micropillars have been obtained relating the applied force and the cross-section of the pillar after the compression. Hence, the SEM image has been part of the measurement system. The tip has had to be placed exactly over each pillar. The indenter X-Y tables have provided enough resolution for this operation.

A variant test is a Micropillar bending (Figure 6.1d). The flat tip contacts the pillar and the table is moved, thus bending it.

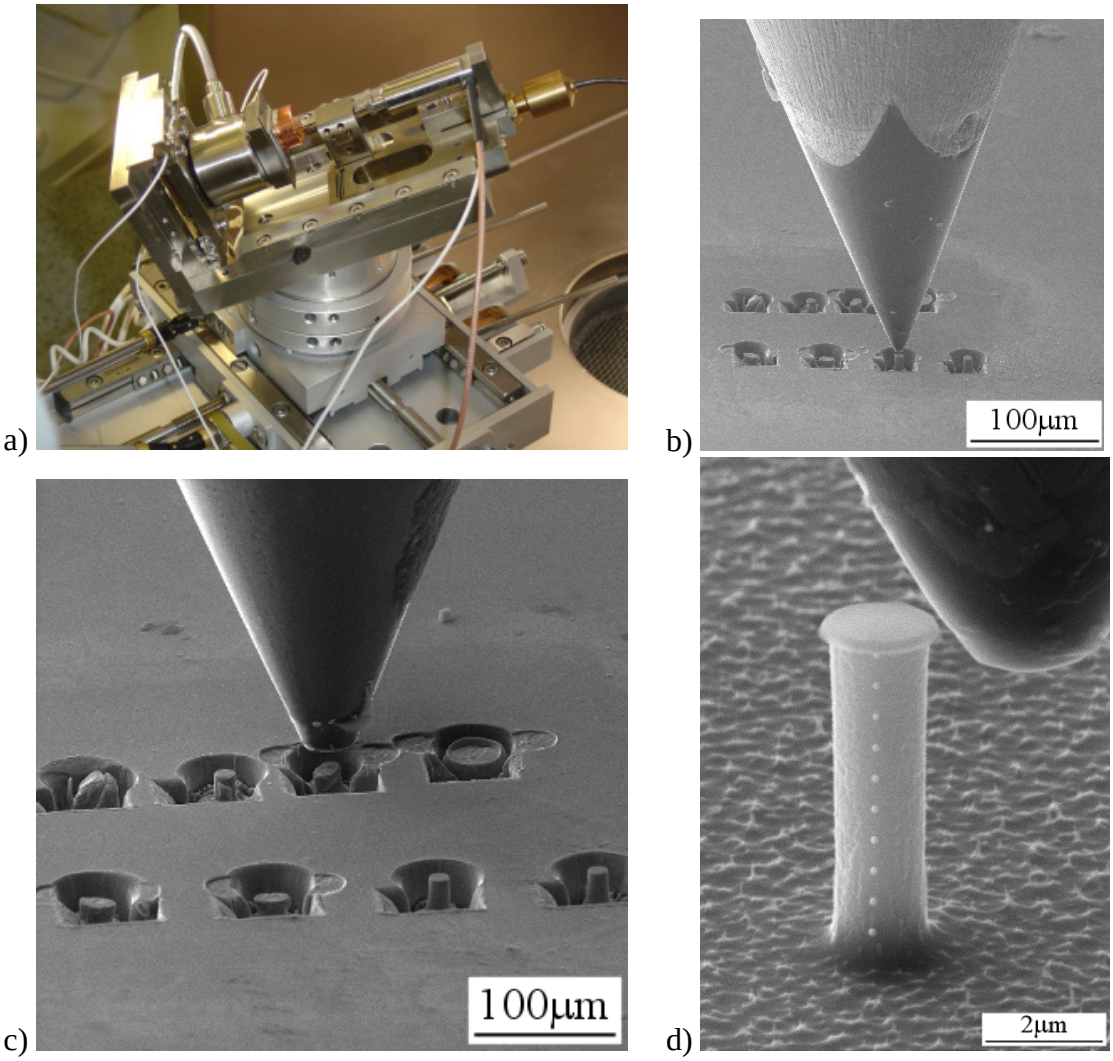

Figure 6.13: Micro Pillars tests. a) Setup of Cu micro pillars, b) Precise tip positioning, c) compression of Cu micro pillars, d) Positioning for micro pillars test bending.[74]

6.2.8 Outside of SEM applications

A complementary test involving Micropillar tests has been realized outside the SEM. The advantage here has been to have a small indenter. It has thus being fit under an optical microscope having a micro Raman Spectroscopy[75]. The tip positioning is realized with help of the optical microscope. The pillar compression is thus measured through a laser beam that had a spot size of few micrometers. Installation and setup has been straightforward. Raman results have shown the shift in the stress/strain curve proportional to the pillar compression.

An application like pillar compression is an example that has shown the advantage of a design where the SEM load system is placed in the indentation head and not under the sample, as it is the actual design of the SEM indenter.
Due to the load cell high compliance, the pillar base moves down. This movement is added to the pillar's deformation itself. A Raman laser spot (a fix point outside the

[74] Source: Benedikt Moser and Kilian Wasmer – EMPA-Thun
[75] Raman Spectroscope can be found as an optional device **to be integrated** in a nanoindenter, as for example announced for the CSM Instruments nanoindenter.

indenter frame) is thus more susceptible to measure not only the pillar, but also the tip.

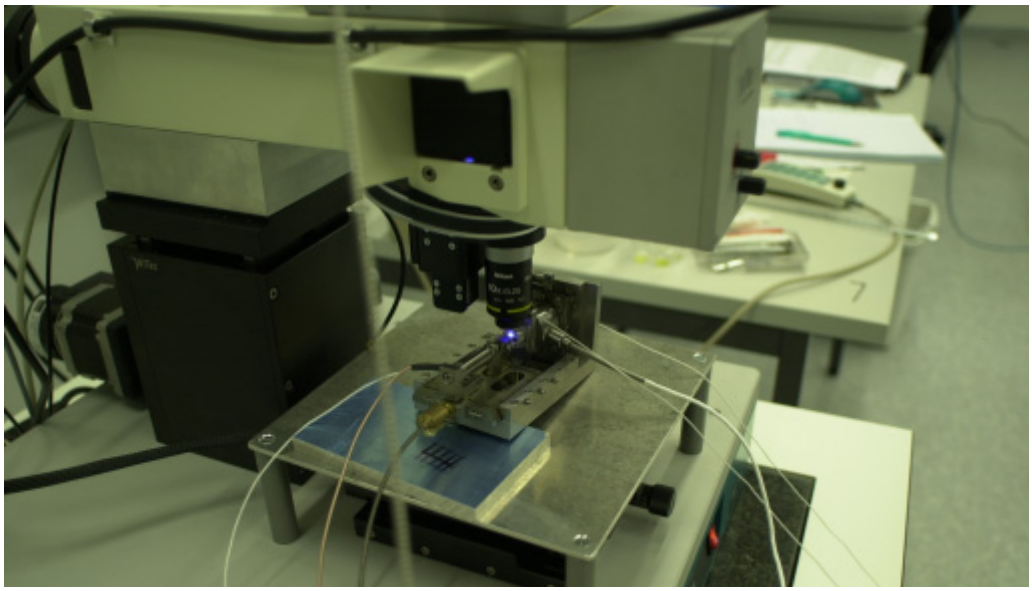

Figure 6.14: Installation of the SEM indenter to perform Raman microspectroscopy during compressing of micro-pillars[76].

6.2.9 Micro machining

Micro machining can be defined as a special scratching test. The main parameter for its characterization is the cutting load, but in the case of an in-situ device, the goal is rather to visualize how the material behaves (chip formation) during milling.

The geometric parameter of the diamond tip will affect the sub surface crack pattern and generate cracks, particles and chips at the material's surface. These later surface features can be undesirable depending on the application, as for example a reproducible scribing process. However, these processes are necessary for material removal as during ductile machining of GaAs surfaces or wire sawing of Silicon, as mentioned in [19].

Few tests have been realized using the SEM indenter for this goal, which is thus an unexplored topic. The developed turning stage (Figure 5.27) can be used as a lathe and the XY table can draw patterns almost in any material. In these tests, the tool has been the diamond indentation tip.
An example of surface machining is shown in Figure 6.15. A GaAs <100> wafer has been scratched with a cube corner tip with a lower load in both <011> and <001> direction. The picture shows the ductile deformation of the GaAs. The angle of the tip pushes the chip to the side

[76] Source, Kilian Wasmer – EMPA-Thun, Thomas Wermelinger – ETH Zurich, D-MATL.

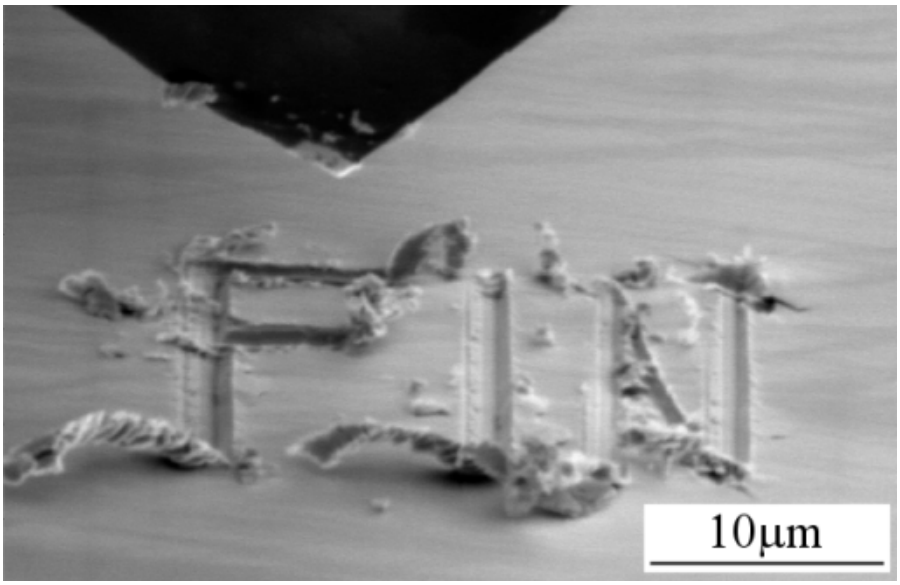

Figure 6.15: Example of machining. X-Y stage with a cube corner diamond tip in GaAs.

6.3 Work overview and main contributions

6.3.1 Bases for in-situ tests

This thesis has started with a short explanation of material testing and the role of nanoindentation in material characterization. This has been followed by an account of the advantages of in-situ material tests, as they provide the possibility to correlate the traditional output of each instrument with live images from the test.
The term in-situ indentation can be understood as the action of placing an indenter inside a Scanning Electron Microscope (SEM). Dynamic experiments in a SEM are not a new topic but it has been a surprise to find that very few experiments have been realized involving in-situ indentation. Even being clear its added values for normal (ex-situ) indentation.

6.3.2 A SEM indenter

A SEM indenter has been developed at the beginning of the thesis. This development has had an undoubted value to understand and explore more about in-situ indentations and the development of SEM compatible positioning systems and instruments. The use of stick-slip actuators has been one of these inputs for the design. One major goal of this study has been to demonstrate that a stick-slip actuator could be used to perform a material characterization as indentation or scratching. A complete stick-slip based instrument can have its size considerably reduced and its operation simplified.
Despite of their jump-back that is associated with the slip phase and their relative low driving force, it has been shown that stick-slip actuators can be dimensioned for indentation and scratching without changing the measurement. So far, no evidence has been found of stick-slip effect over an indentation. Nevertheless, more tests are needed to complement the materials used in the experiments.

6.3.3 Models of indentation with stick-slip actuators

To better understand and analyze the impact of using stick-slip in indentation and scratching, it has been necessary to know more about indentation and stick-slip actuators working together. The first step has been to model the indentation behavior

and to have a model that describes the actuator. Finally, these two models have been integrated in as a virtual indenter (the *indenter model*). This operational model has thus been utilized to have a first view of how is the interaction between reaction forces arising from the tip penetration over the actuator and its response as the amount of unloads over the sample due to an increasing jump-back size. The same models have later on been utilized to find a compromise between driving force and a minimum jump-back in the actuator slip-phase.

6.3.4 Comparison between continuous and stick-slip indentation

Simulation has helped to prepare a setup to reproduce a stick-slip indentation using the actual SEM indenter. This has provided a direct comparison between what has been called a *continuous indentation* and a *stick-slip indentation*, with exactly the same conditions. The same procedure has been later adapted for scratching.
Conducting this test inside the SEM has provided a visual comparison between these two indentation driving modes, in addition to the P x h graph (force versus penetration depth). Scratching has also profited of this facility, as the indenter device had not implemented the lateral force measurement.
Finally, a prototype of a Stick-slip indenter has been build, providing more information about the material's response under partial reloads during indentation.
Results of indentations, targeting different materials, have provided so far no evidences of physical changes in the imprint shape. This conclusion has been obtained by analyzing the P x h curve of a sample indented using a Stick-slip indenter or in a continuous mode. However, scratching having a certain amount of jump-back has revealed a pattern that can be associated with the stick-slip actuators. This has shown that despite the lack of evidence that partial unloads may modify the P x h graph, it is still safe to keep the jump back as small as possible. To determine the amount of jump-back that effectively may influences the indentation test still needs further tests with a wider range of materials.

6.3.5 Optimization of stick-slip actuators

As mentioned above, it is better to make the jump-back as small as possible. Thus, the next topic presented has been a demonstration of procedures and concepts that can be used to minimize the amount of jump-back, yet still having the necessary driving force required for indentation or scratch. Electronic and mechanical concepts have been explained and simulated using the indenter plus stick-slip model previously developed. Effective measurements have been carried out showing how to take profit of the work with the stick-slip legs in different combinations or arrangements. In the end, it has been possible to create a guideline about how to have a certain driving force with the smallest amount of jump-back.

6.3.6 Conceptual design of a SEM indenter and positioning systems

Using optimized stick-slip actuators; concepts of indenters have been shown, taking profit of these actuators. Hybrid designs have also been presented, especially for cases where no jump-back is tolerated or higher indentation forces are required.

6.3.7 Design for SEM

Finally, a small collection of information concerning designs for SEM environment has also been presented. One part has been compiled from the literature, while another part has its origin in practical solutions that have worked in a fine and simple way, or

new approaches learned after pitfalls faced during system designs for the SEM environment.

6.4 Original contributions

A SEM indenter for in-situ material characterization is an important contribution of the thesis, but it cannot be classified as being completely original. The concept of in-situ indentation has already been presented elsewhere [Paragraph 1.2]. The originality of this concept has been to develop several stick-slip systems used for material's characterization. The good performance and easy integration of these actuators has motivated a specific study of using stick-slip for indentation and scratching. This has effectively been a new approach.

Commercial nanoindenter sample positioning systems have not been available with sub micrometer sample positioning system. Only in the end of this work, this option became available[77], showing an increased demanded for these facilities. A precise sample positioning system, still compact and stiff, has been at the beginning of the work delivered for the in-situ indenter.

GaAs, Zr-BMG, Fused Silica have been submitted to different amounts of jump-back sizes, creating a sequence of reloads during indentation. The main differences between the reloads normally applied during indentation (as to reduce creep) and those found on the stick-slip are the amplitude and duration of the slip event.
Stick-slip unloads take place in the microsecond range and are caused by a backwards movements of the tip (typically having from 5-10nm up to a step size - the saturation point, as an extreme example). So far, there have no been registry of this sort of unloads as being part of a nanoindentation test. Hence, its comparison (visual and through the P x h curve) with traditional continuous tip displacement has been also new.

The studied materials have not shown any evidence that forbids the use of stick-slip actuators for indentation or scratching, as long as the amount of jump-back stays on a certain level. This level is related to each material's response. At least for the tested materials, a 20nm jump-back has demonstrated to produce no problems for indentation ***and*** scratching. For indentation only, even higher jump-backs have not presented problems.
This opens the opportunity of using cheap and small actuators to drive the tip in the μm range (step mode) or nm range (scanning mode), and to reach the sample surface (setup operation – in the mm range). The principle *mm to nm* has only recently been made available in commercial nanoindenters, but using bulky linear stages.

Finally, this thesis has also proposed procedures to keep the jump-back below a certain level and still to have a specified driving force. The topic of high trust-force stick-slip actuators with reduced jump-back has been an unexplored topic.
The use of electrical or mechanical solutions for minimizing the jump-back in stick-slip actuators is not a new topic but it still lacks of more experiments and information. How to use a reaction force to minimize the jump back have so far not being reported. Concepts of active or passive solutions customized for indentation and scratching

[77] Tables with resolution below 1μm, as optionally offered by MTS or CSM-instruments.

have been presented here, covering thus an area that has no much study; The use of inertial drives facing increasing reaction forces.

6.5 General comments and future works

Some of the ideas implemented in the SEM indenter (as for example the need of nanopositioning) are today on the market, confirming that the same needs are shared by more users. This creates more opportunities for the concepts here presented.
As several branches of technology converges and are miniaturized, it is expected that the devices for testing them have also to be scaled down and integrated into other instruments.
The creation of compact testing devices is thus a promising field. Designing a compact SEM indenter/scratch is a step that follows naturally. It can profit from the new generations of high resolution SEMs. These microscopes often have a reduced chamber size.
Compact indenters have also applications outside the SEM environment. An example has been shown with the Raman spectroscopy. Contacts[78] have also been made to verify the use of a compact indenter for studding diffraction patterns associated with uniaxial stress state and plastic flow of submicron cylindrical samples. The setup, a synchrotron beamline, requires a specific DOF, not only for sample positioning, but also for the entire instrument in reference to the generated beam. The frame shape of the indenter also needs customization due to a correct reading of the diffracted signal on a detector behind the sample.

The idea of using stick-slip for indentation/scratching will certainly find resistance from material researches, as it can effectively exist materials less tolerant to quick and repetitive unloads. Thus, it is necessary to test more materials and determine the maximum jump-back that could be allowed in each case.
A complete jump-back suppression may be a complex task (yet, it has been here presented alternative *hybrid* solutions). However, its reduction is not. Having in mind the maximum allowed jump-back size is thus a starting point for designing a stick-slip indenter.

The jump-back must be inside a specific range, independent of the environment where the actuator is placed (high vacuum or air). There will be no sense in optimizing the system in air, if the behavior is not similar in vacuum. Realizing this optimization directly in vacuum will just add unnecessary complexity to the test.
Matching the correct foot-carrier material is thus necessary. Wear rate and changes in the friction coefficient must be as similar as possible in both environments. A specific tribologic study must be performed in both environments and they should preferentially involve the real conditions (a stick-slip movement with different normal loads).

Measurement constraints in the actual SEM indenter have their origin in the integrated load and displacement sensors. To use direct off the shelf solutions has the advantage that the components have already been characterized (mechanically and electronically) and can in principle be easily replaced. However, it also means that the size of the instrument will depend on the available size the sensors. As an example, a

[78] Robert Maass - Paul Scherrer Institute.-.Swiss Light Source (SLS)

linear stick-slip stage with build-in optical encoder is not much bigger than the encoder itself. The minimum size is constrained by the sensor size.
So far, the main design limitation found has been a more sensitive load measurement system. Semi conductor based load cells (with high sensitivity) are quite bulky (several cubic centimeters) and compliant. Their integration is a problem. In commercially available sensors, the fact that they are s*ensitive* and *compact* for a load system often also means *compliant* and *fragile*. Piezoelectric based load measurement systems (compressing the actuator) are stiff, sensitive and compact, but are not suitable for *quasi-static* measurements.

A more compact and sensitive displacement and load measurement system is an unsolved demand; thus, a continuous work. New sensor technologies can always improve the material characterization system in terms of compactness and results.
Details about the sensor's performance, size and stiffness will guideline the design, as for example the best place for the load sensor (indentation head or sample positioning system). Small displacement sensors will also help to integrate them into the sample positioning system. Finding better and smaller load sensors can solve the lack of lateral measurement during scratching in the actual SEM indenter.

Finally, a short-term work is a better control system for the actual SEM indenter.
A basic control system and user interface for indentation and scratching has been developed during this work in order to provide the necessary interface and control for testing the SEM indenter. Nevertheless, a complete control system has been out of the scope of this work, but it is indubitably a necessary step in the future.
A system with effective real time control will improve the actual system, which still has a limited performance under load control.
A future work to be done is the development of a controller for a Stick-slip indenter and scratching.
A controller must deal with the periodic load fluctuation (although small) from the slip-phase, ignoring or compensating it. Yet, it should correctly respond to real events, like for example breaks or material chip-outs. Finally, no periodic noise should be part of the final measurement, as this will only divert the interpretation of the result.

References

1. *Mechanical Testing and Evaluation*. 10 ed. ASM Handbook. Vol. 8. 2000: ASM International.
2. Kuhn, H.A., *Overview of mechanical properties and testing for design*, in *ASM Handbook: Mechanical Testing and Evaluation* H. Kuhn, Medlin, D. , Editor. 2000, ASM International. p. 49-69.
3. Vander Voort, G., *Microindentation hardness testing*, in *ASM Handbook: Mechanical Testing and Evaluation* H. Kuhn, Medlin, D., Editor. 2000, ASM International. p. 221-231.
4. Hay, J.C. and G.M. Pharr, *Instrumented indentation testing*, in *ASM Handbook: Mechanical Testing and Evaluation* H. Kuhn, Medlin, D., Editor. 2000, ASM International. p. 232-243.
5. Bhushan, B., *Springer handbook of nanotechnology*. 2004, Berlin ; New York: Springer. xxxvi, 1222 p.
6. Fischer-Cripps, A.C., *Nanoindentation*. 2 ed. 2004, New York: Springer. xxii, 263 p.
7. Kammrath & Weiss. [cited 2005; Available from: www.kammrath-weiss.com.
8. Butler, E.P. and K.F. Hale, *Dynamic experiments in the electron microscope*. Practical methods in electron microscopy ; v. 9. 1981: Elsevier/North-Holland. xv, 457 p.
9. Touchstone Research Laboratory. [cited 2005; Available from: www.trl.com.
10. Stach, E.A., et al., *Development of a nanoindenter for in situ transmission electron microscopy.* Microscopy and Microanalysis, 2001. **7**(6): p. 507-517.
11. Nanofactory Instruments. . [cited 2005; Available from: www.nanofactory.com.
12. Bangert, H. and A. Wagendristel, *Ultralow-load hardness tester for use in a scanning electron microscope.* Review of Scientific Instruments, 1985. **56**(8): p. 1568-1572.
13. Bangert, A. and A. Wagendristel, *Ultralow load hardness testing of coatings in a scanning electron microscope.* J. Vac. Sci. Technolog. A, 1986. **4**(6): p. 2956-2958.
14. Prasad, S.V. and T.H. Kosel, *The design and some applications of an in situ SEM scratch tester.* Journal of Materials Science Letters (Historical Archive), 1984. **3**(2): p. 133-136.
15. *Robosem*. 2005 [cited; Available from: www.robosem.org.
16. Rabe, R., et al., *Observation of fracture and plastic deformation during indentation and scratching inside the scanning electron microscope.* Thin Solid Films, 2004. **469-70**: p. 206-213.
17. Moser, B., et al., *Observation of instabilities during plastic deformation by in-situ SEM indentation experiments.* Advanced Engineering Materials, 2005. **7**(5): p. 388-392.

18. Michler, J., et al., *Investigation of wear mechanisms through in situ observation during microscratching inside the scanning electron microscope.* Wear, 2005. **259**(1-6): p. 18-26.
19. Wasmer, K., et al., *Cleavage fracture of brittle semiconductors from the nanometer to the centimeter scale.* Advanced Engineering Materials, 2005. **7**(5): p. 309-317.
20. Reimer, L., *Scanning electron microscopy : physics of image formation and microanalysis*. 2 ed. Springer series in optical sciences ; v. 45. 1998, Berlin ; New York: Springer. xiv, 527 p.
21. *Microscopy and microanalysis 1997*. Vol. Vol 3 Supl 2. 1997.
22. Schmaus, R. *An Introduction to materials for use in vacuum (complement)*. 2000 [cited 2005; Available from: http://www.ece.ualberta.ca/~schmaus/vacf/vacmat.html.
23. Slocum, A.H., *Precision machine design*. 1992, Englewood Cliffs, N.J.: Prentice Hall. xv, 750 p.
24. BEI-Kimco Magnetics. *Voice Coil actuators - An applications guide*. [Pdf] 2002 [cited 2006]; Available from: http://www.beikimco.com.
25. Smith, S.T. and D.G. Chetwynd, *Foundations of ultraprecision mechanism design*. Developments in nanotechnology, v. 2. 1992: Gordon and Breach Science Publishers. xv, 348 p.
26. Hysitron Incorporated. [cited 2005; Available from: www.hysitron.com.
27. Bergander, A., *Control, wear testing & integration of stick-slip micropositioning*. 2003, École Polytechnique Federal de Lausanne: Lausanne. p. 171.
28. Ferroperm. [cited 2005; Available from: www.ferroperm-piezo.com.
29. Fuji Ceramics. [cited 2005; Available from: www.fujicera.co.jp.
30. PI Ceramics. [cited 2005; Available from: www.piceramic.de.
31. PI. 2005 [cited; Available from: www.physikinstrumente.de.
32. Piezosystem Jena. [cited 2005; Available from: www.piezojena.com.
33. Cedrat Technologies. [cited 2005; Available from: www.cedrat.com/.
34. CSIRO. [cited 2005; Available from: www.csiro.au.
35. NDEAA lab. [cited 2005; Available from: //ndeaa.jpl.nasa.gov.
36. Shinsei. [cited 2005; Available from: www.tky.3web.ne.jp/~usrmotor/.
37. Elliptec. [cited 2005; Available from: www.elliptec.com.
38. Flexmotor. [cited 2005; Available from: www.flexmotor.com.
39. New Scale. [cited 2005; Available from: www.newscaletech.com.
40. EXFO Burleigh. [cited 2005; Available from: www.exfo.com/en/burleigh.asp.
41. PiezoMotor. [cited 2005; Available from: www.piezomotor.se.
42. Kleindiek Nanotechnik. [cited 2005; Available from: www.nanotechnik.com.
43. Klocke Nanotechnik. [cited 2005; Available from: www.nanomotor.de.
44. New Focus. [cited 2005; Available from: www.newfocus.com.
45. Field, J.S. and M.V. Swain, *A simple predictive model for spherical indentation.* Journal of Materials Research, 1993. **8**(2): p. 297-306.
46. Hainsworth, S.V., H.W. Chandler, and T.F. Page, *Analysis of nanoindentation load-displacement loading curves.* Journal of Materials Research, 1996. **11**(8): p. 1987-1995.
47. Oliver, W.C. and G.M. Pharr, *An improved technique for determining hardness and elastic-modulus using load and displacement sensing*

indentation experiments. Journal of Materials Research, 1992. **7**(6): p. 1564-1583.
48. Loubet, J.L., J.M. Georges, and G. Meille, *Vickers Indentation Curves of Elastoplastic Materials*, in *Microindentation techniques in materials science and engineering* P.J. Blau and B.R. Lawn, Editors. 1985, ASTM special technical publication
49. Malzbender, J., G. de With, and J. den Toonder, *The P-h(2) relationship in indentation.* Journal of Materials Research, 2000. **15**(5): p. 1209-1212.
50. Zeng, K. and C.H. Chiu, *An analysis of load-penetration curves from instrumented indentation.* Acta Materialia, 2001. **49**(17): p. 3539-3551.
51. Larsson, P.L., et al., *Analysis of Berkovich indentation.* International Journal of Solids and Structures, 1996. **33**(2): p. 221-&.
52. Malzbender, J. and G. de With, *Indentation load-displacement curve, plastic deformation, and energy*. Journal of Materials Research, 2002. **17**(2): p. 502-511.
53. Venkatesh, T.A., et al., *Determination of elasto-plastic properties by instrumented sharp indentation: Guidelines for property extraction.* Scripta Materialia, 2000. **42**(9): p. 833-839.
54. Gerberich, W.W., et al., *Elastic loading and elastoplastic unloading from nanometer level indentations for modulus determinations*. Journal of Materials Research, 1998. **13**(2): p. 421-439.
55. Oliver, W.C. and G.M. Pharr, *Measurement of hardness and elastic modulus by instrumented indentation: Advances in understanding and refinements to methodology*. Journal of Materials Research, 2004. **19**(1): p. 3-20.
56. Breguet, J.-M., *Actionneurs "stick and slip" pour micro-manipulateurs*. 1998: Lausanne. p. XI, 152.
57. Matlab. [cited 2005; Available from: www.mathworks.com.
58. Burnham, N.A., S.P. Baker, and H.M. Pollock, *Model for mechanical properties nanoprobes.* J. Mater. Res., 2000. **15**(9): p. 2006 - 14.
59. Altpeter, F., *Friction modeling, identification and compensation* 1999, EPFL: Lausanne. p. 149.
60. Ellis, G., *Control system design guide*. 2nd ed. 2000: Academic Press.
61. Armstrong-Hélouvry, B., P. Dupont, and C.C. De wit, *A Survey of Models, Analysis Tools and Compensation Methods for the Control of Machines with Friction.* Automatica, 1994. **30**(7): p. 1083-1138.
62. Johnson, K.L., *Contact mechanics* 1st ed. 1999: Cambridge University Press. 464.
63. Mindlin, R.D., *Compliance of Elastic Bodies in Contact.* Journal of Applied Mechanics-Transactions of the Asme, 1949. **16**(3): p. 259-268.
64. de Wit, C.C., et al., *A New Model for Control of Systems with Friction.* Ieee Transactions on Automatic Control, 1995. **40**(3): p. 419-425.
65. Cina, R., *Conception d'un micromanipulateur de neurochirurgie*, in *Project de 8ème semestre Microtechnique*, LSRO, Editor. 2001, EPFL.
66. SIOS. 2005 [cited; Available from: www.sios.de.
67. Sensotec. 2006 [cited; Available from: www.sensotec.com.
68. Pharr, G.M. and A. Bolshakov, *Understanding nanoindentation unloading curves.* Journal of Materials Research, 2002. **17**(10): p. 2660-2671.

69. Cook, R.F. and G.M. Pharr, *Direct Observation and Analysis of Indentation Cracking in Glasses and Ceramics.* Journal of the American Ceramic Society, 1990. **73**(4): p. 787-817.
70. Bergander, A., et al. *Monolithic piezoelectric push-pull actuators for inertial drives*. in *MHS2003. Proceedings of 2003 International Symposium on Micromechatronics and Human Science*. 2003. Nagoya, Japan: IEEE.
71. Bergander, A., et al. *Monolithic piezoelectric actuators for miniature robotic systems*. in *9th International Conference on New Actuators (Actuator 2004)*. 2004.
72. Nakazawa, H., *Principles of precision engineering*. Oxford science publications. 1994, Oxford ; New York: Oxford University Press. xiii, 267 p.
73. Smith, S.T., *Flexures : elements of elastic mechanisms*. 2000, Amsterdam: Gordon & Breach ;. xiv, 430 p.
74. Henein, S., *Conception des guidages flexibles*. Réimpression corr. ed. 2004, Lausanne: Presses Polytechniques et Universitaires Romandes. 225.
75. Micro Photonics. [cited 2006; Available from: www.microphotonics.com.
76. CSM Instruments. [cited 2006; Available from: www.csm-instruments.com.
77. Fischer-Cripps Laboratories Pty. [cited 2006; Available from: www.ibisonline.com.au.
78. Stott, F.H., *The role of oxidation in the wear of alloys.* Tribology International, 1998. **31**(1-3): p. 61-71.
79. Halling, J., *Principles of tribology*. 1975, London: Macmillan. XIV, 401.
80. Kong, H.S., E.S. Yoon, and O.K. Kwon, *Self-Formation of Protective Oxide-Films at Dry Sliding Mild-Steel Surfaces under a Medium Vacuum.* Wear, 1995. **181**: p. 325-333.
81. Shirazi, M., L. Karuppiah, and S. Belinski, *Vacuum mechatronics*. The Artech House materials science library. 1990, Boston: Artech House. 87-110.
82. Maurer Magnetic. [cited 2006; Available from: www.maurermagnetic.ch.
83. Mumetal. [cited 2006; Available from: www.mumetal.com.
84. Magnetic Shield. [cited 2006; Available from: www.magnetic-shield.com.
85. ASMEC. [cited 2006; Available from: www.asmec.de.
86. Chudoba, T., et al., *Comparison of nanoindentation results obtained with Berkovich and Cube Corner indenters*. 2006, Philosophical Magazine & Philosophical Magazine Letters.
87. Rabe, R., *SEM In-Situ Indentation Apparatus - A new tool for the characterization of mechanical properties at small length scales*, in *Euromat 2003*. 2003: Lausanne, Switzerland.
88. Moser, B., et al., *Strength and fracture of Si micro-pillars: A new SEM-based micro-compression test*. 2006 (Unpublished).
89. Chudoba, T. and F. Richter, *Investigation of creep behavior under load during indentation experiments and its influence on hardness and modulus results.* Surface and Coatings Technology, 2001. **148**(2-3): p. 191-198.
90. Cheng, Y.T. and C.M. Cheng, *What is indentation hardness?* Surface & Coatings Technology, 2000. **133**: p. 417-424.
91. Li, X. and B. Bhushan, *A review of nanoindentation continuous stiffness measurement technique and its applications.* Materials Characterization, 2002. **48**(1): p. 11-36.
92. Li, X. and B. Bhushan, *Fatigue studies of nanoscale structures for MEMS/NEMS applications using nanoindentation technique.* Surface and Coatings Technology, 2003. **163-164**: p. 521-526.

93. Marshall, D.B. and B.R. Lawn, *Indentation of brittle materials*. Microindentation techniques in material science and engineering, ed. Blau/Lawn. Vol. 889. 1986, Philadelphia: ASTM special publication.
94. Morris, D.J. and R.F. Cook, *In situ cube-corner indentation of soda-lime glass and fused silica.* Journal of the American Ceramic Society, 2004. **87**(8): p. 1494-1501.
95. Morris, D.J., S.B. Myers, and R.F. Cook, *Sharp probes of varying acuity: Instrumented indentation and fracture behavior.* Journal of Materials Research, 2004. **19**(1): p. 165-175.
96. Page, T.F., Pharr, G.M., Hay, J.C., et al, *Nanoindentation characterization of coated systems: P:S2 - a new approach using the continuous stiffness technique.* Materials Research Society Symposium, 1998. **Proceedings 522**: p. 53-64.
97. Roth, A., *Vacuum technology*. 3rd, updated, and enl. ed. 1990: North-Holland. xx, 554 p.
98. Halliday, B.S., *An introduction to materials for use in vacuum.* Vacuum, 1987. **37**(8-9): p. 583-585.
99. Halliday, B.S., *Cleaning materials and components for vacuum Use.* Vacuum, 1987. **37**(8-9): p. 587-591.
100. Miyoshi, K., *Considerations in vacuum tribology (adhesion, friction, wear, and solid lubrication in vacuum).* Tribology International, 1999. **32**(11): p. 605-616.
101. Campbell, P., *Permanent magnet materials and their application*. 1994, Cambridge [England] ; New York: Cambridge University Press. x, 207 p.
102. Magnet Sales. [cited 2006; Available from: www.magnetsales.com.
103. BBA Magnete. [cited 2006; Magnets and magnet systems]. Available from: www.bba.ch.

Blank page

Annexes

Blank page

I Annex: Simulink implementations

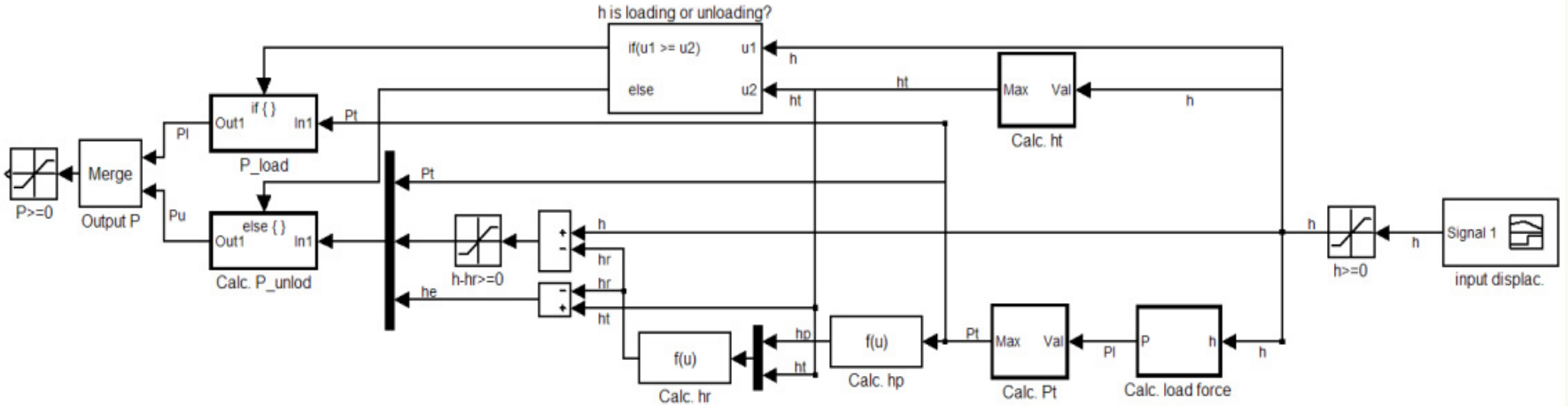

Annex Figure 1: Simulink implementation of Loading –Unloading described in Paragraph 3.2

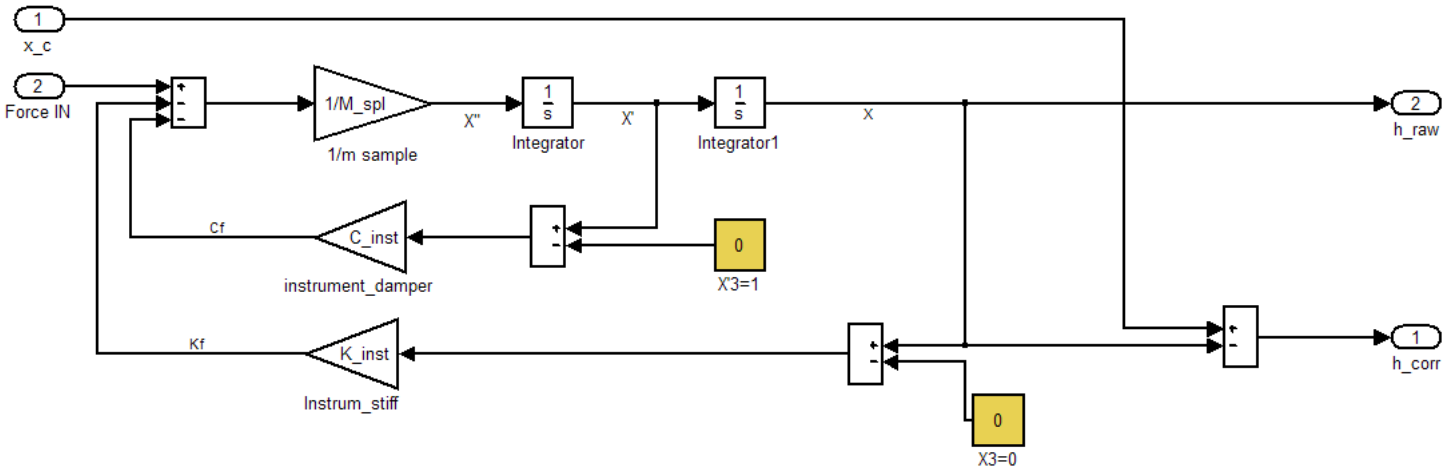

Annex Figure 2: Simulink implementation of the frame stiffness described in Paragraph 3.3

II Annex: Review of partial reloads in indentation

Creep

The creep behavior is a time dependent material characteristic. In indentation, it appears with more or less intensity at each time that the material is plastically deformed. Creep influences the slope of the loading, as well as the first part of the unloading curve [89]. Thus, the determination of material's mechanical properties must consider creep in order to obtain correct values.

Cube Corner stick-slip indentations in Zr-BMG and GaAs have presented creep. The P x h curve has been obtained through a fast indentation at high loads, which initially made it difficult to remark any differences arising from creep (that are normally small changes, in order of several nanometers).
A close verification of these curves has shown that not each reload after a slip phase follows the unloading path (ex. Annex Figure 3 for BMG). There is a small gap between same peak loads. GaAs and Zr-BMG are two distinct materials, making it difficult to find a general explanation for the mechanism that makes partial unloads not follow the same path (for example BMGs have a characteristic deformation phenomena characterized by a serrated flow around the imprint).
The name "creep" simply describes this situation, but not the real mechanism behind this continuous deformation. The acquisition rate does not permit a characterization of the fast unloading (hiding if hysteresis is also present), but contains enough points to describe the reload. In this sense, the observed phenomenon is not a measurement artifact.

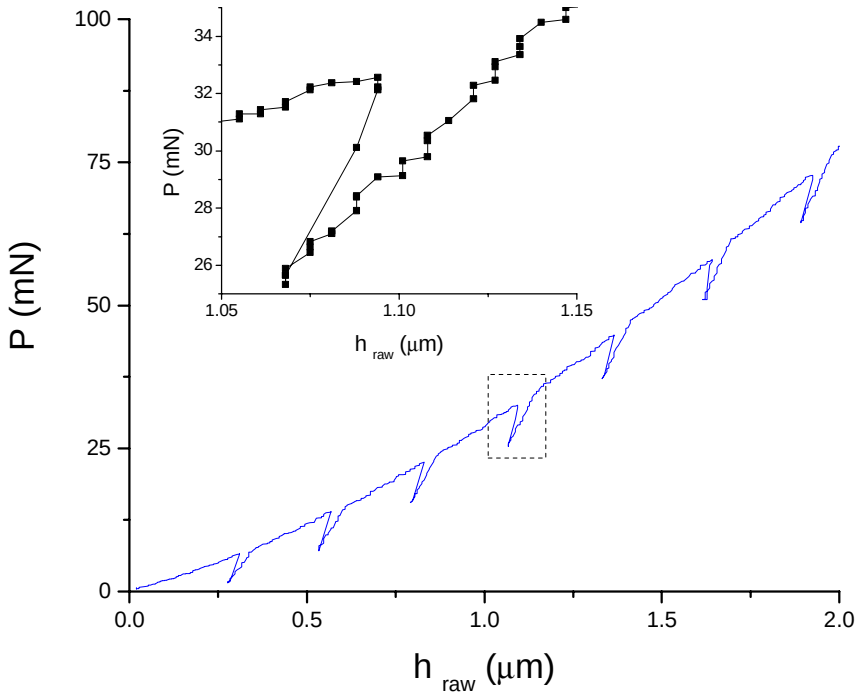

Annex Figure 3: Detail of the observed phenomena in a 200mN CC indentation in Zr-BMG

Each unload has contributed to add a small gap in the curve, but the final shape (called curve envelope) has not changed – at least not for the used experimental conditions.
As a result, it is not yet clear how a series of fast partial unloads could modify the P x h curve shape. Thus, it is necessary to analyze some situations where stick-slip indentation may face problems.
_ ***Constant load rate***. The loading time (Annex Figure 4) has an influence in the calculated Hardness and Modulus, since creep also depends on the indentation velocity. In IIT devices it is common to give a load rate as input. In stick-slip indentation, each drop in load will be compensated by the control system that accelerates the actuator to reach the set load. The higher the jump-back is, the more will be the acceleration over the actuator. The real load rate is thus an average of an oscillating load. This can also be a problem for strain rate sensitive materials.

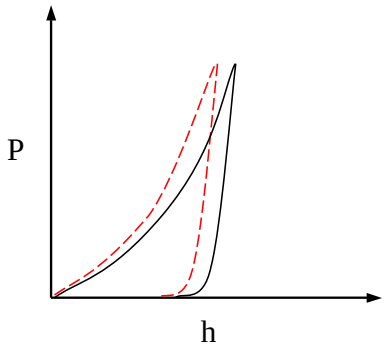

Annex Figure 4: Effect of loading time over the P x h graph (no holding time). Faster loading times can shift the P x h curve to left. Longer loading can have similar effects as long holding time.

Holding period at maximum load. A common way to minimize the creep effect and different load rates is to apply a holding period at the maximum load, (as the creep reduces with time, at a rate of a few nanometers per second). Usually, the suggested holding time is in the order of 10-20s (depending on the material). Nevertheless, it can be much longer for materials with high creeping rate. It is the case for Aluminum. As stick-slip actuators have the ability to work in a scanning mode, there should be no need of a slip phase. The requirement is that the creep rate stays inside the actuator scanning range available after one step. In this case, there should be no difference between the continuous or the stick-slip mode in this stabilization process. The problem will occur if the creep rate is too high, requiring steps and not scanning mode to keep the load. In this case, creep stabilization may be a problem and the suggested holding time could simply not be enough.

Strain rate sensitivity and material hardening

As the material is mechanically deformed, the number of dislocations increases and starts to interact more, thus the stress required to yield the material is higher. This behavior has a direct influence on the P x h curve.
The plastic deformation also occurs during unloading, as when the elastic constrained material around the imprint can cause more dislocations as the material tries to return to its original shape but is blocked by the plastically deformed region. In this case, partial reloads could cause some concerns.

However, at least for a wide range of elastic-perfect-plastic materials (metals and ceramics) as presented by Pharr et. al. [68], unloads plasticity (based on complete unloads) has almost no influence over the P x h behavior. This indicates that for these materials (presented as a relation of Elastic modulus and Yield strength (E/σ_y)), there should be no concern about having reloads during the test.

More care must be taken if the material shows dependence to the application of strain. A material that follows a power-law creep response (as non linear solids) has its response dependent on the strain rate and can be described following Eq. 1.

$$\sigma = K \dot{\varepsilon}^{m_H} \qquad \textbf{Eq. 1}$$

Where $\boldsymbol{\sigma}$ is the stress, $\dot{\varepsilon}$ is the strain rate. $\boldsymbol{K}$ (strengthening coefficient) and $\boldsymbol{m_H}$ (work hardening exponent) are material constants. The strain rate is represented as:

$$\dot{\varepsilon} = \frac{dh}{dt}\frac{1}{h_p} \qquad \textbf{Eq. 2}$$

For strain rate sensitive materials, the indentation depth rate (dh/dt) has an influence on the indentation force and hardness, as can be found, for example, in [90]. In this case, an experiment with constant load as shown in Annex Figure 5, or constant displacement rate may have a direct influence on the non-linear behavior of stick-slip actuators.

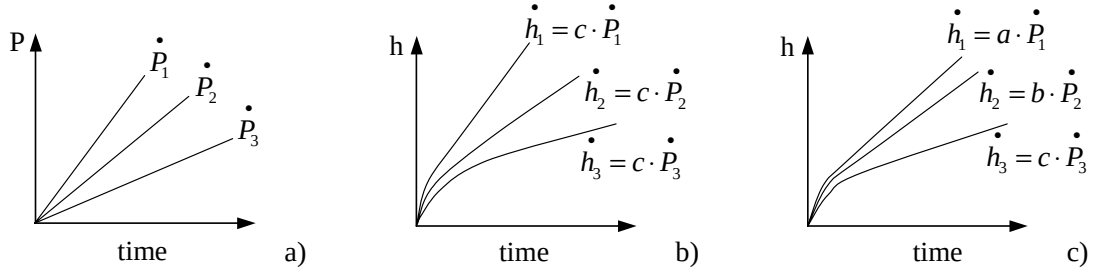

Annex Figure 5: Material response to a three constant rate loading test ($\dot{P}$) in a same material a) Three different $\dot{P}$ are applied, b) response of a strain rate insensitive material – penetration rate $\dot{h}$ is directly proportional to $\dot{P}$, c) response of a strain rate sensitive material – $\dot{h}$ will not be proportional to $\dot{P}$.

To reach a set displacement, the total displacement of an indentation tip driven in a stick-slip mode will be higher (as the jump-back displacement must be counted) than when driving in a continuous mode.
To keep a given load or displacement rate, the tip must be driven faster than in continuous mode, since the rate in stick-slip is calculated over an average velocity. Jump-back size also increases with the reaction force. Thus, the average velocity can only be kept the same if the instantaneous velocity increases.
The contribution of the stick-slip average velocity over the mechanical properties of strain sensitive material can be roughly evaluated using Eq. 2 and the parameter *m* (that has values between 0 and 0.5 for most metals). The difference in velocity

(continuous mode and stick-slip mode) can be experimentally measured or estimated using the equations presented in Chapter 3.

Continuous stiffness measurement (CSM)

This measurement is characterized by superposing a sinusoidal signal over the base load signal, usually at frequencies between 40 and 60Hz. Since the indenter is calibrated (its eigenfrequency is well know), it is possible to analyze the response differences before and during the indentation.
As the tip penetrates the material, the contact stiffness (*S*) changes and this also changes the dynamic of the calibrated system. Thus, stiffness can be determined from the displacement signal or from the phase difference between force and displacement. The advantage of this method is to get the contact stiffness during the entire loading and not only at the unloading part. It is an attractive method for analyzing mechanic properties in thin multilayer films, polymers, creep measurement, fatigue, etc. How this is calculated, its applications and advantages or limitations will not be discussed here, but can be found elsewhere [5, 47, 91].

This technique shows that a harmonic signal can be presented as a component of the basic driving signal, without interfering with the measurement. The amplitude of the force oscillation is kept sufficiently small, not interfering with the deformation process [47]. The harmonic signal (given in load or displacement) is usually reported to be quite small, often in the order of μN or a few nm, but higher (mN or dozen of nm) in polymers.
From the literature, it is not clear if a rule exists specifying the maximum allowable amplitude. As the test is applied at high frequencies, the limitation of the maximum amplitude may be also related with the introduction of a cyclical stress on the material. For example higher load amplitudes (45μN over a load base of 100μN @ 45Hz) have been reported for studying fatigue effect in Silicon MEMS [92].
Discussions involving the possibility to use stick-slip actuators for indentation have quite often mentioned the CSM technique as an example presenting loading-unloading cycles during indentation. The main oversight here is to neglect the type of stick-slip driving signal (a saw tooth), which can introduce a shock stress. The unloading amplitude is also higher than found in CSM.
Nevertheless, the slip phase contains some information that could be used in a similar way as CSM and let here simply as an idea for a further study or application.
The slip phase acts as a step response over the instrument. An oscillatory movement is present after each step and can be detected directly through the carrier displacement or through the load (although it is more difficult to measure it). The drop in load is the input force. The system stiffness and damping can be calculated analyzing the frequency and the amplitude decay. As the indenter penetrates the material, the system's response will change, providing extra information from the indention.

Brittle materials

Perhaps the biggest concern of the fast unload and reload cycles occurs when brittle materials are tested, since cracks are reported to be generated during loading and/or unloading.

Crack formation

As the material is deformed, the volume of the imprint induces residual strain in the material. A confined elastic matrix surrounds a hemispherical plastic zone. During unload, the elastic strained material located outside the plastic zone tries to recover but is blocked by the deformed material [6, 93]. This creates a region under tensile stress, inducing the appearance of certain types of cracks. If the tip is removed at once, all the elastic constrained material will immediately react and all the internally stored energy (related with the material elastic modulus) will be released at once (a shock), probably creating new cracks or at least it may provide enough energy to propagate the existing ones.

Material Indentation by a sharp indenter generates several types of cracks. Some of them are schematized in Annex Figure 6.

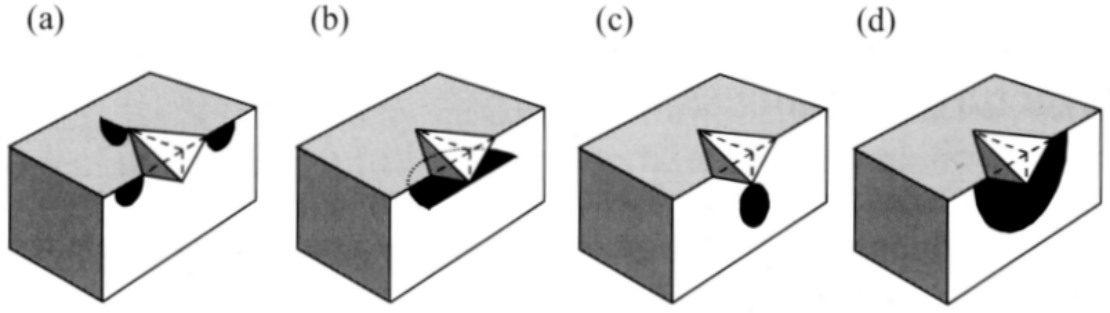

Annex Figure 6: Type of cracks (Vickers indentation). a) radial, b) lateral, c) median d) half-penny [6]

Additionally, there are also cone cracks (typically associated with elastic loads of spherical or flat-punch indenters), secondary and shallow radial cracks [69], not shown in Annex Figure 6.
Radial cracks are oriented normal to the sample surface and appear at the edges of the indentation imprint. They remain often close to the surface. Lateral cracks occur below the surface, near the (imprint) base of the deformation zone. They are horizontal and symmetrical to the load axis and often extended to the surface. A median crack also propagates parallel to the axis of loading. It is generated under the plastic deformation zone and often aligned with the corners of the imprint. Median cracks may extend upwards to the surface and join with radial cracks forming full circles, or circular segments forming half-penny cracks [6, 69]. Often the final crack morphology is of the half-penny type. However, it is only fully observed after a destructive material analyze (Fractographie), or in optically transparent materials (using optical microscopes).

Cracks are formed during loading and/or unloading. Nevertheless, it is not always easy to spot them, or to have a correct identification of their type.
For example, it has been found that lateral cracks closes and median crack reopen during reloads in Soda Lima glass (Vickers indenter) [6].
The final crack appearance can thus be a combination of cracks initiated in both events (for instance, as it is believed how half-penny cracks are formed in some materials).

Stick-slip indentation may favor crack formation, as loading-unloading is present in each step. Since cracks appear on the material's surface or under the imprint, the loading-unloading process may anticipate a chip formation or a material fracture around the imprint. A very fast unloading can also induce a shock stress, that can feed, for example, a lateral crack. In this case the material may not absorb the energy as easily as during a slow unload.

Each material has a resistance to crack creation or propagation (fracture toughness), so that the internally induced stress will not necessarily contribute to generate cracks.
Materials with high fracture toughness should be more insensitive to stick-slip indentation.
For a given combination of material, maximum load and tip, there is a range during loading or unloading (as a function of a percentage of a maximum load), where cracks are not detected, or where at least they not grow. Annex Figure 7 and Eq. 3 exemplify one of the common ways to determine the fracture toughness $\boldsymbol{K_c}$ (MPa $m^{1/2}$) through indentation. $\boldsymbol{E}$ and $\boldsymbol{H}$ are material properties, $\boldsymbol{P}$ is the applied load, $\boldsymbol{c}$ is the crack length and ξ is a parameter describing the indenter geometry.

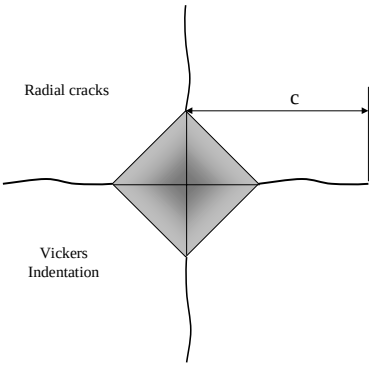

$$Kc = \xi\left(\frac{E}{H}\right)^{1/2}\frac{P}{c^{3/2}} \qquad \textbf{Eq. 3}$$

Annex Figure 7: Fracture toughness parameters

A review about crack formation has been presented by Cook [69], with a good illustration of the different crack events (during load and unload), thanks to an indenter assembled over an inverted optical microscope. The tests have been carried out with samples having different structural and mechanical properties (crystalline and amorphous materials) using a Vickers tip as indenter and peak loads of 40N@0.5µm/s. The test has shown that radial cracks have started almost immediately in the tested crystalline materials (around 0.8N), while most of the observed new cracks (ex. radial or lateral) during unloading did not appear before unloading up to 65% of the peak load.

The threshold load to initialize cracks disappears when sharp indenters are used. For some of the materials tested, cracks (as radial cracks) are reported to appear immediately [94-96]. For example, during the formation of the imprint, a Cube Corner indenter displaces more than three times the volume of material as the Berkovich (at the same set load), creating greater stresses and strains around the imprint.

If the combination of a certain tip with stick-slip indentation can favor crack formation or create longer cracks, this also means that it could have a direct influence on the material's characterization. For example, if the goal is to calculate fracture toughness, an instrument that interferes with the measurement, inducing longer cracks, will output a more "conservative" $\mathbf{K_c}$ (Eq. 3). The main problem, in this case, will be the difficulties to compare the measurements of different instruments.
However, for material characterization based on the analysis of P x h curves, failures will only be a concern if the graph is effectively changed by the presence of cracks or chips. Thus, these events should be first detectable.

Observing the P x h graph can be used to identifying if something happens just after each actuator slip phase. Still, this cannot always be utilized.
Complete reloads in soda lime glass (with Vickers) have been reported in [69] to leave an extremely damaged imprint, including chipping outs. Yet, no perceptible changes have been noticed in the P x h graph. In normal conditions, no sudden tip displacement (called pop-in) or change on the graph's final shape has been connected with the crack event (since it has been an in-situ test). The unique event registered, as mentioned, has been due to a chip out observed during reloading Sapphire. Similar results have been observed in [45, 95]. Radial cracks and damaged imprints have been present in the tested materials, but no changes have been found in the graph.

The P x h graph from experiments realized using the SEM indenter have not shown an evident difference due to a crack event when using Berkovich or Cube Corner tips, except with CC and Fused Silica.
This is a typical combination known to have an impact on the P x h graph. In the literature, indentations with acute indenter, as CC, have been reported to cause a small pop-in in the P x h curve. This characteristic has also been used to help fracture toughness calculation (in fused silica and glassy carbon [45]). If a pop-in is present during loading, the unloading part differs from a P x h curve that has not shown this event.

Morris et al. [95], have reported that pop-ins have changed the unloading curve (e.g., for fused silica a ≈ 11% difference in the power law fitting parameter $\boldsymbol{m}$ has been calculated). However, during the tests presented in this chapter, it has not been possible to observe this occurrence. With or without pop-in, the curves' overlap (not shown here) have had a good visual agreement (using raw data).
In [95], it has been also shown that cracks could have an influence on the P x h curve, but not in the same way as pop-ins do. Different tips (from sharp to wide apex angles) have been used to induce cracks. In materials that have presented cracks (most with sharp tips), the unloading curve (normalized using $\mathbf{h_p}$ and not $\mathbf{h_{max}}$) has not overlapped. Materials that have not presented cracks have had superposable unloading curves for all the tips utilized.
Thus, a test with and without (externally visible) cracks should have output different P x h curves. But this has not been often detected in the tests, even using a commercial nanoindenter. If a crack has influence over the graph, it should be caused by the influence of more than one type. Radial cracks and shallow lateral cracks have been visualized during the tests in GaAs. Nevertheless, no sign of any event has been registered in the P x h graph. On the other hand in-situ SEM indentations with a

wedge tip in GaAs have shown pop-in that seems to be connected when half-penny cracks reaches the surface[79].

Certainly with better time and force resolution, some of the events, as for example a material breakout, can be registered. On the other hand, there are some examples in the literature [69] of the fact that cracks or chips formed in glasses or ceramics do not appear to interfere in the final shape of the P x h graph or even are not registered on it.

[79] Cédric Pouvreau – EMPA-Thun, Private communication.

III Annex: Design for the SEM environment

Vacuum

Vacuum basics

The following relations indicates the most common units for vacuum:
1atm = 1013.25mbar = 101325 Pascal (Pa) = 760 Torr [78]

The vacuum level is defined by the following range: [81]

Low vacuum (LV)	-	From normal atm down to 3333Pa
Medium vacuum (MV)	-	From LV down to 1.333Pa
High vacuum (HV)	-	From MV down to $1.333x10^{-3}$ Pa
Very high vacuum (VHV)	-	From HV downs to $1.333x10^{-6}$ Pa
Ultra high vacuum (UHV)	-	From $1.333x10^{-9}$ Pa and beyond

For example, the typical operational range of the Zeiss 962 SEM is mainly in the high vacuum range.
The vacuum obtained through a vacuum system depends on the rate of gas influx compared to the rate of the gas pumped from the system. The pumping rate is related to the pump type, which will nevertheless not be detailed here. Gas flux is controlled through a proper material selection and design. A part of the air influx comes through the vacuum system/vacuum chamber (leaking). However, another part is originated internally, what is called outgassing of the components.

Materials used in the vacuum environments should have low vapor pressure, even at maximum operating temperature [81]. An alloy that contains some high vapor pressure elements (as for example with low bowling points) can start to vaporize at a given temperature. This phase transition occurs with more intensity is the vacuum increases. For instance, Zn in HV has its vapor point at 150^{o}C. Materials used in the SEM indenter should be selected in order to avoid this problem.

Materials have adsorbed gases, trapped and dissolved during manufacture and process.
Adsorption is a process where molecules are attracted to and become attached to the surfaces of a solid. It has a chemical or a physical origin. A material placed in a vacuum environment, will thus start outgassing (for more details see Chapter 4 of *Vacuum technology* [97])
Outgassing depends on the total of gas absorbed, the occurrence of the process, surface characteristics and temperature. Outgassing is measured as the outgassing rate divided by the unit area (as Torr·l/s·cm^2).

Typical structural materials for vacuum are Austenitic stainless steels (as 304 – DIN 1.4301, that also is non-magnetic), Standard steel (care must be taken to protect it against corrosion), Aluminum and its alloys (anodizing or alloys with high Zn content

should be used with care) [22, 98]. Nickel alloys, Cu alloys (as Arcap® - also non-magnetic) and Titanium are also other materials with good applicability to vacuum and are used in SEM manipulators and instruments devices.
Usually, the major problem with metal outgassing is not related to the material itself but how a component has been designed or finished. Oxidation and rough surfaces (as sandblast finishing) are places where gasses are adsorbed or trapped. Porosity, cracks and cavities are other examples.
An important design consideration is to **leave holes completely unblocked**. Places that include screw fixation must have their ends vented to avoid trapped air or special screws (with a pass-through hole) must be used. This avoids what is commonly called as virtual leak.
Ceramics and glasses can be used in vacuum environment. Aluminum oxide ceramics can be found with diverse porosity but the pores are completely closed. Piezo actuators can also be used in vacuum without disturbing it.

A strong outgassing source can come from materials found in cables, lubricants, sealants, adhesives and also from organic materials deposited during handling or instrument storage.
Lubricants must be customized for vacuum applications (as having low vapor pressure – less volatile). Dry lubricants also must be made vacuum compatible.
PVC cables or similar materials will outgas. Cables with PTFE isolators are preferred.
Adhesives have similar problems. However, the outgassing rate reduces considerably after curing (bi-component glues are preferable, as for example epoxy glues).
Handling will leave impurities, as finger grease, over the instrument surface. Cleaning with a proper solvent can remove them. Yet, material cracks or small regions (as joint gaps) can trap the solvent.
The outgassing rate can be provided by the manufacture of each component like glue, lubricants and sealants, but it will be more difficult to be found for cables, ceramics or other materials used during construction. A good source is the NASA's Outgassing Data for Selecting Spacecraft Materials [80].

Outgassing and cleaning procedures
An outgassing rate consideration gets more importance in UHV systems as it can effectively increase the amount of time necessary to reach the target vacuum level. For this reason, UHV compatible component are backed before they are installed inside the vacuum chamber. As the degassing process increases with temperature (it is related to each material vapor pressure), backing speeds up degassing and it is a 'have to' procedure before utilization. The baking process is carried out at temperatures around 150-200^{o}C and under vacuum.
However, there are alternative outgassing/cleaning processes. They can be not so good as bake out, but are still enough for HV-VHV systems (see for instance [99]). Degassing chambers, ultrasonic bath, solvent cleaning, etc. are some examples. It is always important to verify the compatibility of each instruments part with the chosen cleaning process. A device designed for a SEM should be easily cleaned.

Heat dissipation in vacuum conditions

Conduction: Components are placed in contact, providing a path for the heat flow *Q*, following the relation:

[80] Online version is available at http://outgassing.nasa.gov

$$q = -c_k \frac{\partial T}{\partial x} \qquad \textbf{Eq. 4}$$

$$Q = qA$$

Where q is the heat flux, c_k is the thermal conductivity of the material, Q is the heat transfer rate and A is the area perpendicular to the heat flow direction.

Convection: Is a form of heat transfer where a fluid is involved. In this case, the rate flow Q is function of the temperature difference and not the temperature gradient.

$$Q = h_{flu} A(\Delta T) \qquad \textbf{Eq. 5}$$

Where h_{flu} (W/m^{2o}C) is the fluid conductive heat transfer, T is the overall temperature difference between the solid and the fluid.

Radiation: Through electromagnetic radiation emitted by a body, due to its temperature.

$$Q = F_\varepsilon F_G s A(T_1^4 - T_2^4) \qquad \textbf{Eq. 6}$$

Where s is the Stefan-Boltzmann constant (5.669x10-8 W/m^2.K^4), T_1 and T_2 are the absolute temperatures of the first and the second body (K), F_ε is the emissivity function and F_G is the geometric view factor function.
Or, to simplify, in the case of a cylindrical vacuum chamber much larger than the body (surface of the body (A_1) – inner surface of the chamber (A_2) ≈ 0):

$$Q = s A_1 \varepsilon_1 (T_1^4 - T_2^4) \qquad \textbf{Eq. 7}$$

ε_1 is the emissivity of the body.

Conduction is the first way in which the heat from the instrument is removed. However, the fixation system between the instrument and the SEM stage can be quite small, reducing flow (proportional to the area). Furthermore, each connection has an inherent thermal resistance. The end of a thermo path is the SEM chamber. This explains why a system can need a long time for thermo stabilization.
Convection is used to remove high amounts of heat, as for example when the sample must be heated up. Forced convection is a usual procedure to remove heat. This implies to use, for example, a chamber feed-through to circulate the fluid from the outside to the inside, in a closed system. There are also conductions involved in the transfer, so the cooling system needs to be placed as near as possible to the heat source.
Finally, radiation will only be an efficient way to remove heat if the body is at a high temperature or the chamber is kept at a very low temperature. In addition, the instrument body must be emissive, what can be done using vacuum compatible coatings (ex, carefully anodized).

A practical example

During the design of stick-slip nanopositionig tables, optical encoders have been utilized to measure the displacement. At that time, a truly vacuum version of the optical head has not been available and a standard version has thus been utilized to verify its compatibility with the SEM environment. The typical vacuum inside the SEM has not directly disturbed the sensor. On the other hand, each sensor had its own interpolator that has been placed in the tables' body (cable connecting the optical head

and the interpolator had a limited length). The heating produced by each interpolator has thus been transferred to the positioning system body. The equilibrium has been reached once the body has been at almost 40°C, measured where the sample is placed.
Today, a vacuum version of this same sensor includes some modifications in cabling in order to generate less outgassing and the interpolator is now placed outside the vacuum chamber. However, the drawback is the need of more wires. With the interpolator inside, only four wires have been necessary to transmit the data through the SEM chamber (plus one unique cable providing power for all sensors). With the interpolator outside, there is a minimum of six wires only for data transmission.

Sensors calibration and operation

An in-situ calibration can be a difficult task. The reference instruments must also be placed inside the vacuum chamber and they must have previously been calibrated in this condition.
A quick verification can be realized making, the same test with and without vacuum inside the chamber. Nevertheless, some steps must be respected, as to let enough time for pressure and thermo equilibrium.
For example, some load cells are delivered hermetically sealed. As the vacuum increases, the difference between the internal and external pressure increases. Thus, the value drifts. Vacuum compatible measurement systems are quite often vented to have the same inner and outer pressure, avoiding induced stress due to internal pressure.
Strain gauge bridges are essentially resistances (usually from 350 to 5000 Ohms) being fed by a voltage of 3 to 5V. If the heat cannot be removed from the load cell, the value will drift, as thermo stress will be involved.

Friction changes in Vacuum

It is often assumed that the stick-slip interface has no lubricants. This is true that solid or liquid lubricants are not intentionally added, although they are nevertheless present on the interface as thin oxide films, water vapor and other adsorbed contaminants (as hydrocarbons).

Taking the example of oxide layers, if the actuator contact pressure is high enough to break it, wear will be present and the friction coefficient can change. Thus, a quite complex mechanism can be originated, as [78]:

- Oxide debris are released in the wear trace, they can be lost (wear) or be placed in a new position. Depending on the load and the size of the wear debris, a smooth polished surface can be formed (mild wear – low loads) up to very high wear (big particle size, high loads).
- As these debris move freely over the wear trace, they break in small parts and finally start to accumulate in small fends or grooves, forming compact and hard layers, acting as load bearings.
- The bearing surface can have its texture modified (as through heating), creating thus a glazed surface that contributes to the sliding of the parts.

Generally, it is accepted that oxide layers protect the material. However, the lack of an oxidant gas in a fresh exposed material will not create a new layer, changing the tribology of the foot-carrier interface, at least for materials with a high potential of reaction.

Friction coefficients

Each pair of materials (foot-carrier) will present a specific behavior, as the environmental conditions change. Friction measurements are very dependent on the test conditions. To affirm that the vacuum grade has changed the friction coefficient due to the reduction of oxygen levels in the environment is an incomplete explanation if, for example, the changes of humidity levels have not been considered. The reason is that there has been more than one variable changing during the experiment.
The lack of fully controlled variables could be a reason why it is difficult to find directly a general table showing the different friction coefficients in function of the vacuum grades (what could be very helpful is used, for example, during jump-back optimization). Thus, this small review focuses more on the general aspects or changes rather than giving specific values (presented here as simply indicative values).

Ultra high vacuum environments

As it has been shown in Chapter 5 (paragraph 5.4.1.1), devices operated in UHV have to be baked under vacuum conditions in order to eliminate impurities adsorbed by the material. Otherwise, they start to outgas, making difficult to reach UHV levels. However, this same unwanted layer in a device works also as a lubricant, as naturally found in a stick-slip actuator's foot-carrier contact.
If the material is 'atomically cleaned', there will be a strong molecular attraction at the surface, facilitating adhesion and cold welding between both parts. Thus, it is expected that if the vacuum changes into UHV levels, the friction coefficient will increase, as well as the wear rate. A review of wear, friction and adhesion under UHV conditions is found in [100] (from metals to non-metals pairs).

High Vacuum

With a certain amount of an oxidant gas presented inside the vacuum chamber, it is expected that this protective thin film formed at interface. Still, it will behave differently, as when having an UHV condition.
Stick-slip wear traces using sapphire-stainless steel (1.4310) pairs have shown a certain amount of iron oxide inside and around the trace [27]. Additionally, the contact foot-carrier contains another wear phenomena, called fretting[81]. Fretting can contribute to create a locally high temperatures due to quick deformations of the contact, catalyzing oxidization.
When an actuator drives the carrier, the contact wears and the exposed material reacts again with the remaining oxygen of the environment. As the vacuum increases, less oxygen will be present in the chamber. Thus, the oxide layer will take longer to form. However, oxide layers with different thickness (from thin but tenacious ones to thick and brittle ones) can have quite different behaviors.
The contact between steel against steel in vacuum is an example. At a vacuum of 0.13 Pa, wear has been detected as being lower than in normal pressure but for UHV, the situation has been worse than found in air [79]. Friction coefficients have shown the same behavior that has been observed for mild steel pairs [80]. Friction coefficient has diminished from 0.6 to 0.3 in medium vacuum and increasing to 0.9 for high vacuum environment.

[81] A high frequency, very small amplitude movement between two bodies in contact.

A vacuum environment generally increases the friction coefficient[82] in most metal-metal or metal-non-metal pairs. For non-metal – non-metal pairs, the increase in friction has also been observed, but the mechanism is different (as there is no re-oxidation). As the thin film between the different parts is being outgased (as oxygen or vapor), the friction increases.

Magnetic systems in the SEM

Permanent magnets

As a part of a conceptual design, the goal of this topic is more to provide inputs and show realizations than to provide the necessary background to understand the basics of permanent magnet materials. Still, some basic concepts are given. The first ones are the unities of some physical systems.

Table 1: Common units for permanent magnets in different physical systems

Unit	*Symbol*	*CGI*	*SI*	*English*
Flux	Ø	Maxwell	Weber	Maxwell
Flux Density	B	Gauss	Tesla	lines/in^2
Magnetic force	F	Gilbert	Ampere turn	Ampere turn
Magnetizing Force	H	Oersted	Ampere turns/m	Ampere turns/in
Length	L	cm	m	in
Permeability (in vacuum)	μ_v	1	$0.4\pi \times 10^{-6}$	3.192

Permanent magnets are made of highly magnetocrystaline anisotropy materials. They present this valuable characteristic only if the material is polarized by and external electromagnetic field (often from 3 to 5 times its H_{ci} - the external demagnetization force that the material can withstand). This energy to align its internal magnetization vectors up to its saturation (complete aligned) is thus stored inside the material[83], conferring its magnetic properties. The more energy the material can afford, the stronger are its magnetic properties. However, the polarization can be lost if a stronger opposite field is applied or, more commonly, if the magnet is heated up (see Annex Figure 8b).

A permanent magnet is characterized by its *B* (Tesla) - *H* (ampere turns/m) curve (flux density x magnetizing force - Annex Figure 8a). This hysteresis curve shows the material's behavior as it is magnetized up to its saturation (1st quadrant), demagnetized and saturated on its opposite field (3rd quadrant) and again re-magnetized to close de cycle. The three important points of this curve are: [101, 102]
B_r: Is the remanent flux density, the maximum flux that the magnet can produce under closed circuit conditions.
H_c: Is the coercivity of the material. It shows where the magnet demagnetizes under influence of an opposite magnetic field.

[82] An opposite example is Molybdenum Disulfide. The friction decreases as the vacuum increases.
[83] If the material can keep this orientation, it is sometimes called a 'hard' material. On the other hand, if the material only can show magnetic properties with help of an external source, it is called 'soft'.

Finally, BH_{max} is the point called the maximum energy product. In this point, the material has the highest BxH (kJ/m^3) product and the stronger flux energy delivered into an air gap. The higher this product is, the smaller the volume of the magnet needs to be.

For designed stick-slip miniature stages, the choice is a material that has the maximum energy product, as NdFeB types [84]. This could simply be translated as the maximum mechanical attraction force with the smallest volume. Neodymium Iron Boron (NdFeB) and Samarium Cobalt (SmCo) are those called 'rare earth' magnets. Alnico (Al-Ni-Fe-Co alloys) is another class of permanent magnets, but with a BH_{max} that is not as strong as the class before. A chart comparing these different materials is presented in Annex Figure 8b
The 'attraction force' generated by a magnet depends on its shape, size and available polarizations. Thus, these features can limit its applications. Typical shape examples are cylinders, disks, rings, cubes and rectangles (available in different combinations of dimensions - Annex Figure 9).

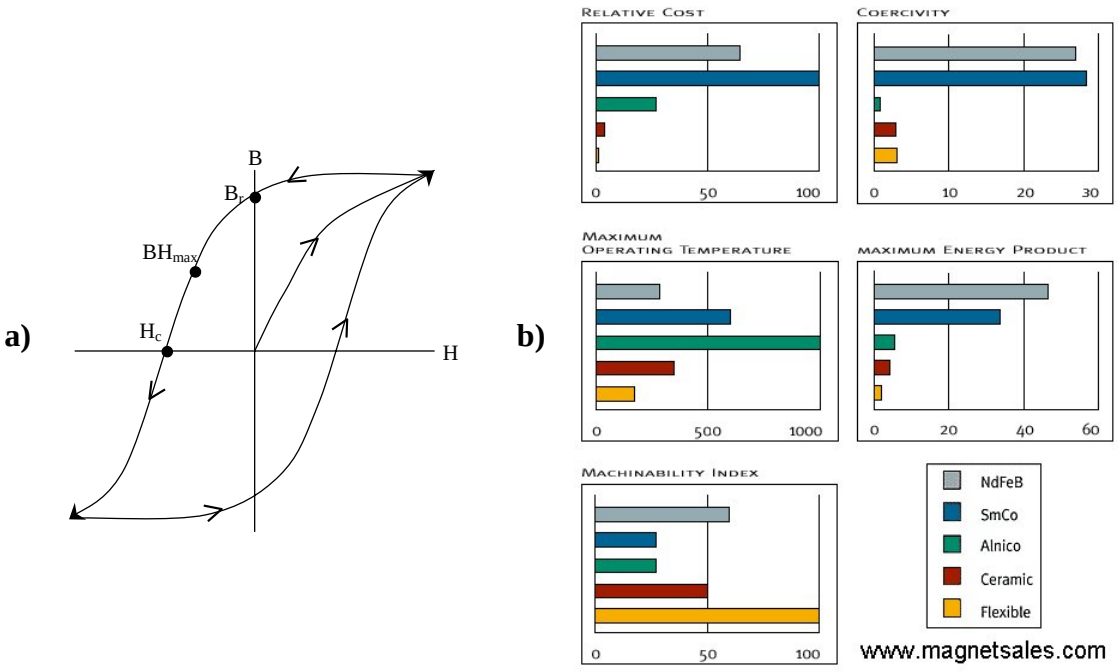

Annex Figure 8: a) B-H curve of a permanent magnet. b)Comparison of different properties among different type of magnetic materials.

For producing enough preload forces over the actuator, the carrier has been pulled down by an NdFeB axially polled magnet. For the Y-stage, small rectangular magnates have been chosen while for the turning stage the choice has been for a disk magnet.
To know the attraction force from a magnet over a ferromagnetic material is not trivial, as it depends on the number and intensity of the flux lines that intercept the target material (function of shape, distance, permeability coefficient, etc.). A

[84] At this time, the strongest magnet commercially available has been being produced by Vacuumschmelze GmbH & Co. It is a NdFeB magnet having an BH_{max} of 451kJ/m^3, 25 times stronger than the maximum available in natural ferrite magnets.

straightforward solution for design purposes is the Force x Airgap distance provided by magnet manufactures (for example, in Annex Figure 10).

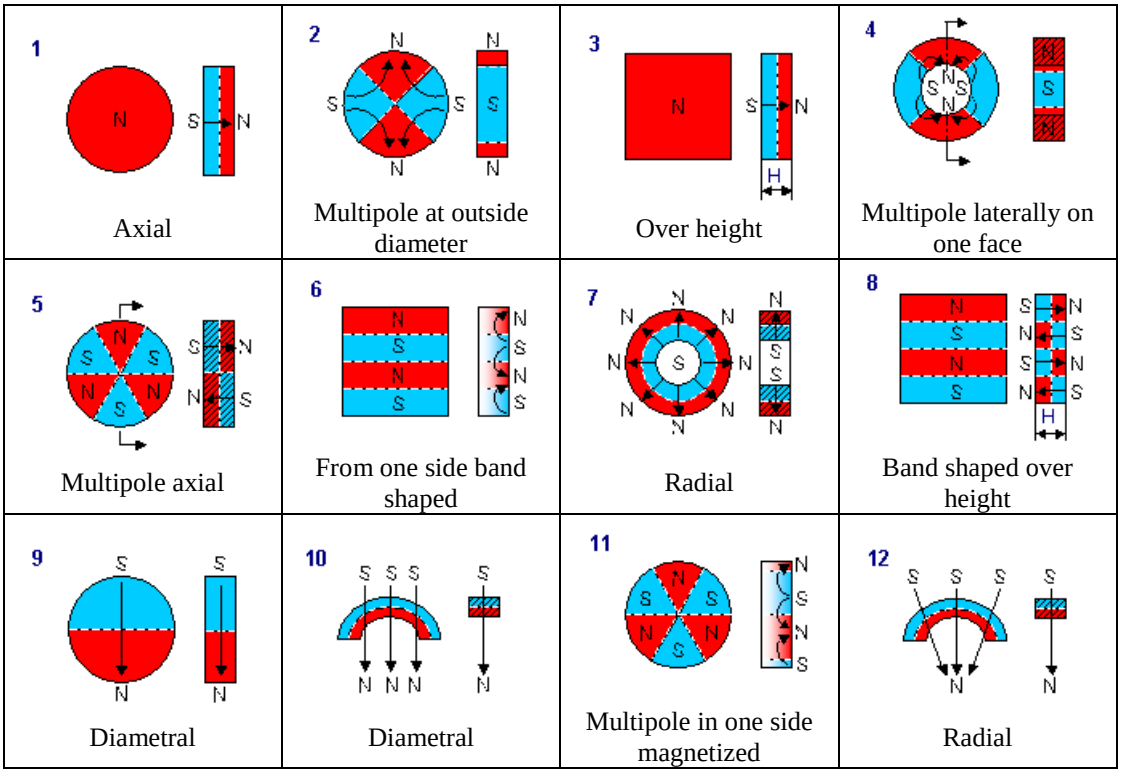

Annex Figure 9: Types of magnet polarizations [103] (not available for all types of materials).

However, the best evaluations are mainly found through FEA analysis[85]. The trust force of a magnet is linear to its length (thickness). The lost of attraction force due to an increase of the airgap can be noticed in Annex Figure 10. The influence of the gap on the force gets smaller as the poled area of the magnet increases. For example, the M601.8 describes a 2mm diameter axial polled NdFeB magnet having 1.2mm thickness. M611.8 is an identical version, except that it has a diameter of 3mm.

Shielding a magnet source has proved to be a hard task during the design phase of a SEM compatible positioning stage. The best approach has been what is called a hands-on approach, making use of a 'sample kit' and a Teslameter for dimensioning a magnetic shield.
This practical approach has been utilized for finding the best configuration to shield the stage. A 'kit' contains a set of materials with different properties and sizes (thickness). With the help of an instrument able to measure the magnetic flux density (Teslameter), it has been possible to measure the flux intensity in a specific region and test the attenuation caused by the shield selection.
As a common rule, the material that must be placed as near as possible to the source (magnet) is the one with the highest saturation point (and often lower magnetic permeability). For example, the first material utilized has been *Netic* Annex Figure 11) and after that, for a very high attenuation of a weak field, a high permeability

[85] Several Finite Element Analyses packages able to model permanent magnets forces are available on the market. A free version, called Finite Element Method Magnetic (FEMM, by David Meeker) is available by download at http://femm.foster-miller.net

material has been thus applied, as for example the Co-Netic. The Teslameter is used to verify the results as well as saturation, when more layers need to be added.

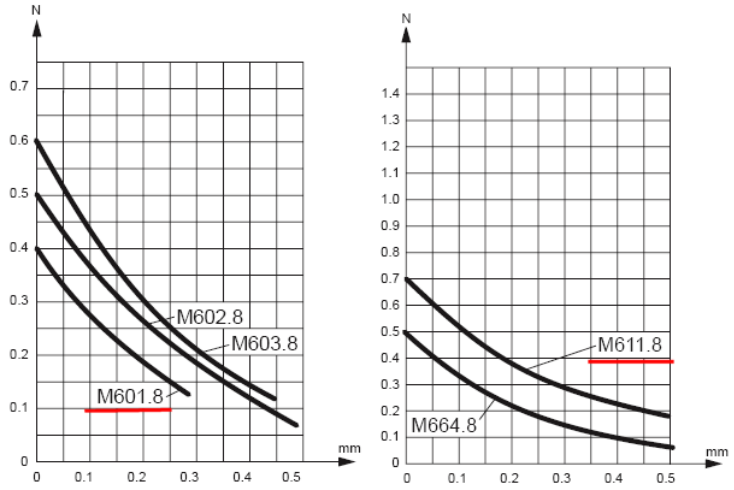

Annex Figure 10: Force x Airgap graph. M601.8 and M611.8 are disk magnets having same material and thickness but different diameters [82].

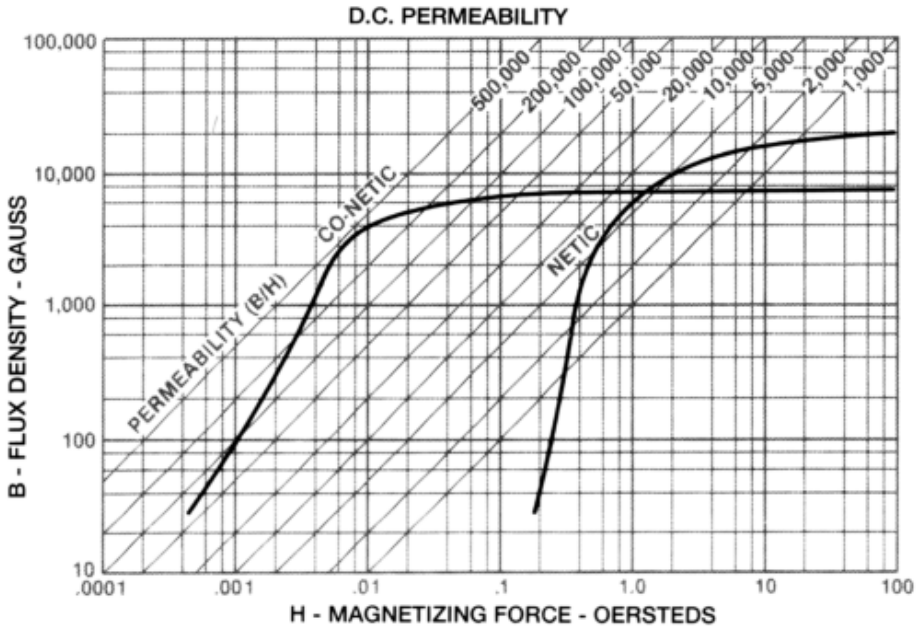

Annex Figure 11: Material behavior of two high permeability magnetic shield alloys [84].

Blank page

Curriculum Vitae

Name:	RABE, Rodolfo Guglielmi
Nationality	Brazilian
Date of birth	27.11.1972
Address	Rte de la Maladiére 20 – Chavannes-Renens CH 1022 - Switzerland
Phone:	+41 (0) 21 693 7833 / +41 079 774 2133
E-mail	rodolfo.rabe@epfl.ch

Education

Since 2002	École Polytechnique Federal de Lausanne – EPFL –Switzerland Doctoral studies in Micromechanics
1999 - 2001	Federal University of Santa Catarina – UFSC – Brazil Master in Engineering Science Mechanical design in Precision Engineering
1991 - 1997	Federal University of Santa Catarina – UFSC – Brazil Mechanical Engineering, area of Production Engineering

Professional Experience

2005 - 2006	Research Engineer at the Swiss Federal Laboratories for Materials Testing and Research – EMPA – in Thun, Switzerland Nanomechanics Group, in the field of in-situ indentation and scratching in a SEM.
2002 - 2005	Research assistant at École Polytechnique Federal de Lausanne, Laboratoire de Systèmes Robotiques – LSRO. European project ROBOSEM – Robots in the Scanning Electron Microscope
2001 - 2002	Research Engineer at the Swiss Federal Laboratories for Materials Testing and Research – EMPA – in Thun, Switzerland. Nanomechanics Group In-situ tests in the SEM
1997 - 1998	Internship at CERTI Foundation – (Reference Centre for Innovative Technologies) – Brazil Mechaoptoelectronic group Design and detailing of the mechanical modules for measurement systems
1993 - 1995	Internship at CERTI Foundation – (Reference Centre for Innovative Technologies) – Brazil Metrology and Automation group University program for young researches, a CNPq program. (National Council for Scientific and Technological Development)

List of publications

R. Rabe, J.-M. Breguet, P. Schwaller, S. Stauss, F.-J. Haug, J. Patscheider and J. Michler, "*Observation of fracture and plastic deformation during indentation and scratching inside the scanning electron microscope*", Thin Solid Films, Volumes 469-470, 2004, Pages 206-213

S. Mazerolle, R. Rabe, T. Varidel, A. Bergander and J.-M. Breguet, "*High thrust Force Linear Actuators*", ISR 2004, International Symposium on Robotics, 23-26 March 2004, Paris, France.

S. Mazerolle, R. Rabe, S. Fahlbusch, J. Michler, J.-M. Breguet, "*High Precision Robotics System for Scanning Electron Microscopes*", IWMF 2004, 15-17 October, Vol. 1, pp. 17-22, Shanghai, China.

J.-M. Breguet, S. Mazerolle, R. Rabe "*The Laboratory in Scanning Electron Microscope concept: Lab-in-SEM*", MECHROB 2004, Special session Micro- and Nanorobotics, September 13-15, Part IV, pp. 1362-1367, Aachen, Germany.

C. Ballif, K. Wasmer, R. Gassilloud, J. Suthues, R. Rabe, C. Pouvreau, Breguet, J.-M. Solletti, A. Karimi, D. Schulz, J. Michler, "*Aspects of cleavage fracture of brittle semiconductors from the nanometer to the centimeter scale*", Nanofair, 14-16 September, St- Gallen, Switzerland.

S. Mazerolle, R. Rabe, T. Varidel, A. Bergander, J-M. Breguet, "*Precision Manipulators operating inside Scanning Electron Microscopes*", Nanofair, 14-16 September, St- Gallen, Switzerland.

Michler J., Rabe R., Bucaille J.-L., Moser B., Schwaller P., Breguet J.-M. "*Investigation of wear mechanisms through in situ observation during microscratching inside the scanning electron microscope*", Wear, 259 1-6, Pages 18-26. 2005.

K. Wasmer, C. Ballif, R. Gassilloud, C. Pouvreau , R. Rabe , J. Michler , J.-M. Breguet, J.-M. Solletti , A. Karimi, D. Schulz . "*Cleavage Fracture of Brittle Semiconductors from the Nanometre to the Centimetre Scale*" Advanced Engineering Materials 7 (5): 309-317. 2005.